Inhibition of respiratory pathogens *Mycobacterium tuberculosis* and SARS-CoV-2 by human serum and monoclonal antibodies

A thesis submitted by Hwa Shi-Hsia

For the degree of Doctor of Philosophy

from University College London

Faculty of Medical Sciences

Division of Infection and Immunology

2021

Declaration

I, HWA Shi-Hsia, confirm that the work presented in this thesis is my own. Where information has been derived from other sources, I confirm that this has been indicated in the thesis.

_____

Abstract

Antibodies are a key host immune response against pathogens. Yet the effects of antibodies on *Mycobacterium tuberculosis* (Mtb) at the cellular level are incompletely understood, as is the effect of HIV co-infection on antibody-mediated immunity to SARS-CoV-2. By investigating these questions at the epicenter of the HIV/TB co-epidemic in KwaZulu-Natal, South Africa, I have: 1) Cloned immunoglobulins from B cells of Mtb-exposed donors and investigated the effect of Mtb-specific polyclonal and monoclonal antibodies on infection of macrophages; 2) Characterised antibody responses in viraemic, virologically suppressed, and HIV-negative Covid-19 patients to determine whether HIV status and viraemia influence neutralization of SARS-CoV-2. Sera from TB-exposed individuals on average increased host cell survival and inhibited intracellular bacterial growth compared to non-specific control serum, although there was a wide range of individual variation. I cloned several Mtb-specific antibodies from South African donors including one which significantly inhibited intracellular bacterial growth in THP-1 monocytes and primary macrophages. I developed a live virus neutralisation assay for SARS-CoV-2 to circumvent the problem of a lentiviral pseudovirus neutralization assay being incompatible with samples containing antiretrovirals for HIV. Among Covid-19 patients, the kinetics of RBD-binding and neutralising antibodies differed little between HIV-uninfected and virologically suppressed people living with HIV (PLWH), whereas viraemic PLWH had a much lower and delayed response. In addition, I observed that plasma from individuals either previously infected with earlier variants of SARS-CoV-2 or vaccinated with AstraZeneca's AZD1222 recombinant adenovirus vaccine showed decreases in neutralisation against newer variants of concern. Taken together, these results demonstrate that antibody-mediated immunity is relevant to the control of TB but is highly heterogeneous. Similarly, there is individual heterogeneity in the neutralisation response to SARS-CoV-2, with the latter partially determined by HIV status and suppression state.

Impact Statement

Mycobacterium tuberculosis (Mtb), the bacillus causing tuberculosis, is commonly thought of as an intracellular pathogen residing in infected cells. Therefore it was assumed in the past that antibodies could have little role in preventing infection or controlling the development of disease. However, a few historical findings and a growing number of studies in the past decade have shown that certain antibody parameters are associated with protection against Mtb infection and progression to TB disease, and a number of human and animal monoclonal antibodies have been identified that have functional effects in blocking specific Mtb target antigens. I have designed a screening pipeline that selects Mtb-specific B cells in an antigen-agnostic manner, rather than screening for only a limited number of known antigens. If scaled up and optimised in future, this could enable the discovery of more Mtb targets that can be inhibited by antibodies. This in turn could then inform the design of new vaccines and immunotherapeutics such as monoclonal antibodies, which may become important tools in combatting TB due to the rise of drug-resistant strains worldwide.

During the Covid-19 pandemic, I developed several methods for quantifying antibodies that bind and neutralise SARS-CoV-2. These include a live virus neutralisation assay that can be used with plasma from people living with HIV (PLWH) on antiretroviral therapy (ART), which cannot be tested in the commonly performed lentivirus-based pseudovirus neutralisation assay. This enabled me and my colleagues to test plasma samples from PLWH in KwaZulu-Natal, South Africa, where there is a very high prevalence of HIV. We have been able to shed more light on antibody responses to SARS-CoV-2 in PLWH who are virologically suppressed with ART versus HIV viraemic, including in the face of variants of concern. Our findings emphasize the importance of ensuring that all PLWH receive appropriate care and medication to decrease the spread of Covid-19. We have collaborated with vaccine clinical trial investigators in South Africa and contributed to decision-making on a national level. I also supported a local biotechnology start-up in testing their monoclonal antibody candidates. Shortages of drugs and vaccines in low- and middle-income countries have shown the importance of building local biotechnology capacity for infectious diseases.

Table of Contents

Declaration 2

Abstract 3

Impact Statement 4

Table of Contents 5

List of Figures 11

Acknowledgements 15

Funding 15

Abbreviations 17

Chapter 1: Introduction 18

1.1 Tuberculosis and *Mycobacterium tuberculosis* 19

1.2 History of TB 21

1.3 Genome and evolution of Mycobacterium tuberculosis 22

1.4 Structure of the bacillus surface 23

1.5 Formation and progression of TB granulomas 26

1.6 Diagnosis of TB disease and latent infection 29

1.7 Chemotherapy 32

1.8 Animal models for tuberculosis disease 32

1.8.1 Zebrafish 33

1.8.2 Mice 33

1.8.3 Guinea pigs 34

1.8.4 Rabbits 34

1.8.5 Nonhuman primates 34

1.9 Macrophages and other phagocytes in *Mycobacterium tuberculosis* infection 36

1.10 Human B cells and antibody responses to Mtb 40

1.11 B cell antigens in *Mycobacterium tuberculosis* 42
1.11.1 Protein antigens 45
1.11.2 Carbohydrate antigens 47
1.12 Isolation of naturally occurring human anti-Mtb monoclonal antibodies 48
1.13 Modern tuberculosis vaccine candidates 48
1.13.1 ChAdOx1-85A/MVA85A 49
1.13.2 BCG revaccination 50
1.13.3 MTBVAC 50
1.13.4 M72/AS01E 50
1.13.5 VPM1002 51
1.14 SARS-CoV-2 and Covid-19 52
1.15 Overview of coronaviruses 52
1.16 SARS-CoV-2 emergence and the Covid-19 pandemic 53
1.16.1 Variants of Concern 57
1.17 Animal hosts and the search for origins 58
1.17.1 Bats as a reservoir of SARS-related CoVs 58
1.17.2 Candidates for natural intermediate hosts 59
1.18 Virus genome, virion structure, and life cycle 61
1.19 Structure and function of the Spike protein 63
1.20 Measurement of neutralising antibodies 66
1.21 Humoral immunity from natural infection 67
1.22 Vaccine development 68
1.22.1 Inactivated viral vaccines 70
1.22.2 Recombinant adenovirus-vectored vaccines 71
1.22.3 Protein nanoparticle vaccine 72
1.22.4 mRNA vaccines 72

1.23 Syndemics: Covid-19, tuberculosis, and HIV 73
1.23.1 Problems with access to care and vaccines 74
1.24 Aims 76
Chapter 2: Materials and Methods 77
2.1 Ethical approval 77
2.2 Clinical samples and primary cell culture 77
2.3 Cell lines 79
2.4 Plasmids 80
2.5 Bacteria 81
2.5.1 Escherichia coli 81
2.5.2 *Mycobacterium tuberculosis* and other mycobacteria 81
2.6 SARS-CoV-2 virus stocks 83
2.7 Flow cytometry and fluorescence-assisted cell sorting (FACS) 83
2.7.1 B cell sorting 83
2.7.2 Bacterial antibody labelling experiments 84
2.7.3 Monocyte and macrophage receptor expression 84
2.8 Primary B cell culture, sampling, and lysis 85
2.9 Human immunoglobulin and Mtb antigen ELISAs 85
2.9.1 ELISA procedures 87
2.10 Antibody cloning and expression 89
2.10.1 Heavy and light chain RT-PCR and cloning 89
2.10.2 Monoclonal antibody production and purification 90
2.11 Western blotting 91
2.12 Immunoprecipitation 92
2.13 Protein sequencing by mass spectrometry 92
2.14 THP-1 monocyte infection with Mtb 92

2.15 Primary macrophage infection with Mtb 93

2.15.1 Intracellular Mtb growth and host cell death measured by flow cytometry 93

2.15.2 Timelapse microscopy 93

2.15.3 Quantitative PCR (qPCR) of Mtb DNA copies 94

2.15.4 RNA-seq of infected macrophages 94

2.16 SARS-CoV-2 receptor-binding-domain ELISAs 95

2.17 Surrogate virus neutralisation test (sVNT) 96

2.18 ACE2 staining 96

2.19 SARS-CoV-2 virus titration and antibody neutralisation assays 97

2.20 SARS-CoV-2 plaque picking 98

2.21 Image analysis 99

2.22 Statistical analysis 100

Chapter 3: Isolation and characterisation of human monoclonal antibodies against *Mycobacterium tuberculosis* 101

3.1 Introduction 101

3.2 Results 103

3.2.1 Serum IgG from South African healthy volunteers and TB patients reacts with LAM and cell wall proteins 103

3.2.2 B cells binding whole Mtb can be sorted from peripheral blood and lung lymph nodes 107

3.2.3 Characterization of human anti-Mtb monoclonal antibodies 113

3.2.4 Monoclonal antibodies react with mixed Mtb cell wall proteins but not purified Acr, ESAT-6, or HBHA 122

3.2.5 Monoclonal antibody P2E04 targets an unidentified immunodominant protein 126

3.3 Discussion 130

Chapter 4: Human serum and monoclonal antibodies can modulate *Mycobacterium tuberculosis* growth in monocytes and primary macrophages 133

4.1 Introduction 133

4.2 Results 135

4.2.1 Development of a flow cytometry-based assay for antibody-dependent phagocytosis and intracellular Mtb growth 135

4.2.2 mAb P2E04 reduces host cell death and intracellular bacterial load in primary monocyte-derived macrophages 137

4.2.3 Serum from TB-exposed individuals decreases intracellular bacterial load and THP-1 monocyte death 139

4.2.4 Different monoclonal antibodies can exacerbate or inhibit intracellular Mtb growth in THP-1 141

4.2.5 Effects of antibodies on Mtb growth in co-culture with primary human macrophages 145

4.2.6 P2E04 affects intracellular Mtb growth in primary MDM in a donor-dependent manner 149

4.2.7 Differential gene expression in the presence of P2E04 153

4.3 Discussion 158

Chapter 5: Effects of HIV status and SARS-CoV-2 Variants of Concern on antibody responses in South African Covid-19 patients 161

5.1 Introduction 161

5.2 Results 163

5.2.1 Development of an ELISA for anti-SARS-CoV-2 receptor-binding domain antibodies 163

5.2.2 Development of an immunofocus asssay for quantifying infectious SARS-CoV-2 and neutralising antibodies 165

5.2.3 Antibody responses in Covid-19 patients in the first epidemic wave with and without HIV are similar 171

5.2.4 Antibody responses in the second epidemic wave dominated by the Beta variant of concern are impaired in people with HIV viraemia..... 173

5.2.5 Suitability of a surrogate neutralisation rapid test kit in South African patient samples..... 177

5.2.6 Neutralisation potency of plasma from vaccine clinical trial participants is decreased against Beta VOC..... 179

5.2.7 Two camelid nanobodies retain high neutralising potency against Beta VOC 180

5.2.8 Control of furin cleavage site mutations and plaque cloning a wild-type isolate 181

5.3 Discussion 185

Conclusions..... 190

References..... 194

Appendix A: Sequences of monoclonal antibody variable regions 239

List of Figures

Figure 1: Estimated incidence of TB (all forms) per 100,000 population, 2017 20
Figure 2: Relationship between GDP per capita and undernutrition with TB incidence. 20
Figure 3: Evolution of the MTBC showing characteristic deletions 23
Figure 4: RD1 (shaded box) and its open reading frames..... 23
Figure 5: Structure of the surface of Mtb..... 24
Figure 6: M. bovis BCG cultured without detergent, showing the electron-transparent capsule, and with detergent, showing a much reduced capsule. 26
Figure 7: Phenotypes of Mtb-infected macrophages.. 28
Figure 8: Development of the tuberculous granuloma..... 28
Figure 9: Granuloma surrounded by lymphocytes and secondary lymphoid follicle.41
Figure 10: Overview of global TB vaccine development pipeline, 2019. 49
Figure 11: Electron micrograph of human coronavirus 229E..... 52
Figure 12: Hypothetical mechanisms of SARS-CoV-2 damage to vascular endothelium..... 56
Figure 13: Phylogenetic tree of 21 coronavirus strains..... 59
Figure 14: Trimeric Class 1 fusion proteins of coronavirus, influenza virus, HIV, and Ebola virus.. 63
Figure 15: S1/S2 cleavage sites in selected Coronaviridae. Polybasic motifs highlighted in red.. 64
Figure 16: Two entry pathways of SARS-CoV-2. 65
Figure 17: Relationship between antibody neutralisation and protection based on clinical trials of seven vaccines..... 70
Figure 18: The effects of lockdown on TB case notifications in India. 73
Figure 19: Comparison of Covid-19 and TB vaccine development 75
Figure 20:Serum samples binding to Mtb lipoarabinomannan. 104
Figure 21:Serum samples binding to Mtb cell wall proteins. 105
Figure 22: Half-maximal effective dilution (EC_{50}) for serum samples binding to Mtb lipoarabinomannan and soluble cell wall proteins. 106

Figure 23: IgG secretion by single sorted B cells cultured on irradiated H1299-feeder cells. 108
Figure 24: Sorting Mtb-binding B cells from healthy donor 6037 and TB patient donor 8185. 108
Figure 25: Memory population of Mtb specific B cells. 109
Figure 26: Gating strategy for sorting Mtb-binding, non-IgM, memory B cells. 110
Figure 27: Attempt to sort Mtb-specific from environmental mycobacteria-binding B cells. 112
Figure 28: Binding of monoclonal antibodies (September 2017 batch) to bacteria 115
Figure 29: Gating of Mtb labelled with monoclonal antibody samples. 116
Figure 30: Binding of monoclonal antibodies (January 2018 batch) to bacteria 118
Figure 31: Binding of PID 0219 lymph node monoclonal IgA compared to control antibodies. 119
Figure 32: Binding of PID 0219 lymph node monoclonal IgG compared to other mAbs and control antibodies. 120
Figure 33: Monoclonal antibodies do not cross-react with whole dried E. coli. 122
Figure 34: Monoclonal antibody TB024PBh037 binds to lipoarabinomannan. 123
Figure 35: Monoclonal antibodies bind to soluble cell wall proteins. 123
Figure 36: Monoclonal antibodies do not target alpha-crystallin, ESAT-6, or HBHA. 125
Figure 37: mAb P2E04 labels an immunodominant band in Mtb cell wall proteins and whole cell lysate. 126
Figure 38: Western blots of attempts to immunoprecipitate the antigenic target of mAb P2E04 (serial number 2392). 127
Figure 39: Bands selected for mass spectrometry sequencing. 128
Figure 40: Primary monocyte-derived macrophages display CD32, CD64, and CD89, but not CD16. 135
Figure 41: THP-1 monocytes display CD32, CD64, and CD89, but not CD16. 136
Figure 42: Single monocyte/macrophage populations infected with mCherry-expressing Mtb and stained with fixable viability dye. 137
Figure 43: Fraction of infected macrophages depends on source of antibodies for opsonised Mtb. 138

Figure 44: Low-dose interferon gamma aids in intracellular bacterial control without affecting monocyte viability. 139
Figure 45: Serum from TB-exposed healthy donors decreases intracellular bacterial load and enhances monocyte survival..... 140
Figure 46: Specific mAbs can enhance or inhibit total intracellular bacterial load (integrated MFI) in THP-1 monocytes..... 142
Figure 47: mAb P2E04 inhibits intracellular bacterial growth independently of phagocytosis at early timepoints. 144
Figure 48: MAb HD001HBMEMh095 and Hoechst 34580 independently inhibit mtb growth in co-culture with macrophages. 146
Figure 49: MAbs P2C02 and P2F10 enhance bacterial growth and host cell death over FBS-only medium. 147
Figure 50: mAb P2E04 inhibits Mtb growth in co-culture with MDM from Donor 0011. 148
Figure 51: mAb P2E04 exacerbates Mtb growth in co-culture with MDM from Donor 0018. 149
Figure 52: mAb P2E04 inhibits intracellular Mtb growth in Donor 0044 monocyte-derived macrophages in two independent experiments. 150
Figure 53: Intracellular Mtb fluorescence (arbitrary units) in monocyte-derived macrophages..... 151
Figure 54: gyrA qPCR of purified Mtb CDC1551 DNA. 152
Figure 55: gyrA copies in infected MDM cultures normalised to normal medium control per each donor and experiment. 153
Figure 56: mAb P2E04 slightly decreases uptake of Mtb CDC1551 in monocyte-derived macrophages by 6 hours post-infection..... 154
Figure 57: Quality of cDNA libraries and sequencing..... 154
Figure 58: Principal component analysis of differentially expressed genes in macrophages that were uninfected, low infected, medium infected, or high infected, with or without mAb P2E04. 157
Figure 59: Signal intensity (AUC) but not endpoint titre is affected by ELISA incubation time..... 164
Figure 60: Immunostained SARS-CoV-2 foci in Vero E6 cells at 48 hours post-infection..... 166

Figure 61: Confocal images of cells stained with ACE2-stained (yellow) and DAPI (blue). 166
Figure 62: H1299-ACE2 cell lines are more permissive to SARS-CoV-2 infection than Vero E6 or parental H1299 cells. 167
Figure 63: Morphology of infected foci differs between Vero E6 cells and H1299-ACE2 cell lines.. 168
Figure 64: Infected H1299-ACE2-C7 cells stained with different anti-S primary antibodies. 169
Figure 65: Vero E6 cells infected with isolate 6518 show heterogenous focus sizes. 170
Figure 66: Similar anti-RBD antibody responses in HIV-negative and PLWH in the first wave. 172
Figure 67: Live virus neutralisation titres are similar in HIV-negative and PLWH in the first wave. 173
Figure 68: IgG, IgA, and neutralising responses in HIV-negative and virologically suppressed PLWH are significantly higher than viraemic PLWH in the second wave. 175
Figure 69: Live virus neutralisation titres at ~1 month post-infection are significantly higher in HIV-negative Covid-19 patients than PLWH, and higher in virologically suppressed than viraemic PLWH in the second wave. 177
Figure 70: Surrogate virus neutralisation test (sVNT) correlates strongly with wave-concordant live virus neutralisation assay (LVNA) in South African patient samples. 179
Figure 71: AZD1222 vaccinee and infected placebo recipient plasma neutralisation decreases against Beta virus. 180
Figure 72: Two nanobodies retain high neutralisation potency against both D614G (left) and Beta (right). 181
Figure 73: SARS-CoV-2 infected Vero E6 cells stained with Neutral Red. 182

Acknowledgements

Firstly I would like to thank my supervisor, Alex Sigal, for the opportunity to work on a unique and fascinating project, and all his support and advice over the years.

Colleagues who helped me with the Mtb project specifically were: Deeqa Mahamed, who set up the macrophage and Mtb culture systems and was an unfailing source of encouragement; Yashica Ganga for all her help with samples and tissue culture and her patience and good humour; Hylton Rodel, our lab's programming fundi; Mallory Bernstein for data analysis and statistics; and Ntombi Benede and Gila Lustig who also assisted with data analysis. During South Africa's initial lockdown when students were not permitted on campus, Yashica, Laurelle Jackson, and Sandile Cele did a tremendous amount of work in obtaining virus isolates that allowed me to set up the methods and experiments described in the final section. Jumari Snyman from the labs of Thumbi Ndung'u and Jaclyn Mann has been my "partner in crime" for most of the Covid-19 serology work.

I would also like to thank external collaborators who have been very generous with their time and resources: Alejandro Balazs who hosted me at his lab at the Ragon Institute for two months and taught me how to make recombinant antibodies; Jacqueline Achkar (Albert Einstein College of Medicine) and Clemens Hermann from the lab of Jonathan Blackburn (University of Cape Town) for offering to help us identify my monoclonal antibody.

Finally I would like to thank my partner and my family for all their love and support, especially my father Hwa Jen whose experience as a TB survivor inspired me to study infectious diseases and *Mycobacterium tuberculosis* in the first place.

Funding

The TB project was funded by the European Commission as part of the TBVAC2020 consortium, as well as by the Max Planck Institute for Infection Biology.

The SARS-CoV-2 work was funded by a grant from the Bill and Melinda Gates Foundation to Alex Sigal (Investment INV-018944).

I would also like to thank Keystone Symposia for scholarships to attend the B and T cell symposium in 2019, and the tuberculosis symposium in 2020.

Abbreviations

BCG	Bacille Calmette-Guerin
Covid-19	Coronavirus Disease 2019
EC_{50}	Half-maximal effective concentration (or dilution)
ELISA	Enzyme-linked immunosorbent assay
FACS	Fluorescence-assisted cell sorting
FFU	Focus-forming unit
HIV	Human immunodeficiency virus
Ig	Immunoglobulin
IGRA	Interferon gamma release assay
LTBI	Latent tuberculosis infection
mAb	Monoclonal antibody
MDM	Monocyte-derived macrophage
Msmeg	*Mycobacterium smegmatis*
Mtb	*Mycobacterium tuberculosis*
NT_{50}	50% neutralisation titre
PBMC	Peripheral blood mononuclear cells
PLWH	Person/people living with HIV
PTB	Pulmonary tuberculosis
SARS	Severe Acute Respiratory Syndrome
SARS-CoV-2	Severe Acute Respiratory Syndrome Coronavirus 2
TB	Tuberculosis
TST	Tuberculin skin test
VOC	Variant of concern

Chapter 1: Introduction

Tuberculosis caused by *Mycobacterium tuberculosis* (Mtb) is a global disease of poverty with 10.4 million people developing the disease and 1.7 million dying of it in 2016[1]. In addition, an increasing percentage of cases are multi-drug-resistant (MDR) or extensively drug-resistant (XDR), resulting in expensive and prolonged chemotherapy that often has permanently disabling adverse effects, despite which only a minority of XDR cases are successfully treated. The only currently licensed vaccine, BCG (*Mycobacterium bovis* Bacille Calmette-Guerin) has low efficacy against the development of pulmonary TB, and cannot be given to immunosuppressed persons. This is a serious limitation in regions where TB and HIV are co-epidemic.

A potential route to solving the question of preventing TB infection and developing a better vaccine is to examine immune responses in persons who have been heavily exposed to TB by occupation or environment, yet remain clinically healthy for long periods of time, e.g. healthcare workers. Such persons may either have sterilising immunity, or be latently infected but controlling the bacteria. While phagocytic cells such as neutrophils and macrophages have been the most studied immune system component in TB due to the bacteria's ability to survive and proliferate intracellularly, there are accumulating indications that B cells and antibodies also play a role in controlling TB infection. I aimed to identify individuals living in and near Durban, South Africa, a highly TB-endemic region, who have functional anti-Mtb antibodies, and to isolate monoclonal antibodies from them to determine which aspects of the antibody response are relevant to protection against tuberculosis.

This work was undertaken as part of the TBVAC2020 consortium funded by the European Commission, whose goal is to discover new TB vaccine candidates and correlates of protection[2]. Our role as members of WP1: Vaccine Discovery was to identify B cell antigens targeted by antibodies with a functional role in modulating phagocytosis by and infection of macrophages. If identified, such antigens could be included in future development recombinant protein, DNA, or live attenuated vaccines, and the presence of specific antibodies could be used as a correlate of protection in vaccine clinical trials.

Subsequently during the Coronavirus Disease 2019 (Covid-19) pandemic caused by Severe Acute Respiratory Syndrome Coronavirus 2 (SARS-CoV-2), I volunteered to use my experience in antibody and virus titration assays to to develop methods that would enable us to understand the biology of SARS-CoV-2 strains circulating in South Africa, as well as immune responses to infection in this high-TB, high-HIV prevalence population.

1.1 Tuberculosis and *Mycobacterium tuberculosis*

Tuberculosis (TB) caused by *Mycobacterium tuberculosis* (Mtb) is a global disease with an estimated 10.0 million new cases and 1.4 million deaths in 2019, a disproportionate number of which were among people with HIV[3]. While incidence and deaths have declined in most countries over the past 20 years, we have failed to meet the WHO End TB Strategy milestones for 2020. In addition to morbidity and mortality, 49% of people with TB suffer catastrophic costs of >20% of their household income.

Two-thirds of the global TB burden is shared by eight high-incidence countries: India, Indonesia, China, the Philippines, Pakistan, Nigeria, Bangladesh, and South Africa. Approximately two billion people are latently infected with Mtb but show no clinical signs (LTBI)[3]. However they are at risk of reactivation and developing active TB later in life or upon immunosuppression, such as in the context of uncontrolled HIV infection which can increase the risk of TB by 26-fold. An estimated 8.2% of TB patients are people living with HIV (PLWH), and mortality in coinfected persons is very high, estimated at 374,000 out of 1.7 million TB deaths in 2016[4].

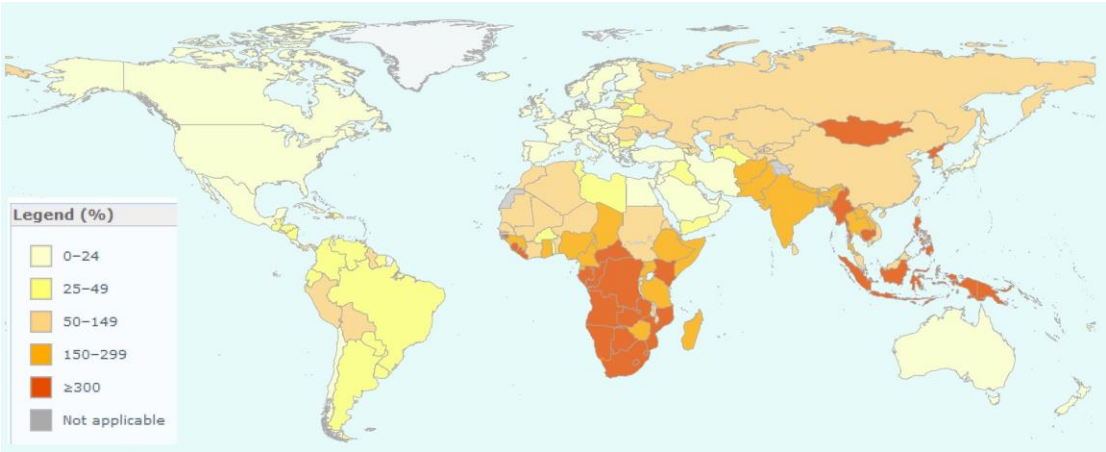

Figure 1: Estimated incidence of TB (all forms) per 100,000 population, 2017 (adapted from WHO Global Health Observatory http://gamapserver.who.int/gho/interactive_charts/tb/cases/atlas.html)

TB is a disease of poverty and its incidence on a per-country basis is correlated with low income and undernutrition (Figure 2).

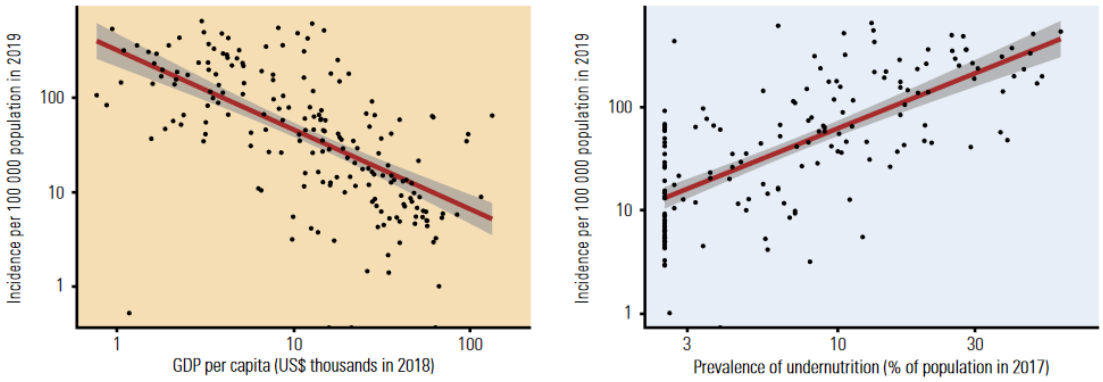

Figure 2: Relationship between GDP per capita and undernutrition with TB incidence (from WHO Global Tuberculosis Report 2020).

The typical symptoms of pulmonary TB include: persistent cough, fever, night sweats, and weight loss[5,6]. Other forms of extrapulmonary TB include abdominal TB, where infection starts in gut-associated lymphoid tissue. This could occur from auto-inoculation in an individual with pulmonary TB when sputum is coughed up and swallowed, or dissemination from the lungs via the vascular route, or dissemination from other organs. Primary infection in cases of abdominal TB can be caused by ingestion of contaminated food or milk (e.g. from a cow with bovine tuberculosis)[7].

TB meningitis mostly occurs in children and can be life-threatening or disabling. Children are also susceptible to miliary TB where the bacilli become widely disseminated via the bloodstream[8]. TB lymphadenitis can occur in both children and adults; in extreme cases the swollen lymph nodes can break through the skin. In Europe it was historically known as scrofula or the "King's Evil" because of the belief that it could be cured by the divine touch of royalty[9].

1.2 History of TB

Mycobacterium tuberculosis was identified as the aetiologic agent of tuberculosis by Robert Koch in 1882[10], by culturing Mtb from various human and bovine TB cases on solidified serum, followed by inoculating guinea pigs. This resulted in the formation of rapidly developing lymphadenitis near the injection site, followed by dissemination to the spleen and liver; the bacilli could be re-cultured from the infected guinea pigs' lymph nodes. He observed that their morphology was "surprisingly like that of the leprosy bacillus", since identified as its congener *M. leprae*. The bacilli were seen in small aggregates and often within tissue cells, but at the edges of "large, cheesy masses" (now referred to as granulomas undergoing caseous necrosis) they were found in large numbers outside host cells.

Mycobacterium tuberculosis is a member of the eponymous Mycobacterium Tuberculosis Complex (MTBC) along with *M. africanum* (which also causes pulmonary tuberculosis, mainly in west Africa)[11,12], *M. bovis* (bovine tuberculosis, an important agricultural, wildlife[13], and zoonotic pathogen), *M. microti* (vole bacillus)[14,15], *M. canetti*, and several others. Based on the low frequency of synonymous mutations in 26 essential genes across 842 MTBC isolates, MTBC was estimated to have emerged about 15,000 to 20,000 years ago[16]. Ancient MTBC DNA and cell wall lipids have been detected in human remains as old as 9,000 and 11,000 years[17]. *M. canetti*, which has a smooth colony phenotype *in vitro* unlike most other MTBC members, was the first lineage to diverge[18].

1.3 Genome and evolution of Mycobacterium tuberculosis

The genome of the virulent strain H37Rv was first published in 1998[19]. It is 4,411,529 base pairs (bp) long with 65.6% GC content, with 3924 predicted open reading frames. Among its distinctive features are a huge number of enzymes, about 250, involved in lipid metabolism. These include families of enzymes involved in degrading host fatty acids, as well as enzymes involved in the synthesis of the unique mycobacterial mycolic acids. Compared to nontuberculous mycobacteria (NTM), members of the MTBC have diminished genomes showing the loss of genes needed for extracellular survival[17].

The *M. bovis* Bacillus Calmette-Guerin (BCG) vaccine was generated by passaging an *M. bovis* isolate from infected cow's milk 230 times on bile potatoes[20]. By this point, it was attenuated in all animal species tested; guinea pigs apparently cleared the infection by 6 months with no lasting lesions. The authors and others found no reversion to virulence after inoculating thousands of animals. We now know that the major factor in the attenuation of BCG is a large 9.5 kb deletion known as Region of Difference 1 (RD1) which was identified by subtraction hybridisation of Mtb strain H37Rv DNA against BCG Connaught DNA[21]. Two other regions were deleted in some but not all BCG strains. Further hybridisation studies identified a total of 16 deleted regions in in *M. bovis*, whereas RD1 was the only that was present in virulent *M. bovis* but absent in all BCG strains[22,23].

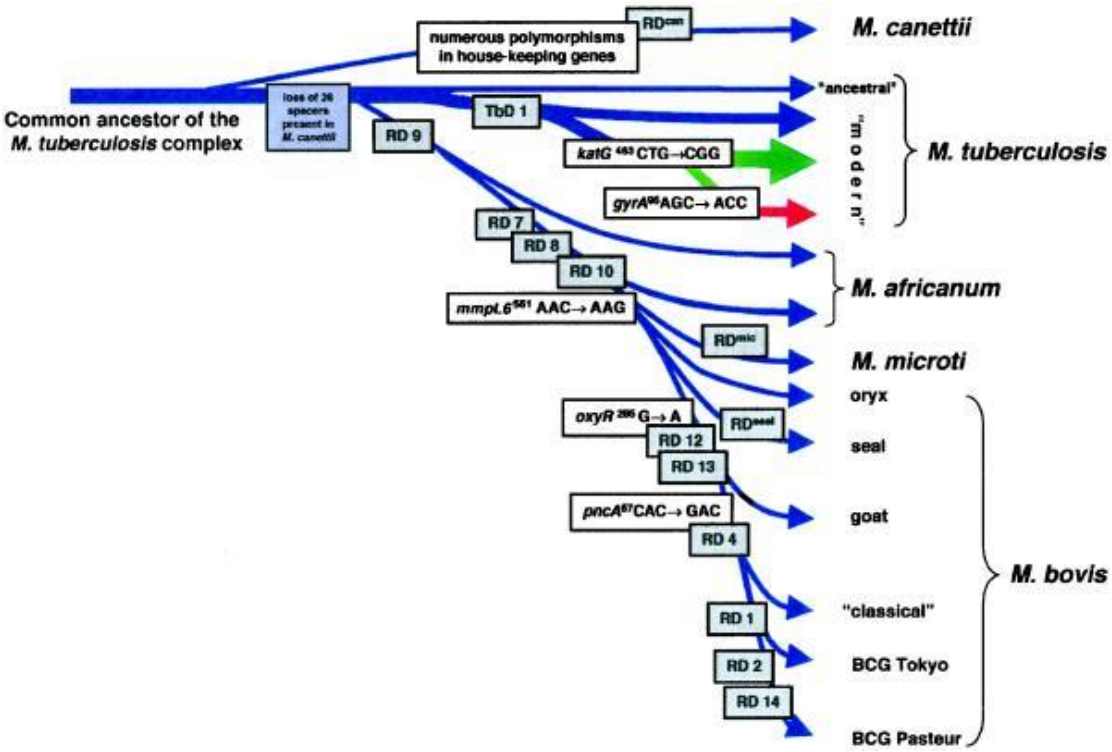

Figure 3: Evolution of the MTBC showing characteristic deletions (from Brosch 2002, "A new evolutionary scenario for the Mycobacterium tuberculosis complex"[18])

RD1 encodes a number of virulence factors and is required for the aggregation of infected macrophages that leads to granuloma formation[24]. Complementation of BCG or *M. microti* with RD1 causes them to develop a spreading colony phenotype in vitro and to become more virulent in vivo[25].

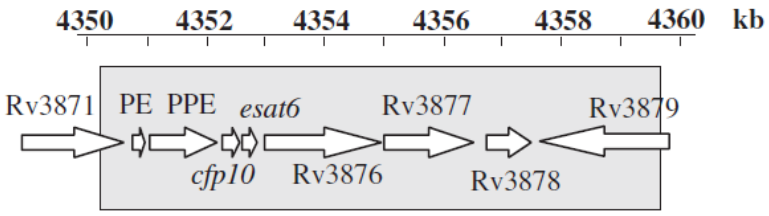

Figure 4: RD1 (shaded box) and its open reading frames. From Pym 2002[25].

1.4 Structure of the bacillus surface

Mtb are rod-shaped bacilli approximately 1-4 µm long and 0.3 -0.6 µm in diameter[26]. The cell wall of mycobacteria is a multi-layered structure. Outside the bacterial plasma membrane is a layer of peptidoglycan (PG) which is more heavily cross-linked than

that of *E. coli*, followed by a layer of arabinogalactan which is covalently tethered to the PG[27], followed by a unique membrane composed of mycolic acids known as the mycomembrane[28], outer membrane, or envelope. This is surrounded by an outer capsule of carbohydrates.

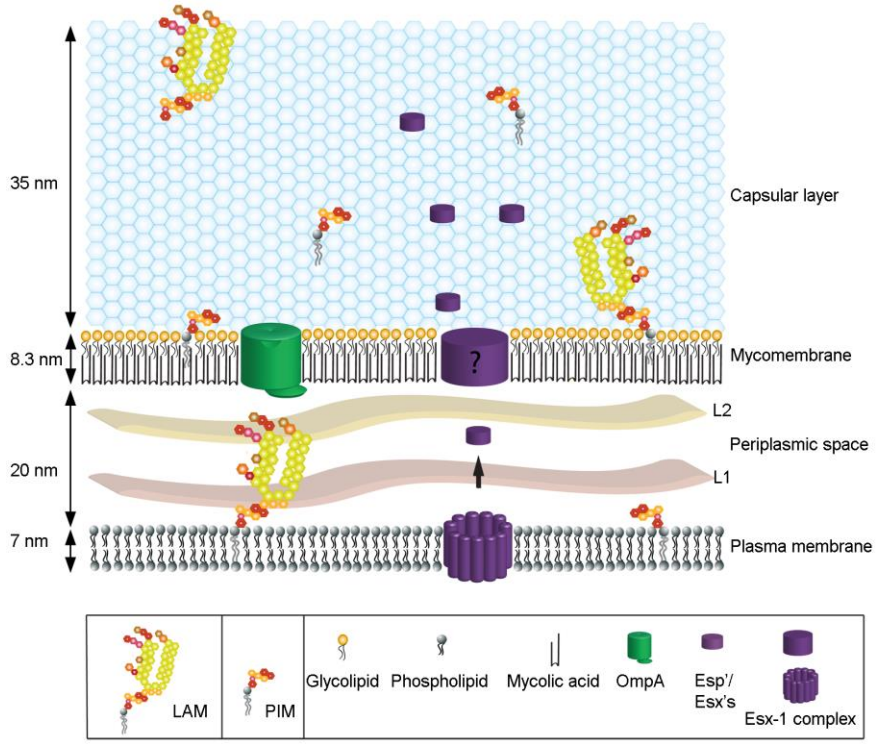

Figure 5: Structure of the surface of Mtb showing the plasma membrane, outer membrane (mycomembrane), and capsule. From Sani 2010[28].

The plasma membrane is composed of phospholipids including phosphatidylinositol mannosides (PIMs) which are unique to Actinomycetes[26]. Liporabinomannan (LAM) and lipomannan are glycolipids associated with the plasma membrane but LAM is also shed abundantly in infected hosts. Pathogenic mycobacteria have LAM capped with mannose residues (ManLAM) whereas nonpathogenic mycobacteria have PILAM capped with phosphatidyl inositol[29].

The inner membrane contains a number of Type VII secretion systems encoded in genetic loci named ESX-1 to -5. The genes forming the transmembrane secretion machinery are named eccA through eccE (ecc = *esx* conserved component) followed by a number for the locus[30]. These loci also encode a number of small proteins which

are transport substrates, notably the virulence factors ESAT-6/CFP-10 described below.

The mycomembrane is composed of mycolic acids, very long-chain branched fatty acids (70-90 carbons long)[26] that are either covalently attached to the arabinogalactan layer of the cell wall, or non-covalently associated such as trehalose dimycolate (TDM). These include alpha-, methoxy-, hydroxy-, and keto-mycolates. Mycolic acids contain cyclopropane groups, and the cyclopropane synthetase *pcaA* is a criticial factor for the formation of the cord-shaped bundles of bacilli that are also associated with virulence *in vivo*[31,32]. The hma gene is necessary for synthesis of the hydroxy- and ketomycolic forms[33].

The protein composition of the outer membrane is less well characterised. One empirically confirmed outer membrane protein (OMP) is the porin OmpATb, which was identified based on homology to *E. coli* OmpA[34], but there are few other instances. A bioinformatics approach to predict if proteins could be OMPs based on their β-strand content and amphiphilicity of the β-strands yielded 144 proteins of unknown function, and the authors validated this approach by showing that two of the predicted proteins were in fact on the surface of the bacteria[35].

The bioinformatics approach risks missing plasma membrane proteins that are attached by other means than transmembrane helices, e.g. lipoproteins that have a conjugated lipid moiety, or subunits of a complex that associate with transmembrane subunits. In an empirical approach, Xiong et al. used a high-urea buffer to remove contaminating cytosolic proteins from plasma membrane fractions prior to electrophoresis and LC-MS/MS peptide sequencing, which identified 349 membrane proteins, 84 of which were described for the first time. 30.9% of the identified proteins were predicted to be involved in cell wall and cell processes[36].

The outermost layer of the mycobacterial envelope is known as the capsule, which appears as a transparent zone in transmission electron microscopy[28,37]. This is composed of primarily of polysaccharides and proteins, with low lipid content. Many of these proteins are exported by ESX-1. Major components of the capsule include alpha-glucan, arabinomannan (AM), and phosphatidylinositol mannosides (PIMs).

Capsular lipids include trehalose dimycolate (TDM), phenolic glycolipids, phthiocerol dimycocerosate (PDIM), and lipo-oligosaccharides[38].

Mtb capsules are much thicker than those of nonpathogenic species such as *M. smegmatis* and have higher glycan and lower protein content. There are conflicting reports as to whether the capsule promotes or inhibits phagocytosis. Stokes et al. found that Mtb Erdman with intact capsules was less efficiently ingested than those with capsules damaged by sonication, by several types of macrophages (mouse peritoneal and alveolar macrophages, human primary monocyte-derived macrophages and THP-1 cell line-derived macrophages). Compared to *M. avium* (an opportunistic pathogen), *M. intracellulare*, or *M. smegmatis*, Mtb was far less efficiently phagocytosed, and the increase following sonication was far greater[39]. On the other hand, Sani et al. found that intact *M. bovis* BCG was more efficiently phagocytosed than BCG with capsules stripped using Tween 80 detergent, by human MDM[28]. However, this discrepancy could be due to differences between Mtb and BCG, as well as treatment method (partial damage by sonication versus complete stripping with Tween 80).

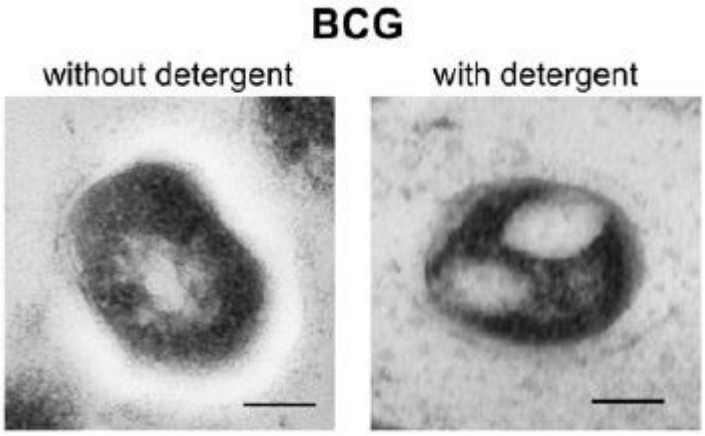

Figure 6: M. bovis BCG cultured without detergent, showing the electron-transparent capsule, and with detergent, showing a much reduced capsule. From Chen 2016[37].

1.5 Formation and progression of TB granulomas

Pulmonary TB infections are initiated by inhalation of aerosolised droplet nuclei smaller than 5 μm which can penetrate deep into the lungs, as larger droplets tend to settle on the ciliated surfaces of the upper airway, are transported to the pharynx, and swallowed. These small droplet nuclei are estimated to contain 1 to 3 bacilli[40]. The

absolute minimal infectious dose of Mtb is estimated to be as low as 1 colony-forming unit (CFU) based on aerosol challenge studies in rabbits[41]. In humans however, prolonged exposure to infected household contacts is usually necessary for transmission to another individual, hence the probability of a single droplet causing infection is low[40].

The initial response of the innate immune system is similar for many bacteria and other foreign particles. Bacilli are quickly ingested by phagocytes such as neutrophils[42] and alveolar macrophages, which may be killed and then ingested by other phagocytes (discussed further below). Eventually a granuloma consisting of an aggregate of infected macrophages forms. Mtb lipids including ketomycolic acids and TDM trigger various pathological changes in the infected as well as neighbouring macrophages, via shedding of Mtb cell wall lipids in extracellular vesicles. Some are converted into foamy macrophages, so called because of their lipid droplet-filled appearance. This provides a rich carbon source for Mtb growth[43].

Another granuloma-associated type of macrophages are epithelioid cells having complex membrane extensions interdigitating with their neighbours[44]. This represents an effort of the host to wall off invading organisms, but bacteria which can survive and replicate intracellularly such as pathogenic mycobacteria and *Salmonella*, hijack this mechanism to obtain new host cells[45].

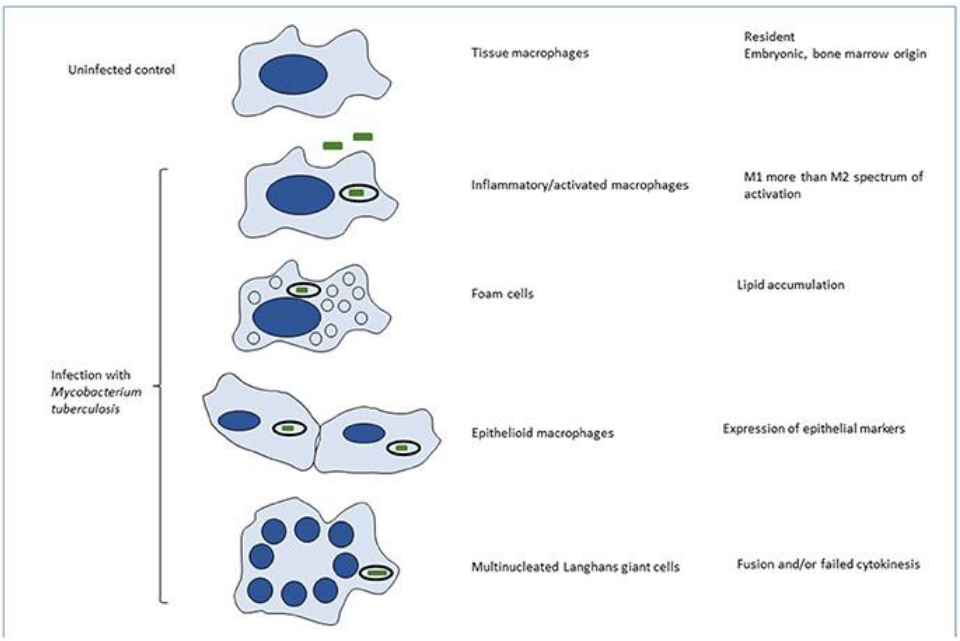

Figure 7: Phenotypes of Mtb-infected macrophages. From Marakalala 2018[46].

Granuloma formation also involves epithelial cells adjacent to the infected macrophage aggregates which are induced to express matrix metalloproteinase 9 (MMP9) by the secreted virulence factor ESAT-6[47]. Eventually a fibrotic capsule forms around the granuloma.

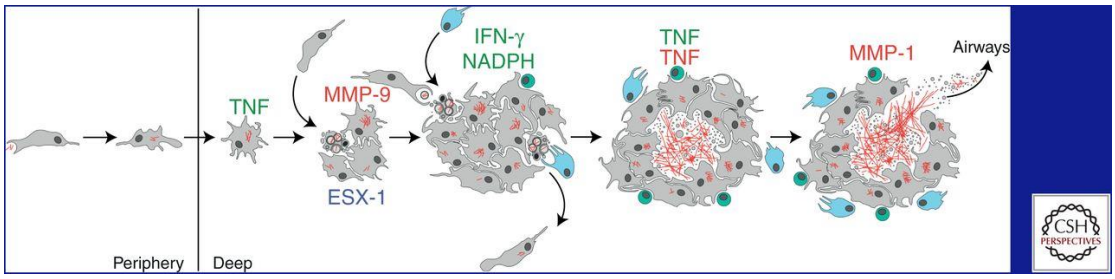

Figure 8: Development of the tuberculous granuloma. From Pagán & Ramakrishnan, 2015[45].

The concentration of tumour necrosis factor alpha (TNFα) is critical for the containment of bacteria in granulomas: it appears to be important for inhibiting bacterial growth in animal models[48], and people undergoing anti-TNF antibody therapy (e.g. infliximab) for autoimmune diseases are at high risk of TB reactivation[49]. Excessive concentrations of TNF on the other hand cause macrophages to undergo

necrosis. Infected macrophages can also be killed by cytotoxic T lymphocytes after adaptive immunity has formed[40].

Dead macrophages in the centre of the granuloma break down into a substance called caseum because of its lipid-rich, cheesy appearance, which contains abundant bacteria[43]. At this point the bacteria may grow extracellularly and may form long cord-like structures that are too large for phagocytes to engulf[50]. This also occurs with other pathogenic mycobacteria such as *M. abscessus* and is associated with higher virulence[51,52].

In human pulmonary TB, large granulomas eventually fill up the alveoli and airways, forming branching structures recently revealed by three-dimensional micro-CT studies of tissue from PTB patients who underwent clinically indicated resection of damaged lungs[53]. In advanced granulomas, the caseum liquefies and the fibrotic capsule ruptures (cavitation), releasing bacteria into adjacent airways. Bacteria can then spread via the airways to other parts of the lung, disseminate intravascularly, or be coughed up and transmitted to new hosts[40].

1.6 Diagnosis of TB disease and latent infection

Chest radiography can detect pulmonary TB lesions with high sensitivity, but requires an experienced radiologist to interpret the results, and there is high variability even among professionals. Recently, an automated system for analysing radiographs has been implemented for screening larger numbers of people; potential cases flagged by the analysis are verified by a human radiologist[54].

Sputum samples are the most commonly used body fluid for TB diagnosis. Detection of Mtb in sputum can be done by smear staining and microscopy, culture, or PCR.

The detection of Mtb and related MTBC in sputum smears is based on the principle of retention of a staining reagent following an acid-alcohol wash, due to the high mycolic acid content of their cell walls. Ziehl-Neelsen staining using the pink-coloured carbol fuchsin is the most common; human cells and other material are counterstained using methylene blue. Alternatively Auramine O can be used for fluorescence microscopy[55].

However, some cases are smear-negative meaning no visible bacilli are detected; this is a particular problem in people with HIV[56].

For nucleic acid amplification assays, the commercial GeneXpert (Cepheid) platform is most commonly used; the current Xpert MTB/RIF test also detects rifampicin resistance mutations in the *rpoB* gene. This enables patients infected with a rifampicin-resistant or multidrug-resistant (RR/MDR) strain to be quickly triaged for confirmatory drug susceptibility testing and put on an appropriate drug regimen. Sensitivity is greater than smear microscopy[57–60]. However, the high cost and requirement for stable electrical supply restricts the rollout of GeneXpert in low-income countries[61].

Culture of Mtb from sputum samples is considered the gold standard for confirming TB disease but is time-consuming due to the slow growth of MTBC. Culture assays can be done by traditional methods, or using an automated platform, the Bactec MGIT (mycobacterial growth indicator tube; Becton Dickinson). This system consists of an incubator equipped with fluorescence sensors and test tubes containing mycobacterial growth medium, antibiotics to inhibit other bacteria, and a fluorescent indicator that becomes unquenched as bacterial growth consumes the oxygen in the tube. Results are recorded as time to positivity. However, this and other automated growth detection platforms are susceptible to false negatives from both tuberculous and non-tuberculous mycobacteria[62]. MGIT can also be used to quantify inhibition of growth by antibodies or drugs[63,64].

The detection of LTBI is also important for identifying individuals at risk of developing TB who need to be monitored for follow-up and given isoniazid preventative therapy[65]. This is done by several methods of detecting a T cell response to Mtb antigens.

The tuberculin skin test (TST) is a based on injection of tuberculin (a glycerol extract of Mtb bacilli) or purified protein derivative (PPD) into the forearm and measurement of the induration that forms 3 days later. The induration reflects the magnitude of the delayed-type hypersensitivity response mediated by T cells. Test protocols used in different countries include the Mantoux and Heaf tests. Modern PPD is made from Mtb culture medium filtrates[66] and contains ESAT-6, HspX, PstS1,Mpb70, Mpb64,

Mpb83, Ag85, and SahH[67]. A comparative test is used for detection of bovine TB in cattle where *M. bovis* and *M. avium* tuberculin are injected into different sites on the tail or neck, and the thicknesses of the skin folds at the sites are measured. The cut-off value is based on the difference between the *M. bovis* and *M. avium* induration[68,69].

TST results can be highly variable and have several practical disadvantages: interpretation of the diameter of induration is complicated with different diagnostic cut-offs depending on the individual's BCG vaccination status, HIV status, country of origin, and various occupation/environmental/comorbidity risk factors[56,65]; nontuberculous mycobacteria can also cause false positives; the subject is required to return to the clinic for evaluation of the results; the inflammatory reaction can be very itchy resulting in scratching which interferes with the test result. TST cannot be administered repeatedly with an interval less than 1 year due to a booster immunisation effect causing false positives[70].

Interferon gamma release assays (IGRA) work on the principle of detecting IFNγ secretion from T cells following overnight stimulation with TB antigens. For TB diagnosis, the selected antigens should be absent from BCG and nontuberculous mycobacteria. A positive test in a clinically healthy individual is assumed to be LTBI. The currently available commercial assays are:

- QuantiFERON-TB Gold (Qiagen; abbreviated as QFT): Whole blood is stimulated with ESAT-6, CFP-10, and TB7.7. IFNγ concentrations in plasma are measured using an ELISA format.[71]
- T-SPOT.TB (Oxford Immunotec): a standardised number of separated PBMC are seeded into ELISPOT plates coated with IFNγ capture antibody, and stimulated with ESAT-6 and CFP-10. IFNγ+ spots are counted.[72]

While these have the advantages of higher accuracy for detection of TB infection and only requiring 1 patient visit, they are more expensive and require laboratory equipment.

In studies where TB exposure was known (outbreaks with an identified index case, TB-exposed healthcare workers), IGRA results were better-correlated with exposure to the index case than was TST, and was unaffected by the students' BCG status[73–75]. Therefore IGRA was thought to more accurately reflect a current infection. On the

other hand, TST may be more sensitive in detecting a past infection, as there was a higher frequency of TST+ IGRA- among non-USA-born persons[70].

1.7 Chemotherapy

The current first-line regimen for TB in South Africa is daily rifampin, isoniazid, pyrazinamide, and ethambutol for 8 weeks, followed by rifampin and isoniazid for 18 weeks (total of 6 months). Recently, a shortened regimen consisting of rifapentine, isoniazid, pyrazinamide, and moxifloxacin daily for 8 weeks, followed by rifapentine, isoniazid, and moxifloxacin for 9 weeks, was found to be non-inferior to the standard regimen[76]. A shortened regimen is expected to increase patient adherence to medication and reduce their exposure to adverse side effects.

Preventative treatment for individuals diagnosed with latent infection includes isoniazid alone for 6 months, or shorter regimens that include rifapentine or rifampin[3].

The mechanism of action of rifampin is inhibition of the bacterial RNA polymerase β subunit rpoB, and mutations in *rpoB* can confer drug resistance[77,78]. Isoniazid inhibits InhA, an enzyme involved in mycolic acid synthesis required for the cell wall, but resistance mutations are mostly in the catalase-peroxidase KatG which converts it to its active form[79].

In recent years, an increasing percentage of TB cases are multi-drug-resistant (MDR) or extensively drug-resistant (XDR), up 10% from 2018 to 2019 globally[3]. In South Africa as of 2014, the MDR rate was 2.8% overall and 2.1% among new cases[80]. MDR and XDR cases require expensive and prolonged chemotherapy that often has permanently disabling adverse effects, despite which only a minority of XDR cases are successfully treated. Two new drugs with good efficacy and less adverse effects, bedaquiline and delamanid, became available in the past 10 years[81].

1.8 Animal models for tuberculosis disease

Using animal challenge models to study granuloma formation and pulmonary TB can give some insight into various stages of the disease but should be interpreted with caution.

1.8.1 Zebrafish

Zebrafish (*Danio rerio*) infected with *Mycobacterium marinum* (Mmar) are a convenient small animal model in which to observe host-pathogen interactions, including macrophage and neutrophil phagocytosis and granuloma formation (reviewed in [45,82]). The larvae are transparent, which enables *in vivo* imaging of fluorescently labelled bacteria, cells, and beads. On the other hand, they are limited by the fact that fish do not have lungs. Fish also have different classes of immunoglobulins; while they share IgM and IgD with mammals, they lack IgG and IgA. IgT/Z appears to be the isotype associated with mucosal immunity in fish[83].

Knockout of RD1 from Mmar causes as a similar attenuation as seen with BCG in mammals, associated with defective granuloma formation[24]. Zebrafish vaccinated with galactose-α-1,3-galactose (alpha-gal) conjugated to BSA developed higher anti-alpha-gal IgM concentrations than those vaccinated with unconjugated BSA or PBS controls (i.e. greater than baseline reactivity to gut microbiota with alpha-gal surface glycans)[84]. Upon challenge, across all animals, bacterial load in tissues (as measured by qPCR of Mmar *16S rRNA* gene normalised to *Danio rerio gapdh* gene) was negatively correlated with anti-alpha-gal antibody concentrations. Vaccinated fish also showed upregulation of *ccr6a* after infection, further suggesting B cell activation.

1.8.2 Mice

Common laboratory mouse (*Mus musculus*) strains such as BALB/c or C57BL/6 can become infected with Mtb by intranasal or aerosol challenge, but do not form organised granulomas. The C3HeB/FeJ or "Kramnik" strain forms more human-like granulomas with a caseating necrotic centre, foamy macrophages, fibrotic capsule, and high bacterial burdens upon low-dose aerosol challenge with Mtb or *M. bovis*[85–87]. Similar to those in humans, the organised granulomas provide a hypoxic niche where drug-tolerant bacteria can persist and evolve, makinng this a more sensitive model for testing drug tolerance and resistance[86].

Transgenic mice expressing human Fc receptors CD89 (Fcα) or CD64 (FcγRI) have been used to study protection by humanised monoclonal antibodies[88].

1.8.3 Guinea pigs

Guinea pigs (*Cavia porcellus*) can form organised granulomas that contain persisting bacilli that are not completely cleared with chemotherapy, as well as dissemination from the lung to seed extrapulmonary lymphadenitis. Following chemotherapy with human-like drug concentrations, guinea pigs decreased bacterial loads faster and had lower relapse rates than BALB/c mice[89,90]. However, guinea pigs also experienced significant drug toxicity at these concentrations. The older lesions can become calcified, which is also a common resolution of human TB granulomas[91].

One pragmatic issue with this model is that there are far fewer available immunostaining reagents for guinea pig proteins than for mouse.

1.8.4 Rabbits

European rabbits (*Oryctolagus cuniculus*) have been historically used in TB research since the 19th century[10]. They can develop granulomas 4-5 weeks post-aerosol challenge, but are resistant to oral infection[41]. Modern studies using mass spectrometry imaging and immunofluorescence to study the composition of granulomas at a fine scale found that the distribution of proinflammatory molecules arachidonic acid, leukotriene A4 hydrolase (LTA4H), and TNFα (in the necrotic centre), and anti-inflammatory COX1 and COX2 (around the rim) were similar between human and rabbit granulomas[92].

1.8.5 Nonhuman primates

Macaques show disease stage-specific shifts in antibody reactivity to Mtb during disease similar to human patients[93]. They also form B cell follicle-like structures in proximity to granulomas that contain plasma cells secreting Mtb-specific antibodies[94,95]. Two commonly used species, rhesus macaques (*Macaca mulatta*) and cynomolgus macaques (*Macaca fascicularis*) differ in their susceptibility to TB and immune parameters, and cynomolgus macaque disease phenotype further differs between the Mauritian, Indonesian, and Chinese genotypes, therefore the selection of

a suitable species and population can be important in designing and interpreting NHP studies[96]. The more resistant Indonesian and Chinese cynomolgus macaques had higher myeloid dendritic cells and a balanced CD4:CD8 ratio compared to rhesus and Mauritian cynomolgus macaques.

B cells in nonhuman primates can be depleted using human reagents such as the anti-CD20 antibody rituximab, which enabled researchers to determine the effect of B cells on TB infection and immune responses[95]. The frequency of B cells in lymphoid tissue was effectively decreased by rituximab, which led to decreases in total and Mtb antigen-specific IgG following infection. Non-invasive monitoring of TB lesions in live monkeys can be performed by positron emission tomography-computed tomography (PET/CT); this method detects uptake of ^{18}F-fluorodeoxyglucose to estimate inflammation[97]. Rituximab-treated monkeys had slightly less [^{18}F]FDG uptake into granulomas, smaller granulomas, and less lung pathology, but a lower frequency of sterilised granulomas. CD3+ cells from rituximab-treated granulomas had higher frequencies of IL-2, IL-10, and IL-17[95]. These findings suggest that the local immune responses are over-suppressed in the absence of B cells.

A recent study compared conventional intradermal BCG vaccination to aerosol and intravenous administration in rhesus macaques. Surprisingly, i.v. but not aerosol BCG produced strong immune responses in bronchoalveolar lavage (BAL) including elevated MAIT and γδ unconventional T cells, and inversion of the alveolar macrophage:T cell ratio. In peripheral blood, i.v. vaccinated macaques had far higher PPD-responsive CD4 T cells and were the only group that had PPD-responsive CD8 T cells. IgG and IgA responses to Mtb whole cell lysate were also significantly higher in both blood and BAL. These monkeys were also better protected against Mtb challenge as shown by lower PET-CT signal, smaller number of granulomas, lower gross pathology, and lower organ bacterial burdens[98]. While intravenous BCG is unlikely to be used in humans for safety reasons, the macaque study nevertheless illuminates vaccine-inducible immune responses important for protection.

1.9 Macrophages and other phagocytes in *Mycobacterium tuberculosis* infection

In vivo, the earliest responding phagocytes to aerosol infection are alveolar macrophages, myeloid dendritic cells, and neutrophils; subsequently more myeloid DCs and interstitial macrophages are recruited to the lungs[99]. In mice, infected alveolar macrophages had the greatest capacity to stimulate CD4 T cells compared to myeloid dendritic cells, recruited interstitial macrophages, monocytes, or neutrophils[99].

Macrophages have a variety of surface pattern-recognition receptors that can recognise bacteria, reviewed by Weiss and Schaible[100] and Marakalala et al.[46]. These include C-type lectins, the mannose receptor, scavenger receptors CD36 and MARCO, Mincle, MCL, DC-SIGN, and Toll-like receptors (TLR) 2, 6, and 9.

The mannose receptor captures virulent strains (Erdman and H37Rv) but not the avirulent H37Ra[101], due to the abundance of ManLAM on their surface. Polystyrene beads coated with Erdman LAM were efficiently phagocytosed more efficiently than albumin-coated control beads by monocyte-derived macrophages, but not by undifferentiated monocytes[102]. On the other hand, there was no consistent difference in the percentage of mannose-capped AM between virulent (Erdman, H37Rv) and attenuated/avirulent (RIRv, RIRa, H37Ra) strains, therefore the density of exposed mannose residues does not fully explain the difference in phagocytosis between strains[103].

In addition to PRRs recognising Mtb surface molecules directly, mycobacteria can be also opsonised by complement or antibodies. Complement C3b deposition can occur via the mannose-binding lectin pathway or the alternative pathway[104]. Binding and phagocytosis is mediated by complement receptor 3 (CR3, consisting of CD11b/CD18) and to a lesser extent CR1 (CD35) and CR4 (CD11c/CD18)[101]. Some strains of Mtb could bind to CR3 without opsonisation in fresh serum (a source of complement) via the β-glucan lectin site of CD11b; this was found to be due to a higher content of glucose, arabinose, and mannose in the mycobacterial capsule compared to strains which required complement, and lower exposure of phosphatidylinositol mannoside which made C3b binding less efficient[105].

Opsonisation of Mtb with antibodies could result in macrophages sensing bacteria via Fc receptors instead, which can affect the fate of the ingested bacteria depending on antibody specificity. Serum from LTBI volunteers induced less macrophage and neutrophil phagocytosis of PPD-coated beads than did serum from active TB patients, but live Mtb treated with LTBI serum were phagocytosed more efficiently and a higher percentage were colocalised with lysosomes[106]. BCG vaccination of human volunteers increased ELISA titres to arabinomannan, which was associated with incrased phagocytosis and growth inhibition of live BCG bacilli. Furthermore, intracellular particles bound to antibodies could potentially be detected by the cytosolic Fc receptor TRIM21, which stimulates proinflammatory cytokine production[107].

However, Mtb has several strategies for avoiding death after being phagocytosed. Live mycobacteria including some NTMs such as M. avium are well known to block phagosome-lysosome fusion, but not dead bacteria[108–110]. Cholesterol in the plasma membrane is required for phagocytosis of mycobacteria, therefore mycobacteria-containing phagosomes have a high cholesterol content which results in their being coated with tryptophan-aspartate coat protein (TACO), which blocks fusion with lysosomes[111]. It is unclear which Mtb molecules bind cholesterol in host cell membranes but glycolipids may be involved. TACO also inhibits TLR-2 sensing of peptidoglycan and activation of NF-κB upon *M. leprae* infection[112]. However, TACO may not fully explain the failure of phagosome-lysososme fusion as BCG-containing phagosomes gradually lost TACO after 1 hour post-infection[113]. TACO was downregulated in THP-1-derived macrophages by treatment with retinoic acid and vitamin D3; this led to significantly decreased intracellular growth of *Leishmania donovani*, another intracellular parasite[114]. This may partially explain the importance of vitamin D in recovery from TB disease.

Transposon screening of Mtb mutants that fail to block phagosome acidification or phagosome-lysosome fusion has revealed several classes of proteins including ABC transporters, enzymes involved in lipid metabolism, a transmembrane transporter of phthiocerol dimycocerosate (PDIMs), a cutinase, and a potassium efflux pump among others[115,116].

Even if phagosome-lysosome fusion occurs, Mtb also has several known proteins that directly counteract antibacterial molecules released into the lysososme such as reactive oxygen species (ROS; superoxide, hydrogen peroxide, and hydroxyl radical), reactive nitrogen intermediates (RNI)[117], and heavy metals. The route of entry also influences the efficiency of macrophage killing, as uptake of pathogens via CR3 helps them avoid triggering ROS[39].

Macrophages that have been activated by IFNγ (from T cells) or TNFα produce nitric oxide (NO) and ROS. These can cross the phagosomal membrane and react to generate RNIs, which destroy bacteria by oxidation. However, Mtb encodes two known superoxide dismutases, SodA and membrane protein SodC[36,118], which can neutralise ROS, as well as several enzymes that neutralise RNIs[119]. In addition, ManLAM from virulent Mtb strains stimulates less TNFα compared to AraLAM from the avirulent strain H37Ra[120], reducing TNFα-mediated responses in the first place.

Infected macrophages can release copper from intracellular stores to raise the concentration high enough to kill bacterial. Mtb contains a metallothionein (cysteine-rich heavy metal-binding protein) called MymT; mutants are more susceptible to copper toxicity[121]. In addition, it is also capable of pumping out zinc and copper with the P-type ATPase transporters CtpC[122] and CtpV[123] respectively, which are located in the inner membrane.

Mtb and the fish pathogen *M. marinum*, but not BCG or nonpathogenic species such as *M. smegmatis*, can also rupture the phagolysosome and escape into the cytosol. Phagolysosome escape is dependent on the Esx-1 type VII secretion system and its substrate ESAT-6. This eventually triggers necrotic cell death mediated by reactive oxygen species (ROS)[124]. PDIMs also reduce phagosome acidification and contribute to escape from phagosomes in macrophages and endothelial cells, apparently by disrupting the organisation of the phagosomal membrane[125,126].

The evasion of lysosomal killing also means that induction of adaptive immune responses is also delayed by interference with antigen presentation to T cells. The 19 kDa lipoprotein is a TLR-2 ligand that inhibits processing and presentation of Mtb antigens on MHC II in mouse macrophages[127]. There may be other unindentified components in live bacilli that also inhibit antigen processing in phagosomes[110].

Mtb continues to grow in dying and dead phagocytes[128]. Infected macrophages secrete cytokines/chemokines such as IL-8 that attracts neutrophils, and IP-10, MCP-1, and MIP-1α/β that recruit other macrophages[100]. Further, dying cells give off "eat me" signals that attract other phagocytes that engulf the dead cell (efferocytosis) and in turn can be infected and killed, forming a chain reaction[124,128]. However, it was later found that apoptotic, as opposed to necrotic, neutrophils can assist macrophages in controlling Mtb. This is due to carryover of myeloperoxidase (MPO) from the dead neutrophils[129]. This enzyme converts hydrogen peroxide (H_2O_2) into hypochlorite (HOCl) which has stronger antibacterial activity.

Alternatively, Mtb and some other pathogenic mycobacteria such as *M. avium* can also trigger the transformation of foamy macrophages filled with lipid bodies. This transformation is triggered by ketomycolic acids, which are produced by Mtb but not *M. smegmatis*, a saprophytic species. The bacteria-containing phagosomes surround and fuse with with lipid bodies, which provide a rich source of nutrients and enable the bacteria to persist in a dormant state as seen by the upregulation of dormancy-related genes and the appearance of intracellular lipid inclusions. Foamy macrophages are severely impaired in their ability to phagocytose additional bacteria or to produce a bactericidal respiratory burst[33].

The intracellular niche also promotes phenotypic drug tolerance in mycobacteria. This refers not to the evolution of drug resistance mutations, but changes in gene expression and metabolism that decrease the bacilli's sensitivity to antibiotics This is also the case for some other intracellular pathogenic bacteria such as *Staphylococcus aureus*, which resists killing by vancomycin, daptomycin, linezolid, and rifampicin[130], and *Salmonella enterica var. Typhimurium* which resists ciprofloxacin[131], when they are inside phagocytes. Drug tolerance is the reason for the long treatment regimens required to cure TB. One of the mechanisms behind tolerance is thought to be upregulation of various efflux pumps[132]. Other than antibiotics, efflux pumps also remove antimicrobial peptides (AMP) secreted by the host cell, as well as exporting lipids such as phthiocerol dimycocerosates (PDIMs) for cell wall remodelling[133].

Infected macrophages downregulate their surface levels of CR3, CR4, and FcγRII thereby reducing phagocytosis of other particles. They also upregulate lymphocyte

function-associated antigen-1 (LFA-1) and its receptor ICAM-1 (CD54) which causes infected cells to form large aggregates. This could represent an early stage in granuloma formation as well as the transport of Mtb to lymph nodes by migrating phagocytes[134]. In C57BL/6 mice, myeloid DCs become the predominant infected phagocyte in lungs by 19 days post-infection and migrate to the mediastinal lymph node (draining lymph node for the lungs), where they present high levels of MHC II and costimulatory molecules. However, they poorly stimulate IFNγ secretion from CD4 T cells due to suppression of antigen presentation by Mtb[99]. In effect, Mtb uses professional phagocytes as Trojan Horses to disseminate itself.

1.10 Human B cells and antibody responses to Mtb

The humoral immune response to tuberculosis is an emerging field; however, there is abundant evidence from human samples that TB infection as well as BCG vaccination stimulate a strong antibody response to Mtb surface antigens, that disease status is reflected by different antibody profiles, and that antibodies to certain antigens are correlated with protection[135,136]. Not only the antigen specificity, but also the glycosylation state of the Fc domain and its binding to different Fcγ receptors marks latently infected versus actively diseased patients[106]; this affects various effector functions such as antibody-dependent killing, antibody-dependent phagocytosis, and NK cell activation.

In the peripheral blood compartment, patients with active TB had lower total B cells (as a fraction of lymphocytes) and higher atypical CD21- CD27- and IgD- CD27- B cells, compared to uninfected controls, LTBI, and successfully treated TB cases. These double-negative B cells are considered to be exhausted. B cells from active TB patients and LTBI individuals also had impaired proliferation responses, IL-10 secretion, and antibody secretion, whereas B cells from successfully treated TB cases were similar to controls. B cells in ATB also expressed less HLA-DR upon stimulation. B cells in ATB and LTBI individuals were also less able to activate T cells upon stimulation with BCG (in PBMC cultures), which suggests that their antigen-presenting function is also impaired, whereas T cells from treated TB cases produced the highest concentrations of cytokines[137].

B cells are recruited to the lung during TB disease and participate in the formation of inducible bronchus-associated lymphoid tissue (iBALT) and follicle-like structures surrounding granulomas, which is correlated with protection against Mtb (Figure 9)[137–140]. These follicles show the presence of CD20+ B cells, CD4+ T cells, and the proliferation marker Ki67[138]. Cytokines required for the formation of iBALT, recruitment of lymphocytes, and organisation into follicular structures include lymphotoxin α, IL-1α, IL-23, IL-17, and IL-22[139]. iBALT appears to be protective in acute viral and bacterial infections, but is also implicated in rheumatoid arthritis, chronic obstructive pulmonary disease, and respiratory allergies/asthma. In the latter chronic inflammatory conditions, excessive neutrophils, Th2 memory T cells, and CXCL12 and CXCL13 recruiting even more lymphocytes to the lung can occur[139].

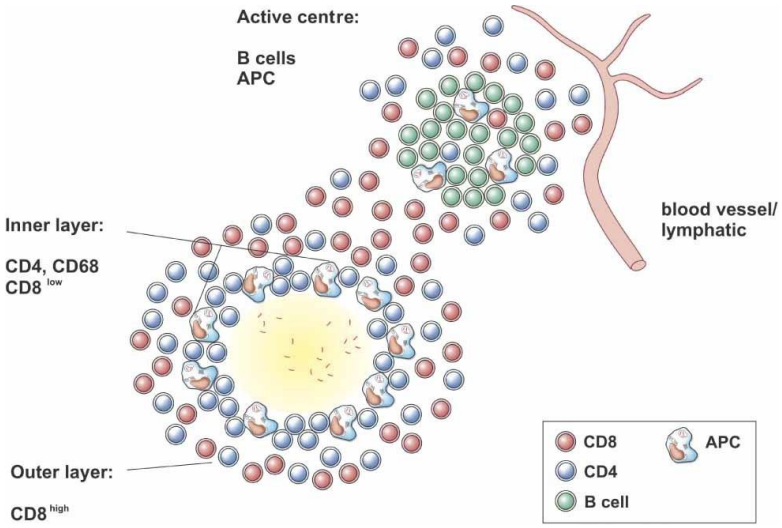

Figure 9: Granuloma surrounded by lymphocytes and secondary lymphoid follicle. From Ulrichs 2004[138].

Antibody-dependent phagocytosis of PPD-coated beads by THP-1 monocytes was higher with IgG from active TB (ATB) patients than latently infected persons (LTB). However, IgG from LTB individuals bound FcγRIIIa, an activating receptor, more than IgG from ATB. This was determined to be not due to differences in IgG subclass titres, but in Fc glycosylation, with LTB IgG exhibiting less fucosylation and more anti-inflammatory glycosylation profiles[106]. Lu et al. also showed that in primary monocyte-derived macrophages, LTB IgG increased co-localisation of Mtb with lysosomes, and enhanced killing of intracellular bacteria in the majority of macrophage

donors, compared to ATB IgG. Surprisingly, some individuals who remain IGRA negative despite high TB exposure (long-term household contacts in Uganda[141] and healthcare workers in China[142]) can also develop high Mtb-specific antibodies, including to antigens included in IGRA. While these "resister" individuals by definition did not show an interferon-γ response to ESAT-6/CFP-10, they did show TNF, IL-2, CD40L/CD154, and CD107a responses. Functional effects on monocyte and neutrophil phagaocytosis and macrophage intracellular bacterial burden were similar between resister and LTB plasma, but resister plasma induced a higher NK cell IFNγ response to PPD[141]. In addition, IgG from some LTB and resister individuals, but no ATB patients, were protective in a human whole blood inhibition assay and a mouse aerosol challenge model[142]. Overall the strongest features discriminating resisters from LTB were the ESAT-6/CFP-10 IgG1 level and the PPD IgG1:IgG2 ratio.

Our lab has previously shown that the fate of infected macrophages following infection is greatly influences by the aggregation state of the bacteria, with large aggregates causing faster cell death than an equivalent load of single bacteria or small aggregates[143]. Macrophages infected with aggregates as opposed to singlet bacilli have a more pro-inflammatory transcriptomic profile associated with TNFα signalling[144]. Therefore, antibodies could modulate phagocytosis and infection of macrophages in a number of ways: a) increasing uptake by antibody-dependent phagocytosis b) increasing or decreasing aggregation state c) Fc receptor signalling d) neutralizing or coating virulence factors either in solution or on the bacterial surface e) complement fixation.

1.11 B cell antigens in *Mycobacterium tuberculosis*

Various methods have been adopted to identify B cell antigens in Mtb for the purpose of serodiagnostics and discovering correlates of protection.

One strategy is to screen TB patient and control serum/plasma against a panel of Mtb antigens. Khan et al. and Shete et al. used a panel of 28 proteins on a multiplex bead array to screen serum from TB patients and controls in Pakistan and Uganda, respectively. In both these studies, five antigens were identified as having significantly higher antibody levels in TB patients than healthy controls or non-TB patients

(Antigen 85A/B/C complex, Rv3881 (EspB), and Rv0934 (PstS1))[145,146]. Protein microarrays designed to cover most of the Mtb proteome (all open reading frames) were used test sera from several hundred suspected TB cases from the Philippines, the UK, Mexico, and the USA. Comparison of confirmed smear-positive versus negative patient samples identified a short list of 13 protein antigens strongly associated with active disease[147,148]. The three proteins overlapping between these three studies were PstS1, Ag85A, and EspB.

Another approach is to use bioinformatics for data mining of sequences of protein antigens and biochemical parameters of non-protein antigens[149,150].

A number of proteins identified as possible humoral antigens are summarised in Table 1. Localisation and function information were taken from the Mycobrowser database[151]. Localisation of proteins as "surface" versus "secreted" can be imprecise, as the composition of culture filtrate is very similar to that of capsular mateial showing that capsular proteins are shed easily[152]. Some selected antigens are described in more detail below.

Table 1: Summary of known or potential antibody targets in Mycobacterium tuberculosis

Name(s)	Rv gene number (for proteins)	Localisation	Function
Alpha-crystallin/HspX	Rv2031c	Inner membrane	Chaperone
Antigen 85 complex		Secreted and cell surface	Mycolyl transferases involved in cell wall mycoloylation and TDM biogenesis
Antigen 85A	Rv3804c		
Antigen 85B	Rv1886c		
Antigen 85C	Rv0129c		
Bacterioferritin (BfrB)	Rv3841	Cytosol and cell membrane	Iron storage
CFP21	Rv1984c	Culture filtrate and membrane	Cutinase
Cut4	Rv3452	-	Cutinase

Name(s)	Rv gene number (for proteins)	Localisation	Function
Enolase	Rv1023	Cell membrane	Glycolysis
ESX-1 secretion system		Cell membrane	Type VII secretion system
eccCb1/Mh1784	Rv3871		
ESAT-6	Rv3875	Culture filtrate and cell wall	Virulence factor
EspC	Rv3615c	Membrane	Unknown
Heparin-binding hemagglutinin adhesin (HBHA)	Rv0475	Surface and intracytoplasmic lipid inclusions	Adhesion to host cells, extrapumonary dissemination Lipid transport
Malate synthase (MS)	Rv1837c	Cytosol and cell membrane	Glyoxylate bypass metabolism
Mycobacterial cell entry 1A (mce1A)	Rv0169	Cell membrane	Host cell invasion
MPT51	Rv3803c	Culture filtrate	Cell wall mycoloylation
MPT83	Rv2873	Membrane lipoprotein	Unknown
Mtb32A/PepA	Rv0125	Culture filtrate and membrane	Serine protease
Mtb39A/PPE18	Rv1196	Cell membrane	Unknown
Mycobacterium curli pili (MTP)	Rv3312a	-	Pili formation, adhesion to host cells
PPE41	Rv2430	Culture filtrate	Unknown
PhoP	Rv0757	Cell membrane	Transcriptional regulator
PstS1	Rv0934	Culture filtrate and membrane	Phosphate transport
TB10.4/CFP7	Rv0288	Culture filtrate	Virulence factor

Name(s)	Rv gene number (for proteins)	Localisation	Function
Arabinomannan (AM)	N/A	Capsule	-
Lipoarabinomannan (LAM)	N/A	Inner membrane	-
Trehalose dimycolate (TDM)	N/A	Outer membrane	-

1.11.1 Protein antigens

1.11.1.1 Alpha-crystallin (Acr, HspX, Hsp16.3)

Alpha-crystallin, also known as HspX, is thought to be involved in the mycobacterial response to hypoxic stress[153] and dormancy[33] during latent infection. It was identified by 2D gel electrophoresis as a dominant protein that appears in Mtb H37Rv cultures during the transition from log phase growth to stationary phase. It was shown to be a functional chaperonin that can stabilise other proteins[154]. Subsequently it was also shown to be induced during hypoxia and macrophage infection; a knockout was not impaired in vitro but had severely reduced growth in bone marrow-derived macrophages (BMDM) and THP-1 monocytic cell line after several days' infection[155]. Passive immunisation of mice with monoclonal antibodies against Acr significantly reduced lung bacterial loads following Mtb challenge[156,157].

In human TB patients, Acr is present in the sputum in sufficient quantity to be detected by a surface plasmon resonance-based device[158]. A study in China found that both TB patients and LTBI individuals have detectable anti-Acr IgG[159], whereas a study in Mexico found that only IgM in LTBI was significantly elevated; the authors also found that in USA individuals, LTBI also had far higher concentrations of Acr in their serum[160].

Single-domain antibodies against Acr have been engineered as potential therapeutics or diagnostic reagents[161].

1.11.1.2 Antigen 85 complex (Ag85A, Ag85B, Ag85C)

The antigen 85 complex members (reviewd by Babaki et al.[67]) are mycolyl transferases involved in the synthesis of TDM and attachment of mycolic acids to arabinogalactan, therefore they are important in the formation of the cell envelope. Additional functions include binding to host proteins fibronectin and elastin which enables invasion of host cells. All BCG strains contain several mutations affecting T cell epitopes of Ag85B. In addition, one of these substitutions affects its mycolyl transferase activity and may destabilise it; this could partially explain the lower immunogenicity of BCG[162]. Antigen 85A has been used as the target antigen in some candidate recombinant vaccines[163] (discussed in more detail below).

1.11.1.3 ESAT-6

The 6 kDa early secretory antigenic target was first identified as a culture filtrate component that strongly stimulated interferon gamma release from T cells of mice that had been previously infected with Mtb[164]. ESAT-6 is encoded by the *esxA* gene in the RD1 region which is one of the major gene regions differentiating Mtb and virulent wild-type M. bovis from BCG[21]. It is secreted as a heterodimer with Culture Filtrate Protein 10 (CFP-10), encoded by *esxB*. ESAT-6 contributes to blocking phagosome-lysosome fusion in human monocyte-derived macrophages and inhibits antigen presentation to CD4 T cells[165]. Anti-ESAT-6/CFP10 IgG1 was associated with sterilising immunity in TB-exposed IGRA- individuals[141].

1.11.1.4 HBHA

The heparin-binding hemagglutinin adhesin (HBHA) is a 21.5 kDa protein which increases extrapulmonary dissemination of Mtb by causing it to adhere to and invade alveolar epithelial cells via attachment to syndecan 1 and 4[166,167]. It also shuttles into the bacterial cytosol where it has a major role in the formation of the intracellular lipid inclusions that are critical for fatty [168]acid metabolism during dormancy.

HBHA is a potential diagnostic reagent for both T cell (IGRA) and antibody tests. HBHA IGRA was more sensitive than PPD and ESAT-6, and furthermore, was able to distinguish latently infected individuals (higher IFNγ response) from TB patients[169].

IgM, but not IgG, from TB patients had significantly higher HBHA ELISA signal compared to healthy controls, and was able to block infection of A549 lung epithelial cells *in vitro*[170]. Opsonisation of Mtb with anti-HBHA monoclonal antibodies (mAbs) prior to infecting mice led to significantly lower bacterial loads in the spleens, but not lungs[171].

1.11.1.5 PhoP (Rv0757)

PhoP is the response regulator component of the PhoPR two-component system which regulates the expression of a large number of other genes involved in virulence; a point mutation in its DNA-binding domain appears to be the determinant of the difference between the virulent Mtb strain H37Rv and the avirulent H37Ra[172]. PhoP itself is immunogenic; IgG titres against PhoP are higher in healthy individuals than TB patients and their close contacts. Furthermore, patients suffering recurrent TB had lower titres than those diagnosed with their first episode[173].

1.11.2 Carbohydrate antigens

1.11.2.1 Arabinomannan (AM) and liporabinomannan (LAM)

Preincubating Mtb Erdman with 9d8, a mouse IgG3 monoclonal antibody against arabinomannan, 9d8, partially protected C57BL/6 and BALB/c mice from intratracheal challenge compared to controls. Mice infected with 9d8-coated Mtb survived longer, although lung and spleen bacillary burdens were no different than controls. However, in the mice infected with 9d8-treated Mtb, the bacilli were confined in granulomas surrounded by iNOS-producing cells, as opposed to the random distribution in the control mice[174]. Vaccination of mice with AM conjugated to either a TB protein Antigen 85B (Ag85B) or heterologous protein *Bacillus anthracis* PA stimulated antibodies that provided passive protection when infused into naïve mice[175].

In human volunteers, BCG vaccination increased serum IgG binding to AM as well as the percentage of THP-1 monocytes that phagocytosed BCG in the presence of sera, and the percentage of BCG in lysosomes. Phagocytosis enhancement was correlated

with serum binding to three specific mannose-containing oligosaccharides identified by glycan microarrays; two of these OS were also targeted by 9d8. Postvaccination sera were able to bind BCG grown with or without detergent, that is, they also recognised AM epitopes in cell wall LAM of capsule-less bacilli[37].

1.12 Isolation of naturally occurring human anti-Mtb monoclonal antibodies

A large number of human antibody sequences were obtained from peripheral blood B cells of German healthy and TB patient donors[176]. Clones with M.tb-binding activity included IgG, IgA, and IgM isotypes. The authors used the A549 cell line as a model for invasion of lung epithelial cells. In general, IgA mAbs had a neutralising effect in this model system while IgG mAbs enhanced infection, including recombinant IgG constructed with the variable regions of neutralising IgA antibodies. Enhancement of infection was caused by uptake of IgG-M.tb complexs via the neonatal Fc receptor (FcRn) which is expressed on A549 cells. Two specific surface antigens identified in this study were ManLAM (mannosylated lipoarabinomannan, found in Mtb) and HBHA. Notably, in an experiment where fluorescently labelled HBHA was used as bait, a TB patient and a healthy exposed healthcare worker had very high frequencies of HBHA-binding CD27+ memory B cells of 0.22% and 0.16% respectively.

1.13 Modern tuberculosis vaccine candidates

A century after the invention of BCG, we still lack more effective vaccines for the prevention of pulmonary TB. As of mid-2019, the following vaccine candidates were in pre-clinical development or clinical trials[177,178]. Some are described in further detail below. Endpoints for evaluation in different trials include prevention of infection (POI; as measured by QFT conversion, initial or sustained), prevention of disease (POD), and prevention of recurrence (POR).

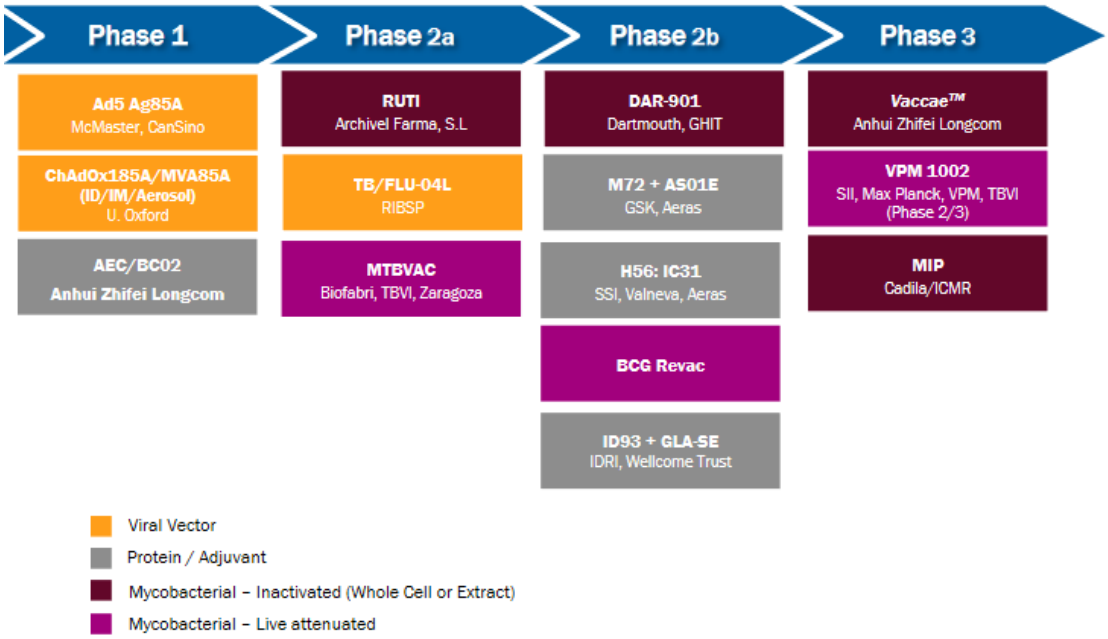

Figure 10: Overview of global TB vaccine development pipeline, 2019. Adapted from Ann Ginsberg (IAVI) presentation to WHO Product Development for Vaccines Advisory Committee, June 2019.

1.13.1 ChAdOx1-85A/MVA85A

The highly attenuated vaccinia virus strain, Modified Vaccinia Ankara, has been used as a recombinant vector for vaccinating against various other pathogens. The chimpanzee adenovirus vector ChAdOx1 is a newer vector which is used to circumvent the problem of anti-vector immunity to human adenoviruses[179,180]. The isolate used as the basis for this vector is related to *Human adenovirus E* and is expected to infect cells via the coxsackie and adenovirus receptor (CAR), a cell adhesion protein present in tight junctions and the lateral surfaces of epithelial cells, giving this vector a wide cell tropism[181,182].

A heterologous triple regimen of BCG/ChAdOx1-85A/MVA85A protected BALB/c mice against an Mtb Erdman aerosol challenge with significantly greater lung and spleen CFU reductions over BCG alone. The triple vaccination also generated more Ag85A peptide-responding polyfunctional CD4 and CD8 T cells than BCG alone[183]. The ChAdOx1-85A/MVA85A regimen was then tested in BCG-vaccinated human volunteers in a Phase 1 trial, which induced strong T cell and Ag85A IgG responses[163].

1.13.2 BCG revaccination

Adolescent revaccination with BCG was practised in several countries in Southeast Asia until the early 2000s[184,185]. The discontinuation was due to a 1995 WHO bulletin regarding a lack of evidence for efficacy and interference with tuberculin skin testing[186]. However, I have not been able to find information comparing TB incidence or immunogenicity measurements in age cohorts from these countries before and after the discontinuation of adolescent revaccination. A revaccination trial in Malawi conducted in the 1980s and followed up till the 1990s found that BCG revaccination conferred some protection against leprosy, but not tuberculosis[187].

BCG revaccination has since been revisited and a Phase 2 POI trial in South African adolescents aged 12-17 found promising results in this high-burden country. While revaccination did not meet the primary endpoint of protection against initial QFT conversion, it had 45.4% efficacy in preventing sustained conversion (three or more consecutive QFT+ results). A larger proportion of BCG than placebo recipients who had converted, later reverted to QFT-, which was thought to signify clearing the infection[188].

1.13.3 MTBVAC

MTBVAC is a live attenuated vaccine based Mtb strain Mt103 created by rational deletion of two important virulence factors: phoP, which regulates a large number of other genes implicated in virulence; and fadD26, which is essential for the biosynthesis and export of PDIM. It was significantly more protective than BCG in guinea pig and rhesus macaque challenge studies, and safe in SCID mice[189]. MTBVAC was also shown to be safe in human adults and newborns, and more immunogenic than BCG in Phase 1 trials[190]; Phase 2 trials have been completed and a Phase 3 efficacy trial in newborns is expected to start in 2022.

1.13.4 M72/AS01E

M72 is a recombinant fusion of MTB32A and MTB39A which are present in both virulent MTBC and BCG; it is formulated with AS01E, a proprietary liposomal adjuvant containg 3-O-desacyl-4'-monophosphoryl lipid A (MPL) and a saponin[191].

Over a 36-month study in Kenya, Zambia, and South Africa, it showed 49.7% efficacy in preventing pulmonary TB. M72-specific CD4 and IgG responses were sustained during the study period[192].

1.13.5 VPM1002

VPM1002 is an engineered recombinant BCG with a deletion of the urease C gene, which neutralises the phagosome environment by producing ammonia, replacing it with listeriolysin O from *Listeria monocytogenes*, a pore-forming protein which allows bacterial DNA and proteins to escape into the cytosol, triggering immune responses and increasing antigen presentation on both MHC I and II[193]. It is being tested in POI trials in newborns as well as POD/POR in adults.

1.14 SARS-CoV-2 and Covid-19

1.15 Overview of coronaviruses

Coronaviruses are members of the *Coronaviridae* in the order *Nidovirales*. They are single-stranded positive-strand enveloped RNA viruses, with genomes approximately 26-33.5 kilobases and virions approximately 125 nm in diameter[194].

The earliest identified coronaviruses were 229E from a human case of upper respiratory disease and avian infectious bronchitis virus. Almeida et al. identified that this was a new type of virus and that these were related, despite reviewers arguing that her electron micrographs were simply poorly imaged influenza virions[195,196]. The hemagglutinin protein of influenza is approximately 13.5 nm in length while the spike protein of coronaviruses is noticeably larger at approximately 150-200 Å (15-20 nm) long and 140 Å wide [197,198]. This "crown" of prominent spikes gave the name to the new viral family.

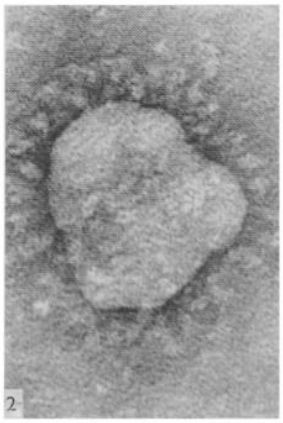

Figure 11: Electron micrograph of human coronavirus 229E. From Almeida and Tyrrell 1967[197].

Coronaviruses are well known as animal pathogens, causing diseases such as avian infectious bronchitis of poultry (IBV or avian coronavirus), mouse hepatitis virus (MHV), feline infectious peritonitis, a highly lethal infection of cats (feline coronavirus), gastrointestinal disease in puppies (canine coronavirus), transmissible gastroenteritis of swine (TGEV), and enteritis in calves (bovine coronavirus). Prior to 2002, the four known human coronaviruses 229E, NL63, HKU1, and OC43 were

usually associated with mild respiratory ("common cold") or gastrointestinal diseases and are very common in infants, including in South Africa[199,200].

Spillover events of emerging coronaviruses from animals into humans have occurred several times. OC43 is thought to have spilled over into humans from cattle, and may have been the cause of an unindentified influenza-like illness pandemic in the 1890s. Many spillovers do not result in further transmission or large outbreaks. For example, a canine coronavirus was recently found to have caused several cases of pneumonia in children in Malaysia but did not spread further[201].

The twenty-first century has already seen three major epidemics caused by emerging coronaviruses. In 2002, the first identified outbreak of a novel and fatal human coronavirus occurred. A severe acute respiratory syndrome (SARS) characterised by acute respiratory distress and hyperinflammation appeared in 2002 in southern China. It subsequently spread to 13 countries and infected at least 8422 people with a case-fatality rate of approximately 11%[202]. A second epidemic occurred in 2003-2004 but it has not been detected in humans since then. Masked palm civets (*Paguma larvata*) were eventually identified as the reservoir.

A new acute respiratory distress syndrome-causing coronavirus emerged in 2012 and was named Middle East Respiratory Syndome Coronavirus (MERS-CoV). The case-fatality rate is 35%, although this is probably an overestimate of the true infection fatality rate given the broad exposure of humans to the reservoir host, dromedary camels. The latter have seroprevalence rates as high as 80.4% in Tunisia, 76.3% in Kenya, and 70.8% in Saudi Arabia[203–205]. Therefore, prior to 2019, some coronavirus vaccines were already in development for prevention of MERS among camel handlers.

SARS-CoV and MERS-CoV are members of the genus Betacoronavirus with their own subgenera *Sarbecovirus* and *Merbecovirus* respectively[206].

1.16 SARS-CoV-2 emergence and the Covid-19 pandemic

In December 2019, a pneumonia patient in Wuhan, Hubei province, China was found to be infected with an unknown betacoronavirus. Subsequent sequencing showed that it was a novel virus with the closest then-known sequence to be BatCov RaTG13 (from

Rhinolophus affinis)[207]. The virus spread quickly throughout Wuhan, where this initial outbreak resulted in 50,006 reported cases, with an estimated 14,448 undetected[208]. This was brought under control by a draconian lockdown of Wuhan, which is a major city and transportation hub.

Subsequently the novel coronavirus spread to multiple countries and a pandemic was declared by WHO on 11 March 2020[209]. The new virus was named severe acute respiratory syndrome coronavirus 2 (SARS-CoV-1) by the International Committee on Taxonomy of Viruses, whereas the disease was named coronavirus disease 2019 (Covid-19) by the WHO[210].

The question of when SARS-CoV-2 spilled over into the human population or by what route remains open for investigation. Phylogenetic analysis suggests that the most recent common ancestor dates back to early November 2019[211]. No unusual patterns in influenza-like illness (ILI) or severe acute respiratory illness (SARI) other than the usual seasonal winter increase were noted in Wuhan immediately before the outbreak[212]. Therefore if a precursor of SARS-CoV-2 was circulating, it had not yet evolved to cause overt symptoms in most humans. Nevertheless, investigators in Italy found banked blood samples with SARS-CoV-2 specific antibodies from as early as September 2019, and viral RNA was found on a swab from a patient with haemoptysis and fever in France in December 2019[213,214].

Since then, nearly every country in the world has experienced multiple epidemic waves of Covid-19. The current number of confirmed cases as of mid-July 2021 is over 19 million, and confirmed deaths over 4 million[215]. However, these are likely underestimated for several reasons: a) under-detection of cases due to lack of access and laboratory capacity shortages, b) false negative RT-PCR tests due to timing of sampling (test conducted after the individual is no longer shedding viral RNA), swab technique, PCR inhibitors in samples etc., c) individuals who died prior to testing. A true measure of the impact of the pandemic may be the number of excess all-cause mortality over typical year-on-year deaths for a given country/region[216].

Various non-pharmaceutical interventions (NPI) have had some success in limiting the size of outbreaks, such as movement restrictions, enforcement of facemask wearing in public places, quarantine of individuals arriving from other countries, selective

shutdown of non-essential industries, remote education and working from home, etc. However, these have also caused significant psychological and economic hardship, and severely decreased access to education and healthcare. Of note, an indirect measure of the effectiveness of NPI in preventing the spread of respiratory viruses is that influenza cases have been drastically reduced worldwide as seen from the Southern Hemisphere winter 2020 flu season onwards[217]. Therefore the Covid-19 pandemic would clearly have been far worse in the absence of NPI.

The typical symptoms of mild-to-moderate Covid-19 hardly need to be reiterated for readers in 2021, but for the record, they can include fever, dry cough, sore throat, nasal congestion or rhinorrhea, fatigue, body aches, diarrhoea, nausea, headache, conjunctivitis, rashes, and loss of taste or smell[218]. The median presymptomatic incubation period is estimated at 7.76 days[219], which is longer than the original SARS, and the serial interval (time between infection of new hosts) is estimated at 3.44 days[220], therefore presymptomatic transmission is a major factor in the scale of the pandemic. Some infected individuals remain completely asymptomatic.

Severe Covid-19 includes respiratory failure, shock, acute respiratory distress syndrome[221]. On a cellular level, these are driven by a hyperinflammatory state ("cytokine storm")[222,223], coagulopathy, and damage to endothelial cells (Figure 12)[224]. Patients can require supplemental oxygen, mechanical ventilation, or even extracorporeal membrane oxygenation. In addition to microembolisms, the vascular damage appears to interfere with the lungs' ability to redirect blood perfusion away from poorly ventilated regions by vasoconstriction[225,226].

Drug therapies for Covid-19 includes neutralising monoclonal antibodies[227], anticoagulants, steroids (e.g. dexamethasone)[228] and anti-IL-6-receptor monoclonal antibodies[229] to reduce inflammation. While the antiviral drug remdesivir was shown to be significantly effective in reducing length of hospitalisation and mortality, the effect size is small and it is cost-prohibitive for many settings.

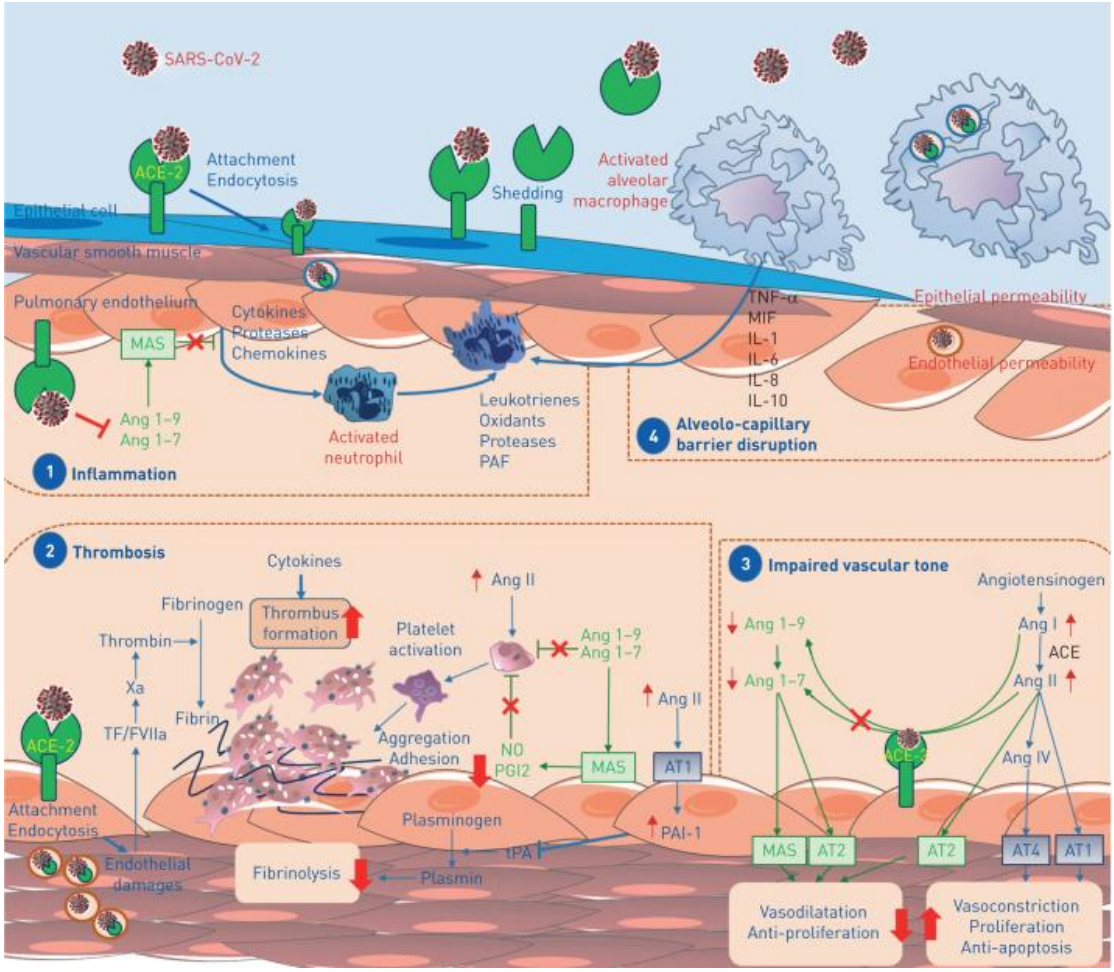

Figure 12: Hypothetical mechanisms of SARS-CoV-2 damage to vascular endothelium. From Huertas 2020[224].

Vaccines for the prevention of Covid-19 have been developed with unprecedented speed, going from proof-of-concept to Phase 3 trials in a matter of months and Emergency Use Authorisation within the year. As of July 2021, there are 108 Covid-19 vaccines in clinical trials[230]. In the case of mRNA vaccines, this was facilitated by the existence of an ongoing MERS vaccine development programme[231]. Similarly, in the case of adenoviral-vectored vaccines, several companies used well-characterised replication-deficient adenoviruses that had already been used in candidate vaccines for other pathogens. These are described in further detail below. However, there is a massive global gap in access to vaccines as well, with high-income countries (HIC) having vaccinated a large proportion of their populations, whereas vaccination rates in low and middle income countries (LMIC) are still low.

1.16.1 Variants of Concern

Since the initial outbreak and global spread, a number of variants of concern (VOC) have evolved, defined as variants with enhanced transmissibility, virulence, and/or immune evasion of vaccines. The VOC identified to date are designated Alpha (PANGO lineage B.1.1.7), Beta (B.1.351), Gamma (P.1), and Delta (B.1.617.2)[232].

In South Africa, the second epidemic wave from November 2020-January 2021 was dominated by the emergence of Beta. This variant has several S mutations including in the receptor-binding domain conferring higher affinity to ACE2. It partially evaded neutralisation by plasma from first wave infections, plasma of vaccinees who received an adenovirus-vectored vaccine encoding reference sequence spike, and the monoclonal antibody drugs bamlanivimab and casirivimab[233–236].

Since the emergence of Delta in India in late 2020 and spread to other geographical locations, it has since become the predominant variant including in South Africa and in under-vaccinated regions of high-income countries. Delta shows both increased transmissibility and immune evasion to convalescent sera, vaccinee sera, and monoclonal antibodies[237]. One reason behind its rapid spread is that viral shedding appears to be several orders of magnitude higher compared to earlier strains from 2020[238]. One underlying molecular mechanism could be the higher efficiency of Delta Spike S1/S2 cleavage and its enhanced ability to enter cells and trigger syncytium formation[237]. Several fatal breakthrough infections of fully vaccinated healthcare workers have been reported from Indonesia and Thailand, where inactivated viral vaccines with lower efficacy have been used[239].

The effect of Alpha and Beta variants on clinical disease appears to be generally small. In a UK study of patients hospitalised for any reason during the November-December 2020 period when Alpha was emerging, there was no significant difference in disease severity between Alpha and non-VOC patients, although Alpha samples had lower RT-PCR Ct values and greater sequencing read depths (higher viral load)[240] consistent with reports of its higher transmissibility than ancestral strains. In a cohort of 846 hospitalised patients in Singapore, Delta was associated with increased disease severity and death compared to ancestral strains, but not Alpha or Beta. Duration of shedding as measured by time from symptom onset to first Ct value >30 was also longer for Delta[241].

The evolution of variants with immune escape mutations may be driven by incompletely neutralising antibodies. Antibody-escaping mutations in S, including some recapitulating mutations in VOC have been observed in patients with immunocompromised conditions, such as chemotherapy for B cell lymphoma, a solid organ transplant recipient, acute lymphoblastic leukaemia, and uncontrolled HIV infection[242–245]. In addition, the emergence of Delta is thought to have been driven by repeat infection in the face of waning natural immunity from previous infections[237].

1.17 Animal hosts and the search for origins

There was an impression early in the initial outbreak in Wuhan that cases were associated with the Huanan Wholesale Seafood Market, including the index patient[207,246]. However, a number of cases were also associated with other markets. The WHO investigation in China in January-February 2021 found no evidence of live animal sales in Huanan or other markets in Wuhan; however, this was probably due to the markets having been shut down and sanitised in January 2020, and permanently shut down several months before the investigative team visited[212]. In addition, the sale of wildlife without a licence and origin certification of the species for sale is illegal in China, so vendors might be disinclined to cooperate with investigators[247].

However, "a variety of live wild animals" at the index patient's workplace had been noted in the first report on SARS-CoV-2[207]. Additional data was serendipitously obtained by a search for a completely unrelated virus, Severe Fever with Thrombocytopenia Syndrome Virus. Xiao et al.[247] conducted monthly visits during 2017-2019 to shops selling wild animals as pets and food items at Huanan, Baishazhou, Dijiao, and Qiyimen markets and was able to obtain data from the vendors on prices and sale volumes. No bats or pangolins were found, however, masked palm civets, raccoon dogs, and American mink, which are all confirmed hosts of SARS-related CoVs, were sold multiple times over the study period[247].

1.17.1 Bats as a reservoir of SARS-related CoVs

Bats (order Chiroptera) are unusually long-lived for small vertebrates and have very high biodiversity, therefore even with an equal probability of zoonotic viruses

emerging from any mammals, we would expect a large proportion to come from bats. They are reservoirs of various zoonotic viruses including the henipaviruses (Hendra and Nipah encephalitis), lyssaviruses (rabies and others), and filoviruses (Ebola).

In addition, it is thought that the physiological adaptations for true flight which is unique among mammals (as opposed to gliding) may have side effects on their immune system, including the high metabolic rate and elevated body temperature being similar to a fever in inhibiting viral replication.

Since the original SARS epidemic, SARS-related (SARSr) CoVs have been found in bats across a wide region of southern China and southeast Asia as far south as Thailand, particularly in rhinolophids (horseshoe bats)[248–253]. SARSr-viruses have also been found in rhinolophid bats in other parts of Eurasia, e.g. Slovenia[254]. The S protein from at least one bat isolate was confirmed to be able to bind human ACE2 and infect human airway cells in vitro[255].

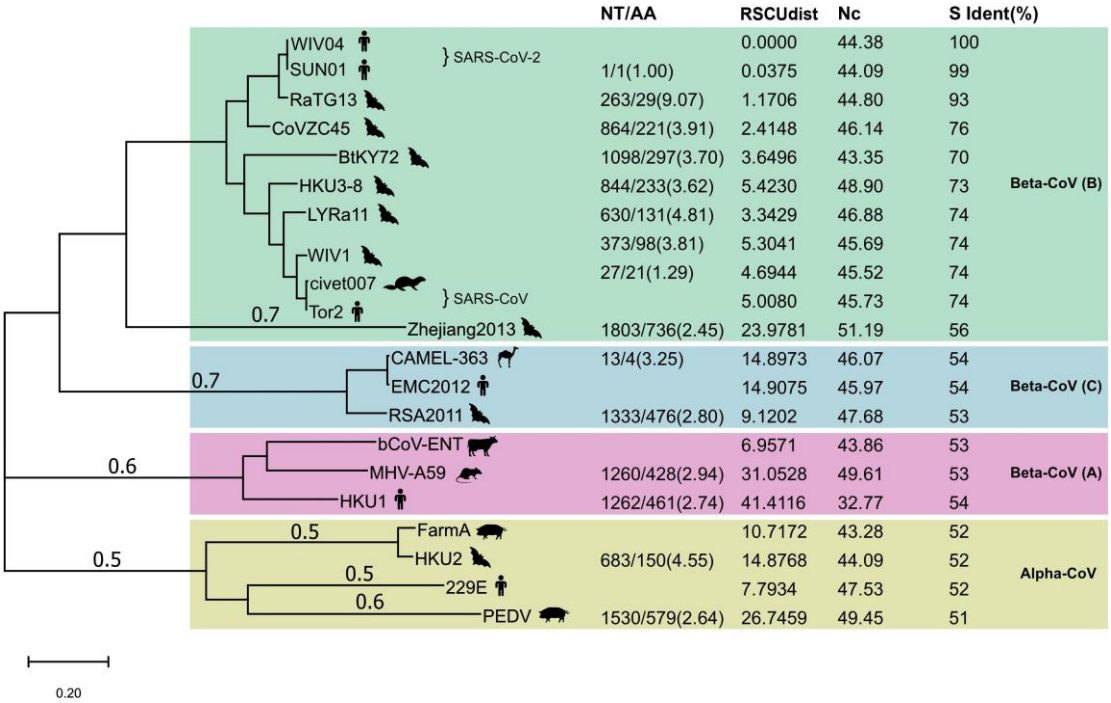

Figure 13: Phylogenetic tree of 21 coronavirus strains. From Lv et al. 2020[250].

1.17.2 Candidates for natural intermediate hosts

1.17.2.1 Palm civets

The masked palm civet (*Paguma larvata*) was identified as the host of SARS-CoV based on occupational exposure of early human cases, sequencing of samples from human patients, and isolation of virus from masked palm civets sold in live animal markets[256,257]. S, sars3a (a minor structural protein associated with S, encoded in ORF3a), and nsp3 were identified as the proteins under the greatest selective pressure in the adaptation from civet to human. The majority of the S mutations were located in the RBD[258].

Multiple spillover events were identified during the 2002-2003 and 2003-2004 outbreaks, showing that masked palm civets were a reservoir of the virus. Palm civet isolates and human isolates in the 2003-2004 outbreak were almost identical. Adaptation to humans was not completely convergent, as the earlier epidemic virus was distinguished by a 29-nt deletion relative to the civet virus, which did not appear in the second outbreak[258].

1.17.2.2 Raccoon dog

The raccoon dog or tanuki (*Nyctereutes procyonoides*) is a canid, not a raccoon; it was also identified as one of the SARS-CoV-infected animal species found in the wildlife meat trade in 2004. Raccoon dogs were also sold as meat in wildlife markets around Wuhan shortly before the initial SARS-CoV-2 outbreak[247].

Experimental infection of raccoon dogs produced only mild lethargy in a few animals and viral replication was found in the nasal conchae. Two out of three naïve animals exposed to direct contact shed infectious virus and seroconverted[259].

1.17.2.3 Pangolins

Pangolins (order Pholidota) are highly trafficked in Asia and Africa due to the demand from traditional Chinese medicine. Malayan pangolins (*Manis javanica*) were proposed as an intermediate host due to the similarity between pangolin isolates and SARS-CoV-2[251,260,261]. However, the recently published Yunnan bat isolates appear to be more similar.

1.17.2.4 Mustelids

Domesticated ferrets (*Mustela putoris furo*) were already well known as a laboratory animal model for another zoonotic respiratory virus, influenza. They can be infected with SARS-CoV-2 and transmit by aerosol/droplets without direct contact[262,263]. Two mustelids, Siberian weasel (*Mustela sibirica*) and American mink (*Neovison vison*) were sold live at markets in Wuhan in the 2-year period preceding the pandemic[247]. Mink are widely farmed for fur in China, Europe, and North America; they are an invasive species in Europe and Britain. Subsequently there were massive outbreaks of SARS-CoV-2 on mink farms from Covid-infected employees as well as possible "spillback" events where humans may have become infected by mink. These resulted in culling of millions of mink.

1.17.2.5 Felids

Cats appear to be susceptible to SARS-CoV-2 infection. Domestic cats (*Felis catus*) can be experimentally infected; 6-9 month-old subadults had milder symptoms and lower viral loads than 70-100 day-old kittens which developed massive lesions in the upper and lower repiratory tracts[263]. Airborne transmission was detected in one of three exposed animals in each age group.

During the first wave in western Europe, a pet cat was apparently infected by its owner and became RT-PCR positive with mild respiratory symptoms. Subsequently, multiple instances of pet cat infection from owners with suspected or confirmed Covid-19 have been documented[264,265]. In the United States, several tigers (*Panthera tigris*) were infected by a zookeeper and lions (*Panthera leo*) were infected from an unknown source[266]. However, cat-to-human transmission has not been documented.

1.18 Virus genome, virion structure, and life cycle

The reference sequence for SARS-CoV-2 is Wuhan-Hu-1 isolated from the index patient, GenBank accession MN908947, 22,903 nt in length[207]. It encodes ORF1ab (replicase complex), spike (S), ORF3a, ORF3b, envelope (E), membrane (M), ORF6,

ORF7a, ORF7b, ORF8, ORF9a, ORF9b, nucleocapsid (N), and ORF10. The product of ORF1ab is cleaved into 16 nonstructural proteins (nsp) whose functions include viral replication and assembly as well as immunomodulatory factors. S, E, and M are transmembrane proteins integral to the viral envelope, but E and M are smaller and less immunogenic than S. Apart from the four structural proteins, the other ORFs are accessory proteins of unknown function but may also include virulence factors[207].

The receptor for SARS-CoV-2 is the angiontensin-converting enzyme 2 (ACE2), which is shared with SARS-CoV. Compared to SARS-CoV S, SARS-CoV2-2 has a larger number of resides within the receptor-binding domain that specifically interact with ACE2 across a broader interface area, which may be one of the factors in its greater transmissibility[267].

SARS-CoV-2 can enter cells via either fusion at the plasma membrane or the endocytic pathway. This depends on whether the full-length S protein has been cleaved to S1/S2. Coronavirus spike proteins can be cleaved by furin during virion assembly, or by the transmembrane serine protease TMPRSS2 upon binding to a new host cell. In TMPRSS2+ cells, fusion of the virion envelope occurs at the plasma membrane. Otherwise, the virion enters by endocytosis. (S structure, processing, and viral entry are discussed in more detail below.)

The full-length genomic RNA is not translated even though it is capped and polyadenylated. First, ORF1a and ORF1b, encoding the proteins of the replicase complex, are translated. The large polyprotein products are cleaved into the 16 proteins of the replicase-transcriptase complex. A series of negative strand templates are transcribed from the 3’ end of the genome, then subgenomic mRNAs are transcribed from the negative strands[194,268].

Assembly of capsids of N protein enclosing the new genomic RNA takes place in the cytoplasm, followed by budding into the ER-Golgi intermediate compartment (ERGIC) to acquire its envelope containing M, E, and S. The progeny virions then exit via the secretory pathway. S can also cause fusion of the host with adjacent cells allowing for direct cell-to-cell spread[194,269,270].

Coronaviruses are susceptible to recombination, as seen with SARS-CoV-2 where the topology of the S gene phylogram puts it close to bat SARSr-CoVs RaTG13 and SL-

CoVZC45[207,250] whereas its ORF1b is in a more basal position within the Sarbecoviruses[207]. Other recently published examples of recombinant coronaviruses include the canine CoV isolated from a human pneumonia case where the sequence of the S2 domain had higher identity with feline CoV[201].

Due to the large size of coronavirus genomes, reverse genetics systems have previously been complicated involving ligation of several cDNA segments and *in vitro* transcription followed by electroporation of the RNA into a suitable host cell line[271]. Recently a system was published with the entire genomic cDNA on one plasmid which allows transfection using normal lipid transfection reagents[272].

1.19 Structure and function of the Spike protein

The Spike protein of SARS-related CoVs is a large transmembrane protein of 1273 amino acids[207]. Spike is a Type I fusion protein, i.e. containing a fusion peptide which is liberated by a proteolytic cleavage upon virion maturation, and then upon some other trigger (e.g. low pH, receptor binding) inserts into the new host cell's plasma membrane[273]. The trimer then bends into a hairpin conformation which pulls the viral envelope and cell membrane together and fusion occurs first of the outer leaflet then the inner, releasing the virion contents into the cytoplasm[268,274]. Other examples of Type I fusion proteins are shown below[198].

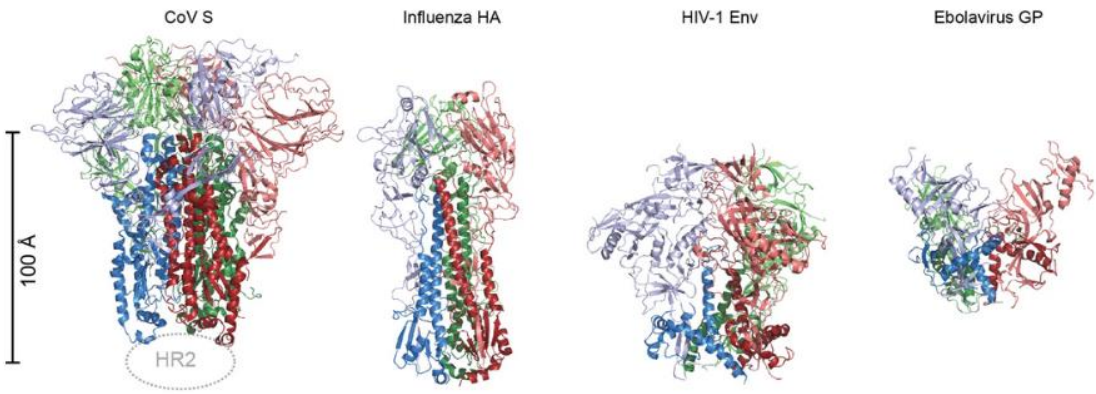

Figure 14: Trimeric Class 1 fusion proteins of coronavirus, influenza virus, HIV, and Ebola virus. Receptor-binding domains are shown in light colours and fusion machinery in dark colours. Adapted from Kirchdoerfer et al. 2016[198].

Attachment to host cells is initiated by one of the RBD in the trimer rotating into an RBD-up conformation which allows it to bind ACE2. In the case of fusion at the plasma membrane S1 then dissociates. Otherwise if the S1/S2 cleavage has not yet occurred, the virion is endocytosed and S1/S2 is cleaved by cathepsin L in endosomes; this usage of different entry pathways is known for other model coronaviruses e.g. murine hepatitis virus[275]. A second cleavage at the S2' site frees the fusion peptide and fusion of the viral envelope with either the plasma membrane or endosomal membrane proceeds.

Polybasic furin cleavage sites in S occur in various members of Coronaviridae including the common cold HCoVs OC43 and HKU1[276]. The furin cleavage site (FCS) in SARS-CoV-2 S has the sequence $_{681}$PRRAR/SV$_{687}$[277]. This is considered to be "suboptimal" (the canonical motif is RX[K/R]R)[278] so not all copies of S are cleaved yet upon virion production. This reduces the probability of S1 dissociating prematurely before contact with a host cell and ACE2 binding.

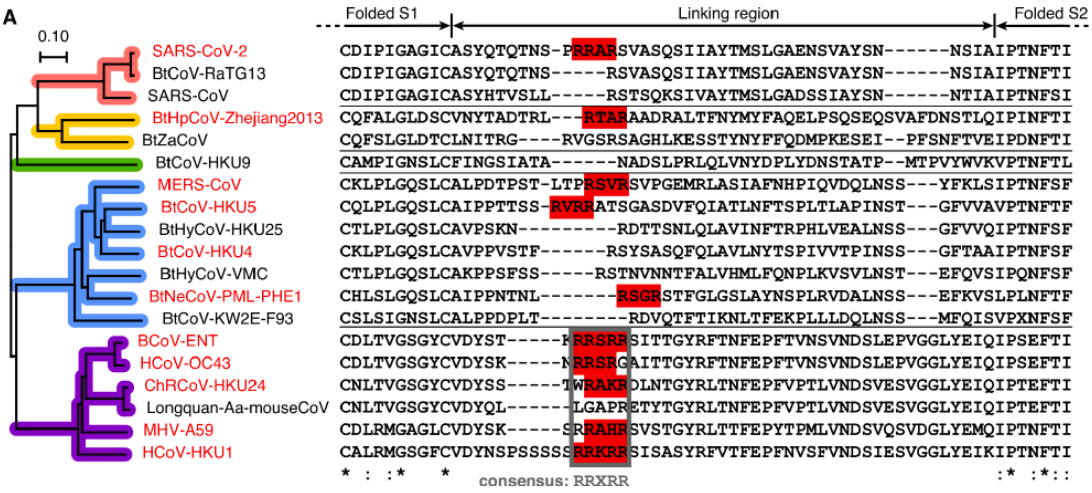

Figure 15: S1/S2 cleavage sites in selected Coronaviridae. Polybasic motifs highlighted in red. From Wu and Zhao 2021[276].

The Vero cell line and its subclone Vero E6 are commonly used for virus propagation due to their easy culture characteristics and lack of Type I interferon production, making them susceptible to many viruses[279]. However, Vero cells do not express TMPRSS2 and therefore only become infected by the endocytic pathway. This created a pitfall for culture of SARS-CoV-2, which was found to rapidly (within a few days'

passage) develop mutations abolishing the polybasic furin cleavage site when cultured in Vero E6 cells (reviewed by Hale et al. [280]). These mutations can include substitutions of one or more of the arginine residues, deletions of the polybasic cleavage site itself, or deletions of the flanking regions which make the cleavage site inaccessible to proteases[281,282]. The emergence of FCS mutations can be avoided by use of TMPRSS2+ cell lines, such as the human lung cell line Calu-3 or transduced Vero-TMPRSS2.

In vivo and in TMPRSS2+ interferon+ cells, viruses entering via the endocytic pathway tend to be inactivated by the interferon-inducible transmembrane protein IFITM2 in late endosomes[277]. This characteristic of Vero cell infection explains the finding that the antimalarial drug hydroxychloroquine inhibits SARS-CoV-2 in Vero cells by blocking endosome acidification and preventing the activity of cathepsin L, in contrast to the severe attenuation of HCQ activity in TMPRSS2+ cells[283]. The previous *in vitro* studies that failed to take this into account unfortunately led to a large amount of resources consumed by the clinical development of hydroxychloroquine and public confusion.

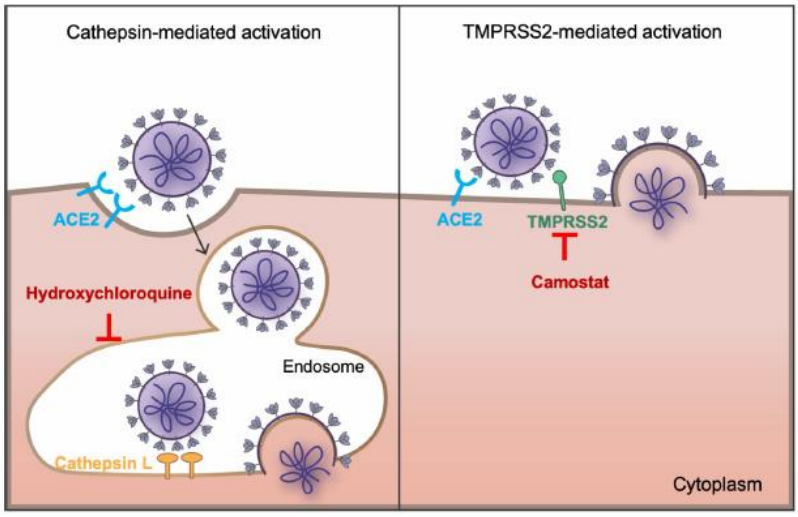

Figure 16: Two entry pathways of SARS-CoV-2 showing fusion at the endosomal membrane (blocked by hydroxychloroquine) or entry at the plasma membrane (blocked by camostat). From Ou et al. 2021[283].

In Vero cells, wild-type viruses have a small plaque phenotype (indicating slower growth) and FCS mutants have a large plaque phenotype[281], whereas the converse is seen in TMPRSS2+ cells[284]. FCS mutant virions tend to aggregate and have a far

higher particle-to-PFU ratio (abundant non-infectious/immature virions) compared to wild-type virus. The high concentration of non-infectious particles can cause apparent decreases in antibody neutralisation titres when a mutant stock is used for neutralisation assays[285]. The FCS mutants are also attenuated *in vivo* in hamsters and ferrets, and not transmissible in ferrets[262,282]. Therefore, the polybasic furin cleavage site in SARS-CoV-2 and other CoVs is a mechanism to evade Type 1 interferon-mediated innate immunity.

1.20 Measurement of neutralising antibodies

There are three main categories of assays for measuring neutralising antibodies against SARS-CoV-2

- Live virus neutralisation
- Pseudovirus neutralisation
- Surrogate neutralisation

Live virus neutralisation assays are based on the format of classical plaque or immunofocus-forming assays. The principle of the assay is that monolayers of a suitable adherent cell line are infected, followed by the addition of a gelling agent to the medium to prevent the virus from diffusing over long distances[286]. Clusters of infected cells are detected by a general stain such as crystal violet to visualise plaques, or immunostaining with antibodies against a viral antigen (immunofocus). Neutralisation assays are performed by incubating serially diluted samples (serum, plasma, monoclonal antibodies) with a known quantity of virus inoculum per well. The titre is usually expressed as the reciprocal of the dilution that neutralises 50% of the input virus.

Pseudovirus assays use pseudotyped virions which can be handled without biosafety level 3 (BSL-3) precautions. These are based on reverse genetics systems where the native envelope protein of the virus is not included, and rescue of virions is done by co-transfecting the plasmids with a SARS-CoV-2 S expression plasmid such that progeny virions bud out coated in S. Two common pseudovirus systems are HIV-based[287,288] and vesicular stomatitis virus (VSV)-based[287,289]. These can also be designed with reporter genes that can be easily detected by fluorescence or

luminescence rather than a lengthy immunostaining procedure. An addition advantage is that pseudovirus stocks with multiple S variants can be generated quickly.

Finally, surrogate neutralisation assays do not involve any virus but are competitive binding assays that measure blockade of the S/RBD-ACE2 interaction. Surrogate neutralisation assays can be in an ELISA format[290] (ACE2 coated on a plate, RBD mixed with plasma samples in suspension), multiplex bead array (Luminex) format[291], thin-film interferometry[292], or flow cytometry[293].

1.21 Humoral immunity from natural infection

Unlike *Mycobacterium tuberculosis*, SARS-CoV-2 clearly presents one immunodominant large B cell antigen: the Spike protein. Neutralising antibodies are mostly directed against the receptor-binding domain; however, some non-RBD neutralising antibodies have also been found. Surprisingly, transfusions of high-titre convalescent plasma had no effect at reducing progression to mechanical ventilation or death in hospitalised patients[294].

The receptor-binding domain of the S1 subunit is the target of most neutralising antibodies. Monoclonal antibodies have been cloned from convalescent human B cells and used to study various aspects of virus neutralisation as well as potential development of therapeutics. Subcategories of RBD-binding antibodies are 1) ACE2-blocking, bind S in its open conformation; 2) ACE2-blocking, bind S in both open and closed conformations; 3) non-ACE2-blocking, bind S in both open and closed conformation; 4) bind S in the open conformation, outside of the ACE2-binding site[295]. Non-RBD neutralising epitopes also exist, for example, the discovery that the S2 stem-helix is the antigen of several mAbs capable of cross-neutralising multiple betacoronaviruses[296], may explain one mechanism for pan-sarbecovirus antibodies found in SARS-1 survivors following Covid vaccination[291]. Engineered bispecific antibodies with strong cross-neutralisation of variants of concern were produced by combining an NTD-binding domain and an RBD-binding domain[297].

While the envelope and membrane proteins are also present on the external surface of the viral envelope, they are much smaller and sterically blocked by the large S proteins. Antibodies against the nucleocapsid (N) protein are useful for determining past

infection e.g. in lateral-flow rapid tests[298]. Anti-N antibodies emerge before anti-S, therefore anti-N serology test are more sensitive for detecting infection at earlier timepoints[299]. On the other hand, anti-N antibodies had disappeared in the majority of convalescent individuals at later timepoints of 9-67 days post molecularly-confirmed infection, so anti-N may not be a reliable marker of prior infection after a few weeks[300].

Duration of immunity in the strict sense can be difficult to test as it requires following up a large number of convalescent subjects for an extended period of time in order to capture re-infection prevalence. Other studies have estimated duration of immunity based on neutralising titres or RBD-IgG titres. In a healthcare worker cohort in Spain, neutralising antibodies increased until day 80 post-symptom onset and remained stable for the rest of the 250-day study period[293]. In most convalescent subjects in California and New York, USA, pseudovirus neutralising titres decayed slowly and remained well above the estimated protective level of 1:20 for at least eight months[301]. Furthermore, while titres dropped, the potency index (neutralisation titre divided by RBD IgG) and breadth of neutralisation (ability to cross-neutralise VOC S) increased over a 2- to 3-month period showing ongoing affinity maturation [302,303]. One source of ongoing antigen exposure could be virus persistence in an intestinal niche. Viral RNA shedding in feces or anal swabs can last longer than shedding from the upper respiratory tract[304], and several individuals who had gastrointestinal tract biopsies months after Covid-19 diagnosis showed N protein and viral RNA (by *in situ* hybridisation) in enterocytes[303].

1.22 Vaccine development

Various platforms have been developed to present the Spike protein to the immune system, ranging from traditional methods such as inactivated whole virus, to new technologies never used at this scale such as mRNA with modified bases. In addition, several of these use engineered versions of the Spike protein sequence that contain modifications for optimal presentation including some combinations of:

- The 2P modification consists of two proline substitutions which stabilise the protein in a prefusion conformation[274]. 2P was originally developed for

candidate MERS-CoV vaccines but was shown to be transferable to other betacoronaviruses.

- HexaPro introduces 4 additional prolines to improve thermostability[305],
- rS2d introduces two cysteines to create a disulfide bond between the RBD and S2 domain. It was found that 2P S proteins are cold sensitive and denature rapidly upon storage at 4°C. This was reversible by incubation at 37°C but is nevertheless undesirable for recombinant protein vaccines. The HexaPro and rS2d modifications both prevent the refrigeration-induced denaturation[306].

A meta-analysis of vaccine efficacy from clinical trials and neutralising antibody titres from vaccinees was used to estimate the minimum protective level of neutralising antibodies (Figure 17). Due to variation in geographical location, demographics, neutralisation assays, and other parameters differing between trials, the authors normalised vaccinee titres against the average titre of naturally infected placebo recipients in each respective trial. It was estimated that the minimum vaccine-induced neutralisation titre required to give 50% efficacy would be 20.2% of the naturally infected convalescent level[307].

A few selected vaccines that have reached Phase 3 trials and/or emergency use authorisation are described in further detail below.

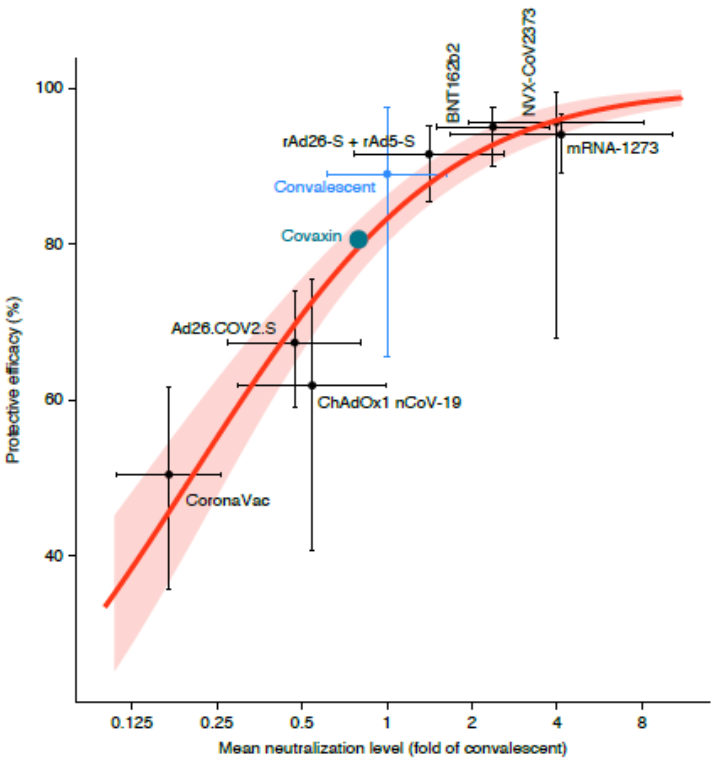

Figure 17: Relationship between antibody neutralisation and protection based on clinical trials of seven vaccines (Covaxin not included in the model). From Khoury 2021[307].

1.22.1 Inactivated viral vaccines

Inactivated vaccines are produced by culturing authentic SARS-CoV-2 in Vero cells and inactivating the virus with β-propiolactone[308]. There are currently three inactivated vaccines in use (Sinovac, Sinopharm, Bharat Biotech).

Efficacy of the Sinovac and Sinopharm products is somewhat lower than that of some of the other platforms described below[307]. One possible reason is that beta-propiolactone inactivation can cause premature dissociation of S1, meaning that some of the inactivated virions may not actually present S1 and RBD. However, this electron microscopy study was performed on a laboratory-scale prepation. At least one of the inactivated vaccines was examined by cryo-EM and most virions appeared to have intact S trimers in a prefusion state[308].

All Covid-19 inactivated viral vaccines are adminstered as two-dose regimens. Efficacy varies widely by geographical setting and predominant variant. For example, the Sinovac vaccine had an efficacy of 83.5 in a phase 3 trial in Turkey during

September 2020 – January 2021[309], but high rates of breakthrough infection are being reported in Indonesia in the presence of VOC Delta. Bharat Biotech's vaccine reported efficacy of 81% in a non-peer-reviewed press release[310].

1.22.2 Recombinant adenovirus-vectored vaccines

Adenoviruses are non-enveloped, double-stranded DNA viruses with genomes of 34-43 kb and capsids of 150 nm in diameter[268,311]. Human adenoviruses typically cause respiratory and enteric infections. Replication-deficient adenoviruses deleted of the early transcription units E1A and E1B are produced in the PER.C6 cell line that supplies essential proteins in trans. They have been used in many vaccine and gene therapy applications, reviewed in [311]. Several human adenovirus-vectored Covid-19 candidate vaccines are currently in use:

The Sputnik V vaccine (Gamaleya) consists of a heterologous prime-boost regimen using 1e11 particles each of Ad26 followed by Ad5 to try to mitigate possible anti-vector immunity. Ad26 was isolated from an infant with respiratory symptoms[312] and pre-existing immunity appears to be lower than against Ad5. In an interim analysis, vaccine efficacy was 91.6%[313].

Janssen's Ad26.COV2.S encodes S with the 2P stabilisation and substitution of two arginines in the furin cleavage site[314]. It is administered as a single dose of 5e10 particles and showed overall efficacy against moderate-to-severe disease of 66.9%, but only 52.0% in South Africa where the vast majority of cases in participants were Beta[315].

A strategy to evade pre-existing anti-vector immunity to human adenoviruses is to use a non-human-origin adenovirus as the vehicle[179]. This had been previously used for several other experimental vaccines such as the ChAdOx1-85A tuberculosis vaccine candidate mentioned above. The S sequence encoded in the ChAdOx vaccine (later designated AZD1222) was the wild-type Wuhan-Hu-1 reference. This vaccine is administered in a two-dose regimen of 5e10 particles each[316].

Convidecia (CanSino Biologics) uses an Ad5 vector administered as a single dose of 5e10 particles. In a phase 2 trial, it stimulated both B and T cell responses, although neutralising antibody titres were low[317]. The Phase 3 trial is ongoing, but interim reults

of 65.7% efficacy against symptomati disease and 90.98% against severe disease have been reported[318].

1.22.3 Protein nanoparticle vaccine

The only protein subunit vaccine that has completed Phase 3 trials so far is NVX-CoV2373 (Novavax). The S protein sequence used in NVX-CoV2373 is 2P-stabilised and has the 3 arginines in the S1/S2 polybasic cleavage site replaced with glutamines to abolish cleavage. The protein is expressed in insect cells (Sf9, *Spodoptera frugiperda*), purified, assembled into nanoparticles with Polysorbate 80, and combined with a saponin-based adjuvant[319]. It is thought that the nanoparticle presentation is more immunogenic than free trimers possibly due to inducing clustering of B cell receptors.

The vaccine is administered as two 5 µg doses. Vaccine efficacy was 96.4% against non-VOC but dropped to 86.3% against Alpha and 51.0% against Beta[320,321].

1.22.4 mRNA vaccines

Both mRNA vaccines in current use (Moderna mRNA-1273, Pfizer-BioNTech BNT162b2) encode the 2P-modified S sequence. The mRNA used in these vaccines has uridine substituted with psuedouridine to enhance translation and avoid excessive proinflammatory responese via Toll-like receptors 7 and 8 (TLR7/8)[322]. The mRNA is packaged in liposomes composed of cholesterol, PEGylated lipids, and phospholipids[323]. These vaccines showed high efficacy in phase 3 trials of 94.1% for mRNA-1273 and 95% for BNT162b2[324,325].

Another mRNA vaccine (CureVac CVnCoV) encoded wild-type Spike and did not use modified bases because it was anticipated that unmodified RNA would help to trigger a stronger immune response[326]. Unfortunately, this had the opposite effect as it had unacceptably high adverse side effects and lower efficacy, possibly due to faster clearance of the foreign mRNA[327,328].

1.23 Syndemics: Covid-19, tuberculosis, and HIV

Approximately 8.2% of the 10 million new TB cases globally in 2019 were in people living with HIV[3]. TB incidence in the WHO African Region had decreased steadily from 2010 onwards, attributed in part to improvements in ART coverage. However, it is feared that decreases in testing, diagnosis, and treatment (e.g. illustrated for India in Figure 18) would have led to a substantial increase in deaths in 2020, with TB excess deaths projected to have increased by 200,000--400,000, and HIV deaths by 229,023–420,000[3,329].

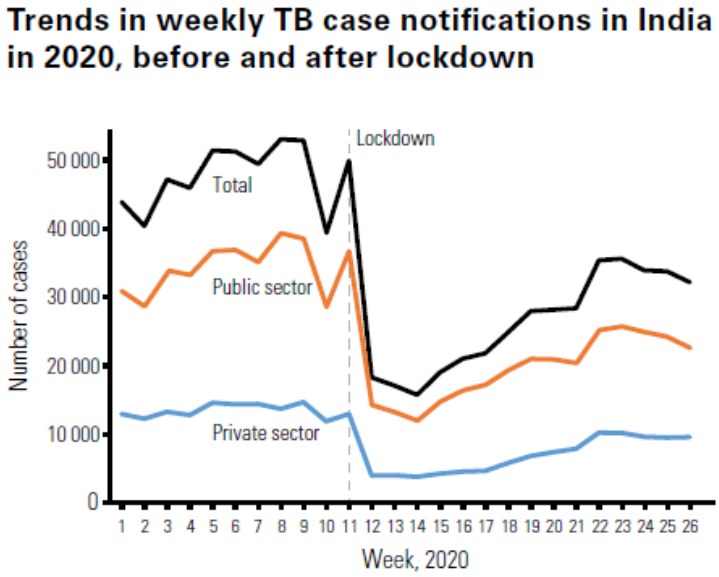

Figure 18: The effects of lockdown on TB case notifications in India. From WHO Global Tuberculosis Report 2020.

The burden of non-communicable diseases such as hypertension and diabetes in sub-Saharan Africa is also increasing; these are also known risk factors for Covid morbidity and mortality. In a large demographic surveillance study in a rural district in KwaZulu-Natal, South Africa, 16.4% of participants had one disease (out of HIV, TB, diabetes, and hypertension) that was not well-controlled, and 9.5% had two or more disease that were uncontrolled. While this multimorbidity was higher in older persons, even among younger women by age 30 only 27.4% did not have any of the four diseases[330].

People living with HIV (PLWH) may be at higher risk for adverse Covid-19 outcomes. Studies from various countries have conflicting findings as to whether there is no significant difference between PLWH and HIV-negative patients[331–335], or if HIV is

independently associated with more severe disease and mortality[292,336,337]. In a Zambian study, while HIV per se was not associated with worse outcomes, severe HIV (defined as one or more of: severe anemia, CD4 <200 cells/µL, active TB, or underweight) was[338]; CD4 <200 was also identified as a risk factor for death in the Western Cape study[336]. A meta-analysis of 28 good-quality studies found that HIV was associated with Covid-19 mortality, but no effect of CD4<200 or receiving antiretroviral therapy (ART)[339]. However, the authors noted that not all studies included CD4 and ART data. Other immunosuppressed conditions such as common variable immunodeficiency are also associated with more severe Covid-19 and a higher frequency of death than the general population.[340]

1.23.1 Problems with access to care and vaccines

Unfortunately, during the pandemic, several countries including South Africa have reported decreases in HIV testing, ART initiation, or ART collection for various reasons including stress on healthcare systems, lockdowns, and global disruptions to shipping and drug supplies[341]. In a worst-case scenario, a six-month interruption of ART across sub-Saharan Africa would be projected to lead to hundreds of thousands of excess HIV-related deaths (not inclusive of additional Covid-19 deaths among PLWH) and a 1.6-fold increase in mother-to-child transmission[329]. ART service delivery urgently needs to be improved.

Reporting of TB cases in many countries fell drastically in 2020, suggesting that a large proportion of new TB cases went undetected and therefore untreated[3]. In contrast to TB for which there is currently only one low-efficacy vaccine in use and a small number in clinical trials, there has been a massively funded global race to develop Covid-19 vaccines, with a number of notable successes[342]. While Mtb is a more complex and challenging pathogen as described above, the lack of success can also be partly attributed to under-funding as most high-income countries failed to fulfil their pledges toward TB research.

	COVID-19	TB
Year causative pathogen identified	2019	1882
Year first vaccine developed	2020	1921
Number of vaccine candidates	109	14
Number of vaccines in phase 3 trials ★★★	31	2
Number of vaccines approved	14	1
Annual deaths	1.7 million in 2020	1.4 million in 2019
Global investment in vaccine development (billion USD)	8.5 (a)	0.117 (b)

Figure 19: Comparison of Covid-19 and TB vaccine development (Faust and Raithby 2021, "The 100th Anniversary Of A Vaccine Against A Deadly Disease: Not A Cause For Celebration")[342]

People living with HIV were unfortunately excluded from many vaccine clinical trials. The AstraZeneca ChAdOx1 nCov-19 trial in South Africa excluded PLWH[343]. Novavax included "medically stable" PLWH in the South African Phase 2ab trial of NVX-CoV2373; however, the number of PLWH was too small to determine efficacy in this subgroup[321]. An international (including South Africa) Phase 3 trial of Janssen's Ad26.COV2.S also included PLWH who had "well-controlled" infection defined as CD4 ⩾300 cells/μL or VL <50 copies/mL[344] but did not report any subgroup analysis. Since no trial to date has reported results for PLWH who are viremic and/or have low CD4 counts, this population could be at risk for low vaccine efficacy as seen in a case study of an individual who failed to seroconvert after two doses of an mRNA vaccine[345].

The shortage of Covid-19 vaccines in high TB- and HIV-burdened countries is also a serious problem, as the benefits of the COVAX programme have been less than anticipated. It is estimated that by the end of 2021, industrialised nations will have acquired a total of 3.3 billion vaccine doses, whereas only 2.3 billion will have been used. This represents a waste of 1 billion doses unless an efficient system can be organised to donate or resell these to LMICs with sufficient lead time for distribution before they expire[346].

1.24 Aims

The aim of my original project was to discover naturally occurring monoclonal antibodies against *Mycobacterium tuberculosis* using a novel method to sort anti-Mtb B cells that would not be biased by pre-selection of purified antigens. We planned to clone antibodies from healthy donor and TB patient peripheral blood, as well as from a unique cohort of TB patient lung lymph node samples. These antibodies would be further screened for functional activity in inhibiting Mtb growth in *ex vivo* macrophage cultures. If successful in isolating such monoclonal antibodies, I aimed to also identify their antigenic targets which could shed light on which proteins or other virulence factors of Mtb are responsible for macrophage invasion and intracellular growth. This could inform vaccine development and antibody immunotherapy in future.

Subsequently, during to the Covid-19 pandemic, I found myself in the position of being one of a very few individuals with a background in general/classical virology and pharmaceutical assay development experience in an HIV-specialist research institute. I volunteered to work on SARS-CoV-2 with the aim of developing methods to accurately and reproducibly quantify infectious virus, quantify antibody binding and neutralisation potency, and to produce high titre, well-characterised virus stocks to facilitate further research on virus biology, immune responses in patients, and vaccine clinical trials in South Africa. Specifically, in this community in Durban, KwaZulu-Natal with a very high prevalence of HIV, we needed to determine if HIV status and immunosuppression associated with HIV viraemia affected the development of immunity to SARS-CoV-2, as well as the impact of emerging variants of concern with the potential to escape humoral immunity.

Chapter 2: Materials and Methods

2.1 Ethical approval

Blood samples were obtained from pulmonary TB patient volunteers and healthy volunteers under the "Collection of Sputum, Urine and Blood Samples" (CUBS) study (Africa Health Research Institute, ethics reference BE022/13). Starting from 2018 Q4, healthy volunteer samples were obtained from the "HIV Negative No TB Symptoms" (HINTS) study, reference BE083/18.

Lung lymph nodes were obtained from TB patients, or from non-TB-disease controls, under the "Lung Tissue & Pleural Effusion Collection for the study of Mycobacterium Tuberculosis Immunology", ethics reference BE019/13.

Covid-19 patient samples including plasma and nasopharyngeal/oropharyngeal swabs were obtained from a cohort study of hospitalised and convalescent patients approved by the University of KwaZulu-Natal Biomedical Research Ethics Committee (reference BREC/00001275/2020). One isolate of SARS-CoV-2 was cultured from a swab obtained from a genomic surveillance program (reference BREC/00001510/2020).

2.2 Clinical samples and primary cell culture

Venous blood was drawn into K_2EDTA or SST Vacutainers (BD) for isolation of peripheral blood mononuclear cells (PBMC) or serum, respectively.

Serum separator tubes were processed according to the manufacturer's instructions (BD). Aliquots of serum were stored at -80°C. Individual aliquots were heat-inactivated at 56°C for 30 minutes prior to use.

To isolate PBMC, anticoagulated blood was diluted with calcium- and magnesium-free DPBS (Lonza), layered over a cushion of Histopaque 1077 (Sigma-Aldrich), and centrifuged for 35 minutes at 400 rcf, room temperature. Buffy coats consisting of PBMC were obtained from the interface between the plasma and the Histopaque. PBMC were frozen in complete RPMI (RPMIc) consisting of RPMI1640 (Lonza) with

6 mM L-glutamine, 10 mM HEPES, 0.1 mM Non-Essential Amino Acids, 1 mM sodium pyruvate (Lonza), and 10% heat-inactivated foetal bovine serum (Hyclone), with 5% cell-culture-grade DMSO (Sigma-Aldrich) in “Mr Frosty” controlled-rate coolers (Nalgene) and stored in liquid nitrogen.

For B cell sorting experiments, PBMC were either used directly, or in a few experiments, B cells were separated prior to staining and bacterial binding using a negative selection kit (Miltenyi Pan B Cell Isolation Kit, Human).

To prepare primary human monocyte-derived macrophages (MDM), CD14+ monocytes were extracted from healthy volunteers’ fresh PBMC by magnetic separation using CD14 Microbeads and LS columns (Miltenyi). CD14+ cells were cultured in RPMI 1640 (Lonza or Gibco) with 6 mM L-glutamine, 10 mM HEPES, 0.1 mM Non-Essential Amino Acids, 1 mM sodium pyruvate (Lonza), and 10% non-heat inactivated human serum (Sigma-Aldrich H4522 or Biowest S4190) (RPMI+HS) with 50 ng/mL GM-CSF (PeproTech) to differentiate them into macrophages. Half volume medium changes were performed every 3 days. MDM were used at 7 to 14 days of differentiation.

For experiments where infection was assessed by flow cytometry, 1 million cells per well were cultured in non-tissue-culture treated 6-well plates (eppendorf). Cells were used at 7 days old. For microscopy, cells were cultured in glass-bottom 6-well plates (MatTek) coated with fibronectin (Sigma-Aldrich F0895) at an initial seeding density of 200,000 fresh CD14+ per well yielding approximately 50% of mature MDM, or 100,000 MDM per well. Timelapse microscopy experiments were performed with 12- to 16-day old cells. Prior to infection, the medium was changed to RPMI 1640 with heat-inactivated human serum or heat-inactivated foetal bovine serum in some experiments. In some experiments, cells were pre-treated with azide-free, low-endotoxin Fc Block (BD Biosciences) at 2.5 μg per 35mm well at least 10 min prior to infection, and the same amount of Fc Block was also added back to the treated wells after the culture medium was replaced with the inoculum.

Lung lymph nodes were obtained from medically indicated surgeries. Following dissection by the surgeons, lymph nodes were transported in RPMI1640 medium on ice to AHRI, cellularised by gently scraping through a 70 μm cell strainer, washed,

resuspended in 90% foetal bovine serum (Hyclone) and 10% DMSO, and frozen and stored in liquid nitrogen.

2.3 Cell lines

THP-1 (human acute monocytic leukaemia, ATCC CRL-1596) and Ramos (Burkitt's lymphoma, IgM lambda B cells, ATCC TIB-202) cell lines were obtained from the American Type Culture Collection (ATCC) and cultured in complete RPMI (RPMIc) comprising RPMI 1640 (Gibco or Lonza) with 10% heat-inactivated foetal bovine serum (FBS, Hyclone or Biowest), 6 mM L-glutamine, 10 mM HEPES, 0.1 mM Non-Essential Amino Acids, and 1 mM sodium pyruvate (all other additives from Lonza)

Vero clone E6 cells (*Cercopithecus aethiops* kidney epithelia, ATCC CRL-1586) were obtained from Cellonex South Africa and cultured in complete Dulbecco's Modified Eagle's Medium (DMEM; Gibco or Lonza) with 10% heat-inactivated foetal bovine serum (FBS, Hyclone or Biowest), 4.5 g/L glucose, 6 mM L-glutamine, 10 mM HEPES, 0.1 mM Non-Essential Amino Acids, and 1 mM sodium pyruvate (all other additives from Lonza)

HEK293T cells (human embryonic kidney, transfected with SV40 T-antigen), were obtained from David Baltimore's lab and cultured in DMEMc.

H1299-H2AZ cells derived from the H1299 non-small cell lung carcinoma cell line, stably transduced with YFP, were obtained from Alex Sigal's work in Uri Alon's lab [347]. H1299-derivative cell lines were cultured in RPMIc.

The generation of H1299-CD40L-IL2-IL21 feeder cells for primary B cell culture was as follows: Human CD40L (also known as CD154) was cloned from mRNA extracted from PBMC of a healthy donor and amplified with primers to create restriction sites for BglII and SalI. The amplicon was digested and ligated into the pBabe.CCR5 plasmid after excising the CCR5 sequence with BamHI and SalI. Viruses were packaged by transfection of HEK29T cells with pBabe-CD40L, pCL-gag-pol, and VSV-G using TransIT-293 reagent (Mirus). The H1299-C3 cells were transduced with virus supernatants by spinfection with 8 μg/mL polybrene at 1000 rcf and room

temperature, for 2 hours. After expansion, cells were trypsinized, stained with CD154:PE/Cy5, and sorted for CD40L expression prior to further expansion.

Lentiviral pHAGE6 vectors containing human IL-2 and IL-21 sequences were also packaged in HEK293T cells and used to transfect the H1299-CD40L cells. Transfected cells were stained with CD154:PE/Cy5 and sorted for CD154+ zsGreen+ (the zsGreen reporter gene is co-expressed with IL-2 and IL-21 in the respective vectors). Cells were single sorted into 384-well plates filled with filtered conditioned medium. Supernatants were screened by ELISA for IL-2 and IL-21 secretion.

Inactivation of H1299-feeders was performed on a X-Rad irradiator (Precision X-Ray), following which they were trypsinised, divided into aliquots, and frozen in RPMIc + 5% hybridoma-grade DMSO (Sigma-Aldrich). For growth of primary B cells on inactivated H1299-feeders, cells were thawed and allowed to attach to tissue culture plates for several hours or overnight prior to adding B cells. Medium for the feeder + B cell co-culture was Iscove's modified Dulbecco's Medium (IMDM) with HEPES and L-glutamine (Lonza) with 10% heat-inactivated FBS and 1x MycoZap-Plus-PR antibiotic-antimycotic (Lonza)[348].

H1299-ACE2 cells for SARS-CoV-2 infection were constructed by Laurelle Jackson by transduction of the parental cell line with a pHAGE2 lentiviral vector encoding human ACE2. Three clonal lines C1, C7, and E3 were produced[269].

2.4 Plasmids

The MoMuLV retroviral vector pBABE.CCR5 encoding human CCR5 and a puromycin resistance marker[349] was obtained from the NIH AIDS Reagent Program. The CCR5 open reading frame was removed by restriction digest. Human CD40L was cloned from PBMC of a healthy donor and ligated into the pBabe backbone to create pBabe-CD40L.

pHAGE6 vectors containing hIL-2 and hIL-21, as well as the backbone vectors for expression of IgG1-kappa (pHAGE6-wtCMV-ABKgibson-BrCr1-ZsGreen-W) and IgG1-lambda (pHAGE6-wtCMV-ABLgibson-BrCr1-ZsGreen-W), and the packaging

plasmids pHDM-Hgpm2 and pHDM-VSV-G for this system were a kind gift from Alejandro Balazs, Ragon Institute.

2.5 Bacteria

2.5.1 Escherichia coli

Escherichia coli (E. coli) strain DH5α for plasmid replication was purchased from Zymo Research. Chemically competent cells were prepared according to standard protocols and stored at -80°C until use (Mix & Go! E.coli Transformation Kit, Zymo Research).

2.5.2 *Mycobacterium tuberculosis* and other mycobacteria

2.5.2.1 Reporter strains of Mycobacterium tuberculosis

Dead *Mycobacterium tuberculosis* strain H37Rv, inactivated by gamma irradiation, was obtained from BEI Resources (catalogue no. NR-14819). Pelleted bacteria were disaggregated by adding 2 mm glass beads and vortexing until macroscopic aggregates were broken up. For flow cytometry labelling experiments, the bacteria were stained with fluorescein isothiocyanate as follows: the bacterial suspension was washed and resuspended in bicarbonate buffer and stained with 20 ug FITC isomer 1 (Sigma-Aldrich) per 1 mL of 1 OD of bacteria, for 30 minutes at room temperature on a rotator, protected from the light. Labelled bacteria were washed in DPBS to remove excess FITC several times and stored in DPBS with 0.01% Tween 20, 0.05% sodium azide, and 2% foetal bovine serum (FBS).

The following 3 fluorescent reporter strains of Mtb were a gift from from David Russell, Cornell University: H37Rv expressing ‘smyc::mCherry (constitutive), CDC1551 and Erdman expressing ‘smyc::mCherry and tet^r::mkOrange (tetracycline-inducible). H37Rv was cultured in 7H9 broth (BD) with Oleic Albumin Dextrose Catalase (OADC; BD) and 50 µg/mL hygromycin for maintenance of the reporter plasmid. CDC1551 and Erdman were cultured in 7H9 with OADC and 50 µg/mL kanamycin (Sigma-Aldrich). Tween 80 (Sigma-Aldrich) was added at 0.05% to prevent aggregation during routine culture; however, growth in surfactant removes the mycobacterial capsule.

2.5.2.2 Preparation of bacterial suspensions for infection

Three to four days prior to infection experiments, bacteria were subcultured at a dilution of at least 1:10 into Tween-free medium to new bacteria to grow with intact capsules. This causes Mtb to aggregate into large, macroscopically visible clumps. To prepare suspensions of singlet bacteria for flow cytometry, cultures were pelleted, disaggregated by adding sterile 2 mm glass beads and flicking the tube by hand 60x, resuspended in DPBS, washed, resuspended, and passed through a 5 µm syringe filter to produce a suspension of single bacteria or very small aggregates of 2-3 bacilli. The concentration was estimated by 600 nm absorbance with a conversion factor of 1 OD ~ 1E8 colony-forming units, which had been previously verified by titration on 7H10 agar plates (data not shown).

For preparation of aggregated bacilli, the 5 µm filtration step was omitted. Suspensions were allowed to settle for 2 min at ambient gravity and passed through a 40 µm cell strainer to remove very large macroscopic aggregates only.

2.5.2.3 Clinical isolates of Mycobacterium tuberculosis

Dr. Alex Pym kindly provided 2 KZN lineage (TKK-01-0081, 0084) and 2 Beijing lineage (TKK-01-0027, 0047) clinical isolates. Non-recombinant bacteria were labelled with FITC prior to antibody staining. Prior to use, bacteria were grown in surfactant-free medium, mechanically disaggregated as above, and stained with FITC for discrimination of bacteria from bubbles and debris in flow cytometry.

2.5.2.4 Mycobacterium smegmatis

Mycobacterium smegmatis (Msmeg) transformed with pVV16 containing smyc'::mCherry for constitutive expression of mCherry was also a gift from David Russell (Cornell University). Msmeg was cultured in 7H9 broth (BD) with Oleic Albumin Dextrose Catalase (OADC; BD), 0.05% Tween 80, and 50 µg/mL hygromycin (Sigma-Aldrich) for maintenance of the reporter plasmid.

One day prior to preparation, bacteria were subcultured at least 1:10 into Tween-free medium to new bacteria to grow with intact capsules. The next day, bacteria were disaggregated as described for Mtb. Bacteria were killed by 254 nm UV irradiation (UVGL-25 lamp, Analytik Jena) for 15 min and stored refrigerated in DPBS.

2.6 SARS-CoV-2 virus stocks

All SARS-CoV-2 isolates were obtained from South African patient swab samples. The two main isolates used in these studies were from AHRI patient 039-13-0013 (representative of first wave virus containing only the D614G spike mutation relative to Wuhan ancestral spike) and genomic surveillance study sample 6518 (representative of second wave Beta VOC). Viruses were propagated in Vero E6 cells. The 6518 swab virus was not infectious in Vero E6 cells and was initially cultured in H1299-ACE2 cells followed by cell-to-cell infection of Vero E6[233,269].

Viruses were harvested at 2-6 days post-infection (depending on experiment) by pooling the supernatant and scraping cells into 50 mL tubes, performing one freeze-thaw cycle at -80°C/37°C, and centrifuging at 1000 rcf for 10 minutes to remove cell debris. Supernantants were aliquoted into screw-cap microtubes and stored in -80°C. Samples were sent to the KwaZulu-Natal Research, Innovation, and Sequencing Platform for deep sequencing by Illumina HiSeq or Oxford Nanopore.

2.7 Flow cytometry and fluorescence-assisted cell sorting (FACS)

2.7.1 B cell sorting

In early sorting experiments, PBMC or lymph node cells from donor samples were thawed and stained on ice with CD19:PE-Cy7, CD27:BV605, and CD38:BV421 (BioLegend). Cells were washed and incubated with inactivated Mtb:FITC (described above) on a rotator in a 2-8°C cold room for 30 min. After incubation, cells were washed 4 times with FACS buffer to remove unbound bacteria. Cells were then stained with DRAQ7 dead cell stain (Biostatus DR710HC).

Cells were then sorted on a FACSAria Fusion (BD Biosciences) in a BSL2 lab for the peripheral blood samples, or a FACSAria in a BSL3 lab for the pulmonary TB lymph node. Some flow cytometry experiments where data was acquired only but cells were not sorted were performed on a BD Fortessa.

Cells positive for CD19 and H37Rv binding were sorted into 96-well plates containing 5000 H1299-E14 feeder cells and 200 uL IMDM+FBS per well. Four to 20 B cells per well were seeded in different experiments to minimise the number of cell culture plates, due to the low survival of antibody-secreting cells observed in this system. In some experiments, single cells were sorted for RT-PCR directly into lysis buffer containing 8 mM DTT, 0.8% NP-40, and 0.25 U/µL RNAse OUT inhibitor (Invitrogen)

In subsequent sorts, additional markers were added to exclude T cells (CD3:PE) and further characterise B cell populations (CD10:PE/Cy5, CD21:PerCP/Cy5.5, IgD:BV785, and IgM: Alexa Fluor 700). In addition, PBMC were treated with Human Fc Block (BD Biosciences) prior to antibody staining. The dead cell stain was changed to Sytox Red (Invitrogen) as it has a narrower emission peak than DRAQ7.

Protein G magnetic beads (Bio-Rad Surebeads) were trialled as control particles in one sort experiment. Beads were uncoated, coated with anti-HIV VRC03 (AIDS Reagent Program) or anti-Mtb HD001HBMEMh804[176]. 0.2 mg of beads were incubated with 5 ug of each antibody in DPBS at room temperature for 5 minutes, washed 3 times with FACS buffer, and mixed with Mtb:FITC and incubated concurrently with PBMC samples. Beads were washed 4 times with FACS buffer before analysis.

2.7.2 Bacterial antibody labelling experiments

Secondary antibodies used in flow cytometry of human mAb-labelled Mtb were anti-human IgG:FITC for the recombinant lab strains and anti-human IgG:PE for the clinical isolates. Isotype controls human IgG1 κ and IgG1 λ (anti-GFP) were obtained from Bio-Rad.

2.7.3 Monocyte and macrophage receptor expression

Fcγ and Fcα receptor expression on THP-1 monocytes and primary monocyte-derived macrophages was verified by staining with CD16:Brilliant Violet 510 (BioLegend), CD32:PE (Bio-Rad), CD64:PerCP/Cy5.5 (BioLegend), and CD89:PE/Vio770 (Miltenyi).

2.8 Primary B cell culture, sampling, and lysis

Supernatants from the sorted B cell – irradiated feeder cell co-cultures were sampled on day 7 or 8 to check for the presence of IgG or IgA, as well as Mtb binding by ELISA as described below. At day 12 or 13, the remaining supernatant was harvested, and cells were lysed[348] and snap-frozen on dry ice + isopropanol slurry and stored at -80°C pending RT-PCR.

2.9 Human immunoglobulin and Mtb antigen ELISAs

Enzyme-linked immunosorbent assays (ELISAs) were designed for two purposes: 1) absolute quantification of total IgG or IgA in samples, 2) detection and relative quantification of anti-Mtb antibodies. Reagents are shown in Table 2 followed by the procedures below.

Table 2: TB ELISA reagents

Assay	**Coating reagent, working dilution or concentration**	**Analyte standard or positive control**	**HRP-conjugated detection antibody, working dilution**
IgG	Goat anti-human IgG Fc (Sigma-Aldrich I2136), 1:20,000	IgG from human serum, reagent grade (Sigma-Aldrich)	Donkey anti-human IgG, Fcγ specific (Jackson ImmunoResearch 709-035-098), 1:10,000
IgA	Rabbit anti-alpha chain (Abcam), 1:5,000	Human IgA from colostrum (Bio-Rad)	Goat anti-alpha chain (Abcam), 1:30,000
Mtb, whole bacteria	*Mycobacterium tuberculosis*, Strain H37RV, Gamma-Irradiated Whole Cells (BEI Resources	Pulmonary TB patient serum, PID 023-11-8104	Goat anti-human H+L (Pierce 31410), 1:5,000

Assay	Coating reagent, working dilution or concentration	Analyte standard or positive control	HRP-conjugated detection antibody, working dilution
	NR-14819), 50 uL of 0.5 OD		
E. coli, whole bacteria	E. coli strain DH5α (Zymo Research), 50 uL of 0.5 OD		
Lipoarabinomannan	*Mycobacterium tuberculosis*, Strain H37Rv, Purified Lipoarabinomannan (BEI NR-14848), 100 ng/well		
Soluble cell wall proteins	Mycobacterium tuberculosis, Strain H37Rv, Soluble Cell Wall Proteins (BEI NR-14840), 200 ng/well		
ESAT-6	Recombinant ESAT-6 produced in E. coli (BEI) , 200 ng/well		
Alpha-crystallin/hspX	Recombinant HspX produced in M. smegmatis (Lionex), 200 ng/well		
Heparin-binding hemagglutinin adhesin	Recombinant HBHA produced in E. coli (Lionex), 200 ng/well		

2.9.1 ELISA procedures

2.9.1.1 Coating, storage, and blocking

Nunc Maxisorp 96-well plates were used. For soluble antigens and capture antibodies, the coating reagent was diluted in bicarbonate buffer[350] to the final concentrations as shown in Table 2. For the quantitative IgG and IgA assays, concentrations of the coating and detection antibodies were optimised by checkerboard titration. For anti-Mtb antigen assays, LAM was used at 100 ng/well and protein reagents at 200 ng/well. Soluble antigens or capture antibodies were allowed to adsorb to plates overnight.

Later, a method was developed for coating ELISA plates with whole bacteria. The purpose of this was avoid missing any antibodies that might target an antigen not present in either the LAM or SCWP fractions. A slurry of the inactivated bacteria was made by vortexing a pellet with 2 mm glass beads for 1 min, resuspending the bacteria in DPBS, allowing the suspension to settle for 2 min, and harvesting the homogenous upper layer. This suspension was adjusted to 0.5 OD and used to coat Nunc plates with 50 uL/well. Initially plates were dried at 60°C for 3 – 4 h based on the procedure of drying smear slides for microbiology on a 60°C hotplate, but this was later changed to drying overnight at room temperature, approximately 20 – 23°C in the AHRI lab, to avoid missing samples reactive to temperature-sensitive antigens.

E. coli was used as a bacteria negative control to check for nonspecific binding of monoclonal antibodies. *E. coli* strain DH5α from a log phase LB culture was washed with DPBS, resuspended, and coated onto Maxisorp plates by room temperature drying in the same manner as for inactivated Mtb. E. coli was inactivated by 5 minutes' shortwave UV irradiation (UVP, Analytik Jena).

Plates coated with soluble antigens or antibodies were washed 3 times with phosphate-buffered saline (Sigma-Aldrich P4417) with 0.05% Tween 20 (Sigma-Aldrich P9416) (PBST), using a Bio-Tek ELx405 plate washer. Plates coated with whole bacteria were only washed immediately before use to minimise loss of bacteria. All coated plates were stored in sealed ziplock bags with silica gel desiccant at 2-8°C for up to 1 month.

Skim milk at 5% w/v was used as a blocking protein initially; however, this caused high background signal which was especially problematic for primary single cell culture supernatants with very low concentrations of antibody. Switching to bovine

serum albumin resolved this problem. BSA (Celtic Diagnostics P6154) was used at 3% for initial blocking and 1% as antibody diluent. Plates were blocked for ≥ 30 min at room temperature prior to sample addition.

2.9.1.2 Samples and controls

Concentrated samples such as human serum and monoclonal antibodies were pre-diluted to within the expected range of the assay, and titrated in duplicate in 4-fold dilution series. Primary B cell supernatants were tested in singlicate at a single dilution of 1:4 due to their small volume and low concentrations.

Purified native human IgG and IgA were used as quantitative standards according to the concentrations on the lot-specific certificates of analysis. Commercial human serum of USA origin (Sigma-Aldrich cat. no. H4522) was used as a control for Mtb antigen ELISAs. However, this material cannot be considered a negative control as it does show anti-Mtb binding therefore it was used simply as a benchmark for plate-to-plate and run-to-run variation. Serum from a TB patient PID 023-11-8104 which came up as strongly reactive in early development was subsequently used as a high positive control. The original concentration was 32.4 mg/mL possibly due to this being a person coinfected with HIV. It was prediluted for usage to a similar total IgG concentration as the samples of interest.

For IgG and IgA quantification assays, sample incubation was performed at room temperature for 1 hour with orbital shaking at 300 rpm. For Mtb antigen assays, sample incubation was performed overnight in a refrigerator.

2.9.1.3 Detection and data analysis

Following sample incubation, plates were washed 3 times, and the respective detection antibody was added and incubated for 1 hour at room temperature, 300 rpm.

Tetramethylbenzidine (Sigma-Aldrich T0440) was used as the colorimetric detection reagent at 100 uL/well. Plates were incubated for 6-8 minutes at room temperature for serum and concentrated monoclonal antibody samples. Assay plates for B cell culture supernatants were incubated up to 2 h because the concentration range was extremely low; however, the positive control dilution series still showed a clear gradient which was clearly distinguishable from background once the blocking reagent was switched from milk to BSA.

TMB reactions were stopped with an equal volume of 1 M sulphuric acid (Sigma 35276). Plates were read on a Bio-Tek ELx808 using Gen5 software, at 450 nm (measurement) and 630 nm (reference). For the IgG and IgA quantitative ELISA, the standard curve and interpolation of samples were calculated in Gen5, using the commercial purified immunoglobulin standard curves. For Mtb antigen ELISAs of serum or concentrated monoclonal antibodies, the blanked data were exported into GraphPad Prism for calculation of EC_{50} and area under the curve (AUC) values of each sample dilution series. In some cases, sample AUCs were normalised against the control IgG AUC in order to compare results between assay runs. For Mtb antigen ELISAs of B cell supernatants tested at a single dilution, each sample was scored as positive/negative based on a cut-off value of the average plus three times the standard deviation of the blanks.

2.10 Antibody cloning and expression

2.10.1 Heavy and light chain RT-PCR and cloning

Sequences of primer sets for gamma heavy chain and kappa and lambda light chains were obtained from Georgiev et al. 2013[351] based on Tiller et al. 2008[352]. Alpha heavy chain 3' primer sequences were obtained from Benckert et al. 2011[353]. Primers were synthesized by Inqaba Biotec (Pretoria).

RNA was purified from lysates using the RNeasy Plus Micro kit (Qiagen). SuperScript IV reverse transcriptase (Invitrogen) was used for reverse transcription, with the same gene-specific 3' primers as the first round of PCR, as I found that using gene-specific primers for this step was more efficient than the original method of using random hexamers (data not shown). Therefore the RT step was performed in 3 separate reactions for heavy chain, kappa light chain, and lambda light chain genes. Two rounds of PCR using HotStar Taq (Qiagen) were perfomed according to the published protocol with the respective primer sets.

Amplicons were Sanger sequenced by Inqaba Biotec. Alignment and clean-up of sequence data was done in Geneious 10 (Biomatters). Long single-stranded oligonucleotides with 40-nucleotide 5' and 3' arms overlapping the ends of the

respective heavy and light chain variable region sites in the pHAGE6 antibody expression plasmids were synthesized by Integrated DNA Technologies or GenScript. Variable region synthetic fragments and a PCR product encoding the gamma heavy chain constant region were assembled into the pHAGE6 backbones by Gibson assembly (New England Biolabs).

In addition to the 7 clones obtained from AHRI donors described in the Results below, the variable regions from 5 previously published Mtb-binding antibody heavy and light chain pairs[176] were also synthesised from GenBank sequences to serve as positive controls in binding assays. These 5 were selected based on reported neutralisation activity (when expressed as IgA) and lack of cross-reactivity with auto-antigens.

2.10.2 Monoclonal antibody production and purification

HEK-293T cells were transfected with the pHAGE6 plasmids and packaging plasmids to produce lentiviral vectors. The supernatants were used to transduce fresh 293T cultures by spinfection with polybrene[347]. After 4 days, successfully transduced cells were sorted for high zsGreen fluorescence. The zsGreen reporter gene is downstream of the heavy and light chains in a bicistronic cassette separated from the light chain by an enteroviral internal ribosome entry site (IRES), therefore zsGreen fluorescence is a strong indicator that the antibody heavy and light chains were also expressed. For small-scale antibody production, cells were expanded into 2x 150 cm^2 flasks, washed with DPBS, and the medium replaced with Freestyle 293 (Gibco). Later, 500 cm^2 triple-layer flasks (Nunc) were also used. Supernatants were harvested after 7 days.

IgG1 was purified using Protein A/G agarose (Pierce 20421) and 10 mL columns, based on a scaled-down version of a protocol provided by the Balazs Lab (Alejandro Balazs and Chris Bullock, Ragon Institute, personal communication). Supernatants were clarified by centrifugation and incubated with agarose slurry overnight on a tube roller. The supernatant-Protein A/G agarose suspensions were poured through a 10 mL column twice to collect all the agarose beads. The agarose was washed with DPBS, and IgG was eluted with 0.1 M glycine, pH 3 by gravity flow into collection tubes containing a 10% volume of 1 M Tris, pH 8.5. Antibodies were concentrated down to

volumes of ≤ 500 uL using Spin-X UF 20, 50 kDA MWCO concentrators (Corning 431490).

After the first batch in September 2017, the following modifications were made in processing the second batch in January 2018 due to results described below: 1) To avoid long exposure of potentially sensitive antibodies to the acidic glycine elution buffer, collection tubes containing the neutralisation buffer were mixed by tapping frequently during the gravity flow elution, as it was noticed that the elution buffer formed a separate layer which did not mix spontaneously. 2) Following the spin concentration step, instead of purification by FPLC as this was not available at AHRI, the 0.2 – 0.5 mL volumes of concentrated antibodies were washed twice with 20 mL tissue culture grade DPBS. The purpose of this step is to remove the Tris-glycine buffer which was previously found to have a detrimental effect on THP-1 macrophage survival at dilutions of ≤ 1:16 (data not shown). 3) BSA was added to a final concentration of 5 mg/mL as a carrier protein to prevent loss from precipitation and adsorption.

IgA1 was purified by the same method, using CaptureSelect™ IgA-CH1 (Hu) Affinity Matrix (Thermo Scientific).

The concentrations of purified antibodies prior to adding BSA were measured by Nanodrop and quantitative IgG or IgA sandwich ELISA. Finally, stock solutions were standardised to 1 mg/mL IgG in 5 mg/mL BSA by the addition of DPBS and sterile 10% BSA solution.

2.11 Western blotting

Proteins in Mtb H37Rv whole cell lysate or cell wall fraction were electrophoresed by SDS-PAGE in precast 10% and 12% PAGE gels (Bio-Rad) with in-house made buffers. The molecular weight marker used was Precision Plus WesternC (Bio-Rad). Proteins were transferred onto PVDF membranes in Trans-Blot Turbo Mini packs (Bio-Rad). Membranes were blocked in BSA and probed with either heat-inactivated serum samples or monoclonal antibody P2E04. Following incubation with goat-anti-human IgG(H+L):HRP (Pierce) secondary antibody, blots were imaged with Clarity Western ECL Substrate (Bio-Rad) on a ChemiDoc XP.

2.12 Immunoprecipitation

Surebeads Protein G magnetic beads (Bio-Rad) and Pierce Protein A/G Agarose beads (ThermoFisher Scientific) were used for immunoprecipitation. Two workflows were tested: 1) coating beads with mAb P2E04 followed by incubation with Mtb H37Rv whole cell lysate (BEI Resources) or 2) incubating P2E04 with WCL in suspension, followed by pulldown with beads. Wash steps were performed by precipitating the magnetic beads with a magnet, or by loading the agarose beads into SigmaPrep mini spin columns (Sigma Aldrich) and washing four times with PBS. Bound samples were eluted with SDS loading buffer for electrophoresis.

2.13 Protein sequencing by mass spectrometry

Immunoprecipitation samples separated on SDS-PAGE gels as above were stained with SYPRO Ruby (Invitrogen) according to the manufacturer's instructions. Gel slices thought to contain proteins of interest were cut out and subjected to in-gel digestion. Digested extracts were handed over to the AHRI Pharmacology Core (John Adamson and Katya Govender) for analysis using a Thermo Scientific Dionex Ultimate 3000 UHPLC system coupled to a Thermo Scientific Q-Exactive Mass Spectrometer. Peptides were aligned to the *Mycobacterium tuberculosis* H37Rv and H37Ra proteomes. H37Rv gene numberings[354] and cellular locations were obtained from Mycobrowser[151].

2.14 THP-1 monocyte infection with Mtb

The general workflow for suspension THP-1 infection experiments was as follows: Infection mixtures were set up in deep-well polypropylene 96-well plates. Singlet Mtb suspensions were diluted to target concentrations in RPMIc and combined with serum samples at 1:20, or monoclonal antibody samples at 50 ug/mL, in the deep-well plates. Plates were covered and incubated at 37°C, ambient air, 100 rpm for 1 hour. At the end of the incubation, THP-1 cells were added to the deep-well plate, mixed, and transferred to 96-well round-bottom plates in order to have several technical replicates

per sample per plate. The final cell count in culture wells was 25,000 monocytes in 100 µL per well. Plates were transferred to a tissue culture incubator at 37°C, 5% CO_2.

At the indicated time points, THP-1 cells were centrifuged, resuspended in DPBS with the far-red fixable viability dye eFluor 660 (eBioscience) at 1:1000. After incubation, cells were centrifuged again, resuspended in FACS buffer without dye, and transferred to a clean plate pre-filled with 1/3 volume of 16% methanol-free formaldehyde (Pierce) for a final concentration of 4% formaldehyde to inactivate Mtb. Fixed cells were exported from the biosafety level 3 lab and analysed on the BD Fortessa using the HTS (high-throughput sampler) attachment.

2.15 Primary macrophage infection with Mtb

Prepared bacterial suspensions were diluted in macrophage culture medium to a targeted multiplicity of infection (estimated CFU per macrophage) and opsonised with antibody samples at 20 ug/mL IgG at 37°C, 100 rpm shaking for 1 hour. MDM were infected by replacing the medium in the tissue culture dishes with these antibody-bacteria mixtures.

2.15.1 Intracellular Mtb growth and host cell death measured by flow cytometry

At the indicated time points MDM were harvested by two rounds of Accutase digestion (Sigma-Aldrich A6964) for 10 min at 37°C followed by vigorous pipetting. Culture supernatant was pooled with the digests to include any dead cells that may have detached previously. Dissociated cells were washed and resuspended in DPBS + 1% FBS. The dead cell penetrant, far red dye DRAQ7 (Biostatus) was added at 1:1000. Cells were analysed on the FACSAria.

2.15.2 Timelapse microscopy

Following infection, DRAQ7 was added at 2.5 µM. In some experiments, Hoechst 34580 at 2 ug/mL (Thermo Scientific H21486) was added as a live cell nuclear stain for tracking macrophages, but either the Hoechst or the 405 nm violet laser excitation proved to be detrimental to the bacteria, therefore it was excluded from subsequent

experiments (results section 4.2.5). Cells were incubated in a 37°C, 5% CO_2 environmental chamber on a Nikon Ti-E-based confocal microscopy system. Images were acquired using the 20x objective at 10-, 12-, or 20-minute intervals (depending on experiment).

2.15.3 Quantitative PCR (qPCR) of Mtb DNA copies

To create a stock of purified Mtb genomic DNA for use as a standard curve for genome copy number estimation, I extracted DNA from a culture of Mtb CDC1551 by bead-beating with Trizol, followed a second extraction with phenol:chloroform:isoamyl alcohol to remove the high protein carry-over. The final concentration was measuring using a Quant-It High Sensitivity dsDNA kit (Invitrogen) to minimise inaccuracy from RNA and protein carry-over. qPCR was performed with iTaq Universal SYBR Green Supermix (Bio-Rad) using a protocol from the Alex Pym lab using primers for the *gyrA* gene (Kayleen Brien, personal communication).

gyrA primer sequences:

- P82: CATCGCCGGGTGCTCTATGC
- P83: TCCATCGCCAACGGGGTCAG

To quantify intracellular bacteria, infected MDM were lysed with 0.1% Triton X-100. Bacterial DNA in culture supernatants and lysates was extracted by heat inactivation, bead-beating with glass beads, followed by AMPure XP magnetic bead pull-down[355]. Copy numbers of the gyrA gene were measured by qPCR using the DNA preparation above as a standard curve. To control for donor-to-donor and run-to-run variation in host cells, the gyrA counts in each sample were normalised to the medium-only control.

2.15.4 RNA-seq of infected macrophages

At 6 hours post-infection, macrophages were harvested as described above and immediately placed on ice. Cells were gated for sorting as uninfected or low, medium, or highly infected based on approximate tertiles of the total infected population in the normal medium control sample. Ten thousand cells per gate were sorted into TRIzol (Invitrogen) and snap-frozen on dry ice + isopropanol slurry. RNA was purified using

a Direct-zol MicroPrep kit (Zymo Research), and reverse transcribed and amplified according to the SMART-Seq2 protocol[356]. cDNA library quality was evaluated on a TapeStation 4200 (Agilent). Nextera tagmentation was performed by the KZN Research Innovation & Sequencing Platform (KRISP, Durban) and next-generation sequencing was performed on an Illumina HiSeq at the Agriculture Research Council (ARC, Pretoria). Werner Smidt from KRISP performed the data analysis.

2.16 SARS-CoV-2 receptor-binding-domain ELISAs

The RBD IgG ELISA was adapted from a draft protocol sent by Galit Alter, Ragon Institute (personal communication). The development and optimisation of a more robust version of the assay is further detailed in Chapter 5.

Nunc Maxisorp 96-well flat-bottom plates (Thermo Fisher Scientific) were coated with 100 µL/well of 500 ng/mL (i.e. 50 ng/well) of recombinant receptor-binding domain (cloned from the Wuhan-Hu-1 reference strain and bearing His and SBP tags (Alter lab, Ragon Institute). Following overnight incubation in the refrigerator, plates were washed with high-salt Tris-buffered saline + 0.05% Tween 20, pH 8, and blocked for 1 hour at room temperature with 200 µL/well Tris-buffered saline (TBS) with 1% bovine serum albumin, then washed again.

Antibody samples were diluted in TBS + 0.05% Tween 20 + 1% bovine serum albumin (TBSAT). Monoclonal antibody CR3022 was used as a positive control and standard curve for RBD IgG (Alter lab, Ragon Institute). Humanised anti-RBD hIgM2001 and hIgA2001 were purchased from GenScript as standards for the IgM and IgA ELISAs respectively. Standards were serially diluted four-fold from 1000 ng/mL down to 0.244 ng/mL. Heat-inactivated plasma samples were tested at 1:100, 1:1000, and 1:10,000 dilutions for IgG and IgM, and at 1:100 and 1:1000 only for IgA as the concentrations were generally lower. Samples were added to wells in 100 µL volumes on duplicate plates and incubated for 1 hour at 37°C before washing.

Detection antibodies were goat anti-human IgG (diluted 1:5000), IgM (1:5000), and IgA (1:10,000) horseradish peroxidase conjugates (Jackson ImmunoResearch) diluted in TBSAT, added to plates at 100 µL/well, and incubated for 1 hour at room temperature. After a final wash, bound antibodies were detected witth 100 µL/well

Ultra TMB peroxidase substrate (Thermo Fisher Scientific). The reaction was stopped with 1 M sulphuric acid after 3 minutes (IgG) or 5 minutes (IgM and IgA).

Optical densities at 450 nm (measurement wavelength) and 595 nm (reference wavelength) were read on a Bio-Tek ELISA plate reader. Diluted sample concentrations were interpolated against a four-parameter logistic curve fit for the respective isotype standard in the Gen5 (Bio-Tek) software. For samples tested at multiple dilutions, the result from the dilution falling within the EC_{20}-EC_{80} range of the standard curve was reported, to avoid inaccuracy in very low or very high OD wells. The values from the duplicate plates were averaged. To determine true positives, cutoff values were established using pre-pandemic control plasma samples from the FRESH study and a commercial normal serum (Biowest); the cutoff for each respective isotype was calculated as the mean + 3 standard deviations of the pre-pandemic controls.

2.17 Surrogate virus neutralisation test (sVNT)

Ten kits of a surrogate virus neutralisation test (sVNT)[290] manufactured by GenScript were kindly provided by Wang Linfa (National University of Singapore). The assay was performed according to the manufacturer's instructions. Heat-inactivated plasma samples were tested at a single dilution of 1:10, therefore results are reported as percent inhibition score relative to the kit's negative control (inhibition $\geqslant$ 30% is positive) instead of endpoint titre.

2.18 ACE2 staining

Vero E6 and H1299-ACE2-C7 cells were seeded into 6-well glass-bottom plates (MatTek) coated with fibronectin overnight. Cells were fixed with 4% paraformaldehyde in PBS, washed with PBS, and incubated with the primary rabbit anti-hACE2 polyclonal antibody (Abcam ab272690) at 2.5 µg/mL in PBST + 1% BSA overnight in a cold room, with rocking. The secondary antibody, goat anti-rabbit IgG Alexa Fluor 555 (Abcam ab150078) was used at 4 µg/mL and incubated for 2.5 hours. Nuclei were counterstained with DAPI. Images were acquired with the 60x objective on a Nikon Ti-E-based confocal microscopy system using the 488 nm laser and standard filter for DAPI, and the 561 nm laser and 462 nm filter for Alexa 555.

2.19 SARS-CoV-2 virus titration and antibody neutralisation assays

SARS-CoV-2 was titrated in both Vero E6 and H1299-ACE2 cells due to the huge difference in infectious titre (results section 5.2.2.1). For both cell lines, cells were seeded overnight prior to infection (16-20 hours) at 25,000 cells per well in 96-well tissue culture-treated plates.

The focus-forming assay for visualisation of infected cell foci was loosely based on Case et al. 2020[357] but with some optimisations and modifications as discussed in the Results. The finalised method is as follows: Virus samples were diluted in infection medium consisting of complete RPMI with 2% heat-inactivated FBS and 1x MycoZap Plus-CL antibiotic cocktail (Lonza). Growth medium was decanted from cell plates immediately before infection with 100 µL/well of the dilutions and incubated for 1 hour at 37°C to allow virus adsorption. Stock solutions of 2x RPMI and 3% carboxymethylcellulose (Sigma-Aldrich) were combined in equal volumes; wells were overlaid with 100 µL of this mixture. I used RPMI instead of DMEM as the basal medium, as one jar of RPMI powder was the only powder/concentrate medium available to hand during global shipping logistics disruptions due to the pandemic.

The next day (18-24 hours post-infection depending on strain) the medium was removed by pipetting . Cells were fixed with 200 µL/well 4% paraformaldehyde (PFA) in PBS for a minimum of 20 minutes. After washing off the PFA using PBS + 0.05% Tween 20 (PBST), plates were incubated with 100 µL/well rabbit anti-SARS-CoV-2 Spike monoclonal antibody BS-R2B12 (GenScript) in a perm-wash buffer consisting of 0.1% BSA and 0.1% saponin in PBS, for either 2 hours at room temperature with 30 rpm side-to-side rocking or overnight in the refrigerator. Plates were washed with PBST and then incubated with 100 µL/well goat anti-rabbit horseradish peroxidase-conjugated secondary antibody (Jackson ImmunoResearch) in perm-wash buffer, for 2 hours at room temperature with rocking. Plates were then washed again and incubated with 50 µL/well TrueBlue precipitating TMB (SeraCare) until distinct staining appeared, about 20-30 minutes. Plates were finally washed with distilled water and air-dried before image acquisition on the Nikon Eclipse microscope using a 2×

phase-contrast objective, which produced fields of view that exactly covered one 96-well plate well or slightly smaller, depending on the plate manufacturer.

Wells containing 10 – 100 foci were selected for counting. Virus titres expressed as focus-forming units per millilitre (FFU/mL) were calculated by taking the average of replicates within the acceptable countable range, dividing by the inoculum volume (0.1 mL), and multiplying by the dilution factor.

For antibody neutralisation assays, plasma samples were heat-inactivated at 56°C for 30 minutes and clarified by centrifugation at 10000 rcf for 5 minutes, then aliquoted and stored at -80°C. Samples were serially diluted in infection medium. Monoclonal antibodies and nanobodies were diluted according to the nominal concentration given by the manufacturers. Samples were titrated in duplicate. Virus stocks of known titre were diluted to 2x the final desired inoculum concentration, then mixed with the antibody sample dilution series and incubated for 1 hour. The virus-antibody mixtures were then added to the cells, and then incubated and processed as above.

The fifty percent focus reduction neutralisation titre for each sample ($FRNT_{50}$) was calculated as follows: Focus counts in all wells on a given plate were normalised to the average of the no-antibody control wells (n = 8) on the same plate, in Microsoft Excel. Normalised counts were copied into Prism (v9, GraphPad) and plotted using a four-parameter logistic with the Top and Bottom parameters constrained to 1 and 0 respectively. The EC_{50} output from Prism was reported as the $FRNT_{50}$. Neutralising titres were expressed as inverse dilution factors for plasma samples, and in nanograms per millilitre (ng/mL) for monoclonal antibodies and nanobodies.

2.20 SARS-CoV-2 plaque picking

The plaque assay method was adapted from Mendoza et al[358]. Vero E6 cells were seeded in 6-well plates at 1e6 cells/well overnight prior to infection. SARS-CoV-2 isolates 13-0013 and 6518 were serially diluted in RPMI + 2% FBS infection medium and wells were infected with 100 µL of diluted virus. Plates were incubated at 37°C for 1 hour and rocked by hand at ~15 minute intervals to distribute the inoculum and prevent drying out. A 2x RPMI stock solution was mixed with an equal volume of sterile 2% SeaPlaque low-melting-point agarose (Lonza) that had been melted in a

microwave; the agarose medium was equilibrated to 37°C in a water bath before overlaying the cells with 3 mL/well. Two days post-infection, cells were overlaid with an additional 2 mL of RPMI-agarose with 0.01% Neutral Red live cell stain (lysososmal). The following day, plaques were visualised by using a small LED torch placed in a pipette tip box as a makeshift lightbox.

Three well-separated large plaques and three small plaques of 6518 were picked by punching a 200 µL pipette tip through the agarose and aspirating ~50 µL from each spot, then triturating the agarose plug in 100 µL of infection medium. This material was used to infect 1 well each of H1299-ACE2 cells in 6-well plates.

The small plaque viruses were further amplified with a 2nd passage into H1299-ACE2 in a 25 cm^2 flask for 6 days. These cells were trypsinised and seeded onto 2x 75 cm^2 flasks of Vero E6 cells each (i.e. an infected donor:target ratio approximately 1:6), incubated for 2 days only to reduce the risk of FCS mutant evolution. The reason for performing a short passage in Vero E6 cells was because of the extremely low productivity of H1299-ACE2 cells; while they are sensitive to infection, little progeny virus is released into the supernatant. While there are some cell lines such as Calu-3 or Vero-ACE2-TMPRSS2 cells which produce high titres of wild-type virus, our lab did not have them at the time.

First passage samples for all six plaque picks, and third passage samples for the small plaque cultures, were sent to KRISP for deep sequencing.

2.21 Image analysis

Image analysis was performed in MATLAB (Mathworks) using scripts which were partially written by myself and partially by other lab members.

For Mtb singlet infection experiments, total bacterial load per field was measured as total mCherry fluorescence, and dead macrophages were counted as the number of DRAQ7+ objects. It proved to be difficult to accurately bacterial load in macrophages infected with singlet bacilli due to the low signal.

For Mtb aggregate infection experiments, cells were segmented based on edge detection, followed by manual correction by trained operators if necessary. This

enabled quantification of bacterial load and DRAQ7 dead cell penetrant dye per individual cell over time.

For enumeration of SARS-CoV-2 foci immunostained with TrueBlue, a local Laplacian filter was applied to sharpen the foci and blur the background, followed by image binarisation. A circular region of interest a few pixels smaller than the diameter of the well was applied to crop out the well edge. Objects falling within a certain size range were counted (larger than minimum cutoff to exclude noise and “satellite” foci and smaller than maximum cutoff to exclude clusters of overlapping foci).

2.22 Statistical analysis

Statistical analyses were done in Prism (versions 8/9, GraphPad). Two-tailed t-tests were used to compare two groups with normally distributed data; the nonparametric Mann-Whitney U test was used to compare non-normal data. For paired/matched non-normal data, the Wilcoxon matched-pairs signed rank test (paired data across two treatments) or Friedman test (matched data across >2 treatments). For non-linear regression, comparison of models was done by the sum-of-squares F test.

Chapter 3: Isolation and characterisation of human monoclonal antibodies against *Mycobacterium tuberculosis*

3.1 Introduction

Previous attempts to isolate monoclonal antibodies against *Mycobacterium tuberculosis* have used two main strategies: a) pre-selecting a known antigen of interest, then using it as bait for sorting or panning B cells or phage display libraries[176,359]; b) cloning antibodies from unselected memory B cells from TB-exposed individuals[176]. While the former approach is more efficient in isolating specific antibodies, by definition it cannot be used for new antigen discovery. The latter approach requires cloning and *in vitro* expression of a large number of antibodies and the use of high-throughput equipment, as most of the cloned sequences would likely not be Mtb-specific, even from donors with high ELISA responses.

I aimed to use an antigen-agnostic approach to pull down any B cells capable of binding whole Mtb bacilli, on the assumption that in at least some of these cases, binding would occur via specific B cell receptors. This approach could potentially enable the discovery of new Mtb surface antigens as well. A caveat with this method is that nonspecific binding could also occur, so additional down-selection steps are required to ensure specificity.

The B cell isolation and antibody cloning pipeline is summarised as follows:

1. Preparation of inactivated, fluorescently labelled Mtb suspensions as bait.
2. Incubation of donor peripheral blood mononuclear cells or lymph node homogenates with the fluorescent Mtb, and sorting for Mtb-binding B cells.
3. Culture of the sorted B cells on a feeder cell line supporting the survival of antibody-secreting cells.
4. ELISA screening of culture supernatants for the presence of IgG and IgA and Mtb-binding activity.
5. RT-PCR of the heavy and light chain gene variable regions and cloning into a lentiviral expression vector.

6. Transduction of a suitable cell line for antibody production.
7. Verification of Mtb antigen binding by the recombinant antibodies by ELISA and bacterial flow cytometry.
8. Attempts to identify the specific antigens by ELISA of purified proteins and immunoprecipitation.

Since the B cells were sorted based on Mtb binding, the resulting mAbs should be expected to label whole bacteria, which can be verified by ELISA or bacterial flow cytometry. There may not always be a one-to-one correspondence between pulldown by FACS and the resulting antibodies, as Zimmermann et al. found that among a large number of mAbs cloned from B cells sorted by HBHA binding, not all bound HBHA.

One strategy to reduce the number of samples to be cloned is to introduce an intermediate step of short-term culture of the primary B cells under conditions that promote antibody secretion. The culture supernatants can then be screened by ELISA for the presence of specific antibodies prior to lysis and cloning. Providing CD40L stimulation using transgenic feeder cells along with exogenous IL-2 and IL-21 was reported to be 77% efficient in yielding IgG-secreting wells, on the basis of seeding an average of 4 B cells per well [348].

For identification of the targets of newly isolated mAbs, ELISA is limited in terms of the number of purified recombinant antigens that are available from public repositories or commercial sources. Another possible approach is to use the mAbs for immunoprecipitation of Mtb lysate, followed by shotgun peptide sequencing by mass spectrometry. However, immunoprecipitation can be technically challenging if the antigen is insoluble, unstable, or not in the same native conformation as in whole bacteria.

3.2 Results

3.2.1 Serum IgG from South African healthy volunteers and TB patients reacts with LAM and cell wall proteins

Serum samples matched to stored PBMCs were screened by ELISA (methods 2.9) to identify candidates with a high concentration of Mtb-binding antibodies. We were able to recruit a limited number (3) of healthy donors from non-TB-endemic countries. However, these individuals had been BCG-vaccinated due to work in healthcare or laboratories. We were unable to recruit any completely TB/BCG unexposed negative control donors. Pooled normal serum from a commercial source (Sigma-Aldrich) was used as an assay control.

Serum from 9 clinically healthy South African participants, 6 participants with pulmonary TB, and 7 participants with TB and HIV showed a wide range of reactivity to Mtb LAM (Figure 20) and cell wall proteins (Figure 21). Dilution curve half-maximal effective concentrations (EC_{50}) are shown in Figure 22 and Table 3. While sera from HIV-negative TB patients was the highest binding on average, differences between participant groups were not significant due to the wide variation.

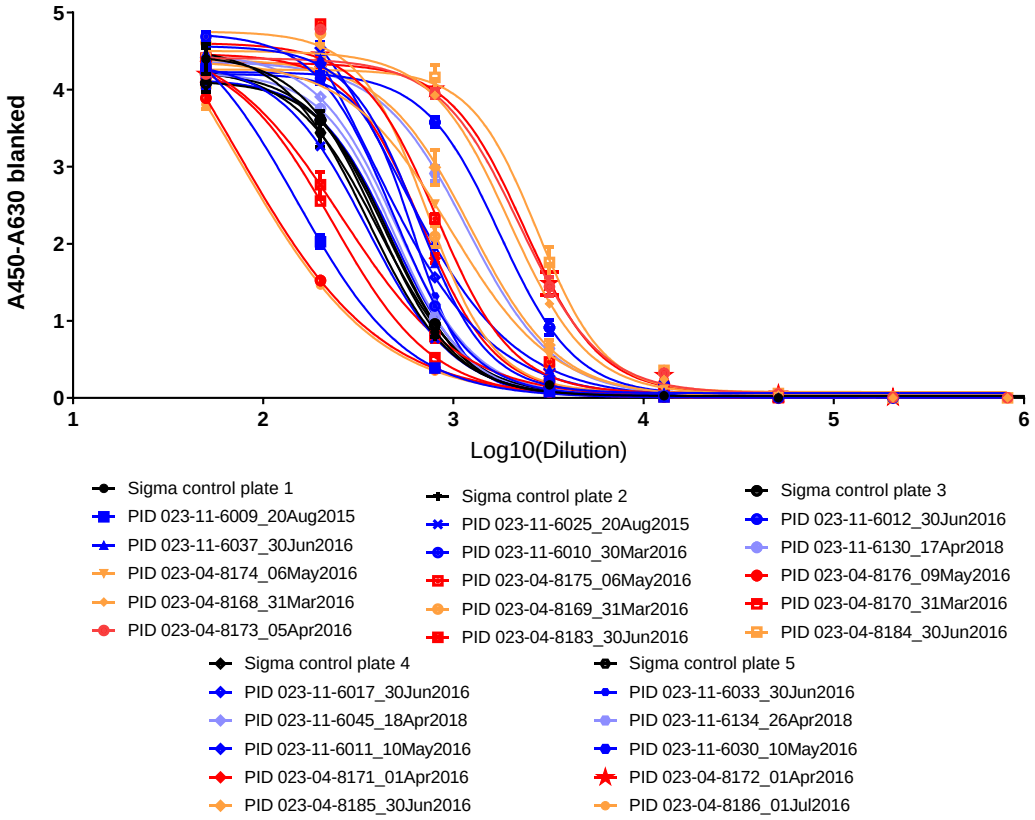

Figure 20:Serum samples binding to Mtb lipoarabinomannan. South African healthy donors are shown in dark blue (n=9), non-TB-endemic country healthy donors in light blue (n=3), TB patient donors in orange (n=6), TB+ HIV+ donors in red (n=7). Black lines show Sigma control serum.

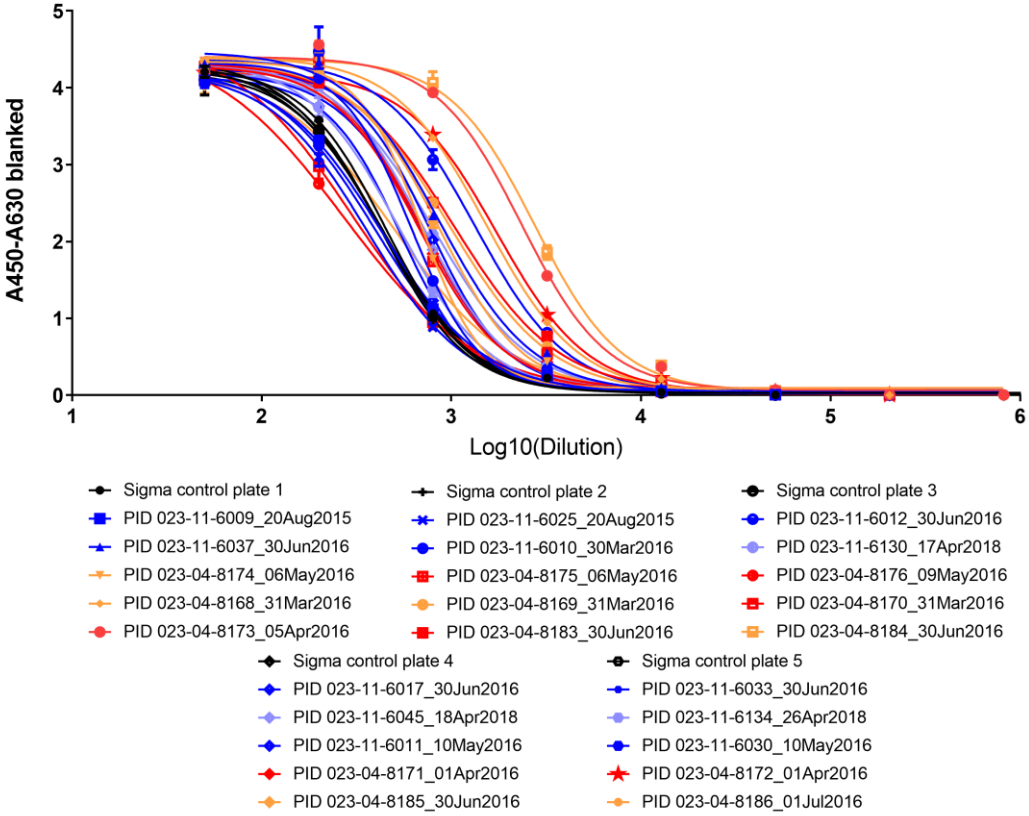

Figure 21:Serum samples binding to Mtb cell wall proteins. South African healthy donors are shown in dark blue (n=9), non-TB-endemic country healthy donors in light blue (n=3), TB patient donors in orange (n=6), TB+ HIV+ donors in red (n=7). Black lines show Sigma control serum.

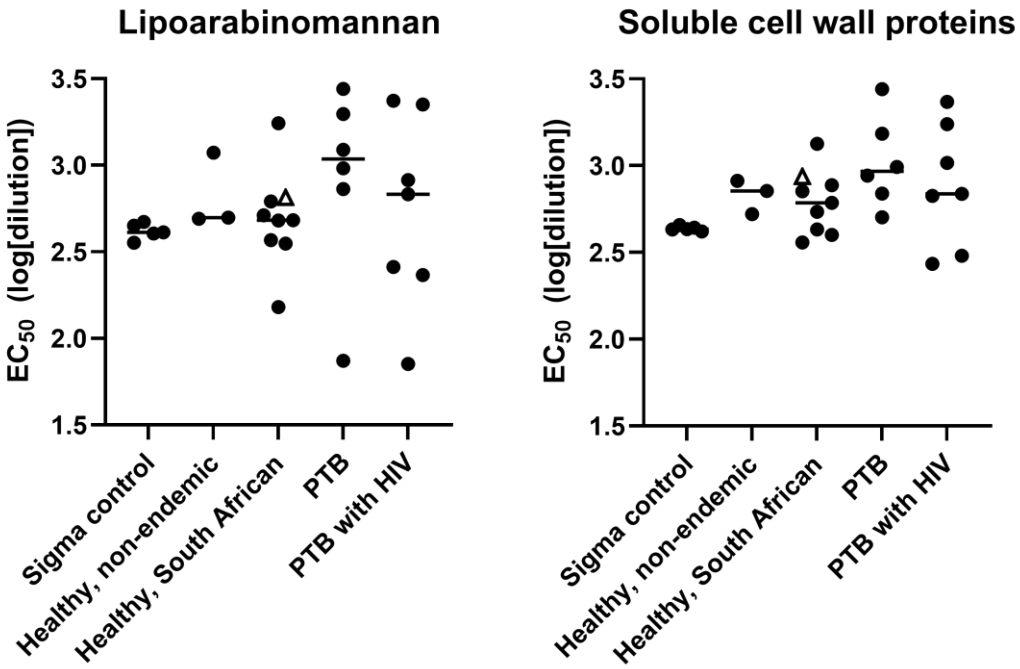

Figure 22: Half-maximal effective dilution (EC_{50}) for serum samples binding to Mtb lipoarabinomannan and soluble cell wall proteins. PTB: Pulmonary TB patients. While there was no significant differences between groups, there was a trend to higher binding in PTB. Healthy donor 6037 who was used for mAb cloning is shown as an open triangle.

Table 3: Summary of EC_{50} parameters for LAM and SCWP serum binding for different sample groups.

	Lipoarabinomannan		Soluble cell wall proteins	
	Geometric mean (log[dilution])	SD (log[dilution])	Geometric mean (log[dilution])	SD (log[dilution])
Sigma control serum	2.619	0.04581	2.637	0.01414
Healthy donors, non-TB-endemic countries	2.820	0.2188	2.830	0.09848
Healthy donors, South African	2.691	0.2801	2.791	0.1822
PTB	2.924	0.5567	3.017	0.2619
PTB with HIV	2.729	0.5547	2.886	0.3533

3.2.2 B cells binding whole Mtb can be sorted from peripheral blood and lung lymph nodes

3.2.2.1 Generation of a feeder cell line for primary B cells

A previously published method showing that the mouse cell line 3T3-msCD40L with addition of exogenous human IL-2 and IL-21 could support primary B cell proliferation and antibody secretion[348] was used as the basis for the development of an in-house cell line stably expressing all 3 of these factors. The human lung carcinoma cell line H1299 was selected as the host since it is adherent and is easy to culture.

H1299 cells were transduced with lentiviral vectors for stable expression of huCD40L, IL-2 and IL-21 as described in the Methods section 2.3. The top 6 clones expressing IL-2 and IL-21 were irradiated at 1200 cGy to prevent the feeder cells from proliferating. To evaluate the ability of the cell lines to support antibody-secreting cells, CD19+ B cells from a healthy donor were singly sorted onto the irradiated H1299-feeders in 96-well plates and incubated for 13 days, at which time supernatants were harvested and screened by IgG ELISA. Clone E14 was selected for future use as B cells cultured on this clone had the highest mean IgG secretion (Figure 23). The H1299-E14 cells were expanded, X-ray irradiated, and frozen to create a ready-to-use working cell bank. These cells were then used for culturing primary B cells from the sorting experiments described below.

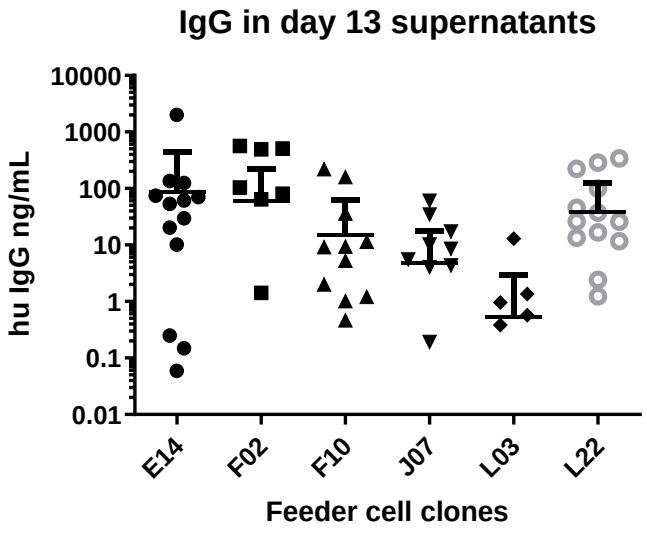

Figure 23: IgG secretion by single sorted B cells cultured on irradiated H1299-feeder cells. X-axis labels are individual clone identifiers.

3.2.2.2 B cells in peripheral blood of a PTB patient and a TB-exposed healthy donor bind whole bacteria

PBMC from healthy donor PID 6037 and TB patient 8185 were stained for CD19 and incubated with FITC-labelled inactivated Mtb (methods: fluorescent bacilli preparation 2.5.2; PBMC staining 2.7.1). Live CD19+ lymphocytes binding to Mtb were sorted as shown in Figure 24. Gating for Mtb binding was somewhat arbitrary as the cells formed a continuous "smear" on the FITC axis with no clear cut-off. Out of the CD19+ population, the Mtb-binding gate held 0.30% for PID 6037 and 0.64% for PID 8185.

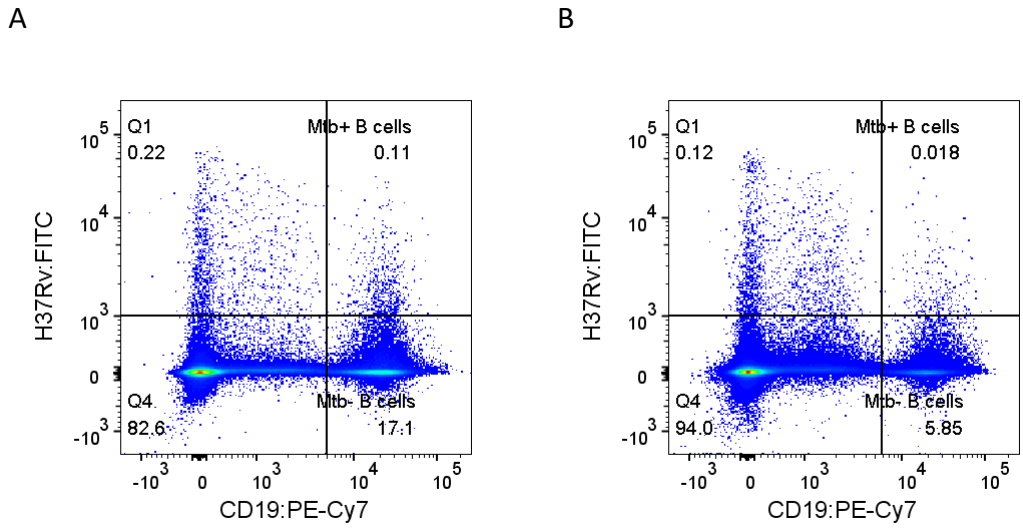

Figure 24: Sorting Mtb-binding B cells from healthy donor 6037 and TB patient donor 8185. Y-axis is Mtb binding as detected by FITC-labelled Mtb strain H37Rv. Upper right quadrant are Mtb binding CD19 B cells.

3.2.2.3 B cells from a TB patient pulmonary lymph nodes that bind whole bacteria are enriched for memory cells

For the PID 0219 lymph node sorting experiment, H37Rv vs CD19 cells were plotted with 2% contour lines and the H37Rv:FITC cut-off was drawn above the last contour for the no-bacteria control sample. All CD19+ Mtb-binding cells were sorted. CD27 was also recorded for information only. The percentage of CD27+ cells in the Mtb-

binding sorted population was higher than in the non-Mtb-binding population (Figure 25).

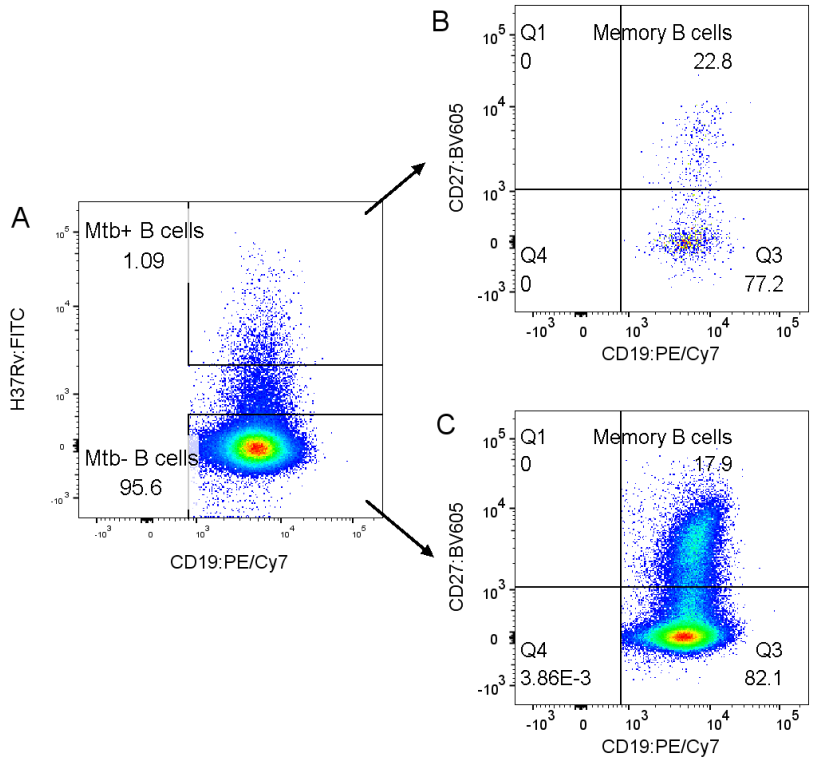

Figure 25: Memory population of Mtb specific B cells. A: Sort gates, with upper gate being Mtb bound B cells. B: Memory cells (CD19+CD27+) in the Mtb-binding population. C: Memory cells in the non-binding population.

3.2.2.4 Mtb-binding B cells are enriched in the memory population in healthy donor PBMC

Subsequently, additional B cell phenotypic markers were added to the panel to distinguish memory B cells from immature and naïve populations (methods 2.7.1). CD3 was also added to definitely exclude T cells. Cells of interest were gated as CD3- CD10- IgD- IgM- CD21+ CD27+ and sorted into Mtb-binding and non-Mtb binding populations using the H37Rv:FITC as bait. The following four donors were used for this experiment: PID 023-11-6037 (healthy South African), 023-11-6090 (healthy, non-TB-endemic country of origin), PID 023-04-8173 (TB patient, high serum IgG binding to LAM and cell wall proteins), and PID 023-04-8176 (TB patient, low serum IgG binding). Both TB donors were also HIV positive.

The gating strategy is shown in Figure 26 and frequencies of different B cell populations are shown in Table 4. Cells were singly sorted into PCR plates filled with lysis buffer.

Surprisingly, the donor from the non-TB-endemic country had the highest detected frequency of Mtb-binding memory B cells. A technical issue that arose during sample preparation may explain this observation. PBMC from donors 6037, 8173, and 8176 agglutinated after incubation with bacteria, forming visible aggregates that could not be dispersed by pipetting, flicking, or vortexing vigorously. These samples had to be passed through a cell strainer before sorting as the aggregates clogged the cytometer's sample injection port. I had also observed this problem with some samples in the past but did not previously record which samples agglutinated.

Agglutination may have been caused by too low a ratio of bacteria to Mtb-binding B cells during sample preparation, causing several B cells or other Mtb-binding lymphocytes to bind to a few bacteria, similar to the phenomenon of "rosette" formation or hemagglutination. This may have caused loss of cells of interest and distortion of the proportion of Mtb-binding cells measured.

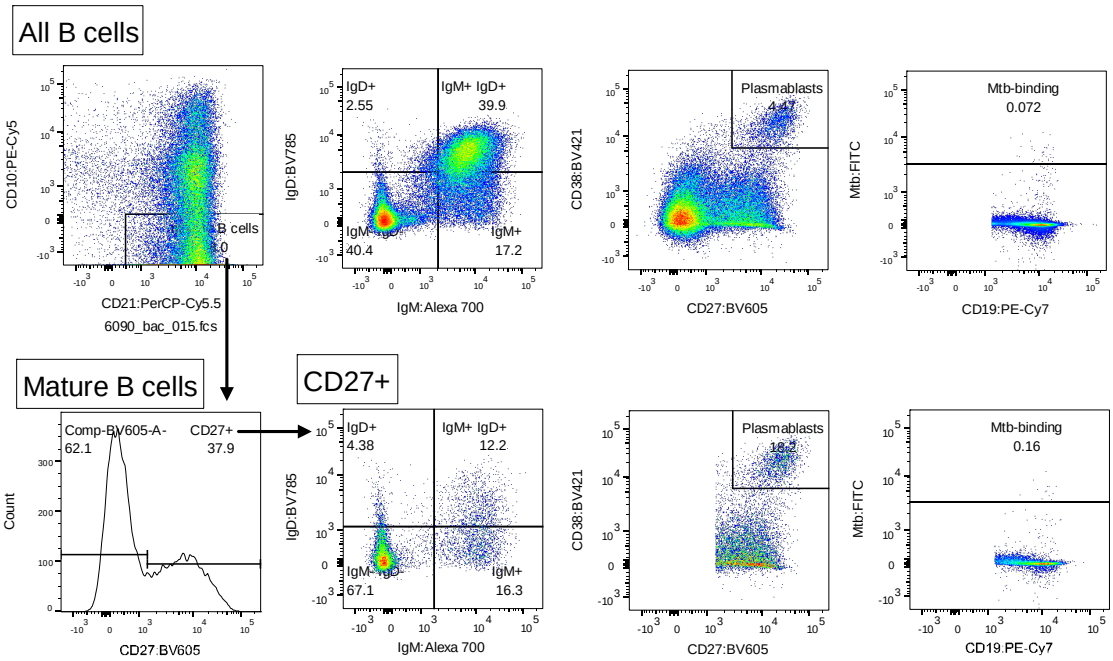

Figure 26: Gating strategy for sorting Mtb-binding, non-IgM, memory B cells. Sample shown is from donor 6090. Top left panel shows the total CD19+ B cell population; bottom left panel shows the CD10- CD21+ mature B cell subpopulation. Columns 2-4 show IgM- IgD-

class-switched cells; CD27+ CD38++ plasmablasts; and Mtb:FITC-binding cells in the total B cell (top row) and CD27+ memory (bottom row) populations.

Table 4: Frequencies of B cell subpopulations from four donors.

	Frequency in total CD19+ population					**Frequency in mature memory population**		
Donor ID	CD10-CD21+	CD27+	IgD-IgM-	Plasmablasts	Mtb-binding	IgD-IgM-	Plasmablasts	Mtb-binding
PID 6037	43.6	18.7	31.7	0.78	0.052	63.4	4.11	0.092
PID 6090	48	18.2	40.4	4.47	0.072	70	21.2	0.19
PID 8173	49.5	10.2	3.94	3.22	0.12	18.6	19	0.044
PID 8176	55	15.4	9.31	1.63	0.057	30.1	1.28	0

3.2.2.5 Attempted two-colour sorting of B cells binding to *Mycobacterium tuberculosis* versus *Mycobacterium smegmatis*

To determine if any Mtb-binding B cells had been induced by environmental mycobacteria, Msmeg *smyc'*::mCherry (methods 2.5.2.4) was used as a counter-bait. PBMC from a non-TB-endemic country of origin, donor 6090, and a South African TB patient 8278 were stained and incubated with a mixture of inactivated Mtb and Msmeg. Class-switched cells were gated as CD19+ IgD- IgM- and sorted on Msmeg vs Mtb quadrants as shown in Figure 27. There was surprisingly little binding to Msmeg in both samples. The frequency of Mtb-binding B cells was higher for the healthy donor sample than the TB patient.

However, it was also noted in this experiment that the TB patient sample became highly clumped and may have lost cells of interest as noted for some samples above.

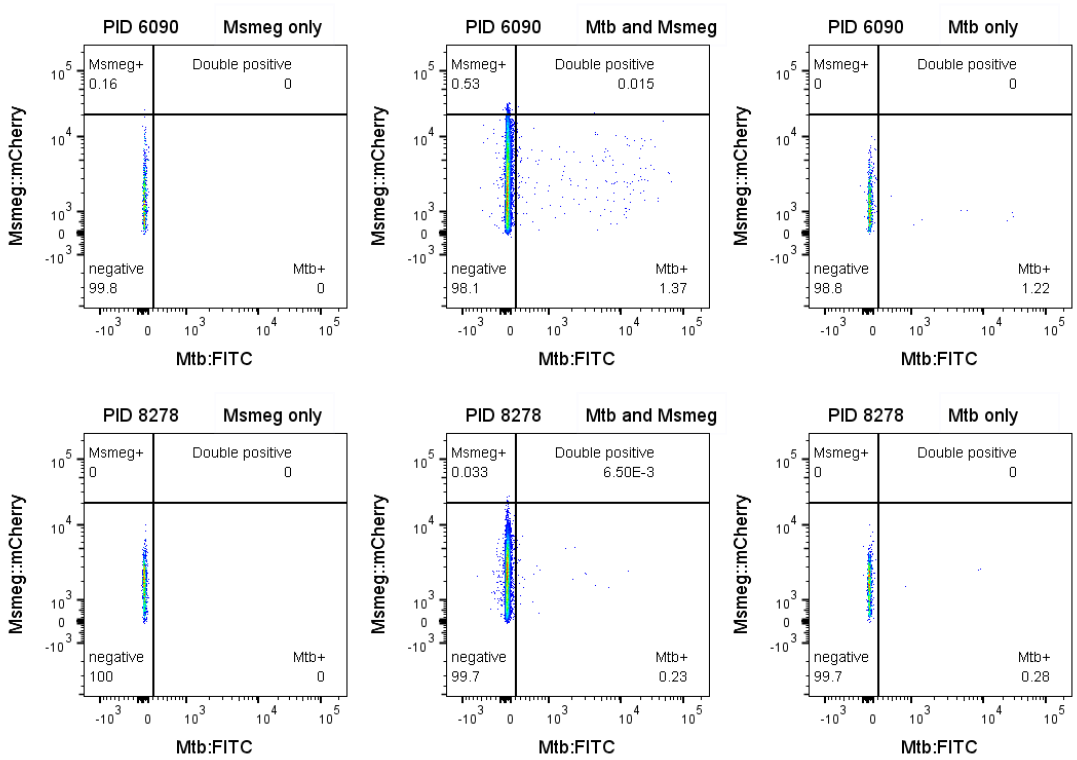

Figure 27: Attempt to sort Mtb-specific from environmental mycobacteria-binding B cells. CD19+ IgD- IgM- B cells from healthy donor 6090 and TB patient donor 8278 incubated with Msmeg::mCherry and/or Mtb:FITC.

3.2.2.6 Yields and specificity of sorting methods

For the healthy donor PID 6037 sort, a total of 146 wells were filled with 20 sorted B cells per well. Supernatants from these were sampled after 10 days' co-culture with the feeder cells (methods 2.8) and tested for the presence of human IgG by sandwich ELISA (methods 2.9). Of these, 77 or 53% had detectable IgG. The probability of a single sorted cell surviving and producing IgG was calculated using the binomial distribution as 3.7%.

In the Mtb whole-bacteria ELISA, 42 wells were positive for Mtb binding by whole-bacteria ELISA (55% of the 77 antibody-secreting wells); however, 19 of these were negative in the human IgG-specific sandwich ELISA. At this point it was noted that that, since the detection antibody in the whole-bacteria ELISA was anti-human IgG H+L, it was also detecting Mtb-binding antibodies of other isotypes, possibly IgA or IgM. Twelve of these wells (29% of the total 42 that had Mtb-binding signal) were confirmed to contain IgA by IgA-specific sandwich ELISA.

Wells that had high Mtb reactivity and were confirmed to contain Ig of only 1 isotype (as wells containing both IgG and IgA would mean that the surviving B cell population contained at least 2 different clones) were selected for RT-PCR (methods 2.8).

From the lymph node of PID 0219, a total of 206/500 wells or 41.2% were positive for IgG, giving a survival rate of 10.1% on a per-cell basis. However only 5/500 wells were clearly positive for Mtb binding, and of these, only 1 had a high specific signal:total IgG ratio (well C03). One of the two had high anti-Mtb Ig but zero detectable IgG suggesting that it was another isotype (well D02). Due to the difficulty of performing ELISA assays manually in biosafety level 3, I did not perform an IgA ELISA on these samples. However, RT-PCR using a 3' alpha-chain-specific primer yielded a product from D02 which was successfully Sanger sequenced.

Sequences of the 5 heavy and light chain pairs from PID 6037 PBMC and 2 pairs from PID 0219 lymph node are shown in Appendix A. These sequences were reproduced as long single-stranded oligonucleotides and cloned into lentiviral vectors with IgG1 Fc by Gibson assembly as detailed in methods section 2.10.

3.2.3 Characterization of human anti-Mtb monoclonal antibodies

3.2.3.1 Monoclonal antibodies derived from sorted peripheral B cells bind to inactivated bacteria

The IgG1 antibodies from PID 6037 and from the MPIIB study, expressed in 293T cells were tested against inactivated H37Rv by ELISA (see methods 2.9; Figure 28) and flow cytometry to confirm binding. Antibodies with serial numbers 2383 to 2394 are from PID 6037; 2412 to 2417 were cloned from previously published sequences in GenBank[176]. For wells where 2 versions of the vector were constructed due to Sanger sequence ambiguities (P1F06 and P2G10) or multiple heavy chain sequences (P2E04), the binding data enabled us to resolve which was the "correct" version.

Two antibodies appear to be affected by the temperature of the coating step. P2F10 binding was adversely affected when the assay plates were dried at 60°C, suggesting that its antigen is temperature-sensitive. Conversely P2C02 gave a stronger signal on heat-dried than room-temperature-dried bacteria, therefore its antigen may have been

masked by other molecules on the unheated bacteria. ELISA EC_{50} values are shown in

Table 5.

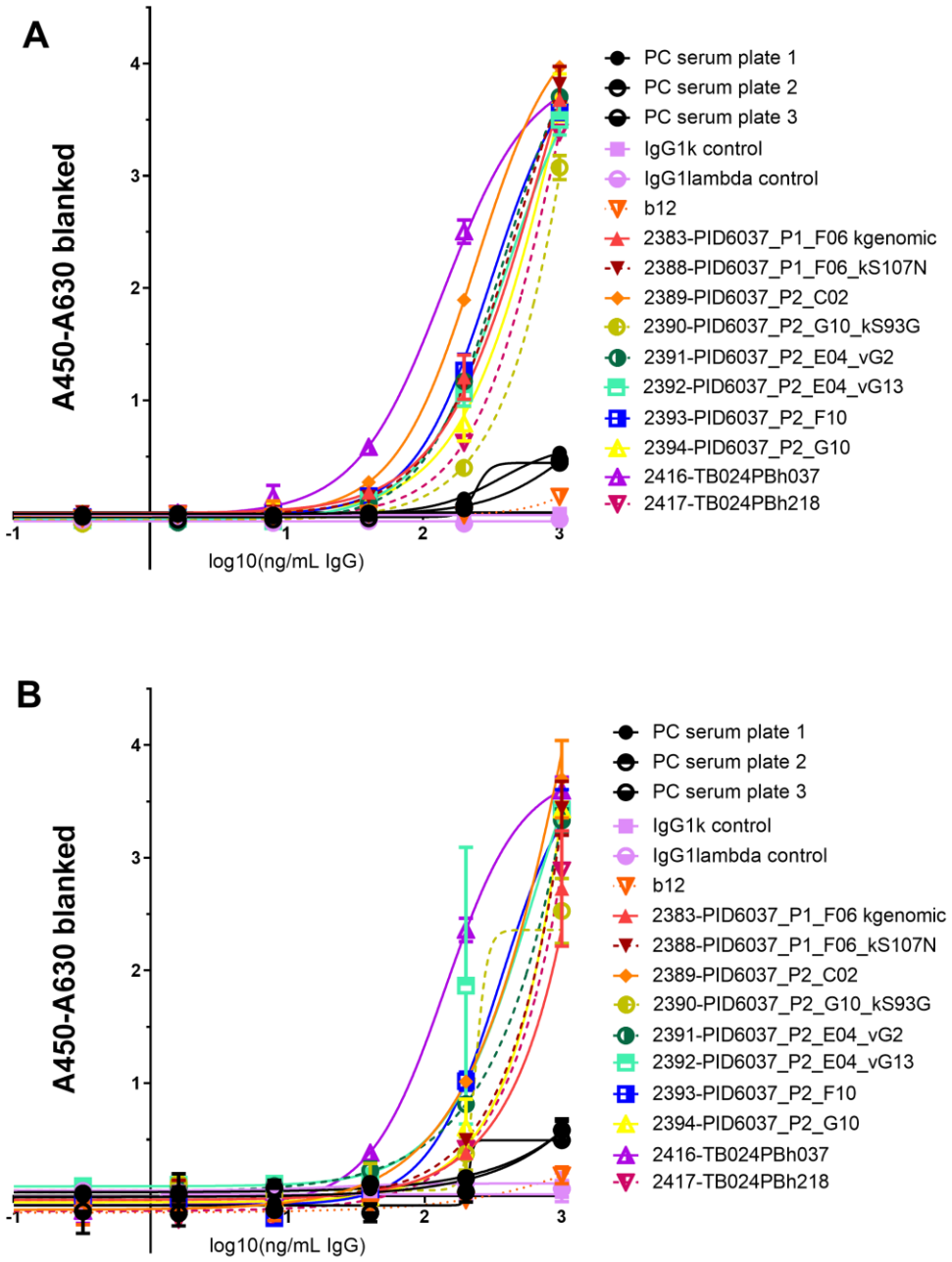

Figure 28: Binding of monoclonal antibodies (September 2017 batch) to bacteria dried at A: 60°C and B: room temperature (approximately 23°C).

For bacterial flow cytometry (methods 2.7.2), inactivated H37Rv bacteria were stained with FITC and gated on FITC+ events to avoid counting debris or bubbles due to their

small size. Example plots of bacteria stained with 3 antibodies and secondary anti-human IgG:PE are shown in Figure 29.

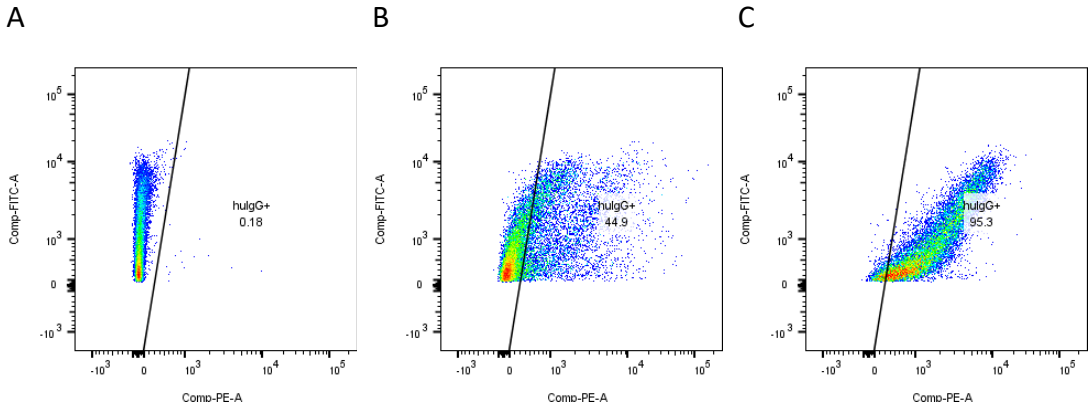

Figure 29: Gating of Mtb labelled with monoclonal antibody samples. A: human IgG1kappa isotype control (Bio-Rad). B: PID6037_P2E04. C: HD001HBMEMh804.

Table 5: Mtb binding data for monoclonal antibodies, by ELISA and flow cytometry. Pairs of antibodies derived from the same original B cell sort well are colour-coded. The data are heat-mapped per column.

Antibody	ELISA dried 60°C (AUC)	ELISA dried room temp (AUC)	FACS (% stained)	FACS (MFI)
2383-PID6037_P1_F06 kgenomic	2068.00	1278.00	17.3	147
2388-PID6037_P1_F06_kS107N	2084.00	1620.00	21.8	186
2389-PID6037_P2_C02	2523.00	1979.00	32.8	263
2390-PID6037_P2_G10_kS93G	1423.00	1201.00	19.8	178
2391-PID6037_P2_E04_vG2	2051.00	1747.00	22.0	164
2392-PID6037_P2_E04_vG13	1920.00	2286.00	44.9	370
2393-PID6037_P2_F10	2047.00	1864.00	44.8	378
2394-PID6037_P2_G10	1871.00	1663.00	25.9	217
2412-HD001HBMEMh095	n/d	n/d	36.0	309
2413-HD001HBMEMh804	n/d	n/d	95.3	1484
2415-TB033PBh129	n/d	n/d	72.2	737
2416-TB024PBh037	2740.00	2608.00	66.5	639
2417-TB024PBh218	1662.00	1362.00	25.2	200
b12 (HIV)	53.98	79.55	0.1	59
IgG1 κ control (GFP)	23.34	38.10	0.2	60
IgG1 λ control (GFP)	80.21	90.96	0.1	55
PC serum plate 1	272.60	300.30	0.3	63
PC serum plate 2	198.90	321.20	n/a	n/a
PC serum plate 3	217.70	228.50	n/a	n/a

A second batch of all 10 monoclonal antibodies was produced in January 2018, with better yields in the range of 0.8 – 1.4 mg from 300 cm^2 of HEK293T cells each. All antibodies bound strongly to whole bacteria (Figure 30).

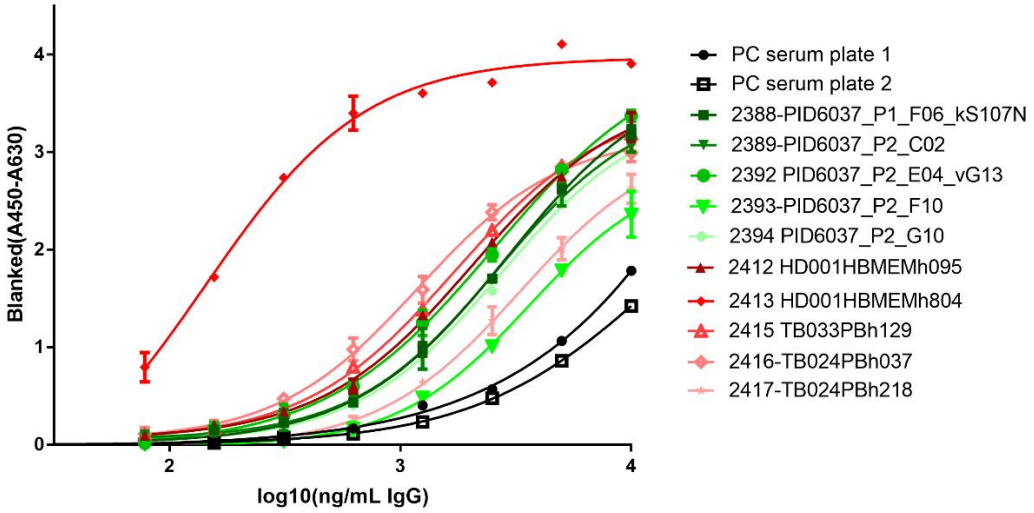

Figure 30: Binding of monoclonal antibodies (January 2018 batch) to bacteria dried at room temperature (approximately 23°C).

Later, two clones from a TB patient lung lymph node were obtained as described in the previous section. Both bound strongly to whole inactivated bacteria as well as to the cell wall protein extract (Figure 31, Figure 32). The D02 antibody was originally IgA; surprisingly, a recombinant version that was expressed as IgG was about three times weaker in binding to cell wall proteins (compare Figure 31B, Figure 32B).

A

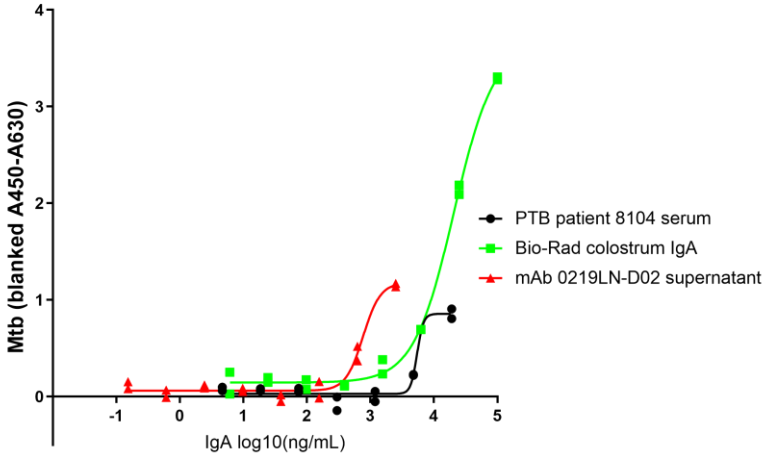

	IC50
PTB patient 8104 serum	~ 5448
Bio-Rad colostrum IgA	20590
mAb 0219LN-D02 supernatant	766.1

B

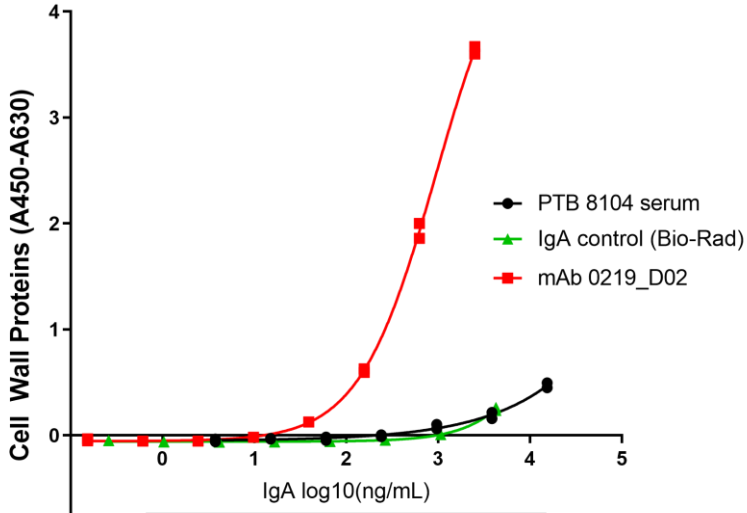

	IC50
PTB 8104 serum	~ 2107758220
mAb 0219_D02	939.6
IgA control (Bio-Rad)	~ 41103

Figure 31: Binding of PID 0219 lymph node monoclonal IgA compared to control antibodies. A: dried whole bacteria; B: Cell wall protein fraction. Black: PTB patient serum; green: polyclonal colostrum IgA; red: mAb 0219_D02.

A

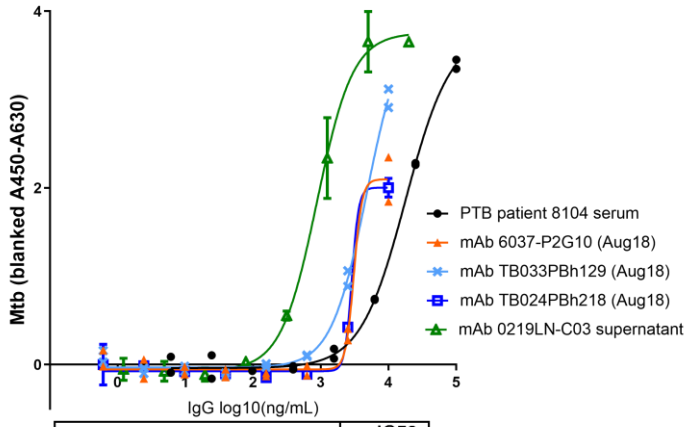

	IC50
PTB patient 8104 serum	17884
mAb 6037-P2G10 (Aug18)	~ 3075
mAb TB033PBh129 (Aug18)	4764
mAb TB024PBh218 (Aug18)	~ 2863
mAb 0219LN-C03 supernatant	879.6

B

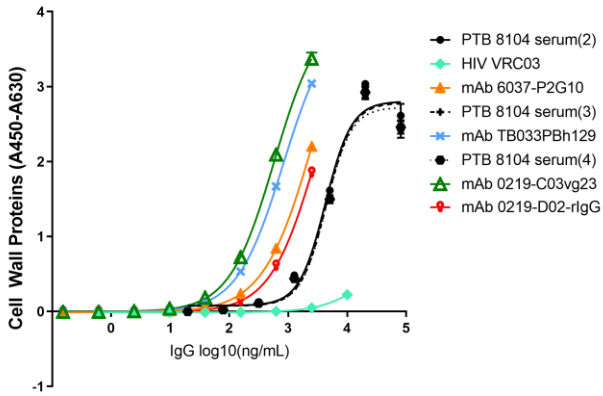

	IC50
PTB 8104 serum(2)	4261
HIV VRC03	21684
mAb 6037-P2G10	2811
PTB 8104 serum(3)	4437
mAb TB033PBh129	818.5
PTB 8104 serum(4)	4387
mAb 0219-C03vg23	578.5
mAb 0219-D02-rIgG	2927

Figure 32: Binding of PID 0219 lymph node monoclonal IgG compared to other mAbs and control antibodies. A: dried whole bacteria; B: Cell wall protein fraction.

3.2.3.2 Monoclonal antibodies display different binding profiles across live bacteria from lab strains and clinical isolates

The 5 monoclonal antibodies cloned from AHRI PID 6037 and the selected clones from the literature were tested for binding to live bacteria of the laboratory strains CDC1551 and Erdman carrying the reporter plasmid described above (methods 2.7.2). We also wanted to determine if their antigens were present in recent clinical isolates that had not been subjected to extended *in vitro* culture. Therefore, 2 recent clinical

isolates of the Beijing lineage and 2 isolates of the KwaZulu-Natal (KZN) lineage were also tested against selected mAbs.

The 5 mAbs derived from a South African healthy donor (PID 6037), 2 from German TB-exposed healthcare workers (HD…) or 3 from German TB patients (TB…)[360] show differences in binding profiles across these seven strains (Table 6). The only mAb whose target has been identified by the original authors and confirmed in our lab is TB024PBh037 which binds lipoarabinomannan (LAM). This gave a moderately high signal in H37Rv ELISA, labelled about half of CDC1551 and Beijing isolate bacilli, a minority of Erdman bacilli, and nearly all the KZN lineage bacilli.

Table 6: Binding of monoclonal antibodies to seven strains of Mtb by flow cytometry. H37Rv was inactivated, all others were live.

Antibody	H37Rv*	CDC 1551	Erdman	TKK-01-0027 Beijing	TKK-01-0047 Beijing	TKK-01-0081 KZN	TKK-01-0084 KZN
2388-PID6037_P1_F06	21.8	33.8	32.5	61.6	32.0	88.9	94.1
2389-PID6037_P2_C02	32.8	51.3	27.3	52.7	26.7	82.5	92.7
2392-PID6037_P2_E04	44.9	59.8	36.7	44.5	26.8	78.4	90.5
2393-PID6037_P2_F10	44.8	21.2	24	42.5	26.7	73.6	89.2
2394-PID6037_P2_G10	25.9	62.1	26.5	28.6	23.3	72.1	79.6
2412-HD001HBMEMh095	36	63	28.9	22.4	22.3	63.0	72.0
2413-HD001HBMEMh804	95.3	51.9	30.9	83.2	43.7	97.2	99.0
2415-TB033PBh129	72.2	63.1	30.6	10.2	15.0	15.2	22.6
2416-TB024PBh037	66.5	52.2	25.8	61.9	51.2	94.3	98.2
2417-TB024PBh218	25.2	9.88	16.9	6.1	6.4	13.8	8.2
IgG1 κ isotype control	0.2	0.08	0.45	2.4	1.9	12.9	2.7
IgG1 λ isotype control	0.1	0.071	5.67	1.9	1.3	7.0	2.6
No-primary control	nd	0.046	0.11	0.4	0.3	0.5	0.6
Unstained	nd	6.69E-03	5.23E-03	0.0	0.0	0.1	0.0

3.2.3.3 Monoclonal antibodies from AHRI and Max Planck donors do not cross-react with *E. coli*

E. coli was used to check if any of the monoclonal antibodies displayed non-specific binding to this unrelated species. All had signal lower than or similar to the PID8104 TB patient serum and much lower than the Sigma-Aldrich polyclonal IgG (Figure 33).

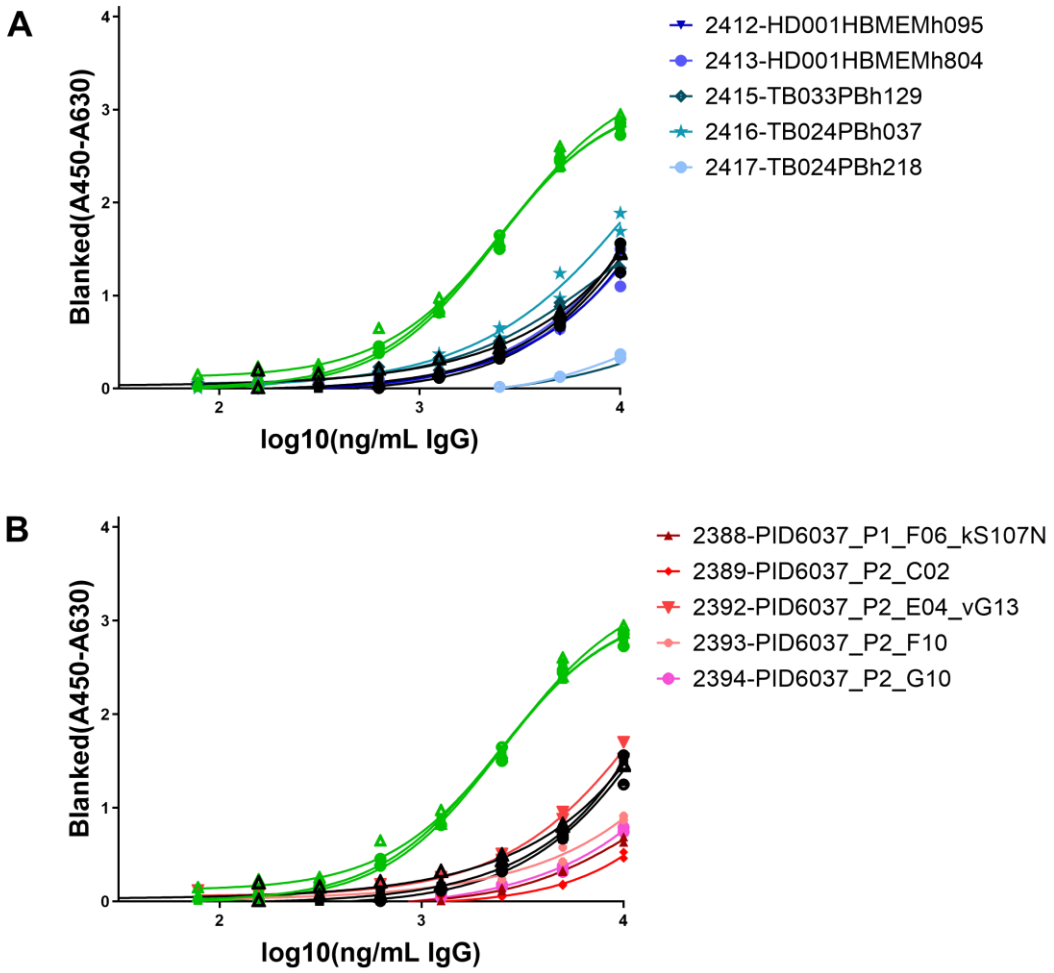

Figure 33: Monoclonal antibodies do not cross-react with whole dried E. coli. A: Zimmermann et al. clones; B: AHRI PID 6037 clones. Black: PTB patient serum; green: commercial polyclonal IgG (Sigma); pinks: AHRI mAbs; blues: MPIIB mAbs. Y axis shows blanked 450 nm optical density.

3.2.4 Monoclonal antibodies react with mixed Mtb cell wall proteins but not purified Acr, ESAT-6, or HBHA

The January 2018 batch of monoclonal antibodies was used to examine binding to native LAM and soluble cell wall protein fractions, and to recombinant Acr, ESAT-6, and HBHA as these had been identified as antibody targets with protective effects, as mentioned in the introduction. ELISAs were performed as described in methods section 2.9.

3.2.4.1 Lipoarabinomannan and cell wall protein ELISA

Most monoclonal antibodies did not bind LAM higher than control serum with the exception of TB024PBh037 which was reported to do so by the original authors[176] (Figure 34). Therefore we were able to confirm that cloning by DNA synthesis and expression from the pHAGE6 vector in our hands reproduced the same binding specificity originally reported for this antibody.

Several other antibodies did bind strongly to the soluble cell wall protein mixture namely P2E04, P2F10, HD001HBMemh095, HD001HBMemh804, TB033PBh129, as well as TB024PBh037 (Figure 35).

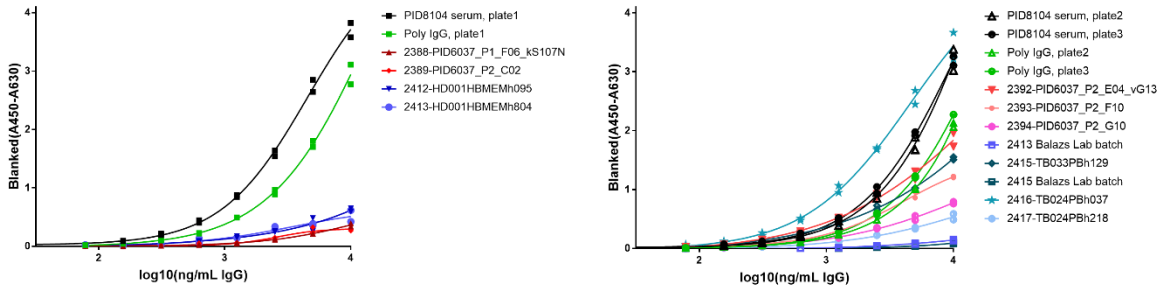

Figure 34: Monoclonal antibody TB024PBh037 binds to lipoarabinomannan. Graphs are grouped by assay plate because there was an interruption between plates 1 and 2 during the addition of the TMB colourimetric substrate. Black: PTB patient serum; green: commercial polyclonal IgG; pinks: AHRI mAbs; blues: MPIIB mAbs. Y axis shows blanked 450 nm optical density.

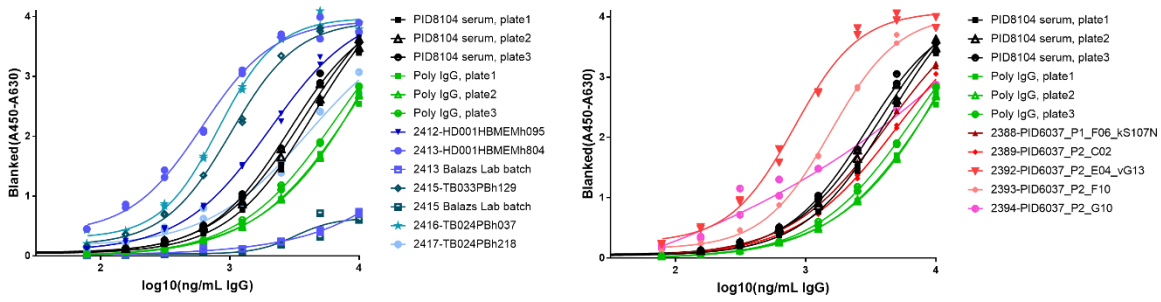

Figure 35: Monoclonal antibodies bind to soluble cell wall proteins. Graphs are grouped by source of the monoclonal antibodies. Right: MPIIB; left: AHRI PID 6037. Black: PTB patient serum; green: commercial polyclonal IgG; pinks: AHRI mAbs; blues: MPIIB mAbs. Y axis shows blanked 450 nm optical density.

3.2.4.2 Alpha-crystallin, ESAT-6, and HBHA ELISA

To attempt to identify if any of the mAbs targeted previously identified B cell antigens, several purified recombinant proteins were obtained from a repository (BEI Resources) or a commercial supplier (Lionex). Two additional controls were included in this set of experiments: TB patient PID8168 serum was used as a new positive control along with the previously used PID8104 as 8104 was running out. Anti-HIV antibody b12 was included as a "dirty" negative control with some nonspecific binding to rule out false positives.

The two PTB patient sera showed strong binding to all three proteins. None of the monoclonals bound to Acr or ESAT-6 higher than b12 (Figure 36). Several monoclonals bound to HBHA more strongly than b12, but much less than the serum controls (in contrast to the soluble cell wall protein mixture where several monoclonals were clearly binding more strongly than PID8104 serum), so it is unclear if these are false positives or weak true positives. Therefore, the antigens of most of these 10 monoclonal antibodies remain to be identified.

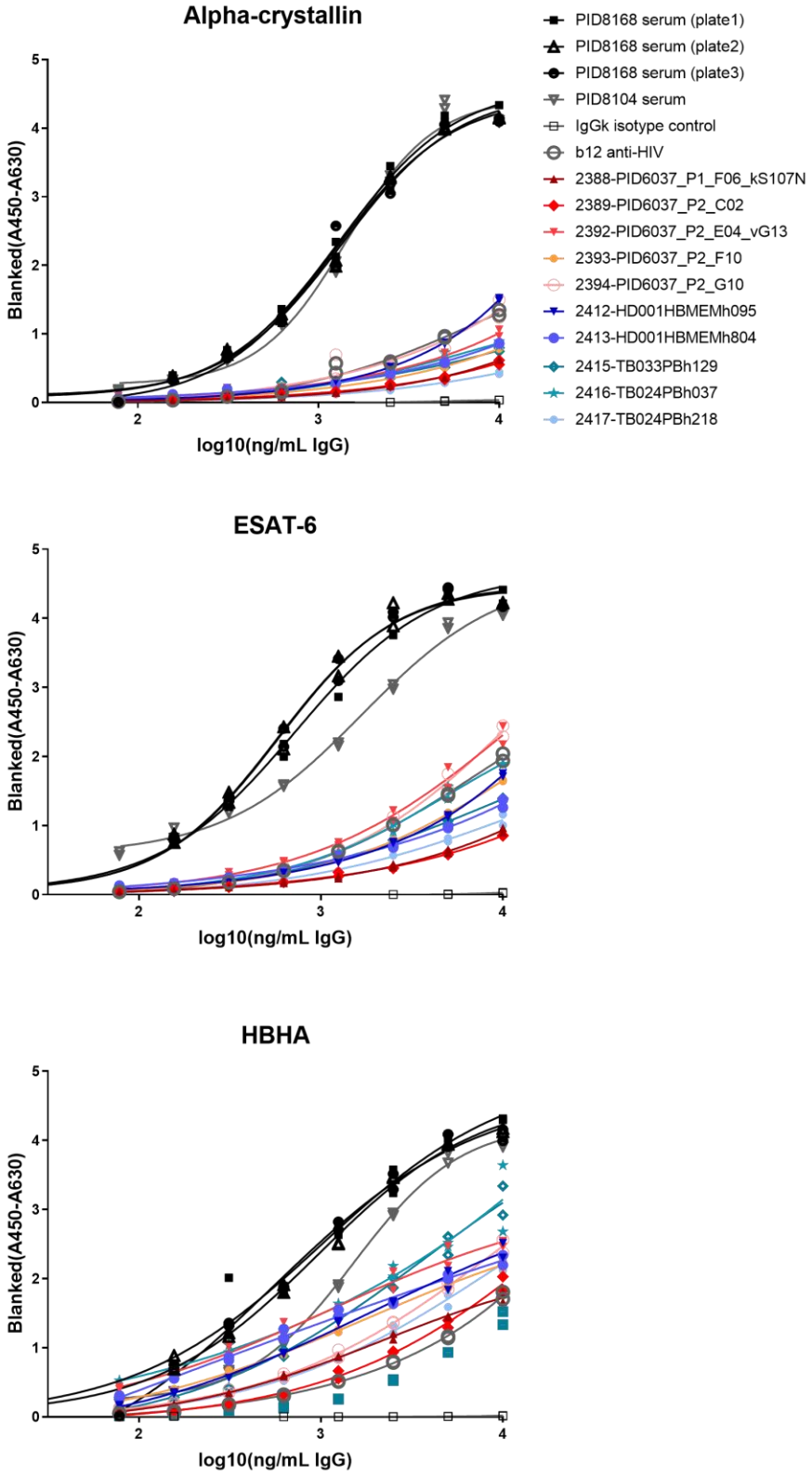

Figure 36: Monoclonal antibodies do not target alpha-crystallin, ESAT-6, or HBHA. Black: PTB patient serum; gray: monoclonal negative controls; pinks: AHRI mAbs; blues: MPIIB mAbs. Y axis shows blanked 450 nm optical density.

3.2.5 Monoclonal antibody P2E04 targets an unidentified immunodominant protein

P2E04 was selected for further characteristion based on its strong binding to the cell wall protein fraction (Figure 35) as well activity against Mtb in infected monocytes and macrophages (discussed in the next chapter). Western blotting of soluble cell wall protein and whole cell lysate obtained from BEI Resources showed that P2E04 strongly labelled a band around 61-62 kilodaltons (kDa) (methods 2.11). This band also appeared to be immunodominant in the serum of PID 6037 from whom this antibody was cloned, and also in the serum of a pulmonary TB patient. There were two faint bands at higher molecular weights (Figure 37).

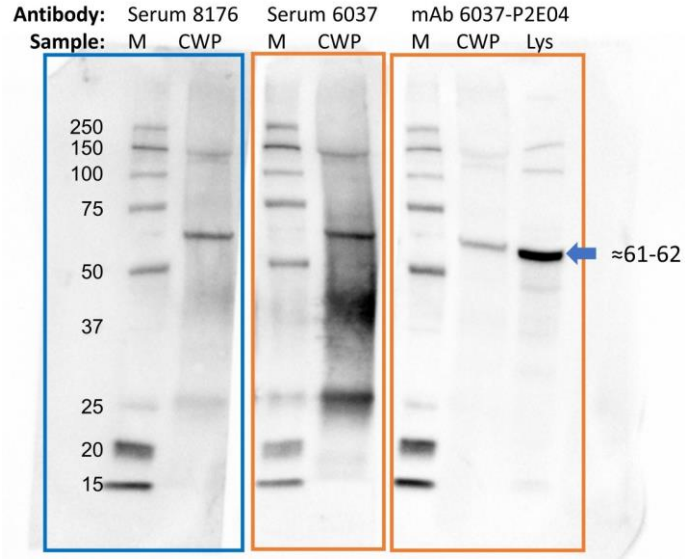

Figure 37: mAb P2E04 labels an immunodominant band in Mtb cell wall proteins and whole cell lysate. Western blot of Mtb cell wall proteins (CWP) and whole cell lysate (Lys) probed with TB patient 8176 serum, healthy donor 6037 serum, and mAb P2E04 derived from a donor 6037 B cell.

However, I was unsuccessful in purifying the antigen by immunoprecipitation (IP) (methods 2.12). Parameters tested included different types of Protein A beads to anchor mAb P2E04 (magnetic, agarose), various formulations of extraction buffers, sonication, using different types of detergents (dilute SDS, Triton X-100, CA-630) and titrating their concentration. None of the tested conditions yielded a visible 62 kDa

band clearly in eluates and it appeared to remain mostly in supernatants after the Protein A bead incubation. Some examples are shown in Figure 38.

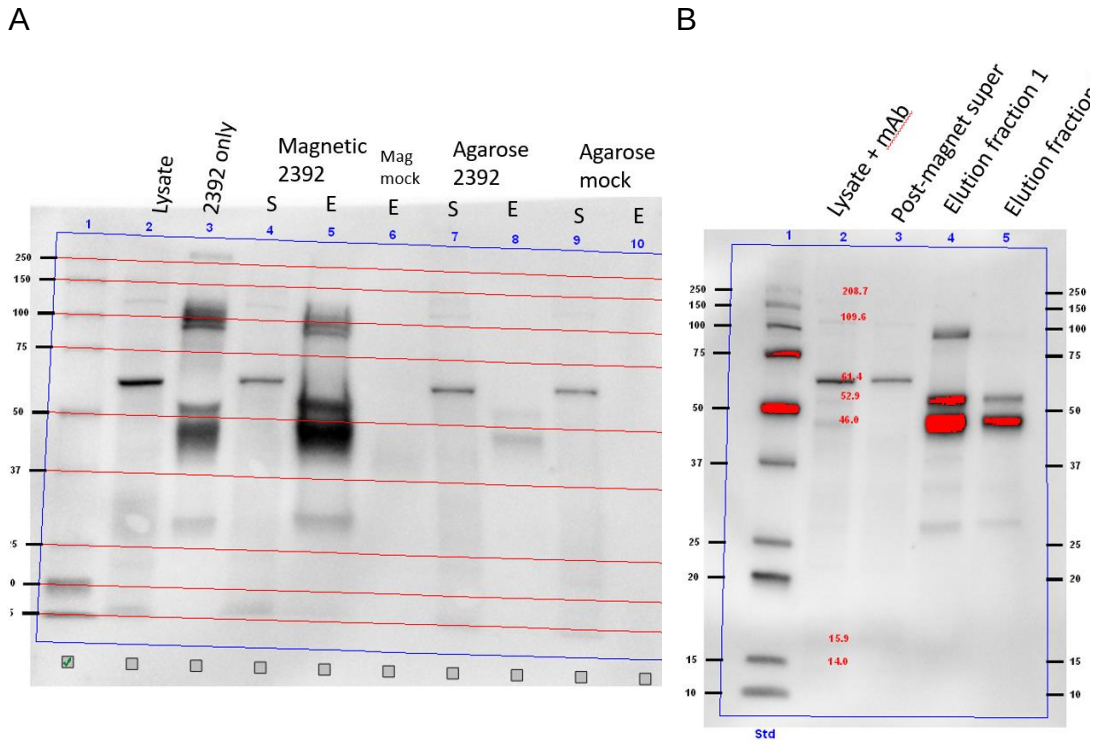

Figure 38: Western blots of attempts to immunoprecipitate the antigenic target of mAb P2E04 (serial number 2392). A: Magnetic and agarose protein A beads. S = supernatant; E = eluate. B: Immunoprecipitation attempt with magnetic beads in the presence of 0.125% Triton.

The mass spectrometry work was conducted by John Adamson and Katya Govender (Pharmacology Department, AHRI) on polyacrylamide gel slices from a SYPRO Ruby-stained gel (methods 2.13). As I could not see any distinct bands around the estimated molecular weight, I cut slices slightly above the position of the denatured IgG heavy chain (two lower slices outlined in yellow in Figure 39). A slice around the same region was also cut from the unpurified cell wall protein lane. The strong band around ~77 kDa (the two higher MW slices) was also sent for sequencing even though it does not have the expected molecular weight from pre-IP Western blots, as it appears to be very abundant even in the unpurified whole cell lysate and cell wall fraction, as I wanted to check if it might be the target antigen complexed with another protein.

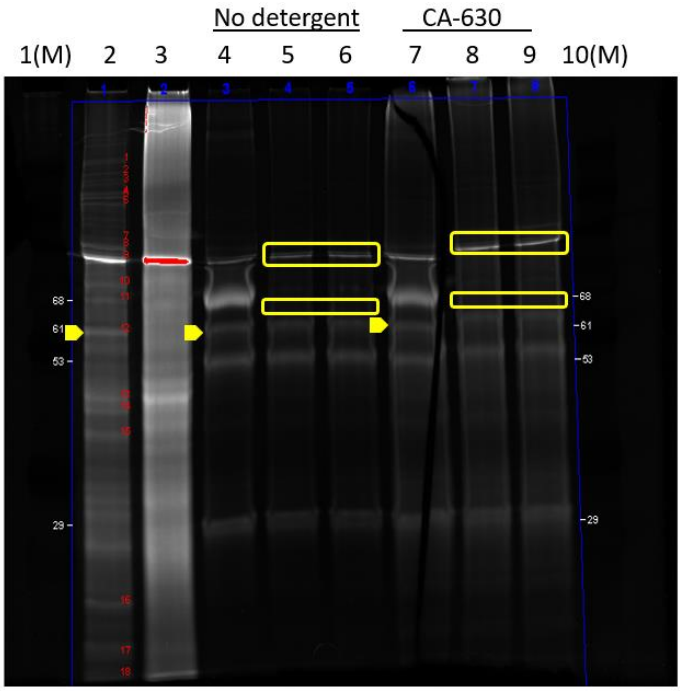

Figure 39: Bands selected for mass spectrometry sequencing. SYPRO Ruby stained polyacrylamide gel of mAb P2E04 eluates. Yellow boxes indicate slices cut out for shotgun peptide sequencing by LC-MS. Lane 1: whole bacteria lysate. Lane 2: Cell wall protein fraction. Lanes 4-6: Eluates from immunoprecipitation without surfactants. Lanes 7-9: Eluates from immunoprecipitation with CA-630. Lanes 4 and 7 have additional mAb spiked in before SDS-PAGE to show where the antibody heavy (arrowhead) and light chains and BSA carrier protein appear.

The following Table 7 lists possible candidates that appeared in the lower gel slices only, with predicted molecular masses within 55-65 kDa. The abundant ~77 kDa band was identified as metE, methionine synthetase with a predicted mass of 81.5 kDa. Another probably spurious protein that appeared in nearly all samples was the 60 kDa chaperonin GroEL1 (predicted mass 55.8kDa). The known or predicted functions, and the known locations of these proteins were obtained from Mycobrowser[151].

Table 7: Proteins identified by shotgun sequencing from mAb P2E04 immnoprecipitation with predicted molecular masses close to previously observed Western blot band.

Name	Predicted MW (kDa)	Description	Gene number	Function (Mycobrowser)	Location (Mycobrowser)
accA3	63.7	Probable bifunctional protein acetyl-/propionyl-coenzyme A carboxylase (Alpha chain) AccA3: biotin carboxylase + biotin carboxyl carrier protein (BCCP)	Rv3825	Involved in long-chain fatty acid synthesis (at the first step).	Membrane fraction and culture filtrate
FadD28	62.6	Long-chain-fatty-acid—AMP ligase	Rv2941	Involved in phthiocerol dimycocerosate (PDIM) biosynthesis.	Membrane fraction and culture filtrate
LH57_01475	59.9	Acyl-CoA synthetase	Not found		
accD5	59.3	Probable propionyl-CoA carboxylase beta chain 5	Rv3280	Key enzyme in the catabolic pathway of odd-chain fatty acids, isoleucine, threonine, methionine, and valine	Membrane fraction and culture filtrate
zwf2	57.3	Glucose-6-phosphate 1-dehydrogenase 2	Rv1447c	Involved in pentose phosphate pathway	Membrane fraction
accD4	56.6	Probable propionyl-CoA carboxylase beta chain 4	Rv3799c	Key enzyme in the catabolic pathway of odd-chain fatty acids, isoleucine, threonine, methionine, and valine	Membrane fraction Not in culture filtrate
gabD2	55.3	Putative succinate-semialdehyde dehydrogenase [NADP(+)] 2	Rv1731	Involved in 4-aminobutyrate (GABA) degradation pathway	Membrane Not in culture filtrate

3.3 Discussion

Mtb-binding B cells can be sorted and cloned using an antigen-agnostic approach

Using whole inactivated Mtb as bait, I found that Mtb-binding B cells were enriched in the memory B cell subpopulation versus total CD19+ B cells in the peripheral blood of healthy donors as well as in a lung lymph node from a pulmonary TB patient. The Mtb-binding memory B cell frequencies were on a similar order of magnitude to HBHA-binding memory B cells in a TB patient and a TB-exposed healthcare worker found by Zimmermann et al[176]. I was able to culture primary B cells sorted using this method and determined that some of the Mtb-specific antibody-secreting cells were IgA as well as IgG. Paired heavy and light chain sequences were obtained for a few Mtb-specific antibodies.

However, the method suffers from a number of technical problems which need to be resolved in order to design an efficient pipeline for isolating Mtb antibodies. First, it is possible for a small number of non-Mtb-specific B cells to bind the fluorescent bacteria despite multiple washing steps. Therefore the Mtb-binding FACS step could be regarded as an enrichment step but not a definitive cut-off for specific B cells.

A commonly used method for improving specificity in B and T cell antigen-specific sorting is to label the bait antigen with two different fluorophores and sort for double-positive cells. I attempted to label inactivated Mtb with rhodamine (TRITC), but for unknown reasons, all rhodamine-labelled bacteria became extremely sticky despite pre-treatment (blocking) with FBS and would bind to human cells as well as FITC-labelled Mtb, resulting in an even higher frequency of non-specific events (data not shown).

Second, it was observed that B cells from donors who were expected to have a higher percentage of Mtb-specific B cells based on clinical status and/or serum ELISA, aggregated irreversibly after incubation with Mtb. Subsequently a lower frequency of Mtb-binding B cells was observed in these samples, compared to a non-TB-exposed donor. I interpreted this aggregation as being due to multiple B cells binding to a few bacteria (analogous to the formation of erythyrocyte-virus rosettes in influenza

haemagglutination assays), resulting in the loss of cells of interest. The ratio of fluorescent bait bacteria to PBMC needs to be increased in order to prevent loss.

Finally, the viability and antibody secretion of sorted primary B cells in our system was low despite being based on a published method that reported much higher efficiency[348] as well as higher viability in test runs during the development of the feeder cell line. Other authors have reported that the use of CD40L-transfected feeder cells (in addition to autologous irradiated PBMC) preferentially encourages the growth of naïve B cells and inhibits IgG secretion by memory B cells, whereas memory B cell proliferation was most efficiently promoted by stimulation with IL-2 and R848 (resiquimod), a TLR7/TLR8 agonist[361]. I did not have an opportunity to compare irradiated autologous PBMC feeders versus my feeder cell line with or without R848, as we lost access to the X-ray irradiator due to equipment maintenance problems.

Human monoclonal antibodies bind to the surface of whole Mtb bacilli of different strains

The seven recombinant antibodies cloned from AHRI study donors as well as the five reproduced from the Max Planck study (Zimmermann et al.[360]) were validated for Mtb binding by both ELISA and bacteria flow cytometry. The 10 antibodies tested by flow cytometry labelled whole Mtb with different strain-specific profiles across 3 laboratory strains and 4 clinical isolates. Mtb is known to be very heterogenous with individual bacilli in different metabolic states even in a clonal culture, possibly leading to different distributions of surface antigens.

Monoclonal antibody targets remain unidentified

Apart from TB024PBh037 which was reported by the original authors Zimmermann et al. to bind LAM and was confirmed to do so in our laboratory, the antigens of the other 11 mAbs have not been identified. Even though two of the other Max Planck antibodies were isolated by sorting B cells using HBHA bait, I did not detect HBHA binding by ELISA, which highlights the difficulty of isolating and validating antibodies even with a purified recombinant protein bait. For potential future

therapeutic or diagnostic applications, a mAb would ideally target an antigen that is present at high frequency in most strains of Mtb under *in vivo* conditions, but not on Msmeg or other environmental mycobacteria.

None of the antibodies cross-reacted with *E. coli* used as a negative control. Since we used whole bacteria, a bait with a complex composition and a high probability of nonspecific binding, the mAbs should also be checked for cross-reactivity with other antigens. Other authors used lipopolysaccharide (LPS), insulin, and double-stranded DNA as Mtb-unrelated control antigens[176].

My attempts to identify the target of P2E04 by immunoprecipitation and mass spectrometry peptide sequencing were unsuccessful as I was unable to precipitate the 62 kDa band that was presumed to be its antigen. One protein detected in some gel slices that has a similar predicted molecular weight is FadD28, which is thought to be involved in the biosynthesis of PDIM, a virulence factor. Another enzyme in the PDIM synthesis pathway, FadD26, was selected for rational deletion in the live attenuated vaccine strain MTBVAC (see Introduction 1.13.3). We sent P2E04 to collaborators who used an IP and MS sequencing protocol optimised for identification of Mtb antigens targeted by serum IgG (Clemens Hermann in the lab of Jonathan Blackburn, University of Cape Town). Unfortunately the sample quality was low, apparently due to poor binding of P2E04 to the IP beads used. They identified eccCb1 (Rv3871) as another possible target. This protein forms part of the ESX-1 complex which is a type VII secretion system essential for secretion of the ESAT-6/CFP-10 virulence factor[25,362]. Mutants are attenuated *in vivo*[363].

Another method for identifying protein antigens is protein microarrays. We also sent P2E04 to collaborators (Jacqueline Achkar, Albert Einstein College of Medicine) for screening on multiplexed nucleic acid programmable protein arrays (M-NAPPA) displaying the entire Mtb proteome. This approach had been used to identify four new antigens recognised by BCG-vaccinated guinea pig serum, and was validated by ELISA[364]. Results for P2E04 are still pending due to the Covid-19 pandemic.

Chapter 4: Human serum and monoclonal antibodies can modulate *Mycobacterium tuberculosis* growth in monocytes and primary macrophages

4.1 Introduction

Phagocytes are considered to be the first line of defence against Mtb infection; they also express Fc receptors that mediate the uptake of antibody-opsonised particles and can affect the outcome of phagocytosis. Antibody-dependent cellular phagocytosis (ADCP) of beads coated with various Mtb antigen fractions was higher for serum from individuals with active TB disease than latent TB infection[365].

While neutrophils and alveolar macrophages are the first phagocytes to encounter Mtb in the lung, they are also technically challenging to handle *in vitro*. We did not have a study protocol for obtaining bronchoalveolar lavage (BAL) samples from healthy volunteers. While we were able to obtain a limited number of clinically indicated BAL samples from TB and non-TB disease patients, these were frequently contaminated with fungi despite Amphotericin B treatment (data not shown) making them an unreliable source of macrophages. I therefore decided to use THP-1 leukemia cell line monocytes and GM-CSF *ex vivo* differentiated primary monocyte-derived macrophages (MDM) from healthy donor peripheral blood.

Although undifferentiated THP-1 monocytes have different characteristics than fully differentiated MDM, they have been used in phagocytosis assays including for Mtb antigens[365,366]. The use of suspension cells also facilitates testing larger numbers of samples using a flow cytometer equipped with a high-throughput sampler.

Other authors have mostly studied *in vitro* antibody-dependent phagocytosis and intracellular bacterial loads for short periods of 1 – 24 hours, whereas Mtb is a slow-growing organism and can persist in macrophages for longer periods of time. Experimental designs that only examine the effect of antibodies on opsonisation and initial phagocytosis might not capture downstream effects of antibodies on exacerbating or controlling infection and intracellular bacterial growth. The following

experiments include monitoring of infected phagocytes up to 3 – 4 days post-infection in order to characterise these effects.

Using a medium-throughput THP-1 infection assay with duplicate sets of cells fixed at early and late time points, I first sought to determine whether polyclonal serum from healthy and pulmonary TB patient volunteers in our study population could affect phagocytosis, as has been reported in other geographical locations. Next, I tested the effect of human monoclonal antibodies isolated from either AHRI or Max Planck participants and found that Mtb-specific monoclonal antibodies could either inhibit or exacerbate intracellular bacterial growth.

Subsequently I used time-lapse microscopy to track total and intracellular bacterial growth in primary MDM in the presence of different monoclonal antibodies. I also tested the effect of Fc receptor blockade to determine whether the effects of mAb P2E04 were Fc receptor-mediated.

4.2 Results

4.2.1 Development of a flow cytometry-based assay for antibody-dependent phagocytosis and intracellular Mtb growth

4.2.1.1 Verification of Fc receptor expression on THP-1 monocytes and GM-CSF-differentiated macrophages

Expression of Fc receptors (FcR) on primary MDM cultured in our protocol was verified by flow cytometry (methods 2.7.3). Macrophages were harvested by gentle scraping (no trypsin) to avoid cleavage of surface proteins and stained with FcR antibodies and viability dye (Figure 40). MDM from 7 to 15 days old expressed CD32 (FcγRII), CD64 (FcγRI), and CD89 (FcαRI), but not CD16 (FcγRIII), which is consistent with previous reports of monocyte FcR expression[367].

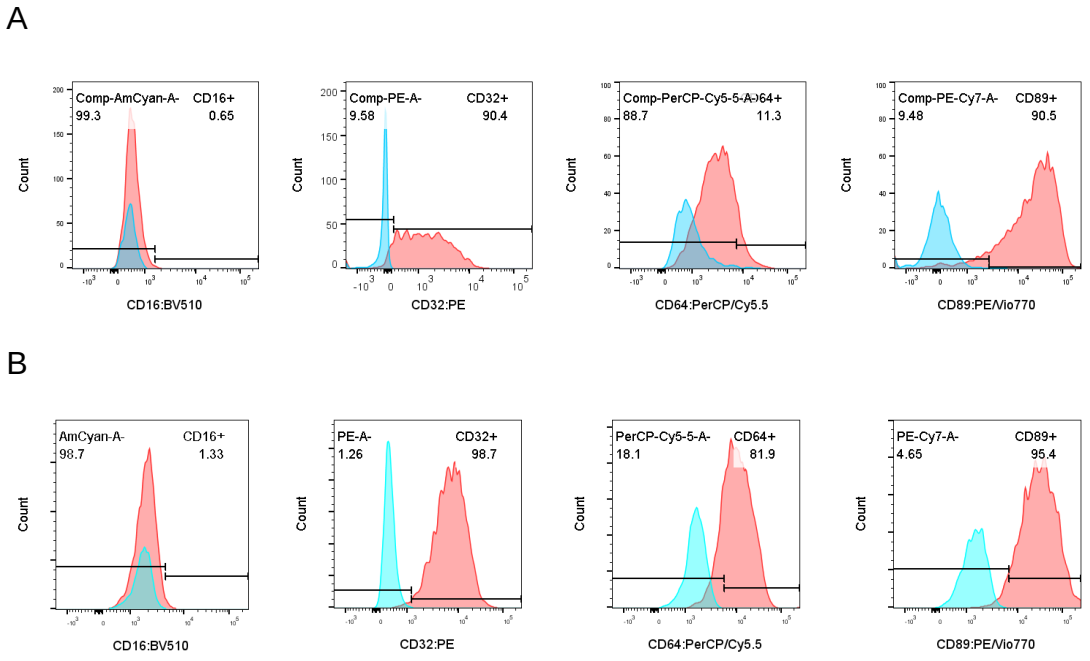

Figure 40: Primary monocyte-derived macrophages display CD32, CD64, and CD89, but not CD16. PID 0011 monocytes differentiated for 7 days; B. PID 0018 monocytes differentiated for 15 days.

Expression of Fc receptors on non-adherent THP-1 cells was also confirmed by flow cytometry. All cells expressed FcγRI and FcγRII; a minority had FcαRI; FcγRIII was not detected (Figure 41).

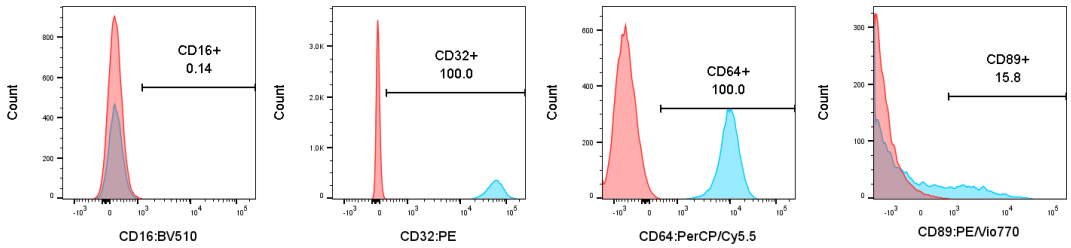

Figure 41: THP-1 monocytes display CD32, CD64, and CD89, but not CD16. THP-1 cells gated on single cells, DRAQ7- (live), stained for CD16 (FcγRIII), CD32 (FcγRII), CD64 (FcγRI), and CD89 (FcαRI).

4.2.1.2 Outline of quantifying infection and host cell viability

Figure 42 shows the general gating strategy for measuring uninfected vs. infected and live vs. dead populations in the following infection experiments. Cells were infected with fluorescent Mtb CDC1551 and then stained with a fixable viability dye at specified time points, fixed, and acquired. Phagocytosis was evaluated by the frequency or integrated MFI (MFI × frequency of infected population)[366] of cells fixed at early time points (1-2 hours post-infection) and intracellular bacterial growth on cells fixed at later time points (3 days post-infection).

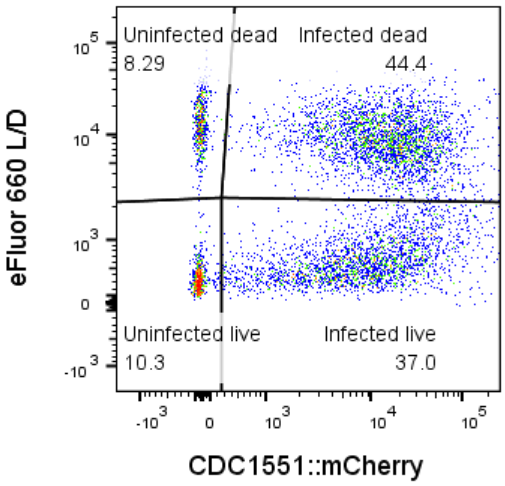

Figure 42: Single monocyte/macrophage populations infected with mCherry-expressing Mtb and stained with fixable viability dye. X-axis is Mtb associated with THP-1 monocytes after washing (bound or internalised), y-axis is live/dead stain.

4.2.2 mAb P2E04 reduces host cell death and intracellular bacterial load in primary monocyte-derived macrophages

In a preliminary experiment, monocyte-derived macrophages were infected with singlet suspensions of live fluorescent mCherry-expressing Mtb strain H37Rv (methods 2.5.2.2, 2.15.1). I initially used primary monocyte-derived macrophages as this was the same type of cell as used in our timelapse microscopy system further described below. Only 5 of the 12 mAbs were initially tested in the FACS experiment due to unavailability of the others, as the yields for the first batch prepared in September 2017 were low.

Rifampicin 40 ug/mL was included as a control to decrease infection and bacterial gene expression, as we did not have any positive control antibody with confirmed Mtb-inhibiting function. Cells were washed 6 h post-infection with the mAb + bacteria mixtures and harvested for analysis at 2 days post-infection. Similar to the original authors' report, the 3 mAbs isolated by Zimmermann et al.[360] did not reduce Mtb infection (Figure 43). From PID 6037, mAb P2F10 also slightly enhanced infection, while P2E04 reduced the percentage of infected cells as well as the bacterial load in the infected population, even though they had similar binding activity shown above.

However, this method was problematic because the prolonged Accutase digestion and scraping needed to detach mature differentiated macrophages from the culture surfaces resulted in high non-specific cell death leading to problems with reproducibility (data not shown). Therefore in subsequent flow cytometry experiments, THP-1 monocytes were used.

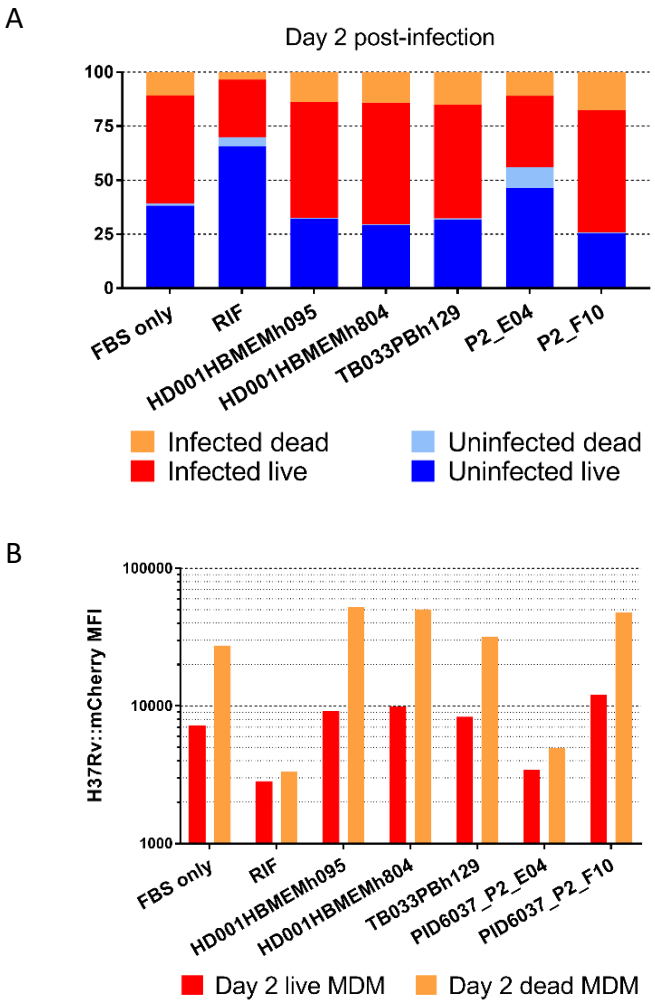

Figure 43: Fraction of infected macrophages depends on source of antibodies for opsonised Mtb. Rifampicin (RIF) used as positive control for bacterial killing. A: Populations of infected, uninfected, live, and dead macrophages. Y-axis shows percentage of total B: Median bacterial loads (relative fluorescence units) in infected macrophages.

4.2.2.1 Low concentrations of interferon-gamma improve THP-1 monocyte control of intracellular Mtb

In an Fc receptor-humanised mouse model, treatment of mice with interferon-gamma (IFNγ) was important for control of antibody-mediated control of infection[368]. Other authors have also used IFNγ treatment of macrophages to simulate the effect of an ongoing infection[369]. Therefore I titrated IFNg on THP-1 cells overnight prior to infection with a singlet suspension of Mtb followed by staining and fixation at 24 and 72 hours post-infection for flow cytometry (methods 2.5.2.2, 2.14). An input of 1 CFU/monocyte was used for this experiment.

As expected, very high concentrations of recombinant IFNγ were detrimental to host cell viability, while IFNγ in the range of tens of U/mL increased infection frequency, did not negatively affect viability, and decreased median fluorescence intensity of the constitutively expressed reporter mCherry (bacterial load) in dead cells (Figure 44). Therefore in subsequent experiments 50 U/mL IFNγ was added to the culture medium (dotted line).

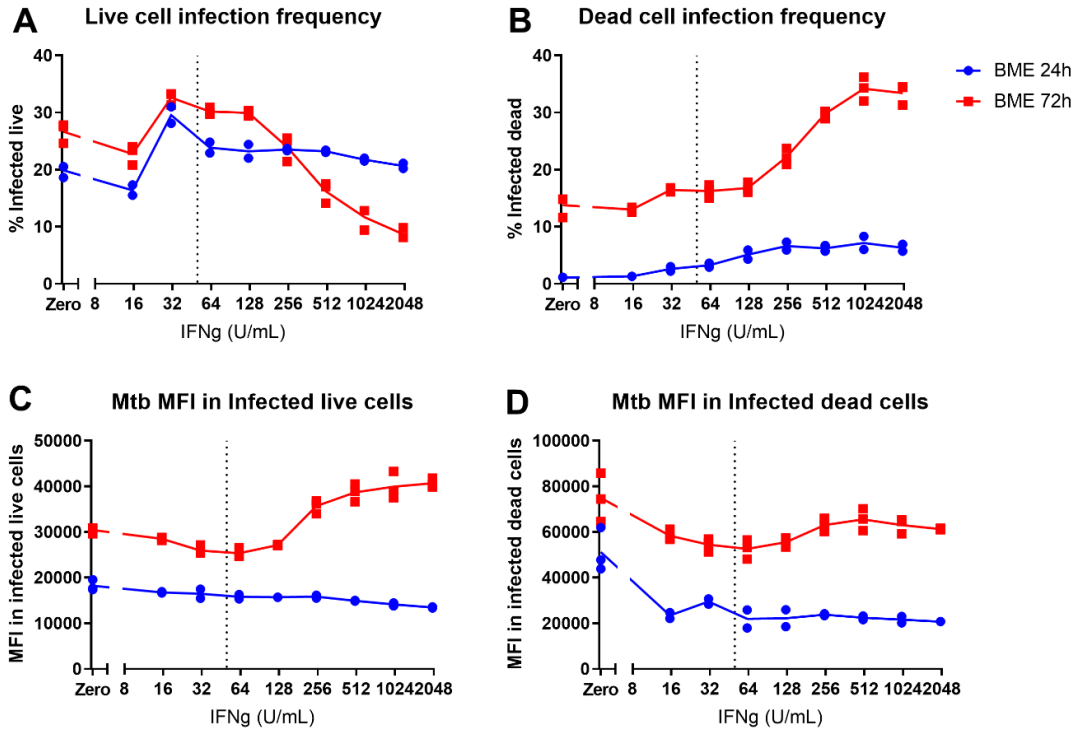

Figure 44: Low-dose interferon gamma aids in intracellular bacterial control without affecting monocyte viability. Interferon gamma titration on THP-1 infected with Mtb fixed at 24 or 72 hours post-infection. Vertical dotted line shows the 50 µg/mL concentration used in subsequent experiments below.

4.2.3 Serum from TB-exposed individuals decreases intracellular bacterial load and THP-1 monocyte death

The aim of this experiment was to determine whether polyclonal serum could modulate infection and intracellular bacterial growth in THP-1 monocytes. Serum samples included in this experiment were: 9 pulmonary TB patients (PTB) and 13 TB-negative, HIV-negative donors, plus three samples of commercial pooled normal human serum (one lot of Sigma-Aldrich and two different lots of Biowest). Mtb CDC1551 was

opsonised with samples diluted to 1:20 for 1 hour before infecting THP-1 as detailed in methods sections 2.5.2.2, 2.14.

Commercial human serum clearly increased the intracelluar bacterial load and decreased infected cell viability relative to cells with FBS only. At 2 days post-infection, serum from both healthy and PTB South African donors began to show some trend toward decreasing intracellular bacteria and improving monocyte viability relative to commercial serum, but these effects were not significant (Figure 45). By 3 dpi, serum from healthy South African donors clearly decreased the intracellular bacterial load (p = 0.05), and both healthy and PTB donors' serum increased infected monocyte viability above the commercial control serum (p = 0.03 for healthy donors and p = 0.02 for PTB donors).

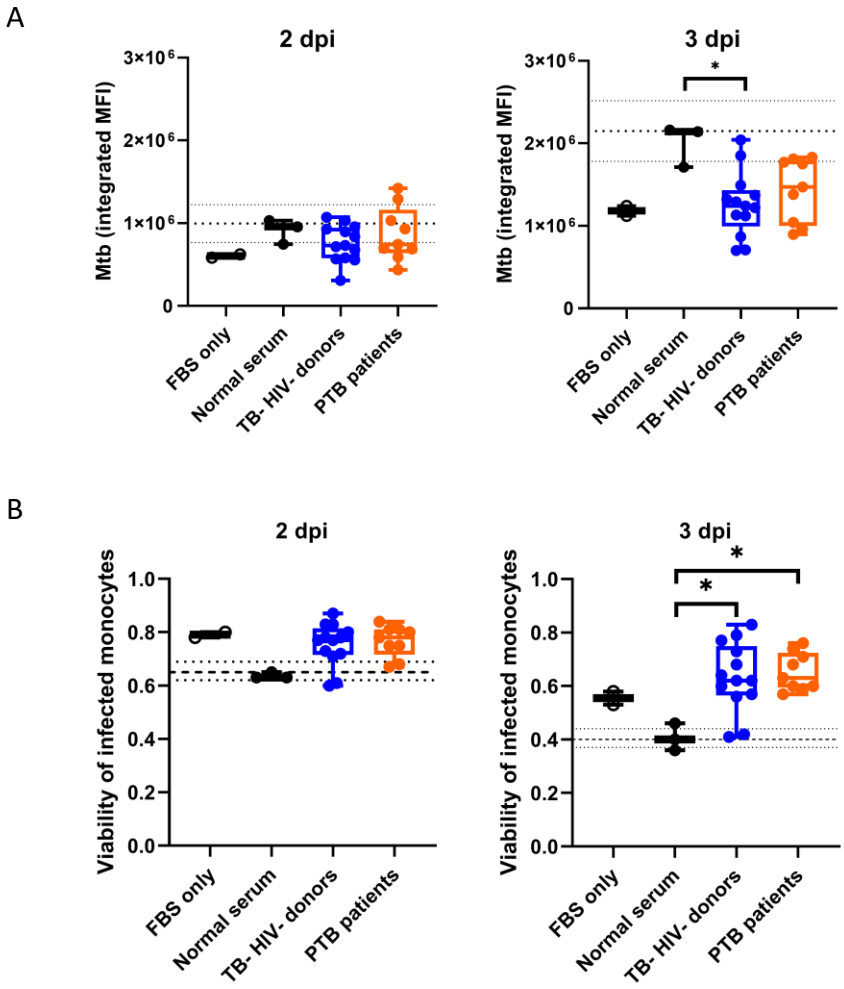

Figure 45: Serum from TB-exposed healthy donors decreases intracellular bacterial load and enhances monocyte survival. Infection of THP-1 monocytes with fluorescent Mtb

in the presence of human serum. A: Total bacterial load measured as integrated MFI. B: Viability of infected cells measured as frequency of live infected over total infected cells. Dotted lines show mean ± 3 standard deviations of the normal human serum control.

4.2.4 Different monoclonal antibodies can exacerbate or inhibit intracellular Mtb growth in THP-1

Monoclonal antibody P2E04 cloned from healthy donor 6037 was selected for functional testing due to its strong binding to Mtb soluble cell wall protein fraction and whole Mtb CDC1551 (the strain used in the following experiments) shown in Chapter 3.

THP-1 monocytes and Mtb were prepared as previously described except that the input MOI was reduced to 1 CFU/monocyte because of the lower total concentration of monoclonal IgG compared to polyclonal serum IgG. The selected antibodies were P2E04, HD001HBMEMh095, and TB024PBh037, and negative controls mAb F10 (influenza H5), and purified nonspecific polyclonal IgG (Sigma-Aldrich). These were titrated across a range of 0.20 to 25 μg/mL. I also tested two different procedures for antibody treatment: opsonising the bacteria with antibodies prior to infection, or treating the cells with antibodies prior to adding bacteria. The pre-incubation workflow would be more similar to the physiological conditions *in vivo*, and also reduces the number of steps that must be performed in BSL3. Other authors have shown that similar results were obtained when preincubating cells with antibody vs. opsonising bacteria first (Chen et al. 2016, figure S6[370]).

Cells infected with opsonized bacteria vs. cells preincubated with antibody showed a similar pattern across the five antibodies, which persisted up to 3 days post-infection. There was a dose-dependent decrease in the integrated MFI in the presence of P2E04, and a smaller decrease in the presence of HD001HBMEMh095. Surprisingly, the control mAb F10 (influenza) had similar effects to HD001HBMEMh095. The anti-LAM antibody TB024PBh037 enhanced infection at lower concentrations (Figure 46).

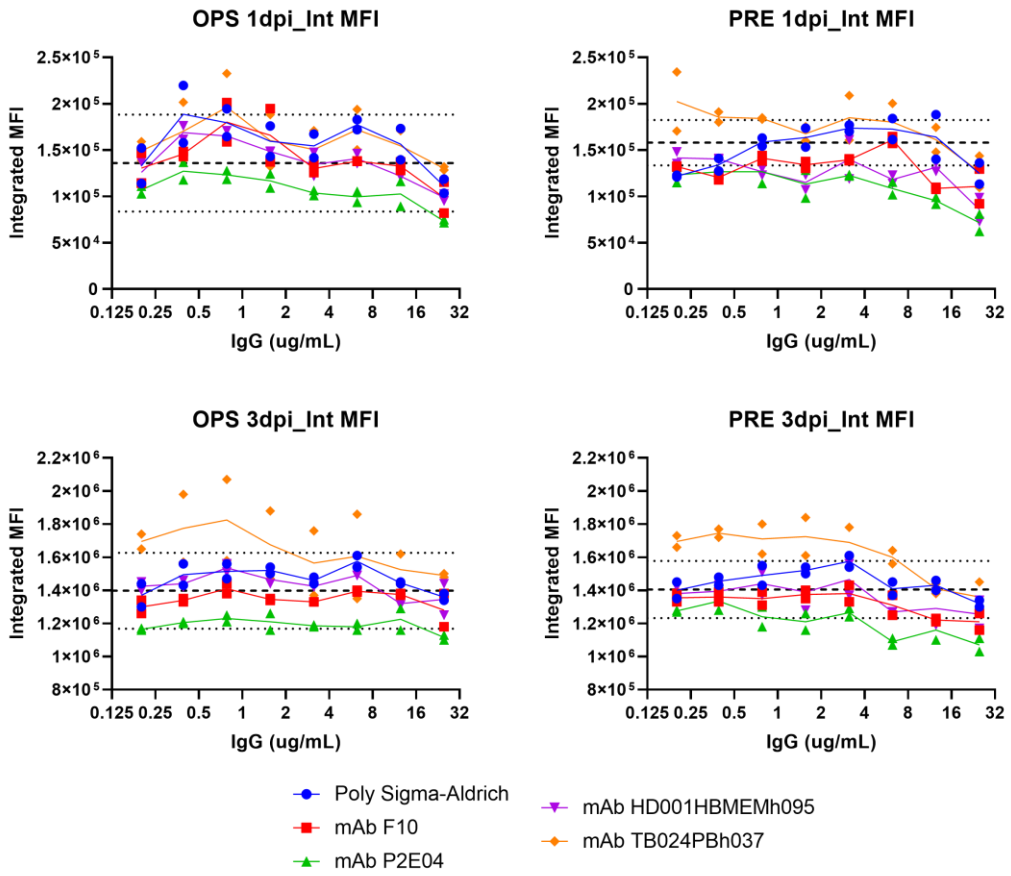

Figure 46: Specific mAbs can enhance or inhibit total intracellular bacterial load (integrated MFI) in THP-1 monocytes. THP-1 infected with Mtb either opsonised with mAbs or cells pretreated with mAbs, at 1 and 3 days post-infection. Dotted lines show mean ± 3 standard deviations of the FBS medium-only control.

I also tested the effect of mAb P2E04 in a background of nonspecific human antibodies by using human serum in the culture medium (as previous experiments were done in medium with FBS). A concern had been raised that an alternative explanation for reduced phagocytosis could be reduced cell health due to cytotoxic effects of the antibody or buffer, so mock infected conditions for both P2E04 and the buffer control were included to determine if either one had negative effects on cell health in the absence of infection.

Results are shown in Figure 47. At two hours post-infection, cells infected in HS medium had a far higher bacterial load than cells infected in FBS medium. At three days post-infection, cell counts were also calculated as an estimate of cell health. The

counts were calculated as count per second (event rate in the single cell gate) multiplied by the high-throughput sampler flow rate of 2 μL/s.

By 3 days, the input cells (250,000/mL) in uninfected control wells had almost doubled by 3 days in FBS medium (equivalent to 458,000/mL) whereas they grew less in HS medium (311,000/mL). For the infected controls in FBS, the average of 243,000 monocytes/mL was similar to the input cell count, whereas in HS, the average of 26.3/s equivalent to 13,200/mL was only 5.3% of the original input, suggesting that the vast majority of the cells had died.

As shown in the previous experiment with serum (Figure 45), 1:20 or 5% non-specific commercial normal human serum increased intracellular Mtb load and had a deleterious effect on host cell viability; in this experiment 10% nonspecific serum apparently further exacerbated these effects. Cells infected in human serum medium had about a 2.5-fold higher bacterial load at 2 hours post-infection, which suggests that these effects might be partly attributed to increased phagocytosis at earlier timepoints as well as increased intracellular bacterial growth. Integrated MFI values are also shown at 3 dpi, but since most of the cells were dead, these values may not be meaningful.

In foetal bovine serum medium, while there was no difference in integrated MFI at 2 hours post-infection, there was a strong dose-dependent inhibition by mAb P2E04 of integrated MFI at 3 dpi. Cells infected in the presence of P2E04 had significantly lower MFI than the controls down to the lowest tested concentration of 1.56 μg/mL. All infected cell wells in both the P2E04 and buffer control titrations had cell counts (Figure 47E) similar to the control wells, showing that the effects of P2E04 on intracellular Mtb load were not due to indirect cytotoxic effects on the monocytes.

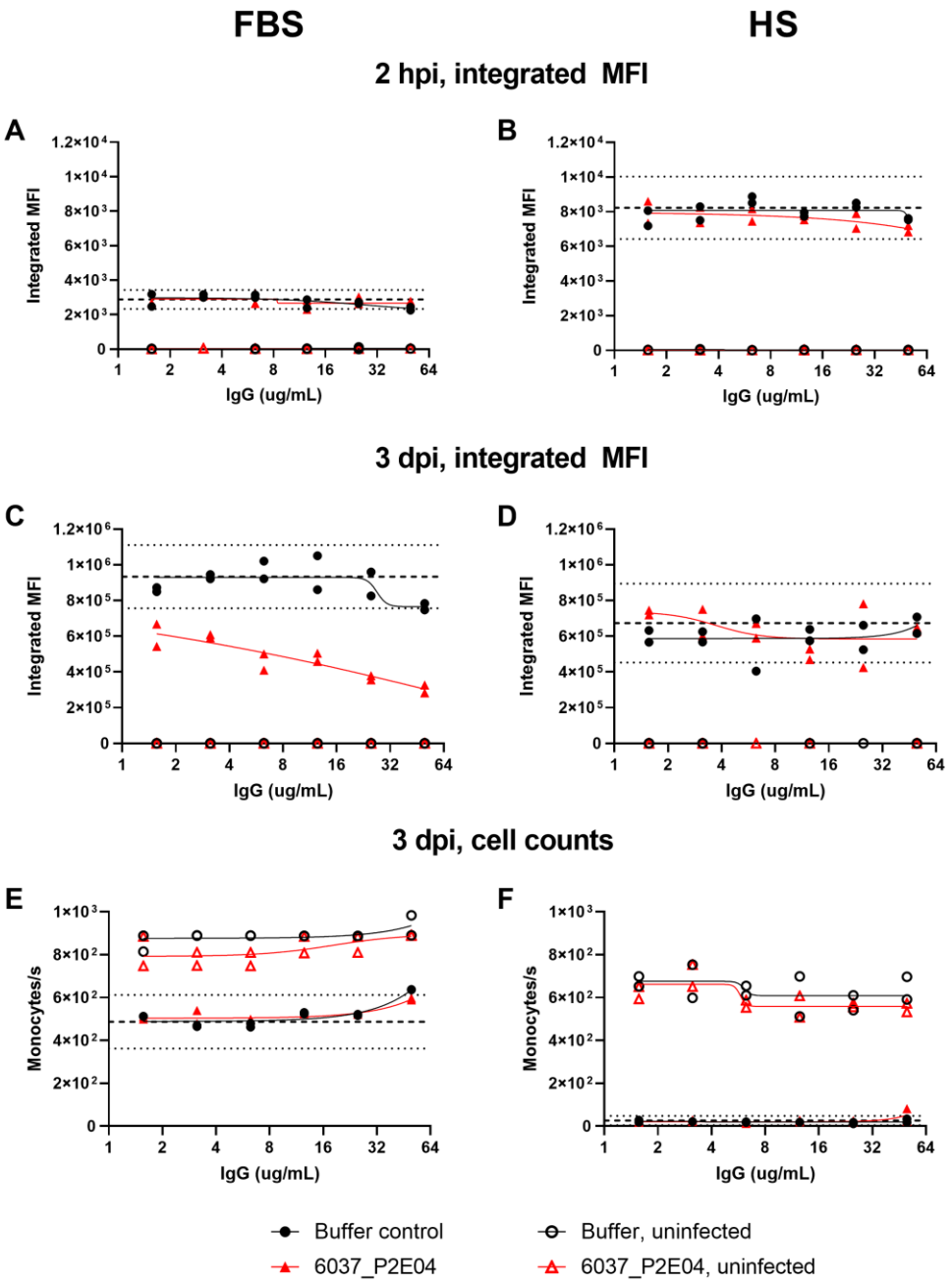

Figure 47: mAb P2E04 inhibits intracellular bacterial growth independently of phagocytosis at early timepoints. Integrated MFI (infected frequency x MFI) and relative cell counts of THP-1 monocytes, in medium with foetal bovine serum (left) or normal human serum (right). A, B: integrated MFI at 2 hours post-infection. C, D: integrated MFI at 3 days post-infection. E, F: Relative cell counts per second at 3 days post-infection. Dotted lines show mean ± 3 standard deviations of the medium-only controls.

4.2.5 Effects of antibodies on Mtb growth in co-culture with primary human macrophages

We used time-lapse microscopy to track the kinetics of bacterial growth in co-cultures with primary human monocyte-derived macrophages (cultured as described in methods 2.2). Suspensions of mCherry-expressing Mtb CDC1551 were prepared and opsonised with antibody samples, then used to infect MDM (methods 2.15). The following experiments were done without washing off non-phagocytosed bacteria, which made it difficult to perform image segmentation (outlining each macrophage in order to determine individual intracellular bacterial loads). Therefore the total bacterial load was measured as the sum of bacterial mCherry fluorescence.

4.2.5.1 Effects of monoclonal antibodies in the absence of human serum

The following experiments were performed in medium made with foetal bovine serum (FBS), therefore the only human immunoglobulins present were the monoclonal antibodies.

Antibody HD001HBMEMh095 (plasmid no. 2412) originally sequenced by Zimmermann et al. was selected for testing as the original authors had reported strong neutralization by the IgA version and strong enhancement by the IgG recombinant in an A549 (lung epithelial cell line) infection assay due to internalisation of opsonised bacteria via the neonatal Fc receptor. We found that this antibody, expressed as IgG, inhibited the growth of bacteria in infected macrophages (Figure 48). Initially Hoechst 34580 was used as a live cell nuclear stain to facilitate tracking individual cells for image analysis. Unfortunately, either the stain or the violet laser excitation or both had a clear detrimental effect on the growth of the Mtb even at the lower concentration of 0.2 ug/mL, so it was excluded from future experiments. Nevertheless, HD001HBMEMh095 reduced bacterial load compared to control across all 3 paired conditions.

A

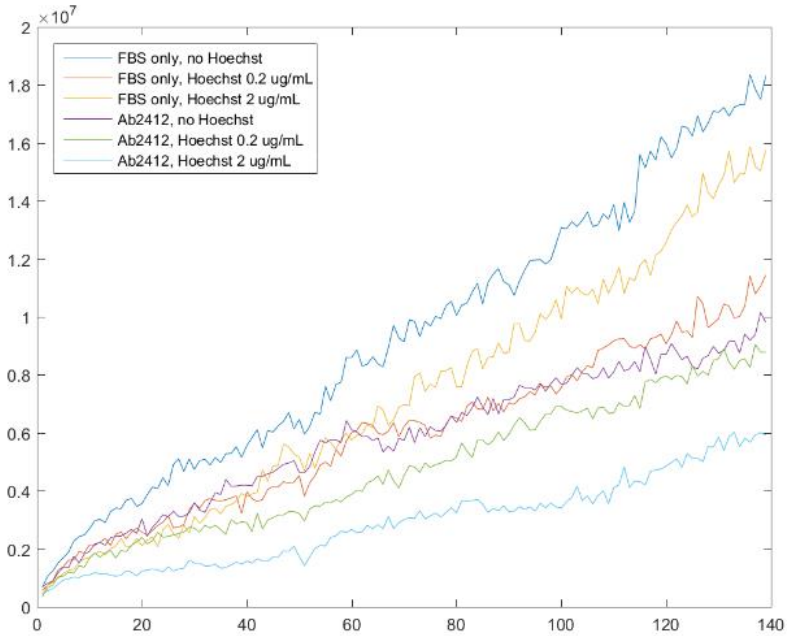

B

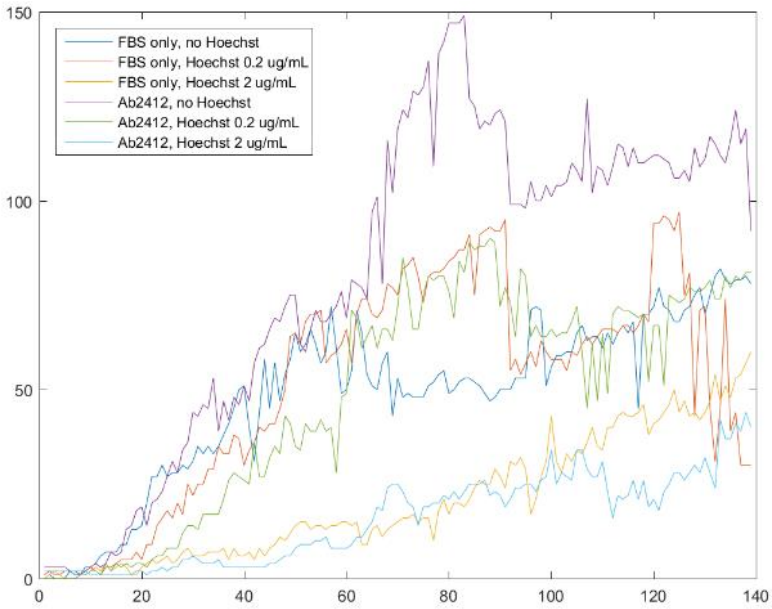

Figure 48: MAb HD001HBMEMh095 and Hoechst 34580 independently inhibit Mtb growth in co-culture with macrophages. MDM were from Donor 6017. A: bacterial load increase (relative fluorescence units) and B: number of dead macrophages in the presence of mAb HD001HBMEMh095, with 0 - 2 ug/mL Hoechst 34580. X axis units are frames of 20 min, 24 h = 72 frames.

We then tested two of the AHRI PID 6037 mAbs. P2E04 from the September 2017 batch had been consumed and was not available at this point, so I used P2C02 and P2F10 which were the next highest binding mAbs in the H37Rv ELISA and FACS (see previous chapter). Opsonisation with P2F10 dramatically increased the bacterial load compared to control from early in infection as expected from the FACS experiment, while P2C02 only increased it slightly during the first day and about double by the fourth day of infection (Figure 49). Cell death largely paralleled the bacterial load. When the two mAbs were mixed in a 1:1 ratio, the effect was intermediate.

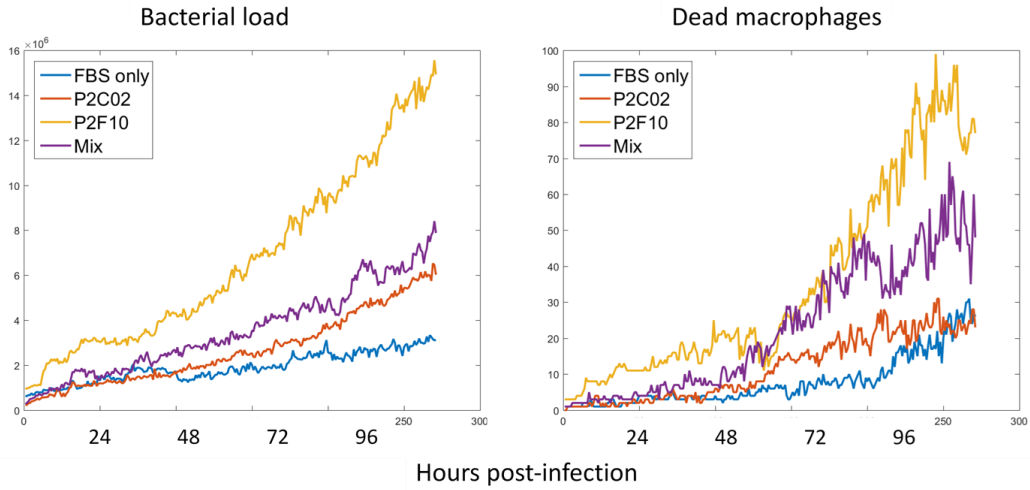

Figure 49: MAbs P2C02 and P2F10 enhance bacterial growth and host cell death over FBS-only medium. MDM were from Donor 6009. A: bacterial load increase (relative fluorescence units) and B: number of dead macrophages in the presence of two PID6037 antibodies. X axis units are in hours.

4.2.5.2 The effect of P2E04 on total Mtb growth in macrophage co-cultures is macrophage donor-dependent and Fc receptor-dependent

Mtb bacilli *in vivo* would be exposed to protective antibodies in a background concentration of several mg/mL of antibodies with various other specificities which could compete for binding to Fc receptors on phagocytes. I compared the effects of P2E04 in media made with heat-inactivated human (Sigma-Aldrich) versus bovine serum (Hyclone). While bacterial fluorescence intensity was initially higher in human serum medium compared to bovine serum, it later plateaued and remained lower up to 72 hours post-infection while bacteria in bovine serum continued growing. MAb

P2E04 reduced the rate of Mtb growth in both species' medium (Figure 50A). Subsequent experiments were done in medium with heat-inactivated human serum as being more reflective of the *in vivo* conditions.

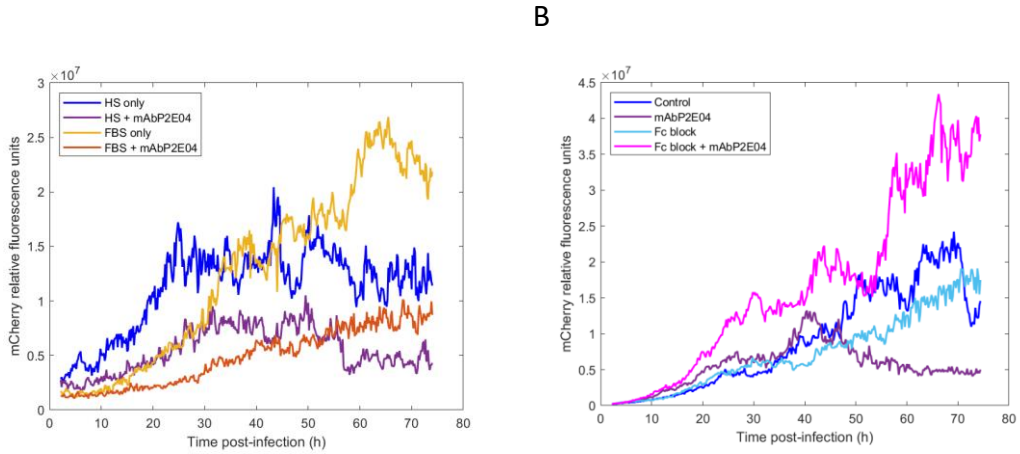

Figure 50: mAb P2E04 inhibits Mtb growth in co-culture with MDM from Donor 0011. A: In media formulated with either 10% human serum or FBS. B: Interaction with Fc receptor blockade (in human serum medium).

To further investigate whether control of bacteria by mAb P2E04 may be mediated by uptake via Fc receptors, I pretreated macrophages with an Fcγ-blocking reagent (no azide/low endotoxin human Fc block, BD Biosciences) and also added back the same concentration of Fc block after the infection step. As before, mAb P2E04 decreased the bacterial fluorescence intensity. Fc block alone had little effect on bacterial growth, whereas Fc block + P2E04 dramatically increased the amount of bacteria (Figure 50B).

As we were not always able to recall the same blood donor for CD14 monocyte isolation, I tested the effect of mAb P2E04 on Mtb growth in co-culture with macrophages from a different donor, PID 0018. Surprisingly, in macrophages from this donor, the effect of P2E04 was reversed and it exacerbated bacterial growth compared to the buffer control condition, IgG negative control VRC03 (AIDS Reagent Program), and IgA nonspecific control (human colostrum IgA, Bio-Rad) (Figure 51 A). This effect was reproducible in 2 subsequent independent experiments using the same donor macrophages. Treatment with Fc Block fully or partially reversed this effect (Figure 51 C and D).

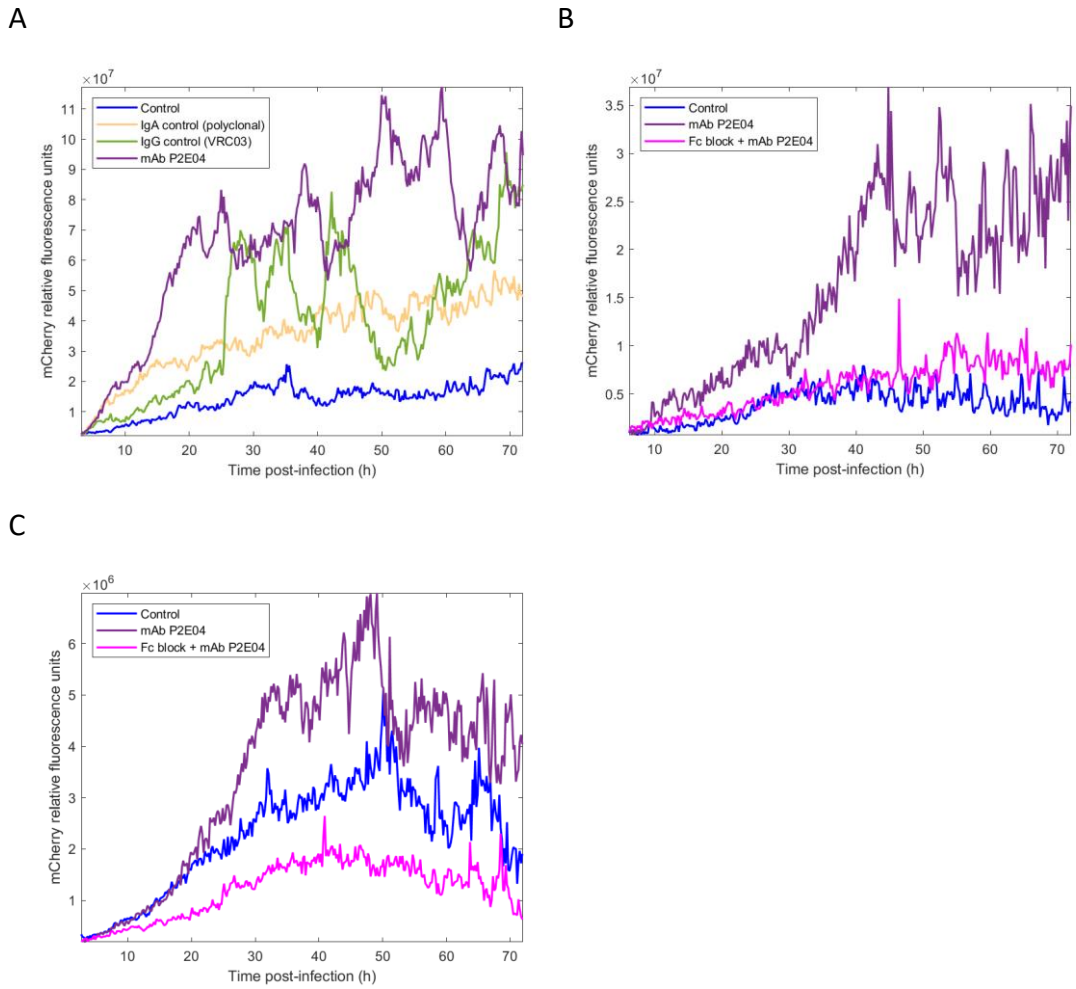

Figure 51: mAb P2E04 exacerbates Mtb growth in co-culture with MDM from Donor 0018. A: Comparison with control antibodies. B and C: two independent experimentscomparing the effect of Fc receptor blockade.

4.2.6 P2E04 affects intracellular Mtb growth in primary MDM in a donor-dependent manner

Infection of macrophages with singlet bacteria presented a few problems for single-cell image analysis: 1) the low mCherry signal from singlet bacteria made it difficult to quantify bacterial load accurately at early time points; 2) the presence of extracellular bacteria interfered with image segmentation, i.e. the delineation of single macrophages as regions of interest over which to integrate the bacterial fluorescence signal. Therefore in subequent experiments, the Mtb inocula were prepared as small aggregates of bacteria (<10µm) instead of singlets (methods 2.5.2.2) to provide a higher fluorescent signal per infected macrophage, and macrophage cultures were washed after the initial 6 hours of infection to remove extracellular bacteria. Timelapse

images were analysed in Matlab to segment individual macrophages and track their bacterial load.

Macrophage donor 0044 was used for 2 independent experiments on separate occasions. In both experiments, P2E04 significantly slowed the growth of intracellular Mtb relative to the medium-only control condition (Figure 52), from a doubling time of 18 ± 1 h to 52 ± 4 h ($p = 0.008$). In addition, the average macrophage survival time increased from 39.68 ± 16.44 h, to 33.48 ± 18.77 h in the presence of P2E04.

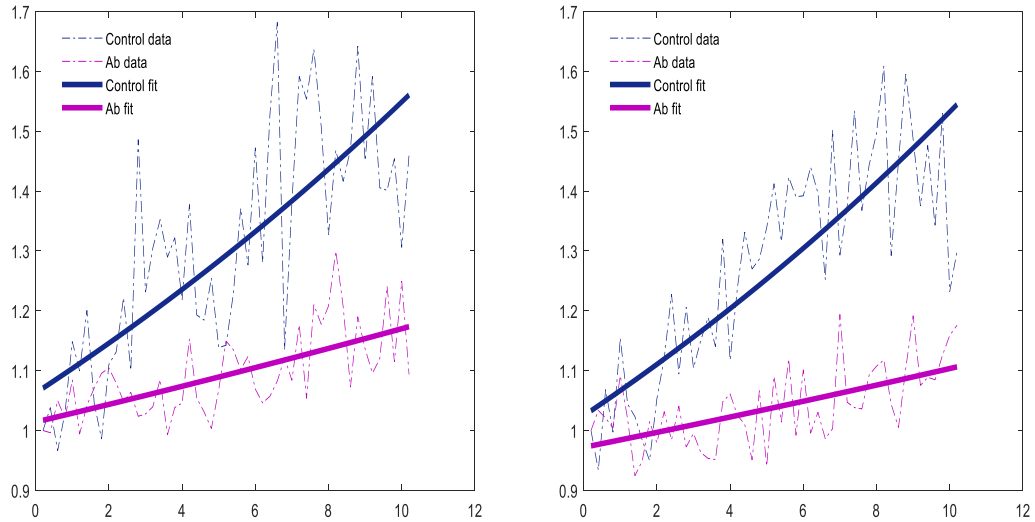

Figure 52: mAb P2E04 inhibits intracellular Mtb growth in Donor 0044 monocyte-derived macrophages in two independent experiments. Y axis shows fold increase over baseline; X axis units in hours.

Inconsistent results were found in two subsequent experiments with different donors (Figure 53 and Table 8). In donor 0042 macrophages, intracellular bacteria grew slightly faster in the presence of mAb P2E04. Whereas in donor 0052, the doubling time was four times slower in the presence of P2E04 than the medium control, and this effect was partially reversed by Fc receptor blockade. These support our previous findings that monoclonal antibodies can modulate Mtb infection and intracellular bacterial growth in macrophages, even in a background of high nonspecific IgG (in the macrophage culture medium), but that the effect is donor-dependent.

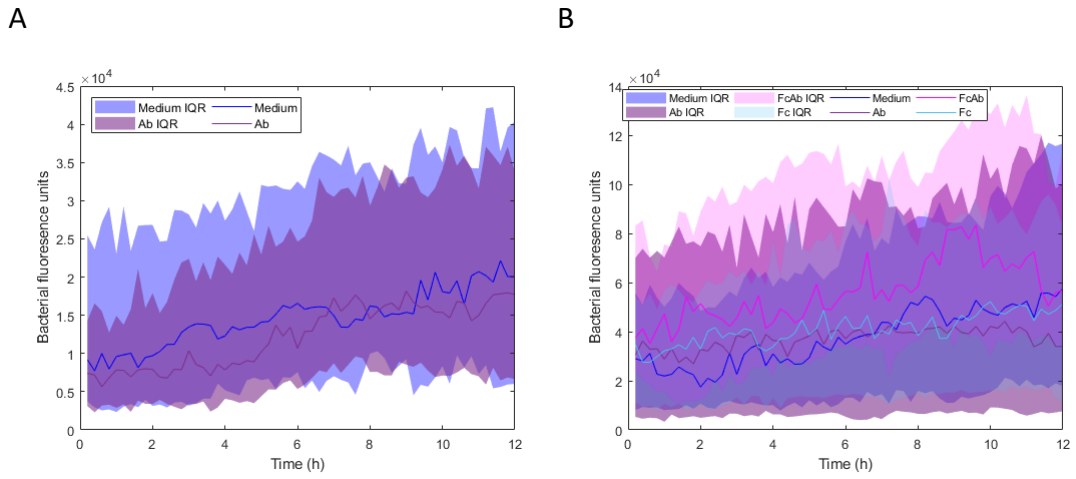

Figure 53: Intracellular Mtb fluorescence (arbitrary units) in monocyte-derived macrophages. Lines: median; shaded areas: interquartile range. Ab: mAb P2E04, Fc: Fc Block reagent. A: Macrophage donor 0042, B: donor 0052.

Table 8: Doubling times of intracellular Mtb and numbers of single cells analysed.

	Macrophage donor 0042		Macrophage donor 0052	
	Cells	Median doubling time (h)	Cells	Median doubling time (h)
Medium control	70	10.21	32	8.23
mAb P2E04	62	7.38	34	33.25
Fc Block	ND	ND	38	19.12
Fc Block + mAb P2E04	ND	ND	35	14.16

4.2.6.1 Quantification of intracellular bacteria by qPCR

I created a stock of purified Mtb genomic DNA from a CDC1551 culture for use as a standard curve for genome copy number estimation by quantitative PCR (methods 2.15.3). Based on the total DNA concentration and using the genome size of Mtb strain H37Rv of 4,411,529 base pairs as an estimate (I was not able to find a genome size reference for strain CDC1551), the yield of purified DNA was 1.39 copies per colony-forming unit (determined by titration of the original culture immediately before DNA extraction). In qPCR, the Cq vales correlated well with the input DNA across a range

of 1 to 0.000064 ng per reaction (Figure 54), i.e. about 210,000 to 13 copies per reaction.

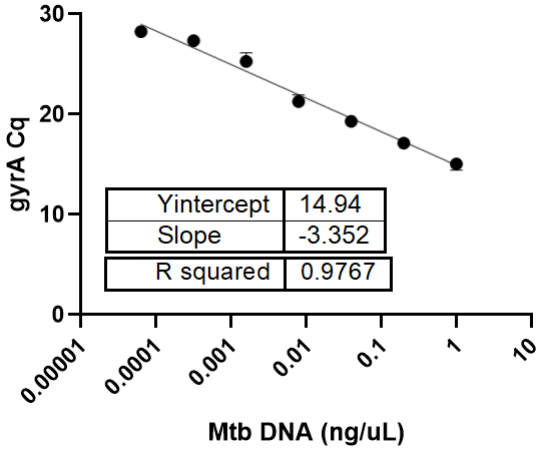

Figure 54: gyrA qPCR of purified Mtb CDC1551 DNA.

I then performed three independent repeats of an infection experiment of monocyte-derived macrophages from five healthy donors. Cells were treated with 1) medium containing heat-inactivated normal human serum only, 2) Fc receptor blocking reagent (BD), 3) mAb P2E04, 4) Fc block plus mAb P2E04. Cells were infected with approximately 5 CFU per MDM of CDC1551 and incubated for 48 hours, then harvested and processed.

Results from these experiments were inconclusive as there was high variation between runs even after normalising each sample to the medium-only control in each run (Figure 55). One possible cause could be the extraction method which involved multiple washes prior to bead-beating. This protocol had been developed for usage on clinical sputum samples, where the expected host (human) DNA load, mucus, and other debris could be much higher than in purified MDM cultures. It was difficult to see the pellets during wash steps for the MDM lysate samples. Therefore the extraction method could have contributed to sample loss and high variation in this essay. The method would need to be re-optimised for this type of *in vitro* culture sample.

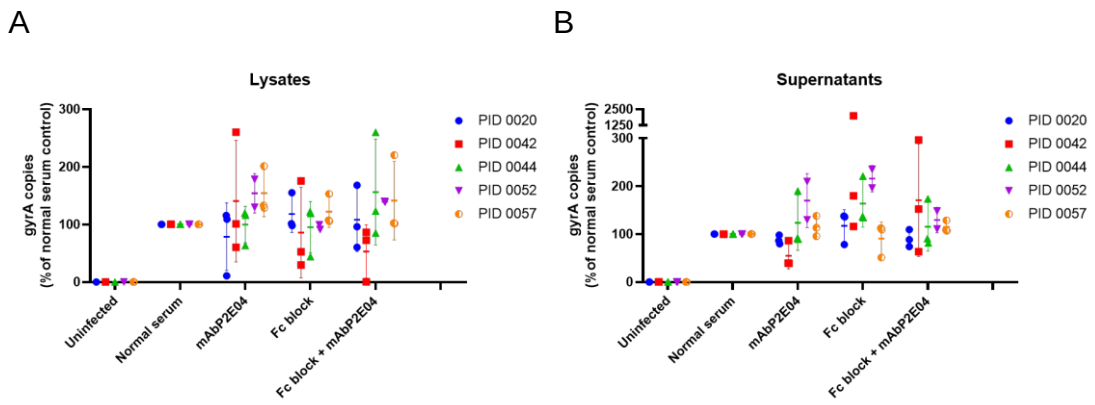

Figure 55: gyrA copies in infected MDM cultures normalised to normal medium control per each donor and experiment. Results show five individual macrophage donors and three independent runs. A: MDM lysates; B: culture supernatants.

4.2.7 Differential gene expression in the presence of P2E04

An RNA-seq pilot experiment was performed as detailed in methods section 2.15.4, to determine if there was any effect of mAb P2E04 on host cell gene expression during Mtb infection. MDM in this experiment were from Donor 6111. For this experiment, the macrophage medium was made with heat-inactivated commercial human serum, not FBS.

Six hours post-infection, cells were dissociated with Accutase and placed on ice. Live MDM from the no-mAb tube were gated by mCherry fluorescence and sorted into uninfected and low, medium, and high approximate tertiles. At six hours post-infection, there was a slightly lower frequency of infection in the presence of mAb (Figure 56). Ten thousand cells from each of the four populations in each sample were sorted into tubes prefilled with TRIzol. However, some of the mAb P2E04-medium infected tube

was lost due to spillage (lane H1 in Figure 57B). Good quality cDNA was obtained from the SMART-Seq2 process and handed to KRISP for sequencing (Figure 57).

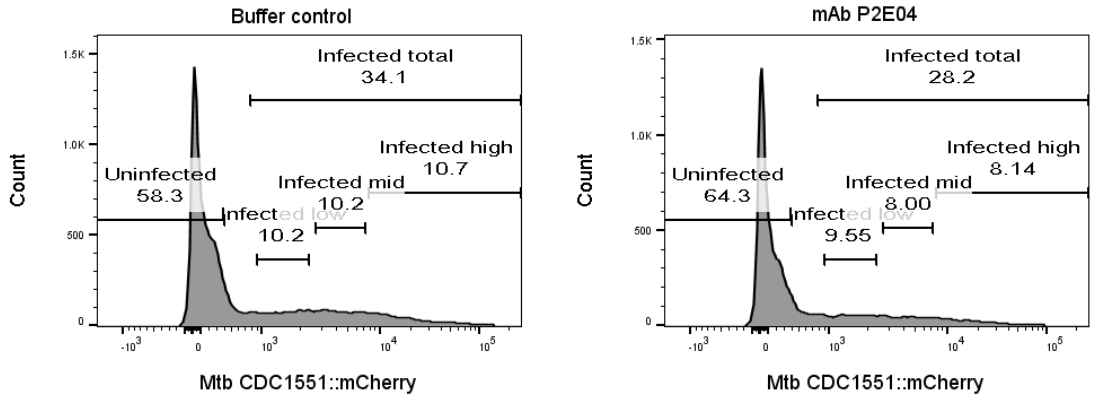

Figure 56: mAb P2E04 slightly decreases uptake of Mtb CDC1551 in monocyte-derived macrophages by 6 hours post-infection. Left: buffer control; right: mAb P2E04.

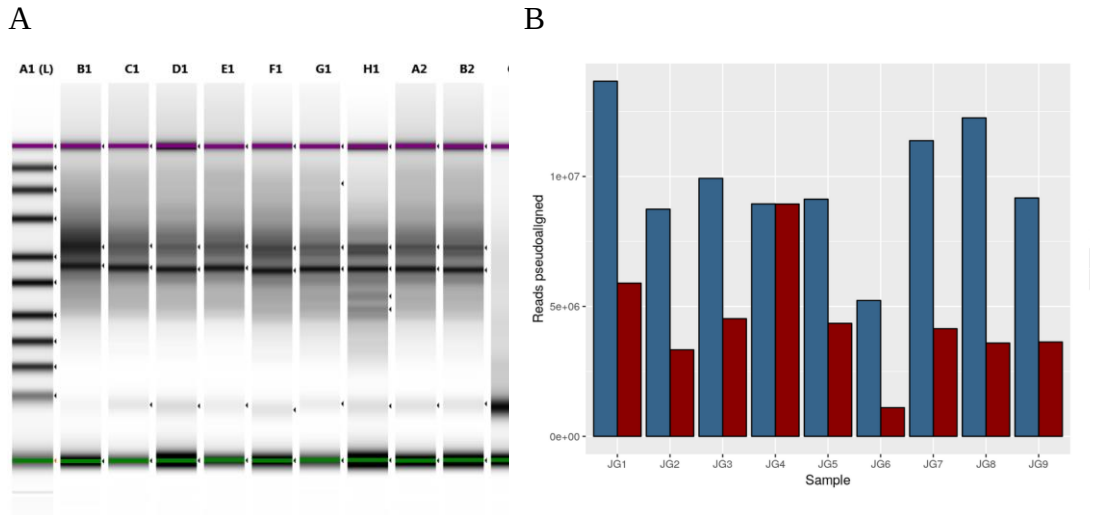

Figure 57: Quality of cDNA libraries and sequencing. A. TapeStation electrophoresis of cDNA following whole-transcriptome amplification. A1 is the molecular weight marker; C2 is the no-template control. B: Reads pseudoaligned to hg19 reference human transcriptome. Batch A is the second run; Batch B is the first run which was repeated because of low quality.

To determine the effect of the antibody, differential gene expression was compared between two models, Model 1 assuming only infection levels (uninfected, low, medium, high) as factors (IL-1β is named as an example):

$$countsIL1B = U + L + M + H$$

Model 2 including a mAb term:

$$countsIL1B = U + L + M + H + mAb$$

The top 25 differentially expressed genes sorted by q-value (out of a total of 445 DE genes) are shown in Table 9. The highest DE gene was CCL4, also known as macrophage inflammatory protein 1β (MIP-1B).

Table 9: Differentially expressed genes in the presence of mAb P2E04.

Ensembl ID	Gene Symbol	Gene Description	p-value	q-value	beta
ENSG00000129277	CCL4	chemokine (C-C motif) ligand 4 [Source:HGNC Symbol;Acc:10630]	0.0000001	0.0007078	0.5558303
ENSG00000056558	TRAF1	TNF receptor-associated factor 1 [Source:HGNC Symbol;Acc:12031]	0.0000009	0.0053967	0.0927916
ENSG00000205358	MT1H	metallothionein 1H [Source:HGNC Symbol;Acc:7400]	0.0000019	0.0079550	0.2917531
ENSG00000125538	IL1B	interleukin 1, beta [Source:HGNC Symbol;Acc:5992]	0.0000040	0.0085406	0.5003410
ENSG00000178385	PLEKHM3	pleckstrin homology domain containing, family M, member 3 [Source:HGNC Symbol;Acc:34006]	0.0000042	0.0085406	0.1398343
ENSG00000205362	MT1A	metallothionein 1A [Source:HGNC Symbol;Acc:7393]	0.0000037	0.0085406	0.5911016
ENSG00000100292	HMOX1	heme oxygenase (decycling) 1 [Source:HGNC Symbol;Acc:5013]	0.0000125	0.0092517	-0.1469211
ENSG00000110944	IL23A	interleukin 23, alpha subunit p19 [Source:HGNC Symbol;Acc:15488]	0.0000114	0.0092517	0.5116366
ENSG00000123610	TNFAIP6	tumor necrosis factor, alpha-induced protein 6 [Source:HGNC Symbol;Acc:11898]	0.0000081	0.0092517	0.1599263
ENSG00000125144	MT1G	metallothionein 1G [Source:HGNC Symbol;Acc:7399]	0.0000067	0.0092517	0.3161414
ENSG00000159128	IFNGR2	interferon gamma receptor 2 (interferon gamma transducer 1) [Source:HGNC Symbol;Acc:5440]	0.0000108	0.0092517	-0.1947081
ENSG00000160326	SLC2A6	solute carrier family 2 (facilitated glucose transporter), member 6 [Source:HGNC Symbol;Acc:11011]	0.0000075	0.0092517	0.0993645
ENSG00000178623	GPR35	G protein-coupled receptor 35 [Source:HGNC Symbol;Acc:4492]	0.0000088	0.0092517	-0.1690442
ENSG00000187193	MT1X	metallothionein 1X [Source:HGNC Symbol;Acc:7405]	0.0000128	0.0092517	0.1985439
ENSG00000261768	SLC2A6	solute carrier family 2 (facilitated glucose transporter), member 6 [Source:HGNC Symbol;Acc:11011]	0.0000075	0.0092517	0.0993645

Ensembl ID	Gene Symbol	Gene Description	p-value	q-value	beta
ENSG00000261919	NCF1	neutrophil cytosolic factor 1 [Source:HGNC Symbol;Acc:7660]	0.0000097	0.0092517	0.1994523
ENSG00000262795	IFNGR2	interferon gamma receptor 2 (interferon gamma transducer 1) [Source:HGNC Symbol;Acc:5440]	0.0000118	0.0092517	-0.1955640
ENSG00000110047	EHD1	EH-domain containing 1 [Source:HGNC Symbol;Acc:3242]	0.0000144	0.0093445	-0.2715198
ENSG00000123689	G0S2	G0/G1switch 2 [Source:HGNC Symbol;Acc:30229]	0.0000145	0.0093445	0.2434168
ENSG00000112096	SOD2	superoxide dismutase 2, mitochondrial [Source:HGNC Symbol;Acc:11180]	0.0000249	0.0147641	-0.0709906
ENSG00000169429	IL8	interleukin 8 [Source:HGNC Symbol;Acc:6025]	0.0000253	0.0147641	0.2289450
ENSG00000134070	IRAK2	interleukin-1 receptor-associated kinase 2 [Source:HGNC Symbol;Acc:6113]	0.0000265	0.0147847	0.1944246
ENSG00000132297	HHLA1	HERV-H LTR-associating 1 [Source:HGNC Symbol;Acc:4904]	0.0000372	0.0182372	1.0161018
ENSG00000152229	PSTPIP2	proline-serine-threonine phosphatase interacting protein 2 [Source:HGNC Symbol;Acc:9581]	0.0000349	0.0182372	0.1928965
ENSG00000197262	CCL4L2	chemokine (C-C motif) ligand 4-like 2 [Source:HGNC Symbol;Acc:24066]	0.0000371	0.0182372	0.5087042

In principal component analysis of the differentially expressed genes, the cells with mAb P2E04 were clearly separated from the cells without mAb mostly across PC1 and infection level mostly across PC2 (Figure 58). One unexpected result was that in the presence of mAb, the medium infected cells were closer to the uninfected cells than were the low infected cells. I believe this may have been due to a sample mix-up as the mAb-medium infected (sample no. 7) was the one where part of the original sample was lost and the cDNA was somewhat more degraded than the others when the quality was checked by TapeStation prior to Nextera. Whereas the sequencing results showed that sample no. 6 (supposedly mAb-low infected) had the lowest number of aligned

reads (compare Figure 57A vs. B). Unfortunately there was no way of determining if this was the case or at what point in the process it may have occurred.

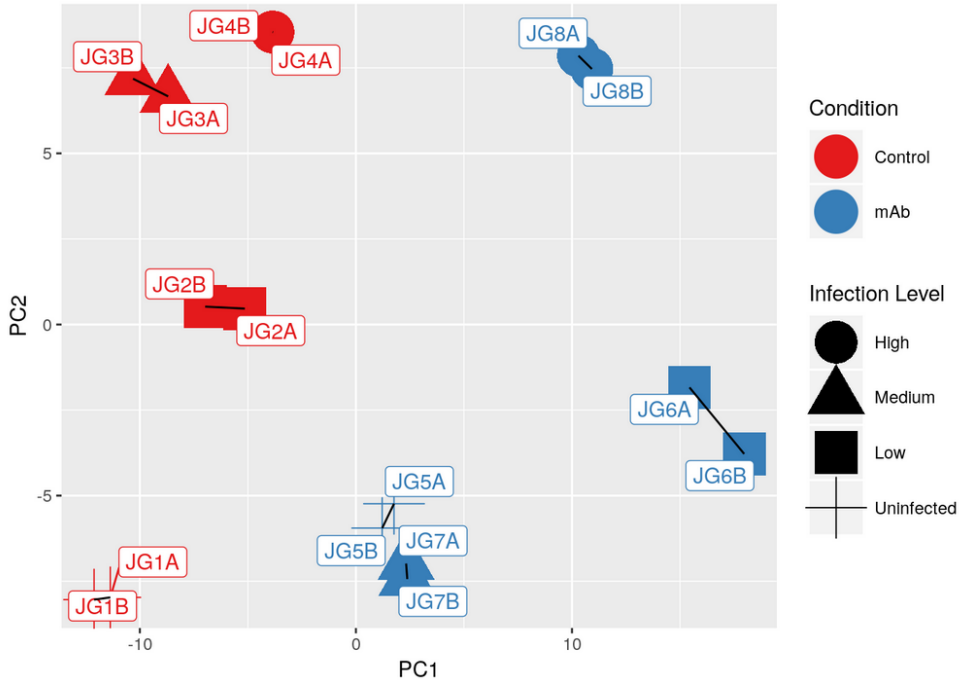

Figure 58: Principal component analysis of differentially expressed genes. Symbols indicate macrophages that were uninfected, low infected, medium infected, or high infected. Red: medium control, blue: mAb P2E04. Points marked A and B denote the two squencing runs.

4.3 Discussion

Monoclonal human antibodies can modulate intracellular bacterial growth in THP-1 monocytes

THP-1 monocytes are a phagocytic cell line that is more convenient to culture and reproducible than primary monocyte-derived macrophages. THP-1 are susceptible to Mtb infection and strongly express Fcγ receptors and to a lesser extent, Fcα receptors thus are capable of antibody-dependent phagocytosis. Human serum samples from both TB patients and healthy South African donors significantly reduced intracellular bacterial growth in THP-1 compared to US-origin commercial pooled serum.

Monoclonal antibodies had mixed results. Anti-LAM mAb TB024PBh037 reproducibly enhanced intracellular bacterial load from 1 to 3 days post-infection. MAb 6037-P2E04 did not appear to inhibit infection at an early time point, but resulted in a reduced bacterial load at 3 days post-infection. On the other hand, another mAb, HD001HBMEMh095, which strongly labelled Mtb in ELISA and bacterial flow cytometry as shown in the previous chapter, had little effect and was similar to an irrelevant control antibody.

While THP-1 cells are not fully representative of authentic *in vivo* macrophages, they could be differentiated into adherent macrophages using phorbol myristate acetate (PMA). Analysing adherent cells by flow cytometry requires a labour-intensive step of enzymatic dissociation[37], but an alternative read-out using adherent cells that is still amenable to high- or semi-high-throughput assays could be measured by fluorometry using a plate reader similar to the "deconstructed granuloma" assay[371].

The effect of monoclonal antibodies on infection of primary macrophages is donor-dependent

A few mAbs derived from healthy donors inhibit the growth of Mtb in co-culture with monocyte-derived macrophages. However, there is also a macrophage donor-dependent interaction as some of the donors' macrophages were more permissive for Mtb growth in the presence of P2E04. The lower bacterial load in other macrophage donors appears to be due in part to inhibition of intracellular bacterial growth; the

image analysis tracking Mtb in single macrophages shows that the intracellular bacterial load is not merely due to differing efficiency of phagocytosis, but a significantly slower growth rates in the presence of P2E04. The mechanisms of inhibition may include increased phagosome-lysosome fusion, TRIM21 binding by Mtb-bound antibody, or direct inhibition of bacterial growth by antibody alone. As Fc receptor blockade could reverse the effects of P2E04, these effects appear to be at least partially Fc receptor-dependent.

The time-lapse macrophage experiments suffered from high variation in the effects of P2E04 seen in different experiments as it appeared to enhance or inhibit Mtb growth in some cases. However, this was determined to be due to the individual macrophage donors and not experimental error as, when macrophages from the same donors were tested in independent experiments, the effect was consistent within donors. This donor-to-donor variation in the effect of antibodies on Mtb infection of primary macrophages has been noted by other authors with polyclonal IgG, where pooled IgG from LTBI donors made macrophages from some donors restrictive of Mtb growth whereas others were more permissive[106]. Other work from our lab showed wide donor-to-donor variation in gene expression upon infection with Mtb[144]. The biological reasons behind different individuals' response to mAb P2E04 remain to be elucidated.

mAb P2E04 induces differential expression of genes involved in control of intracellular bacteria

A pilot transcriptomic experiment showed many differentially expressed genes in cells infected in the presence of mAb P2E04. These included cytokines and chemokines previously reported to be involved in the response to *Mycobacterium tuberculosis* infection such as CCL4/MIP-1β, IL-1β, and IL-23. Receptors and signal transduction proteins among the top 25 DE genes included TRAF1, TNFα-induced protein 6, and IFNγ receptor 2 (downregulated). SOD2 was downregulated in the presence of mAb P2E04; other authors have found that lowering SOD2 expression improves control of intracellular mycobacteria by increasing reactive oxygen species (ROS) and promoting phagosome-lysosome fusion[372,373].

Other upregulated genes included metallothioneins 1H, 1A, 1G, and 1X; these proteins bind heavy metals such as copper, zinc, and selenium and are thought to also have antioxidant functions. Infected macrophages have been shown to upregulate metallothioneins while releasing zinc into phagosomes, which inhibits intracellular bacterial growth[122]. Meanwhile, heme oxygenase 1 (HO-1) was downregulated. This enyzme, which degrades heme, is anti-inflammatory in macrophages, indirectly reduces ROS, increases the availability of iron[374] (which is a limiting factor for mycobacterial growth[375]), and suppresses apoptotic cell death. The presence of HO-1 has been shown to favour the survival of *M. abcessus*[376] and Mtb[377] in macrophages, therefore its downregulation in the presence of antibody could contribute to restriction of Mtb. Collaborators at KRISP advised that in future experiments, it would be preferable to increase the number of biological replicates (primary macrophage donors) and technical replicates (independent repeats/occasions) due to these being large sources of variation, and to reduce the number of experimental conditions (only 1 infection level instead of 3).

Chapter 5: Effects of HIV status and SARS-CoV-2 Variants of Concern on antibody responses in South African Covid-19 patients

5.1 Introduction

Early in the pandemic, several laboratories published methods for culture, titration, and antiviral assays for SARS-CoV-2[357,358,378]. The plaque assay is a classical method of quantifying infectious virus titre in viruses that infect adherent cells and can be adapted for any virus that lyses its host cells[286]; for non-lytic virus/host combinations, immunostaining can be used.

Neutralising antibodies are a correlate of protection against Covid-19[307]. These can be measured by live virus neutralisation or pseudovirus neutralisation assays. The latter are safer and more convenient to perform. However, the popular HIV-based pseudovirus systems are not suitable for testing large numbers of plasma/serum samples in a high-HIV-prevalence setting where many patients are on antiretroviral (ARV) medication, as an IgG purification step is required to remove interference by ARV[379].

As our lab did not have an established protocol for SARS-CoV-2 titration, I aimed to adapt published protocols in order to accurately quantify the infectious titre of our virus stocks and be able to perform robust and reproducible neutralisation assays on our patient cohort samples. I also modified and optimised a draft receptor-binding domain (RBD) ELISA protocol to improve its robustness and sensitivity. These assays enabled us to characterise anti-RBD and functional neutralising antibody responses in acute and convalescent plasma samples in a hospitalised patient cohort recruited from hospitals in the Durban area. We were interested in comparing antibody responses between patients with and without HIV in this high-HIV-prevalence population.

Furthermore, we observed that in the second epidemic wave dominated by the Beta variant of concern, there were more patients with detectable HIV viraemia as opposed to the first wave where the vast majority of PLWH were virologically suppressed on ART. While the reasons for this remain to be elucidated, this enabled us to further dissect the SARS-CoV-2 antibody response between virologically suppressed versus

viraemic PLWH. We also tested second wave samples for cross-neutralisation of the earlier wave D614G representative isolate as well as a Delta isolate to determine whether Beta infection could confer humoral immunity against variants that emerged later.

In addition to the in-house cohort study, I used the neutralisation assay in our collaborations with vaccine clinical trial investigators and a local biotechnology company to support the development of vaccines and immunotherapeutics on the African continent. Effective vaccines and antiviral drugs are critical to controlling the pandemic, especially vaccines, as non-pharmaceutical interventions can only slow but not stop the spread of the virus. Vaccine efficacy can differ across geographical regions for myriad reasons including nutrition, age structure, comorbidities, and genetic background, therefore it was critical to test the efficacy of candidate Covid-19 vaccines in sub-Saharan Africa[234,321]. Neutralisation assays on plasma from vaccine trial volunteers can provide important supporting information in addition to the main efficacy endpoints. I tested plasma samples from the AstraZeneca and Novavax (unpublished) South African clinical trials against D614G and Beta virus isolates to compare their cross-neutralistion potency.

Several monoclonal antibody products have been shown to reduce morbidity and mortality in Covid-19 patients[236], but given their high cost and lack of availability outside of high-income countries, the development of local immunotherapeutic products in low- and middle-income countries (LMICs) should be supported[380]. Camelid-derived nanobodies have been shown to have therapeutic activity against other pathogens, and have the potential to be delivered by oral or mucosal routes. I tested a panel of 13 nanobodies produced by a local biotechnology start-up to assist them in determining which candidates could be advanced to preclinical animal testing.

5.2 Results

5.2.1 Development of an ELISA for anti-SARS-CoV-2 receptor-binding domain antibodies

We initially received a draft RBD ELISA protocol from the Ragon Institute (Galit Alter, personal communication) as well as purified receptor-binding-domain (RBD) and human monoclonal antibody CR3022 which was used as a quantitative standard. CR3022 is a human monoclonal antibody (mAb) from a SARS survivor[381]; it neutralises SARS-CoV-1 but not SARS-CoV-2 but does cross-react strongly with the SARS-CoV-2 RBD, therefore it is a suitable positive control for ELISA but not neutralisation assays. When we tested this protocol on a small number of samples, we noted that the optical density (OD) signal was low overall which gave the assay a small quantitative range. We attributed this to the brief incubation times of 30 minutes (at room temperature for all steps except sample incubation at 37°C) probably resulting in sub-maximal binding.

The reagents and general procedure are described in the Methods chapter section 2.16. We performed a modified protocol with an extended coating incubation of overnight in the refrigerator, and extended the other incubation periods to 1 hour. Due to the building climate control in the AHRI labs experiencing day-to-day variation in the actual room temperature, we also performed the blocking and secondary antibody incubations in a 25°C incubator. This resulted in significantly increased raw OD signal, which in turn should improve the range of the assay. I designed a 2×2 experiment to compare the protocol versions as well as to determine the robustness of the assay when performed by different operators. We compared two different readouts reporting antibody titration data: Area under the curve (AUC) and endpoint titre (dilution at which signal drops below the negative controls). While AUC was significantly affected by the incubation time as expected, endpoint titres were not. There was no significant difference between operators, showing that assay performance was robust.

We therefore proceeded with the modified version with the extended incubations. Subsequently the assay results were expressed as nanograms per mL of RBD-binding IgG, IgM, or IgA, treating the monoclonal antibodies as standard curves although the samples were polyclonal.

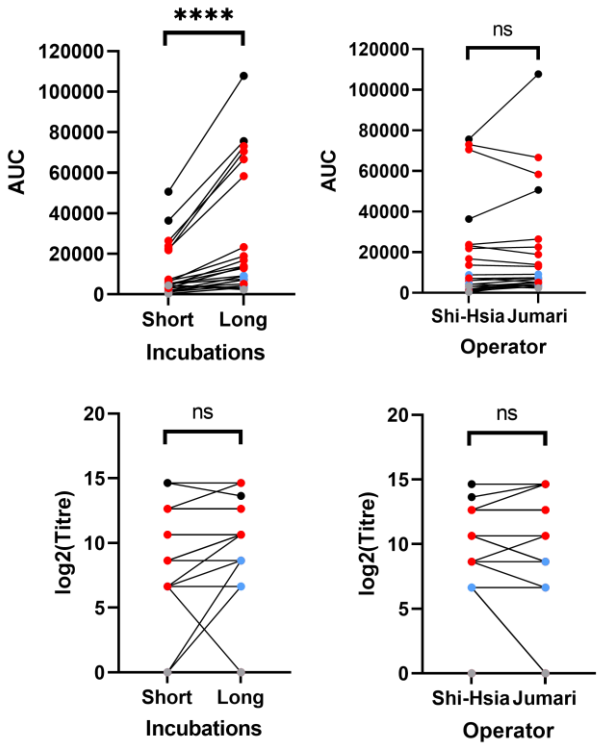

Figure 59: Signal intensity (AUC) but not endpoint titre is affected by ELISA incubation time. Points are colour-coded as follows: Black: monoclonal antibody CR3022; gray: pre-pandemic normal pooled human serum; light blue: pre-pandemic sera from the FRESH study (HPP); red: convalescent sera from Covid-19 patients 2-3 weeks post-symptom onset.

As we did not receive any anti-RBD IgM or IgA from the Ragon Institute, we used commercial monoclonal antibodies hIgM2001 and hIgA2001 (GenScript) as quantitative standards for these isotypes respectively. Pre-pandemic negative controls run on each plate included a commercial pooled normal human serum (Biowest) and three samples from the FRESH HIV study (HPP); these were used to determine a cutoff value for seroconversion (average plus three standard deviations of the pre-pandemic controls).

After titrating a number of patient plasma samples we determined that it was not necessary to do a full titration for each sample, so samples were tested for IgG and IgM at three dilutions of 1:100, 1:1000, and 1:10,000. Plasma samples were only diluted 1:100 and 1:1000 for IgA ELISA as the concentration was generally lower.

The usage of the assays in a clinical study of hospitalised and convalescent Covid-19 patients is further described below.

5.2.2 Development of an immunofocus asssay for quantifying infectious SARS-CoV-2 and neutralising antibodies

The immunofocus assay was originally based on a published protocol[357]. However due to global shipping logistics delays, reagents took a long time to arrive. While waiting I performed a few proof of concept experiments to determine if we could detect and quantify immunostained foci of SARS-CoV-2 in infected Vero E6 cells even with suboptimal reagents (non-low-melting agarose overlay (Lonza SeaKem LE) and DAB substrate). The agarose was difficult to keep in a temperature range that would not solidify but also not be hot enough to kill cells. DAB substrate gave light brown foci which were distinct to the naked eye but difficult to scan or photograph (Figure 60A). Two different primary antibodies, CR3022 (Ragon Institute) and HC2001 (GenScript) gave similar results (data not shown). Despite the suboptimal staining, this enabled me to calculate the infectious titre of some of our virus stocks.

Subsequently when the carboxymethylcellulose (gelling agent for overlay medium) and TrueBlue (precipitating TMB, substrate for horseradish peroxidase) arrived, the TrueBlue yielded much more intense staining (methods 2.19). This enabled cells to be fixed at an earlier timepoint with smaller plaque/focus sizes.

The method was downscaled to 96-well microtitre plates for routine usage for virus titration and antibody neutralisation assays as detailed in methods section 2.19. Note that CMC overlay in the large 6-well plates yieled comet-shaped foci after 2 days' incubation due to convection (Figure 60B), but was suitable for a shorter incubation time of $\leqslant 1$ day in 96-well plates with no comet formation (e.g. Figure 65 shows typical appearance).

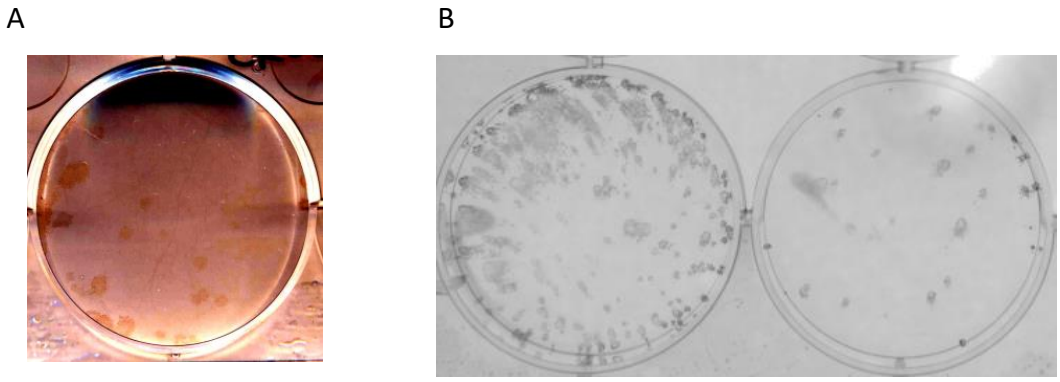

Figure 60: Immunostained SARS-CoV-2 foci in Vero E6 cells at 48 hours post-infection. A: Agarose overlay, DAB stained, imaged on flatbed scanner. B: Carboxymethylcellulose overlay, TrueBlue (TMB) stained, imaged on Bio-Rad ChemiDoc XP.

5.2.2.1 ACE2 expression and virus titration in a highly sensitive indicator cell line

My colleague Laurelle Jackson produced three cell lines that were highly sensitive to SARS-CoV-2 infection by transduction of the lung with a lentiviral vector for ACE2 overexpression[269]. I verified ACE2 expression in the C7 line by immunostaining (methods 2.18), which was far higher than in Vero E6 (Figure 61).

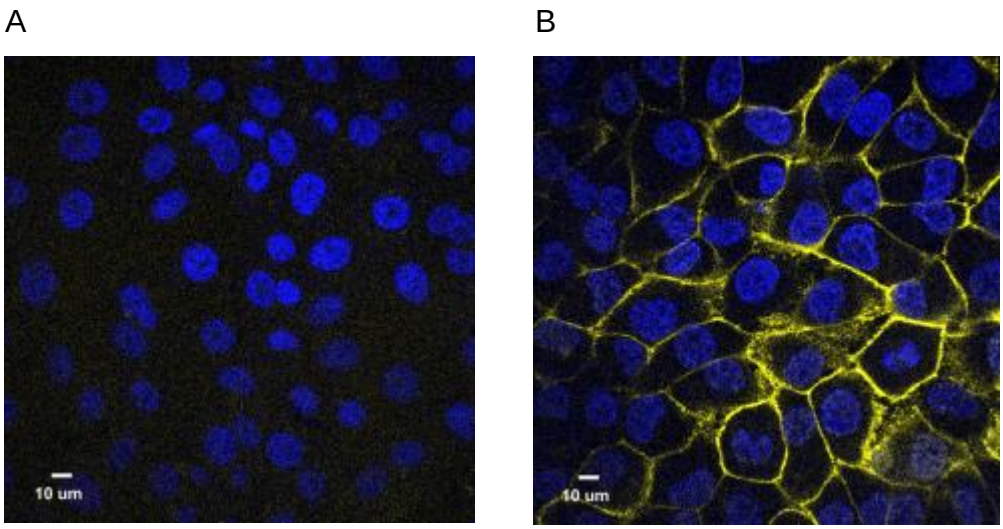

Figure 61: Confocal images of cells stained with anti-ACE2 (yellow) and DAPI (blue). A: Vero E6 and B: H1299-ACE2-C7 cells.

All three of these cell lines were many-fold more sensitive to infection than Vero E6 cells (Figure 62). In addition, plaque/focus morphology differed with Vero E6 cells

forming classical plaques by 48hpi, exhibiting cell lysis and little syncytium formation, whereas H1299-ACE2 formed syncytia early in infection and did not lyse until several days post-infection (Figure 63).

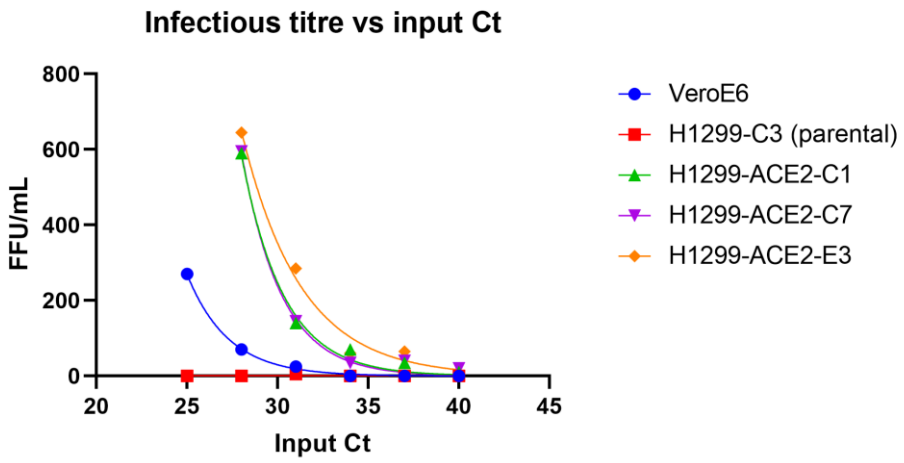

	VeroE6	H1299-C3 (parental)	H1299-ACE2-C1	H1299-ACE2-C7	H1299-ACE2-E3
Exponential growth equation		Interrupted			
Best-fit values					
Y0	16464422	2.156	108545093	219298603	3472984
k	-0.4408	-0.02926	-0.4331	-0.4578	-0.3066
Tau	-2.269	-34.17	-2.309	-2.184	-3.262
Doubling Time	-1.573	-23.69	-1.600	-1.514	-2.261

Figure 62: H1299-ACE2 cell lines are more permissive to SARS-CoV-2 infection than Vero E6 or parental H1299 cells. FFU: focus-forming units.

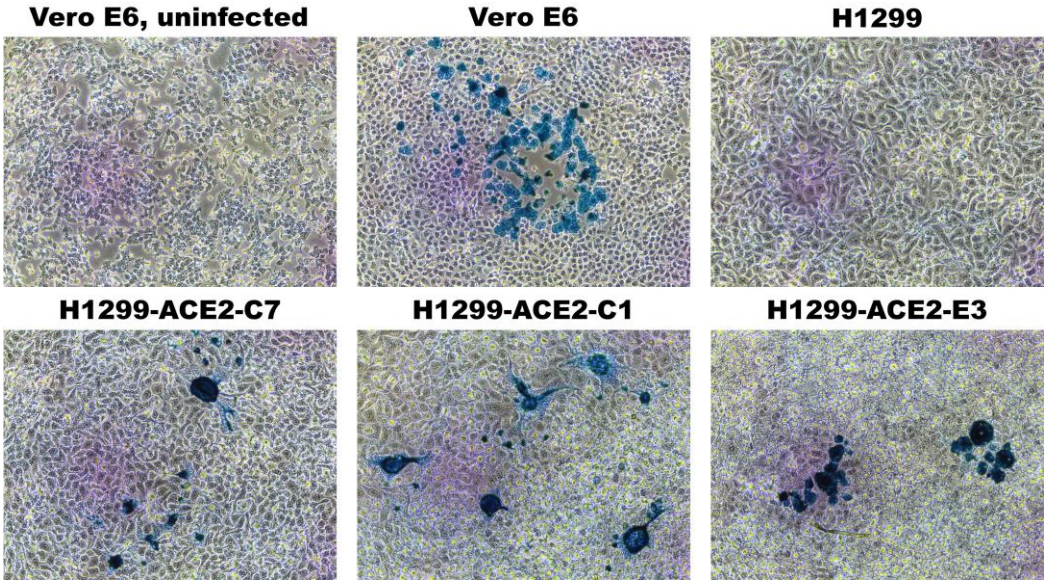

Figure 63: Morphology of infected foci differs between Vero E6 cells and H1299-ACE2 cell lines. Brightfield images of SARS-CoV-2 foci at 48h post-infection in Vero E6, H1299, and H1299-ACE2 clones stained with anti-S antibody and TrueBlue.

The greater sensitivity of H1299-ACE2 cells was seen with multiple virus stocks, but the fold difference varied between isolates and between stocks, suggesting that there would be a high and inconsistent particle-to-FFU (focus-forming unit) ratio in Vero E6 (Table 10). Due to the large differences in sensitivity between Vero E6 and H1299-ACE2, the input inocula for plasma neutralisation assays mentioned in the following sections are calculated based on virus stock titrations in the respective cell lines used for the neutralisation assays.

Table 10: Differences between titres in Vero E6 cells and H1299-ACE2-C7 cells for four independent virus stocks from two isolates.

Isolate	Stock date	Titre in VeroE6	Titre in H1299-ACE2	Fold difference
13-0013 (B.1.1.117, D614G)	25-Aug-20	1.25E+05	2.70E+06	21.60
	12-Sep-20	3.67E+05	5.33E+06	14.52
6518 (Beta variant)	15-Feb-21	5.23E+05	5.08E+06	9.71
6518-clone S3	06-May-21	5.23E+04	3.55E+05	6.79

The focus-forming assay in its final form in 96-well microtitre plates is described in detail in methods section 2.19. For downscaling the assay to 96-well plates, as we did not have an ELISPOT reader at the time, plates were scanned on a Nikon Ti-E confocal microscope using a low magnification 2x objective lens. Spots were counted automatically using a script in MATLAB (written by my supervisor Alex Sigal; described in methods 2.21). I also checked and manually corrected where necessary (e.g. subtracting spot counts caused by debris or adding uncounted spots near the periphery of wells).

Using CR3022 as the primary staining antibody required an anti-human horseradish peroxidase conjugated secondary antibody, therefore it resulted in high background in

neutralisation assays of human plasma samples (Laurelle Jackson, data not shown). I tested several rabbit and mouse anti-Spike mAbs from a commercial source (GenScript). Initially, we used mouse mAb 6D11F2. However, it was susceptible to run-to-run variation in staining intensity resulting in several failed batches of assays where the foci were not easily countable (data not shown). Upon testing several mAbs head-to-head, non-neutralising rabbit mAb BS-R2B12 was found to give strong staining and was used for all assays subsequently (Figure 64).

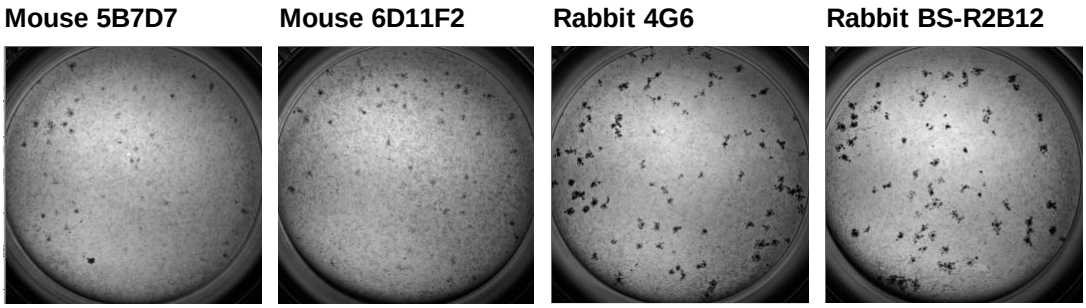

Figure 64: Infected H1299-ACE2-C7 cells stained with different anti-S primary antibodies.

The assay was originally optimised for our 13-0013 (PANGO lineage B.1.1.117) isolate, with fixation of the cells at 24 hours post-infection. However, when we obtained a Beta variant (B.1.351) isolate 6518, I found that the faster growth of the 6518 virus led to larger diameter foci regardless of host cell line, causing inaccuracies in counting foci due to under-counting of large overlapping foci (Figure 65). In addition, isolate 6518 at 24 hpi showed a mixture of large and small foci, which is discussed further below.

In a preliminary virus stock titration experiment prior to plasma neutralisation assays, we confirmed that the measured 13-0013 titre did not change between 18 to 24 hours post infection (hpi) but the measured 6518 titre was 16% lower at 24 hpi (1.06e5 FFU/mL vs 8.93e4 FFU/mL). Therefore, for 6518 samples I shortened the incubation time to 18 hpi for both viruses to minimise overlapping foci.

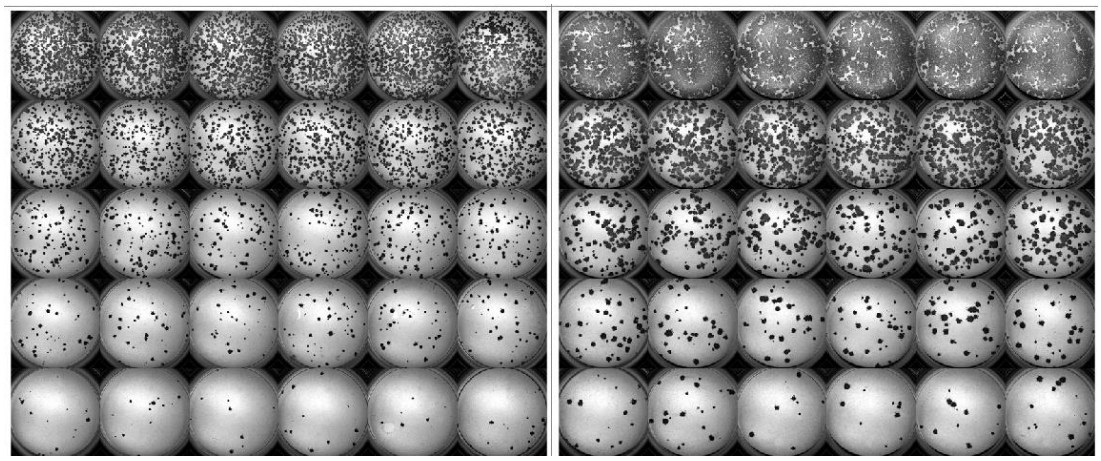

Figure 65: Vero E6 cells infected with isolate 6518 show heterogenous focus sizes. Left: 18 hpi, right: 24 hpi.

This 96-well immunofocus format also was useful for plasma antibody neutralisation assays. Due to the high frequency of people with HIV and taking antiretroviral (ARV) medication in our study, the HIV-based pseudovirus assay would have required purifying IgG from all samples, as ARV-containing plasma severely interfered with the assay (Laurelle Jackson, personal communication). While this approach has been employed by other authors[379], it would be very labour-intensive for large numbers of samples and the purification process could also introduce uncontrolled variation, making quantification of neutralising titres less accurate. We obtained genomic and helper plasmids for a VSV-based pseudovirus but I was not able to rescue the VSV (data not shown). Using live SARS-CoV-2 circumvented these issues.

Some studies using the live virus neutralisation assay are described in the following sections below. In neutralisation assays, rabbit mAb BS-R2B2 was used as a positive control as it had an 50% focus reduction neutralisation titre ($FRNT_{50}$) in the low nanogram/mL range (15.3 ± 2.2 ng/mL against first wave virus, lineage B.1.1.117), and a pre-pandemic serum sample from a TB-negative, HIV-negative donor (AHRI CUBS study) was used as a negative control.

5.2.3 Antibody responses in Covid-19 patients in the first epidemic wave with and without HIV are similar

We obtained patient and convalescent plasma samples from confirmed Covid-19 cases and household contacts in the "Consequences of HIV and TB Co-Infection on Covid-19 Disease Dynamics, Severity and Immune Responses" observational study. Anti-RBD IgG, IgM, and IgA ELISAs were performed as described in methods section 2.16 and neutralisation assays in section 2.19. The results from the first epidemic wave have been published in Clinical Infectious Diseases in a paper co-first-authored with Jumari Snyman[382].

We initially tested samples from the first epidemic wave (mid-2020) from 72 patients (42 HIV-negative, 30 people living with HIV (PLWH)) from weekly timepoints in the first month of study enrolment, and 43 samples at the 3-month follow-up. Median times to seroconversion (defined as significantly above pre-pandemic control cutoffs) were 13 days for IgM, 12 days for IgG, and 14 days for IgA. No significant differences were found between HIV-negative patients and PLWH (Figure 66).

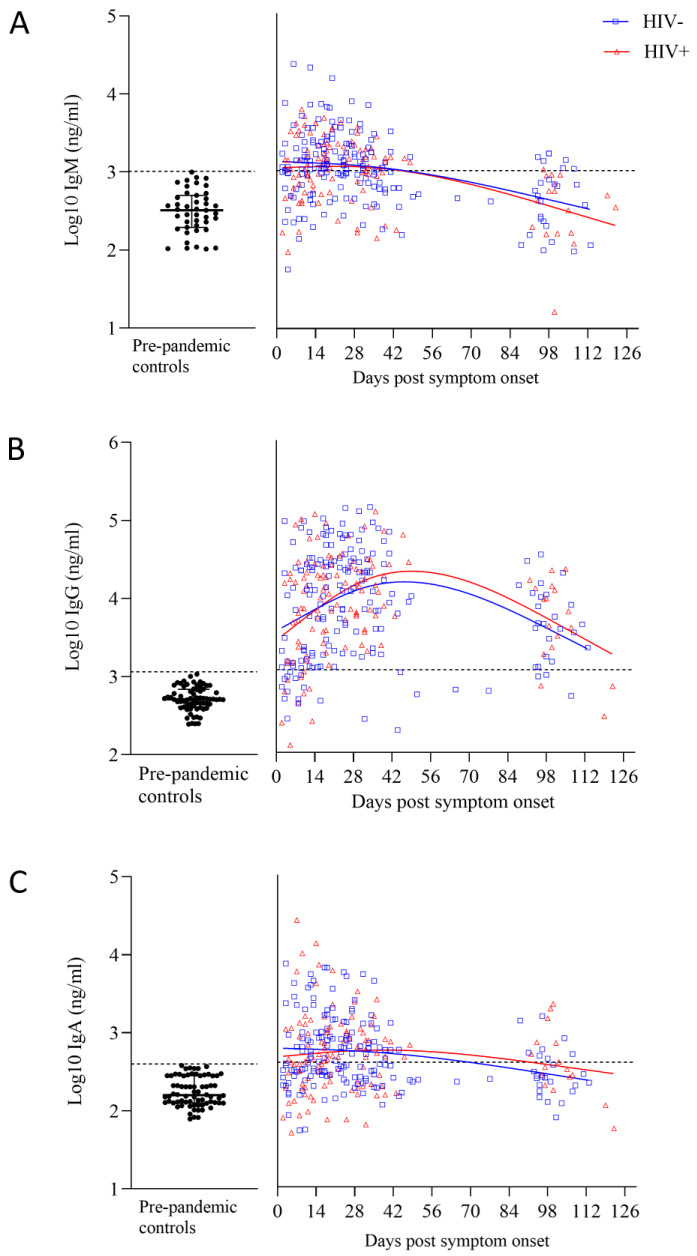

Figure 66: Similar anti-RBD antibody responses in HIV-negative and PLWH in the first wave. Anti-RBD ELISA results for A: IgM, B: IgG, C: IgA of plasma from patients infected during the first epidemic wave. Blue: HIV-negative patients; red: PLWH; black: pre-pandemic controls. Adapted from Snyman and Hwa 2021[382].

For virus neutralisation by first wave plasma samples, I tested a subset of patients (n = 53) who had 3-month follow-up samples available, as well as an earlier sample from approximately 30 days post-symptom onset (IQR 26-62 days). As I was concerned about a large amount of excess of non-infectious particles potentially interfering with neutralisation titre accuracy, I used H1299-ACE2 cells for their higher sensitivity

instead of Vero E6 cells. The virus stock used was an D614G isolate from patient 13-0013 (PANGO lineage B.1.1.117) that had been passaged twice for four days each in Vero E6 cells. I used an inoculum of 100 focus-forming units (FFU) per well.

There was no significant difference in neutralisation titres between HIV-negative and PLWH (Figure 67). IgG as well as IgA ELISAs correlated more strongly with neutralisation than did IgM, probably because IgM started decreasing earlier. [382]At the 3-month follow-up, we found that loss of IgA was correlated with a prior history of TB (p=0.0018).

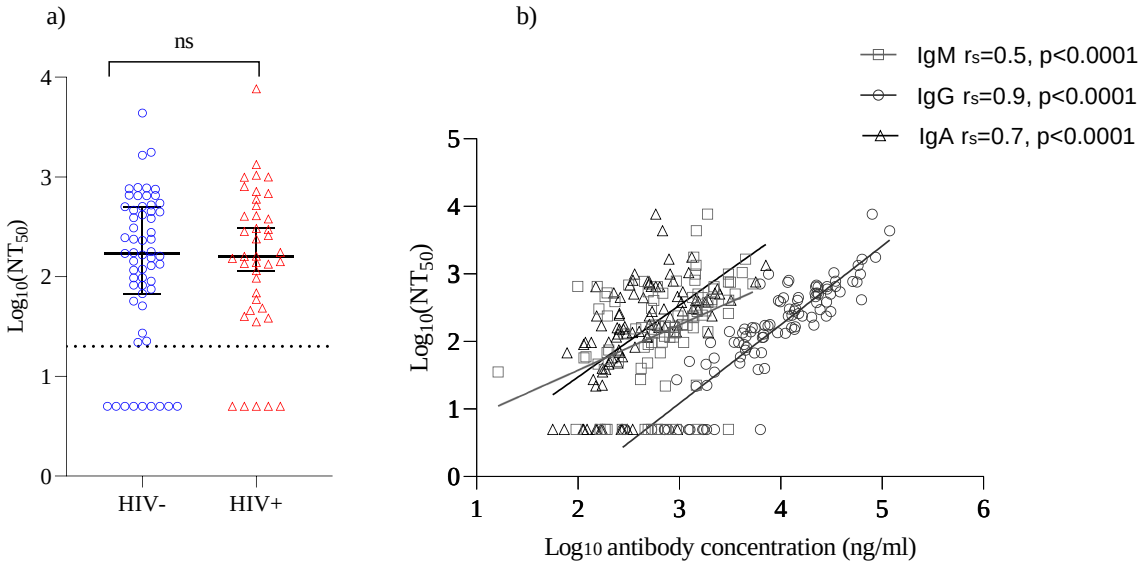

Figure 67: Live virus neutralisation titres are similar in HIV-negative and PLWH in the first wave. A:Neutralisation titres of 97 samples that had matched ELISA data. Dotted line shows the lowest tested dilution of 1:20. B: Correlation of neutralisation with different isotype RBD ELISAs.

5.2.4 Antibody responses in the second epidemic wave dominated by the Beta variant of concern are impaired in people with HIV viraemia

The second epidemic wave which occurred from December 2020 – January 2021 was dominated by the Beta variant of concern which contains several additional mutations in the S1 receptor-binding domain as described above. We obtained longitudinal samples from study visit 1 (enrolment) to visit 5 (~1 month) from 34 second wave Covid-19 patients (total of 16 HIV-, 7 PLWH suppressed on ART, and 11 PLWH who

had detectable viraemia during the study period). The reasons for the higher frequency of viraemia in the second wave are still being investigated[383].

Due to the shorter sampling period of available samples compared to the first wave, log-transformed antibody responses (Figure 68A,D,G,J). were fitted to straight lines (Figure 68B,E,H,K). There was a trend for viraemic PLWH to have lower maximum titres across all four measurements during the sampling period, however, these differences were not significant except for IgG (Figure 68F).

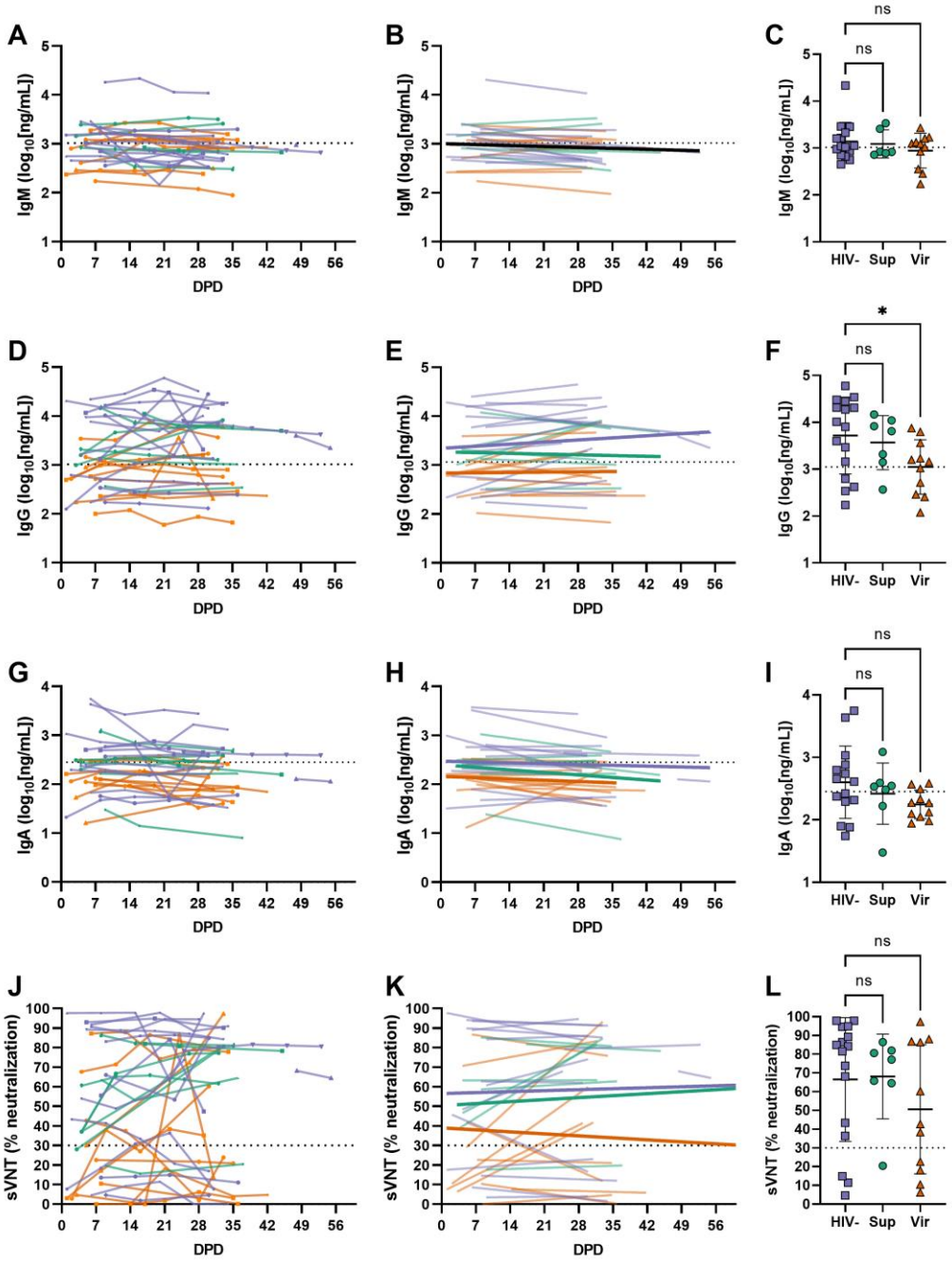

Figure 68: Viraemic PLWH in the second wave have significantly lower IgG responses. Purple: HIV-negative patients; green: suppressed PLWH; orange: viraemic PLWH. Dashed lines: cutoffs based on pre-pandemic controls or 30% recommended cutoff for sVNT. A,D,G,J: Antibody titres over the sampling period for IgM, IgG, IgA, and sVNT. B,E,H,K: straight line trends for individual patients. Bold lines show pooled trends per group. C,F,I,L: Maximum titres per patient during the sampling period. Bars show mean and standard deviation.

For the live virus neutralisation assay, one sample was tested at the closest available time point to ~1 month post-diagnosis per participant. Samples were tested for neutralisation against first wave isolate 13-0013 (B.1.1.117, containing the D614G mutation in S1), isolate 6518 (Beta)[233], and isolate 0134 (Delta). Due to the faster growth of isolate 6518 as described above, we reduced the incubation time to 18 hpi and the inoculum to 70 FFU per well for both viruses.

Due to the small number of participants with 1 month samples at the time this work was performed, the effects of SARS-CoV-2 variants and HIV viremia were analysed separately. Virologically suppressed PLWH and HIV-negative patients were grouped together for this analysis as the IgG ELISA and sVNT results shown above were similar. Against the wave-concordant Beta virus, HIV-negative participants and suppressed PLWH had a median titre of 1:169. The median titre against D614G was 1:74 (2.3-fold lower than Beta; not significant) and 1:44 against Delta (3.8-fold lower than Beta, $p < 0.001$; 1.7-fold lower than D614G, $p = 0.02$) (Figure 69A). There were no significant differences across variants for viraemic PLWH (Figure 69B).

Across all three variants, the median titres in viraemic PLWH were significantly lower than the suppressed + HIV-negative group: 11-fold for D614G ($p = 0.044$), 8.0-fold for Beta ($p = 0.031$), and 44-fold for Delta ($p = 0.049$) (Figure 69C-E). The proportion of viremic PLWH who seroconverted, defined as titres above 1:20, appeared to be lower for both D614G and Beta, and was significantly lower for Delta ($p = 0.05$) which the majority of viraemic PLWH could not neutralise (Figure 69F-H).

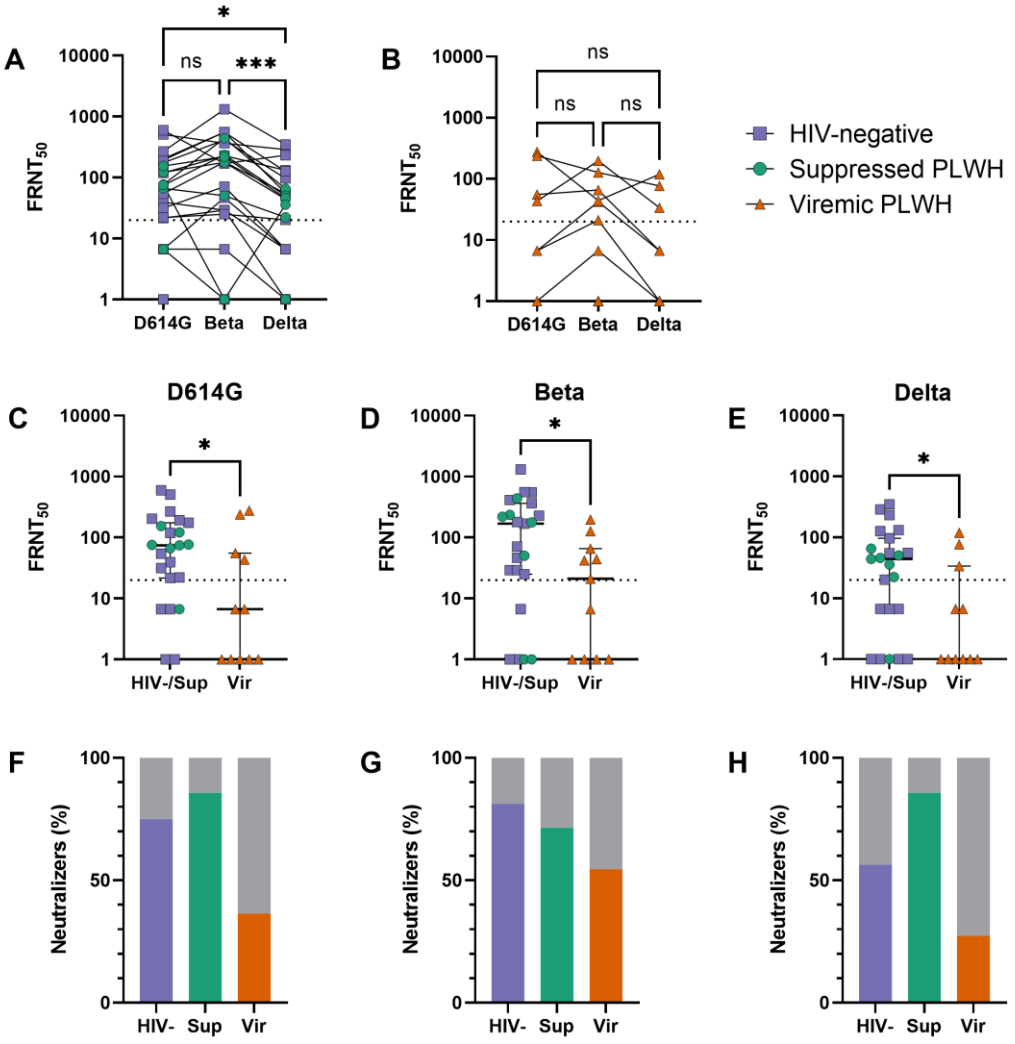

Figure 69: Live virus neutralisation titres at ~1 month post-infection are lower for discordant variants and are affected by HIV viraemia. Samples from individual patients are connected by lines. Dotted line indicates limit of quantification, lowest tested dilution of 1:20 or 1.301 $\log_{10}$. Purple: HIV-negative patients; green: suppressed PLWH; orange: viraemic PLWH. A: Variant cross-neutralisation in suppressed PLWH and HIV-negative participants. B: Cross-neutralisation in viraemic PLWH. C-E: Neutralisation in suppressed PLWH and HIV-negative patients compared to viraemic PLWH. F-H: Proportion of participants who seroconverted.

5.2.5 Suitability of a surrogate neutralisation rapid test kit in South African patient samples

We received several kits of a surrogate virus neutralisation test (sVNT; methods section 2.17) developed by Wang Lin-fa (Duke-National University of Singapore) and produced by GenScript, as they wished to determine the suitability of the test on plasma from South African patients who had been infected with Beta. The principle of

this rapid test is blocking of recombinant RBD-horseradish peroxidase conjugate from binding to hACE2-coated plates; the RBD used in the current version of the kit is based on the Wuhan-Hu-1 reference sequence. The readout is reported as percent inhibition relative to the OD of the negative controls. The manufacturer's recommended cutoff for positivity is 30%.

We tested all the first wave and second wave patient samples mentioned above using the sVNT and compared log-transformed live virus neutralisation assay (LVNA) titres to sVNT percent inhibition. Due to the way the sVNT results are calculated, the assay has a range of 0 to 100%, so I used a four-parameter logistic model with the bottom and top parameters constrained to this range.

For sVNT compared to neutralization of live D614G virus, goodness of fit was similar between the first ($R^2 = 0.90$) and second waves ($R^2 = 0.87$), but lower for neutralization of sVNT compared to the second wave Beta virus ($R^2 = 0.73$) (Figure 70). Differences between HIV-negative and PLWH samples were not significantly different in the first wave, but were for the second wave ($p = 0.038$ for D614G and $p = 0.017$ for Beta). Plasma from PLWH displayed a larger decrease in goodness of fit for both viruses. There were 4/79 (5.1%) false positive results in first wave samples, and 3/95 (3.2%) relative to D614G and 1/95 (1.1%) relative to Beta in second wave samples (false positives defined as $\geqslant$ 30% inhibition in sVNT and < 1:20 in LVNA). There were no false negatives in the first wave, 2/51 (3.9%) relative to D614G, and 5/51 (9.8%) relative to Beta in the second wave samples.

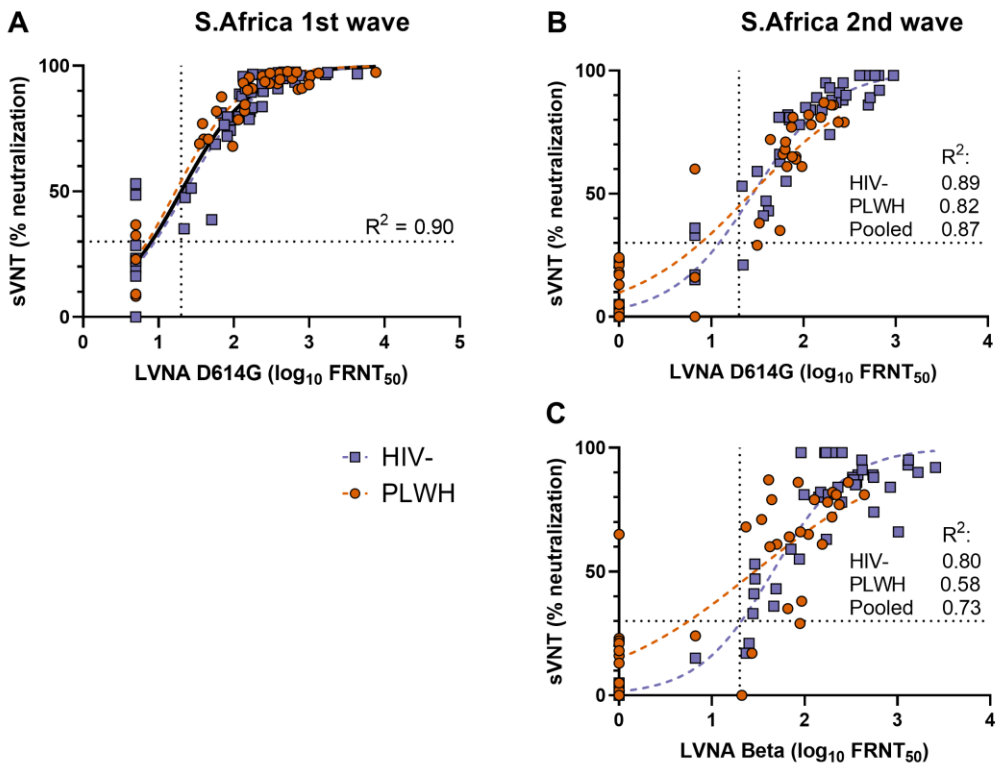

Figure 70: Surrogate virus neutralisation test (sVNT) correlates strongly with wave-concordant live virus neutralisation assay (LVNA) in South African patient samples. A: First epidemic wave samples tested against D614G virus. B: Second wave samples tested against D614G virus. C: Second wave samples tested against Beta virus. Black curve: sigmoidal four-parameter curve fitted to all samples; dashed curves: separate curve fits to HIV- and PLWH samples. Dotted lines: Positive/negative cutoff of 30% for sVNT as recommended by the manufacturer, and 1.301 = $\log_{10}(20)$ minimum tested dilution for LVNA.

5.2.6 Neutralisation potency of plasma from vaccine clinical trial participants is decreased against Beta VOC

We received a subset of participant plasma samples from the phase 1b-2 South African trial of AstraZeneca's AZD1222 recombinant adenovirus candidate vaccine. The dosing regimen in this trial was two doses of 5e10 particles each, at an interval of 21-35 days[316]. Plasma samples included vaccine recipients and placebo recipients who had become naturally infected during the first wave before Beta became the dominant circulating strain.

For these assays I used Vero E6 cells and an inoculum of 70 FFU per well to make it consistent with Public Health England's microneutralisation assay as done for the phase 1/2 trials[316]. I used the same B.1.1.117 and Beta stocks described above. I

reported the $FRNT_{50}$ for each sample against both viruses. Further data analysis was done by other authors as I was blinded as to sample identity. These live virus neutralisation results were published along with the clinical safety and efficacy results, as well as pseudovirus neutralisation results performed at the University of Cape Town[234]. Our results are shown in Figure 2C in the paper, reproduced below (Figure 71). Both groups showed several-fold decreases in neutralisation of Beta compared to B.1.1.117. In the vaccine group, there was one complete nonresponder, and 7 participants who neutralised B.1.1.117 but not Beta. In the placebo group, two participants did not neutralise Beta.

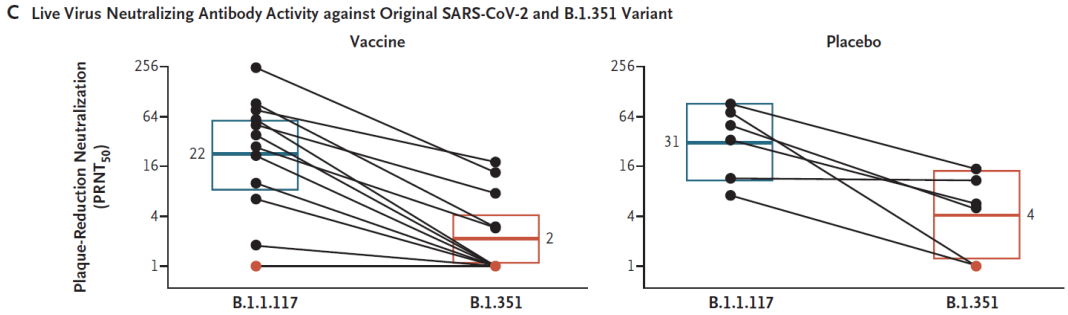

Figure 71: AZD1222 vaccinee and infected placebo recipient plasma neutralisation decreases against Beta virus. Left: vaccine recipients; right: placebo recipients who were infected. Orange points: below limit of quantification of 1:20 (1.3 $\log_{10}$). From Madhi et al.

5.2.7 Two camelid nanobodies retain high neutralising potency against Beta VOC

A South African start-up company, Afrobodies, had generated 13 camelid nanobodies with Spike-binding activity by immunising an alpaca with S protein. Some had been previously determined to have neutralising activity against a Scottish D614G isolate (CVR-GLA-1)[272]. I tested them against our 13-0013 (B.1.1.117/D614G) and 6518 (Beta) isolates and found that while 8 out of 13 had $FRNT_{50}$ lower than 100 ng/mL against B.1.1.117, only two (A1 and B2) remained potent against Beta with $FRNT_{50}$ of 20.7 ng/mL and 31.7 ng/mL respectively (Figure 72). These results have been published as a preprint and submitted to a peer-reviewed journal[384]. Preclinical animal trials for these nanobodies are being planned.

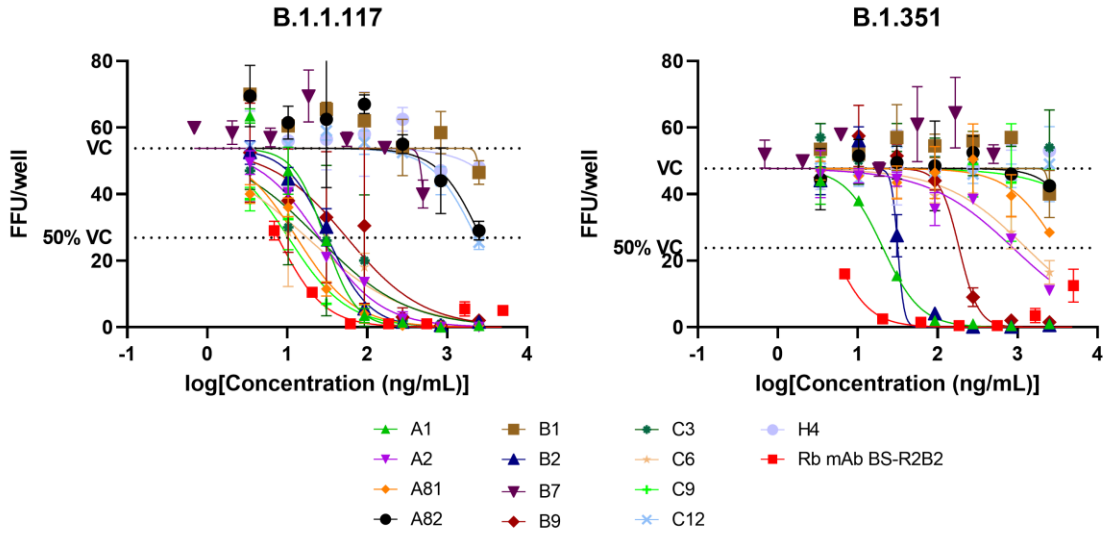

Figure 72: Two nanobodies retain high neutralisation potency against both D614G (left) and Beta (right).

5.2.8 Control of furin cleavage site mutations and plaque cloning a wild-type isolate

We were notified by collaborators who received aliquots of our isolate 6518 (Beta) that it contained a minority population with mutations in the polybasic furin cleavage site (FCS), which prevent cleavage by TMPRSS2. As discussed in the introduction chapter (section 1.19), this mutation emerges rapidly upon passage of SARS-CoV-2 in Vero E6 cells as they lack TMPRSS2, and these mutants are attenuated in TMPRSS2-expressing cell lines and *in vivo* hamsters and ferrets (reviewed by Hale[280]). In Vero E6, wild-type viruses have a small plaque phenotype and FCS mutant viruses have a large plaque phenotype[281] whereas the converse is seen in transduced Vero-TMPRSS2[284].

Upon checking minority variant results of deep sequencing, it was found that our main lab stock of the 6518 isolate contained 40% mutant (grown for 8 days in Vero E6) and my stock used for the neutralisation assays above contained 25% mutant (grown for 4 days in Vero E6). This explains the heterogenous focus sizes of these stocks (e.g. Figure 65) compared to the two isolate 13-0013 (lineage B.1.1.117) stocks, which fortunately had no FCS mutations.

To obtain a stock of the 6518 isolate with wild-type FCS, I performed a plaque assay using low-melting point agarose overlay (SeaPlaque, Lonza) and Neutral Red live cell stain[358] and picked plaques as detailed in methods section 2.20. At 3 days post-infection, plaques were distinctly visible to the naked eye using backlighting from a handheld torch, but could not be photographed well using a mobile phone sealed in a thick plastic bag (we do not have a transilluminator in our BSL-3 laboratory). A representative plaque consisting of mostly clear dead cells surrounded by live cells with dark red cytoplasmic staining is shown in Figure 73B. While the 13-0013 virus stock had plaques of approximately equal size, the 6518 stock produced large and small plaques (data not shown due to difficulty in obtaining clear photographs).

An attempt to perform a similar plaque purification in H1299-ACE2 cells failed as the infected H1299-ACE2 tend to form large syncytia, but do not lyse until many days post-infection when uninfected cells are also dying from medium depletion, making it impossible to distinguish plaques (data not shown).

A B

Figure 73: SARS-CoV-2 infected Vero E6 cells stained with Neutral Red. A: Plaques are faintly visible as clear areas against an orange background of live cells. B: Single plaque photographed on 10x objective.

In the first passage in H1299-ACE2 cells, wells infected with small plaque picks showed cytopathic effect (CPE) with syncytia formation and lysis by 5 days post-infection, whereas the large plaque picks only showed syncytia at 6 dpi, at which time all wells were harvested. Small plaque cultures were scaled up by an additional passage

in H1299-ACE2 followed by a short passage of 2 days in Vero E6 as detailed in methods section 2.20 .

Spike mutations found in the consensus sequences of the passage 1 cultures and the small plaque 3 passage 3 stock are shown in Table 11; minority variant analysis was also performed to check if any mutants arose in the small plaque cultures. All three of the large plaque picks contained the Q677H (flanking) and R682W FCS mutations, but the small plaque picks contained the wild-type FCS.

However, cultures of small plaque 1 and small plaque 2 were probably not clonal as they had large minority variants at other S sites and in other genes (data not shown). Small plaque 3 appeared to be clonal. These differences continued in the scaled-up passage 3 culture. Therefore the small plaque 3 P3 harvest was aliquoted and stored for use in future neutralisation assays. It had one additional mutation in the S gene at S704L; this residue is downstream from the FCS, in the S1-S2 linker region and has been reported in sequences from other geographical locations[385]. I could not find any information as to whether this mutation affects the *in vitro* or clinical phenotypes.

Table 11: Spike mutations (consensus sequence) and infectious titres of plaque picks from isolate 6518.

Culture, passage	Coverage (%)	Amino acid substitutions in Spike (relative to Wuhan-Hu-1 reference)	Q677H, R682W mutant frequencies	Titre in H1299-ACE2 (FFU/mL)
Large plaque 1, P1	98.9	S:L18F,S:D80A,S:D215G,S:L242H,S:K417N,S:E484K,S:N501Y,S:D614G,S:Q677H,S:R682W,S:A701V	0.995, 0.988	3.2e3
Large plaque 2, P1	98.0	S:L18F,S:D80A,S:D215G,S:L242H,S:K417N,S:E484K,S:N501Y,S:D614G,S:Q677H,S:R682W,S:A701V	0.998, 1.0	7.6e3
Large plaque 3, P1	99.2	S:L18F,S:D80A,S:D215G,S:L242H,S:K417N,S:E484K,S:N501Y,S:D614G,S:Q677H,S:R682W,S:A701V	0.974, 0.974	1.2e4
Small plaque 1, P1	97.2	S:L18F,S:D80A,S:D215G,S:L242H,S:K417N,S:E484K,S:N501Y,S:D614G,S:A701V	none	7.3e3
Small plaque 2, P1	98.6	S:L18F,S:D80A,S:D215G,S:L242H,S:K417N,S:E484K,S:N501Y,S:D614G,S:A701V	none	8.7e3

Culture, passage	Coverage (%)	Amino acid substitutions in Spike (relative to Wuhan-Hu-1 reference)	Q677H, R682W mutant frequencies	Titre in H1299-ACE2 (FFU/mL)
Small plaque 3, P1	99.3	S:L18F,S:D80A,S:D215G,S:L242H,S:K417N,S:E484K,S:N501Y,S:D614G,S:A701V,S:S704L	none	1.0e4
Small plaque 3, P3 stock	98.7	S:L18F,S:D80A,S:D215G,S:L242H,S:K417N,S:E484K,S:N501Y,S:D614G,S:A701V,S:S704L	none	3.e55e5

5.3 Discussion

I established an immunofocus titration assay for SARS-CoV-2 in a 96-well plate format that enabled us to quantify infectious virus in our laboratory stocks, perform antibody neutralisation assays, and investigate various other parameters of virus biology. This assay can be used in multiple cell lines, including the commonly used Vero E6 and a highly sensitive human lung cancer line overexpressing ACE2. I was also able to plaque-purify and amplify a subclone of the Beta isolate 6518 free of the furin cleavage site mutation affecting a large proportion of our original lab stock.

H1299-ACE2 are a sensitive indicator cell line suitable for virus titration assays

Titration of various stocks showed a large difference in sensitivity between the commonly used Vero E6 cell line, which has low ACE2 and no TMPRSS2, and the H1299-ACE2 cell lines constructed by my colleague. Even though we did not directly count particles in our virus stocks by electron microscopy, this implies that if the particle-forming unit (PFU) or focus-forming unit (FFU) per mL titre is measured in Vero cells, there is actually a many-fold excess of non-infectious particles as found by electron microscopy studies[285]. A high particle-to-PFU ratio can affect apparent neutralisation titres, as the excess of non-infectious particles will still adsorb antibodies.

We have not yet determined whether the parental H1299 cell line or H1299-ACE2 express the transmembrane serine protease TMPRSS2 as the antibody was received later; this experiment is pending. TMPRSS2 is an important cofactor for SARS-CoV-2 infection and is required for entry at the plasma membrane. In TMPRSS2-negative cell lines such as Vero, the virus is endocytosed, the full length Spike protein is cleaved by cathepsin L freeing the S2 fusion peptide, and fusion occurs at the endosomal membrane[283]. While Calu-3 cells have been recommended by other authors as a TMPRSS2+ virus-sensitive, high-titre producing cell line[262,280], we were only able to obtain it recently due to import restrictions in South Africa. We also found that this cell line grows slowly and has a clumpy phenotype (Laurelle Jackson, personal communication and ATCC information sheet[386]). Therefore, while the H1299-ACE2 cells are poor producers of virus, they are still useful as a sensitive indicator cell line

for titration assays as they grow robustly with a doubling time of approximately 1 day, and form flat monolayers.

Antibody responses to SARS-CoV-2 infection are severely decreased in patients with HIV viraemia

In plasma samples from Covid-19 patients hospitalised during the first epidemic wave from June-November 2020, there was no difference in IgM, IgG, IgA, or neutralising antibody responses between HIV- patients and PLWH. However, there were only 5 viraemic PLWH in this group. In first wave patients, stronger IgM antibody responses correlated with higher disease severity. Other studies have also found a positive correlation between higher disease severity with IgG and neutralising antibody responses[387–389]. This is thought to be due to the higher viral antigen load in severe disease.

The ELISA and neutralisation results for the second wave patients contrast with the first wave, where no significant differences in antibody responses were found across between PLWH, versus HIV- participants. Class-switched and surrogate neutralisation antibody responses were lower in viraemic PLWH and took longer to increase, as did neutralisation titres. In contrast, virologically suppressed PLWH had IgG and surrogate neutralising antibodies that were similar to HIV-negative patients.

During the second wave sample collection period, 501Y.V2/Beta was the predominant variant in South Africa. Live virus neutralisation titres were evaluated at ~1 month post-diagnosis. The slight decrease (not significant) in neutralisation of D614G virus by HIV-negative and suppressed PLWH plasma in this study is consistent with the few-fold decrease we previously observed with 6 samples (2 PLWH)[233], as well as a larger number of patient samples in a Cape Town study[390]. That is, plasma samples from second wave patients are still capable of neutralising an earlier variant. There was a greater decrease in neutralisation of the Delta and 4/16 more HIV-negative samples dropped below the limit of quantification.

For all three virus isolates, the viraemic group had significantly lower titres than the suppressed + HIV-negative groups. This is consistent with findings that HIV viraemia,

but not virologically suppressed HIV infection, is associated with heavily impaired antibody responses following vaccination[345]. While live virus neutralisation assays are resource-intensive which limited our ability to test all samples, we were able to use a rapid surrogate virus neutralisation test on all samples, which gave similar results to the RBD IgG ELISA (sVNT discussed further below).

In patient samples from the second epidemic wave, there was a surprising finding of relatively high RBD IgG and neutralising responses very early after diagnosis, in HIV-negative participants and suppressed PLWH. Possible reasons might include a) a long asymptomatic period, b) delay in diagnosis, c) a prior infection with SARS-CoV-2, as there was a very high seroprevalence in KwaZulu-Natal estimated at 52% as of January 2021[391] d) partial cross-neutralisation due to the high prevalence of seasonal human coronaviruses in South Africa[199,200,392]. These include OC43 which, out of the 4 known seasonal hCoVs, is the most closely related to the sarbecoviruses. Recent work suggests that OC43 exposure may partially cross-prime SARS-CoV-2 responses and provide partial protection against severe Covid-19[393].

A rapid test kit correlates well with live virus neutralisation in both D614G and Beta patient plasma and is unaffected by HIV status

A surrogate virus neutralisation test which measures blocking of the S RBD-hACE2 interaction correlated well with live virus neutralisation assays on these patient/convalescent plasma samples including from PLWH. LVNAs require a biosafety level 3 laboratory and are expensive and time-consuming; while pseudovirus assays are safer, they still require tissue culture facilities and specialized equipment to detect the reporter gene (luminometer or fluorescence reader). Other sVNT assays require specialised instruments[292]. This sVNT assay provides a robust measurement of functional neutralising antibodies that is safer, much faster (~ 1 hour), and has the basic equipment requirements of a typical ELISA, which could make it practical for use in low-resource settings and screening.

Despite the RBD in the sVNT kit being derived from the Wuhan-1 reference sequence, it correlated well with neutralisation of the Beta virus by second wave patients' plasma samples, although there was a decrease in the coefficient of determination compared

to first wave samples. Of note, the decrease in R^2 was worse for PLWH plasma samples than HIV-negative samples. Further development of VOC-specific reagents for the sVNT is under way[291]. In conclusion, the sVNT rapid test could be used in settings with a high prevalence of HIV and SARS-CoV-2 RBD variants, but it may be necessary to set a higher cutoff value if using the original version with reference RBD.

Beta VOC partially escapes neutralisation by plasma elicited by vaccines

Plasma from clinical trial participants immunised with the AZD1222 recombinant adenovirus vaccine exhibited a decrease in geometric mean titre of ~11-fold against Beta versus D614G. The pseudovirus assay used by other collaborators in this study showed a decrease in geometric mean titre from 297 to 74, about 4-fold. There was also a ~8-fold decrease in plasma of placebo recipients who had become infected during the first wave, which is similar to the results we found previously in the AHRI study of first wave patients with individual decreases of 3.2 to 41.9-fold against Beta virus[233].

For samples from the South African trial of the NVX-CoV2373 protein nanoparticle vaccine, the results are not shown here as they are still pending publication and permission from the sponsor. There was a several-fold decrease in mean NT_{50} against Beta compared to D614G. Efficacy results from the South African clinical trial conducted during the second wave were lower than at other sites which were not affected by Beta[320,321].

Camelid nanobodies can neutralise multiple variants and have therapeutic potential

The development of resistance to monoclonal antibody therapy by VOCs with mutations in the receptor-binding domain is a known issue. For example, bamlanivimab and casirivimab are no longer recommended for use due to decreased potency against circulating VOC[235]. Therefore, companies developing mAb therapeutics should proactively screen lead mAbs against new variants. In a panel of 13 camelid nanobodies, out of which 8 had strong neutralising activity against

B.1.1.117, only 2 retained potency against Beta. This suggests that the other 6 were directed against epitopes affected by the K417N, E484K, and N501Y mutations in Beta. The two nanobodies with high cross-neutralisation are being further developed by the manufacturer.

Conclusions

Discovery of monoclonal antibodies against pathogens and other targets can be accomplished in either a “forward” or “reverse” manner: having a known target antigen of interest and using it to pull down specific antibodies, or looking for functional antibodies and then identifying their targets. We chose the latter approach with the potential to discover new antigenic targets that would contribute to the control of bacteria in macrophages, a critical class of cells in the progression of TB disease. In addition, we attempted to isolate Mtb-specific B cells from lung lymph nodes near the site of active disease.

I was partially successful in that I isolated seven monoclonal antibodies against Mtb surface antigens, but was not able to identify their targets. They clearly bound whole bacilli of seven different strains of Mtb as well as cell lysate and cell wall fractions, but none appeared to be specific for three well-known protein antigens (alpha-crystallin, ESAT-6, or HBHA) or a lipoglycan antigen (lipoarabinomannan). I was unsuccessful in immunoprecipitating the 62 kDa antigen of mAb P2E04, as was a collaborator who used a protocol optimised for immunoprecipitation with polyclonal serum IgG. One method that can screen antibodies against the entire proteome of an organism is high-density protein microarrays. We are currently awaiting the M-NAPPA (multiplex nucleic acid-programmable protein array) results for P2E04 from another collaborator.

Two of the mAbs in this study, one IgG and one IgA, were cloned from a lung lymph node of a pulmonary TB patient, which as far as we know are the first TB antibodies isolated from this type of tissue sample. Further isolation of antibodies was hampered by low viability and yield of antibody-secreting cells following sorting, despite detection of many Mtb-binding B cells at the initial FACS step. In future, further improvements in throughput and yield of mAb cloning from lymph node samples could illuminate what antigens these are targeting, and whether B cells and antibodies close to the site of infection and exposed to a heavy antigen load (as opposed to peripheral blood) are having a protective or pathological effect on disease progression.

To study the effects of serum and monoclonal antibodies on phagocytes infected with Mtb, I used two methods: semi-high-throughput, low-content (two colours) flow cytometry of THP-1 cell line monocytes, and timelapse microscopy of *ex vivo* differentiated primary monocyte-derived macrophages. I optimised conditions for THP-1 infection including stimulation with low-dose IFNγ. Using this system I showed that mAb P2E04 decreases intracellular bacterial load in a dose-dependent manner, and conversely, another mAb derived from a TB patient exacerbated intracellular bacterial growth.

Results from the macrophage timelapse experiments were somewhat more difficult to interpret. While timelapse microscope of live cells can provide high-content data to understand host-pathogen interactions, it is also a delicate system subject to high variation from both technical and biological factors. We ultimately decided not to procceed further with the single-cell tracking method as the intracellular fluorescent Mtb signal was affected too much by random vertical (Z axis) movements of the macrophages in our confocal microscopy set-up which has a very thin depth of field.

In addition, I found that the effects of the P2E04 monoclonal antibody were consistent across multiple experiments using macrophages from the same donor, but inconsistent between donors (either inhibiting or enhancing bacterial load). This high variability in responses to Mtb infection between individuals was also observed by previous authors using polyclonal serum[106] and is borne out in transcriptomic data on infected macrophages generated by my colleague[144]. We had previously tried to eliminate this donor-to-donor variation by obtaining Leukopaks from the South African National Blood Service in order to isolate CD14+ monocytes in bulk and aliquot them so the same donor could be used for many experiments, but cryopreservation was detrimental to the monocytes and they did not differentiate into good-quality macrophages (data not shown). One possible future solution would be to use macrophages differentiated from induced pluripotent stem cells (iPSC), which can be manipulated to simulate tissue-resident macrophages such as alveolar macrophages[394].

Other authors have observed that isotype can be a determinant of antibody-dependent enhancement of Mtb infection in a lung-derived epithelial cell line and THP-1 monocytes[176]. Further research into other determinants of Mtb ADE to identify other

factors in the antigen, Fc, and host cell aspects may be warranted to reduce the risk of ADE in the development of vaccines and antibody-based drugs.

Although SARS-CoV-2 is a much newer human pathogen, the relatively simple genome and structure of the virus compared to Mtb means that it presents one clear target for the humoral immune response: the Spike protein.

We previously described clinical characteristics of Covid-19 and frequencies of antibody-secreting cells in patients infected during the first epidemic wave[395]. Among first wave patients among whom the vast majority of PLWH were virologically suppressed on ART and showed no difference in antibody parameters from HIV-negative Covid-19 patients. In contrast, a much larger proportion of PLWH in the second wave had detectable viral loads and low CD4 counts[383]. Although the number of patients analysed to date was small, viraemic patients clearly had lower IgG and neutralising antibody titres, which were slower to increase than the virologically suppressed PLWH and HIV-negative patients. This is cause for concern as a large number of people with HIV in South Africa have uncontrolled viraemia. As of 2020, there were an estimated 7.8 million PLWH in South Africa, but only 5.6 million were on ART and 5.1 million had suppressed viral loads[396].

Immunosuppressed individuals can be persistently infected with SARS-CoV-2 even in the face of antibody therapy, which creates selection pressure for immunological escape mutations[242,245]. My results and others suggest that the failure to clear infection could be partly due to an impaired humoral response. This was also seen in the case of mRNA vaccination where a viraemic individual had no neutralising antibodies, compared to virologically suppressed PLWH whose titres were similar to HIV-vaccinees[345,379]. Thus, failure of healthcare systems to provide effective ARV therapy to all PLWH not only endangers these individuals but creates a community risk of more variants of concern arising. ART service delivery should be improved even in the face of lockdown by offering PLWH creative and flexible solutions for obtaining their medication[397,398].

Immune evasion by variants of concern is a factor driving continued circulation of the virus even in regions that had high seroprevalence from previous epidemic waves[237,391], and may also result in breakthrough infections in regions where less-immunogenic

vaccines were used. It is important to understand to what degree infection or immunisation elicits neutralising antibodies against heterologous variants. Although the number of second wave patients tested was small, viraemic PLWH appeared to have less variant-specific neutralising antibodies, as there was no significant difference in neutralisation of the three variants in viraemic participants. The larger proportion of viraemic participants for whom neutralisation of Delta dropped below threshold is of concern with regard to the potential for re-infection. Potential future work to understand these differences could include monoclonal antibody isolation from PBMCs of patients with and without variant-specific antibodies, or testing plasma samples by ELISA or surrogate neutralisation assays against a panel of Spike proteins with mutations in different epitopes.

References

1. WHO. Tuberculosis Fact Sheet. *WHO* http://www.who.int/mediacentre/factsheets/fs104/en/ (2018).
2. Kaufmann, S. H. E. *et al.* TBVAC2020: Advancing Tuberculosis Vaccines from Discovery to Clinical Development. *Frontiers in Immunology* **8**, 1203 (2017).
3. World Health Organization. *Global Tuberculosis Report 2020*. https://www.who.int/teams/global-tuberculosis-programme/data.
4. Esmail, H. *et al.* The Immune Response to Mycobacterium tuberculosis in HIV-1-Coinfected Persons. *Annu. Rev. Immunol.* **36**, 603–638 (2018).
5. World Health Organization. Tuberculosis (TB) Fact Sheet. https://www.who.int/news-room/fact-sheets/detail/tuberculosis.
6. Kobedi, P. TB Frequently Asked Questions. *NICD* https://www.nicd.ac.za/tb-frequently-asked-questions/ (2021).
7. Debi, U., Ravisankar, V., Prasad, K. K., Sinha, S. K. & Sharma, A. K. Abdominal tuberculosis of the gastrointestinal tract: Revisited. *World J Gastroenterol* **20**, 14831–14840 (2014).
8. Department of Health South Africa. *Guidelines for The Management of Tuberculosis in Children : 2013*. 57 (2013).
9. King's evil | medical disorder. *Encyclopedia Britannica* https://www.britannica.com/science/kings-evil.
10. Koch, R. The etiology of tuberculosis. *Berliner Klinischen Wochenschrift* **15**, 7 (1882).
11. Asante-Poku, A. *et al.* Mycobacterium africanum Is Associated with Patient Ethnicity in Ghana. *PLoS Neglected Tropical Diseases* **9**, e3370 (2015).

12. de Jong, B. C., Antonio, M. & Gagneux, S. Mycobacterium africanum—Review of an Important Cause of Human Tuberculosis in West Africa. *PLoS Negl Trop Dis* **4**, e744 (2010).

13. Bernitz, N. *et al*. Review of Diagnostic Tests for Detection of Mycobacterium bovis Infection in South African Wildlife. *Front. Vet. Sci*. **8**, (2021).

14. van Soolingen, D. *et al*. Diagnosis of Mycobacterium microti Infections among Humans by Using Novel Genetic Markers. *J Clin Microbiol* **36**, 1840–1845 (1998).

15. Emmanuel, F. X. *et al*. Human and Animal Infections with Mycobacterium microti, Scotland. *Emerg Infect Dis* **13**, 1924–1927 (2007).

16. Sreevatsan, S. *et al*. Restricted structural gene polymorphism in the Mycobacterium tuberculosis complex indicates evolutionarily recent global dissemination. *Proc Natl Acad Sci U S A* **94**, 9869–9874 (1997).

17. Gagneux, S. *Ecology and evolution of Mycobacterium tuberculosis*. *Nature Reviews Microbiology* vol. 16 202–213 (2018).

18. Brosch, R. *et al*. A new evolutionary scenario for the Mycobacterium tuberculosis complex. *Proc Natl Acad Sci U S A* **99**, 3684–3689 (2002).

19. Cole, S. T. *et al*. Deciphering the biology of Mycobacterium tuberculosis from the complete genome sequence. *Nature* **393**, 537–544 (1998).

20. Calmette, A. Preventive Vaccination Against Tuberculosis with BCG. *Proceedings of the Royal Society of Medicine* **24**, 1481–90 (1931).

21. Mahairas, G. G., Sabo, P. J., Hickey, M. J., Singh, D. C. & Stover, C. K. Molecular analysis of genetic differences between Mycobacterium bovis BCG and virulent M. bovis. *J Bacteriol* **178**, 1274–1282 (1996).

22. Gordon, S. V. *et al.* Identification of variable regions in the genomes of tubercle bacilli using bacterial artificial chromosome arrays. *Molecular Microbiology* **32**, 643–655 (1999).

23. Behr, M. A. *et al.* Comparative genomics of BCG vaccines by whole-genome DNA microarray. *Science* **284**, 1520–1523 (1999).

24. Volkman, H. E. *et al.* Tuberculous Granuloma Formation Is Enhanced by a Mycobacterium Virulence Determinant. *PLoS Biol* **2**, e367 (2004).

25. Pym, A. S., Brodin, P., Brosch, R., Huerre, M. & Cole, S. T. Loss of RD1 contributed to the attenuation of the live tuberculosis vaccines Mycobacterium bovis BCG and Mycobacterium microti. *Molecular Microbiology* **46**, 709–717 (2002).

26. Brennan, P. J. & Nikaido, H. The Envelope of Mycobacteria. *Annual Review of Biochemistry* **64**, 29–63 (1995).

27. Alderwick, L. J., Harrison, J., Lloyd, G. S. & Birch, H. L. The Mycobacterial Cell Wall—Peptidoglycan and Arabinogalactan. *Cold Spring Harb Perspect Med* **5**, a021113 (2015).

28. Sani, M. *et al.* Direct Visualization by Cryo-EM of the Mycobacterial Capsular Layer: A Labile Structure Containing ESX-1-Secreted Proteins. *PLoS Pathogens* **6**, e1000794 (2010).

29. Józefowski, S., Sobota, A., Hamasur, B., Pawłowski, A. & Kwiatkowska, K. Mycobacterium tuberculosis lipoarabinomannan enhances LPS-induced TNF-α production and inhibits NO secretion by engaging scavenger receptors. *Microbial Pathogenesis* **50**, 350–359 (2011).

30. Bitter, W. *et al.* Systematic Genetic Nomenclature for Type VII Secretion Systems. *PLOS Pathogens* **5**, e1000507 (2009).

31. Glickman, M. S., Cox, J. S. & Jacobs, W. R. A Novel Mycolic Acid Cyclopropane Synthetase Is Required for Cording, Persistence, and Virulence of Mycobacterium tuberculosis. *Molecular Cell* **5**, 717–727 (2000).

32. Rao, V., Fujiwara, N., Porcelli, S. A. & Glickman, M. S. Mycobacterium tuberculosis controls host innate immune activation through cyclopropane modification of a glycolipid effector molecule. *Journal of Experimental Medicine* **201**, 535–543 (2005).

33. Peyron, P. *et al.* Foamy macrophages from tuberculous patients' granulomas constitute a nutrient-rich reservoir for M. tuberculosis persistence. *PLoS pathogens* **4**, e1000204 (2008).

34. Senaratne, R. H. *et al.* Expression of a Gene for a Porin-Like Protein of the OmpA Family from Mycobacterium tuberculosisH37Rv. *Journal of Bacteriology* **180**, 3541–3547 (1998).

35. Song, H., Sandie, R., Wang, Y., Andrade-Navarro, M. A. & Niederweis, M. Identification of outer membrane proteins of Mycobacterium tuberculosis. *Tuberculosis* **88**, 526–544 (2008).

36. Xiong, Y., Chalmers, M. J., Gao, F. P., Cross, T. A. & Marshall, A. G. Identification of Mycobacterium tuberculosis H37Rv Integral Membrane Proteins by One-Dimensional Gel Electrophoresis and Liquid Chromatography Electrospray Ionization Tandem Mass Spectrometry. *J. Proteome Res.* **4**, 855–861 (2005).

37. Chen, T. *et al.* Association of Human Antibodies to Arabinomannan With Enhanced Mycobacterial Opsonophagocytosis and Intracellular Growth Reduction. *Journal of Infectious Diseases* **214**, 300–310 (2016).

38. Ortalo-Magné, A. *et al*. Identification of the surface-exposed lipids on the cell envelopes of Mycobacterium tuberculosis and other mycobacterial species. *Journal of Bacteriology* **178**, 456–461 (1996).

39. Stokes, R. W. *et al*. The glycan-rich outer layer of the cell wall of Mycobacterium tuberculosis acts as an antiphagocytic capsule limiting the association of the bacterium with macrophages. *Infection and Immunity* **72**, 5676–5686 (2004).

40. Grosset, J. Mycobacterium tuberculosis in the Extracellular Compartment: an Underestimated Adversary. *Antimicrobial Agents and Chemotherapy* **47**, 833–836 (2003).

41. Wells, W. F., Ratcliffe, H. L. & Crumb, C. On the Mechanics of Droplet Nuclei Infection. II. Quantitative Experimental Air-borne Tuberculosis in Rabbits. *American Journal of Hygiene* **47**, 11–28 (1948).

42. Dallenga, T. & Schaible, U. E. Neutrophils in tuberculosis-first line of defence or booster of disease and targets for host-directed therapy? *Pathogens and disease* **74**, (2016).

43. Russell, D. G., Cardona, P., Kim, M., Allain, S. & Altare, F. Foamy macrophages and the progression of the human TB granuloma. *Nature immunology* **10**, 943–948 (2010).

44. Adams, D. O. The granulomatous inflammatory response. A review. *Am J Pathol* **84**, 164–191 (1976).

45. Pagán, A. J. & Ramakrishnan, L. Immunity and Immunopathology in the Tuberculous Granuloma. *Cold Spring Harb Perspect Med* **5**, a018499 (2015).

46. Marakalala, M. J., Martinez, F. O., Plüddemann, A. & Gordon, S. Macrophage Heterogeneity in the Immunopathogenesis of Tuberculosis. *Frontiers in Microbiology* **9**, 1028 (2018).

47. Volkman, H. E. *et al*. Tuberculous Granuloma Induction via Interaction of a Bacterial Secreted Protein with Host Epithelium. *Science* **327**, 466–469 (2010).

48. Tobin, D. M. *et al*. Host Genotype-Specific Therapies Can Optimize the Inflammatory Response to Mycobacterial Infections. *Cell* **148**, 434–446 (2012).

49. Iliopoulos, A., Psathakis, K., Aslanidis, S., Skagias, L. & Sfikakis, P. P. Tuberculosis and granuloma formation in patients receiving anti-TNF therapy. *Int J Tuberc Lung Dis* **10**, 588–590 (2006).

50. Clay, H., Volkman, H. E. & Ramakrishnan, L. TNF signaling mediates resistance to mycobacteria by inhibiting bacterial growth and macrophage death but not tuberculous granuloma formation. *Immunity* **29**, 283–294 (2008).

51. Bernut, A. *et al*. Mycobacterium abscessus cording prevents phagocytosis and promotes abscess formation. *PNAS* **111**, E943–E952 (2014).

52. Howard, S. T. *et al*. Spontaneous reversion of Mycobacterium abscessus from a smooth to a rough morphotype is associated with reduced expression of glycopeptidolipid and reacquisition of an invasive phenotype. *Microbiology* **152**, 1581–1590.

53. Wells, G. *et al*. µCT Analysis of the Human Tuberculous Lung Reveals Remarkable Heterogeneity in 3D Granuloma Morphology. *Am J Respir Crit Care Med* rccm.202101-0032OC (2021) doi:10.1164/rccm.202101-0032OC.

54. Breuninger, M. *et al*. Diagnostic accuracy of computer-aided detection of pulmonary tuberculosis in chest radiographs: a validation study from sub-Saharan Africa. *PLoS One* **9**, e106381 (2014).

55. Lumb, R. *et al*. *Laboratory diagnosis of tuberculosis by sputum microscopy: the handbook*. (2013).

56. Reid, M. J. & Shah, N. S. Approaches to tuberculosis screening and diagnosis in people with HIV in resource-limited settings. *The Lancet Infectious Diseases* **9**, 173–184 (2009).

57. Zar, H. J. *et al*. Rapid diagnosis of pulmonary tuberculosis in African children in a primary care setting by use of Xpert MTB/RIF on respiratory specimens: a prospective study. *The Lancet Global Health* **1**, e97–e104 (2013).

58. Steingart, K. R. *et al*. Xpert® MTB/RIF assay for pulmonary tuberculosis and rifampicin resistance in adults. *Cochrane Database of Systematic Reviews* (2013) doi:10.1002/14651858.CD009593.pub2.

59. Nicol, M. P. *et al*. Accuracy of the Xpert MTB/RIF test for the diagnosis of pulmonary tuberculosis in children admitted to hospital in Cape Town, South Africa: a descriptive study. *The Lancet Infectious Diseases* **11**, 819–824 (2011).

60. Lombardi, G. *et al*. Diagnosis of smear-negative tuberculosis is greatly improved by Xpert MTB/RIF. *PLoS One* **12**, e0176186 (2017).

61. Abdurrahman, S. T. *et al*. The hidden costs of installing xpert machines in a tuberculosis high-burden country: experiences from Nigeria. *Pan Afr Med J* **18**, 277 (2014).

62. Peña, J. A., Ferraro, M. J., Hoffman, C. G. & Branda, J. A. Growth Detection Failures by the Nonradiometric Bactec MGIT 960 Mycobacterial Culture System. *J Clin Microbiol* **50**, 2092–2095 (2012).

63. Tanner, R., O'Shea, M. K., Fletcher, H. A. & McShane, H. In vitro mycobacterial growth inhibition assays: A tool for the assessment of protective immunity and evaluation of tuberculosis vaccine efficacy. *Vaccine* **34**, 4656–4665 (2016).

64. Kontos, F. *et al.* Evaluation of the fully automated Bactec MGIT 960 system for the susceptibility testing of Mycobacterium tuberculosis to first-line drugs: a multicenter study. *Journal of Microbiological Methods* **56**, 291–294 (2004).

65. Targeted Tuberculin Testing and Treatment of Latent Tuberculosis Infection. *Am J Respir Crit Care Med* **161**, S221–S247 (2000).

66. US Food and Drug Administration. Aplisol.

67. Karbalaei Zadeh Babaki, M., Soleimanpour, S. & Rezaee, S. A. Antigen 85 complex as a powerful Mycobacterium tuberculosis immunogene: Biology, immune-pathogenicity, applications in diagnosis, and vaccine design. *Microbial Pathogenesis* **112**, 20–29 (2017).

68. USDA APHIS. Bovine Tuberculosis (Mycobacterium bovis) Surveillance Standards 11/2001.

69. Bovine Tuberculosis (TB) testing | Department of Agriculture, Environment and Rural Affairs. *DAERA* https://www.daera-ni.gov.uk/articles/bovine-tuberculosis-tb-testing (2015).

70. Porsa, E. *et al.* Comparison of a New ESAT-6/CFP-10 Peptide-Based Gamma Interferon Assay and a Tuberculin Skin Test for Tuberculosis Screening in a Moderate-Risk Population. *Clinical and Vaccine Immunology* **13**, 53–58 (2006).

71. QuantiFERON-TB Gold. *QuantiFERON* https://www.quantiferon.com/products/quantiferon-tb-gold/.

72. The T-SPOT.TB test technology | The T-SPOT.TB test. *T-Spot International* https://www.tspot.com/uk/why-the-t-spot-tb-test/technology/.

73. Ewer, K. *et al.* Comparison of T-cell-based assay with tuberculin skin test for diagnosis of Mycobacterium tuberculosis infection in a school tuberculosis outbreak. *The Lancet* **361**, 1168–1173 (2003).

74. Kang, Y. A. *et al*. Discrepancy Between the Tuberculin Skin Test and the Whole-Blood Interferon γ Assay for the Diagnosis of Latent Tuberculosis Infection in an Intermediate Tuberculosis-Burden Country. *JAMA* **293**, 2756–2761 (2005).

75. Arend, S. M. *et al*. Comparison of Two Interferon-γ Assays and Tuberculin Skin Test for Tracing Tuberculosis Contacts. *Am J Respir Crit Care Med* **175**, 618–627 (2007).

76. Dorman, S. E. *et al*. Four-Month Rifapentine Regimens with or without Moxifloxacin for Tuberculosis. *N Engl J Med* **384**, 1705–1718 (2021).

77. Ohno, H., Koga, H., Kohno, S., Tashiro, T. & Hara, K. Relationship between rifampin MICs for and rpoB mutations of Mycobacterium tuberculosis strains isolated in Japan. *Antimicrob Agents Chemother* **40**, 1053–1056 (1996).

78. Shea, J. *et al*. Low-Level Rifampin Resistance and rpoB Mutations in Mycobacterium tuberculosis: an Analysis of Whole-Genome Sequencing and Drug Susceptibility Test Data in New York. *J Clin Microbiol* **59**, e01885-20 (2021).

79. Cade, C. E., Dlouhy, A. C., Medzihradszky, K. F., Salas-Castillo, S. P. & Ghiladi, R. A. Isoniazid-resistance conferring mutations in Mycobacterium tuberculosis KatG: catalase, peroxidase, and INH-NADH adduct formation activities. *Protein science : a publication of the Protein Society* **19**, 458–74 (2010).

80. National Institute for Communicable Diseases (South Africa). *South African Tuberculosis Drug Resistance Survey, 2012-14*. https://www.nicd.ac.za/assets/files/K-12750%20NICD%20National%20Survey%20Report_Dev_V11-LR.pdf (2014).

81. Koirala, S. *et al*. Outcome of treatment of MDR-TB or drug-resistant patients treated with bedaquiline and delamanid: Results from a large global cohort.

Pulmonology S2531-0437(21)00053–2 (2021) doi:10.1016/j.pulmoe.2021.02.006.

82. Ramakrishnan, L. The Zebrafish Guide to Tuberculosis Immunity and Treatment. *Cold Spring Harb Symp Quant Biol* **78**, 179–192 (2013).
83. Mashoof, S. & Criscitiello, M. F. Fish Immunoglobulins. *Biology (Basel)* **5**, E45 (2016).
84. Moody, M. A. *et al.* Immune perturbations in HIV-1–infected individuals who make broadly neutralizing antibodies. *Science Immunology* **1**, (2016).
85. Kramnik, I., Demant, P. & Bloom, B. B. Susceptibility to tuberculosis as a complex genetic trait: analysis using recombinant congenic strains of mice. *Novartis Found Symp* **217**, 120–131; discussion 132-137 (1998).
86. Driver, E. R. *et al.* Evaluation of a mouse model of necrotic granuloma formation using C3HeB/FeJ mice for testing of drugs against Mycobacterium tuberculosis. *Antimicrobial agents and chemotherapy* **56**, 3181–95 (2012).
87. Bouté, M. *et al.* The C3HeB/FeJ mouse model recapitulates the hallmark of bovine tuberculosis lung lesions following Mycobacterium bovis aerogenous infection. *Vet Res* **48**, 73 (2017).
88. Tran, A. C. *et al.* Mucosal Therapy of Multi-Drug Resistant Tuberculosis With IgA and Interferon-γ. *Front. Immunol.* **0**, (2020).
89. Ahmad, Z. *et al.* Comparison of the 'Denver regimen' against acute tuberculosis in the mouse and guinea pig. *Journal of Antimicrobial Chemotherapy* **65**, 729–734 (2010).
90. Basaraba, R. J. *et al.* Lymphadenitis as a major element of disease in the guinea pig model of tuberculosis. *Tuberculosis (Edinb)* **86**, 386–394 (2006).

91. Ordway, D. J. *et al.* Evaluation of Standard Chemotherapy in the Guinea Pig Model of Tuberculosis. *Antimicrob Agents Chemother* **54**, 1820–1833 (2010).

92. Marakalala, M. J. *et al.* Inflammatory signaling in human tuberculosis granulomas is spatially organized. *Nature Medicine* **22**, 531–8 (2016).

93. Kunnath-Velayudhan, S. *et al.* Proteome-scale antibody responses and outcome of Mycobacterium tuberculosis infection in nonhuman primates and in tuberculosis patients. *The Journal of infectious diseases* **206**, 697–705 (2012).

94. Phuah, J. Y., Mattila, J. T., Lin, P. L. & Flynn, J. L. Activated B cells in the granulomas of nonhuman primates infected with Mycobacterium tuberculosis. *The American journal of pathology* **181**, 508–14 (2012).

95. Phuah, J. *et al.* Effects of B Cell Depletion on Early Mycobacterium tuberculosis Infection in Cynomolgus Macaques. *Infection and immunity* **84**, 1301–11 (2016).

96. Sibley, L. *et al.* Differences in host immune populations between rhesus macaques and cynomolgus macaque subspecies in relation to susceptibility to Mycobacterium tuberculosis infection. *Sci Rep* **11**, 8810 (2021).

97. Lin, P. L. *et al.* Radiologic Responses in Cynomolgus Macaques for Assessing Tuberculosis Chemotherapy Regimens. *Antimicrobial Agents and Chemotherapy* **57**, 4237–4244 (2013).

98. Darrah, P. A. *et al.* Prevention of tuberculosis in nonhuman primates following intravenous BCG immunization. *Nature in press* **577**, (2019).

99. Wolf, A. J. *et al.* Mycobacterium tuberculosis Infects Dendritic Cells with High Frequency and Impairs Their Function In Vivo. *The Journal of Immunology* **179**, 2509–2519 (2007).

100. Weiss, G. & Schaible, U. E. Macrophage defense mechanisms against intracellular bacteria. *Immunol Rev* **264**, 182–203 (2015).

101. Schlesinger, L. S. Macrophage phagocytosis of virulent but not attenuated strains of Mycobacterium tuberculosis is mediated by mannose receptors in addition to complement receptors. *Journal of immunology (Baltimore, Md. : 1950)* **150**, 2920–30 (1993).

102. Kang, B. K. & Schlesinger, L. S. Characterization of mannose receptor-dependent phagocytosis mediated by Mycobacterium tuberculosis lipoarabinomannan. *Infection and immunity* **66**, 2769–77 (1998).

103. Ortalo-Magné, A., Andersen, Å. B. & Daffé, M. 1996. The outermost capsular arabinomannans and other mannoconjugates of virulent and avirulent tubercle bacilli. *Microbiology* **142**, 927–935.

104. Schlesinger, L. S., Bellinger-Kawahara, C. G., Payne, N. R. & Horwitz, M. A. Phagocytosis of Mycobacterium tuberculosis is mediated by human monocyte complement receptors and complement component C3. *Journal of immunology (Baltimore, Md. : 1950)* **144**, 2771–80 (1990).

105. Cywes, C., Hoppe, H. C., Daffé, M. & Ehlers, M. R. Nonopsonic binding of Mycobacterium tuberculosis to complement receptor type 3 is mediated by capsular polysaccharides and is strain dependent. *Infection and immunity* **65**, 4258–66 (1997).

106. Lu, L. L. *et al.* A Functional Role for Antibodies in Tuberculosis. *Cell* **167**, 433-443.e14 (2016).

107. McEwan, W. A. *et al*. Intracellular antibody-bound pathogens stimulate immune signaling via the Fc receptor TRIM21. *Nature immunology* **14**, 327–36 (2013).

108. Frehel, C., de Chastellier, C., Lang, T. & Rastogi, N. Evidence for inhibition of fusion of lysosomal and prelysosomal compartments with phagosomes in

macrophages infected with pathogenic Mycobacterium avium. *Infection and Immunity* **52**, 252–262 (1986).

109. Hasan, Z. *et al.* Isolation and characterization of the mycobacterial phagosome: segregation from the endosomal/lysosomal pathway. *Molecular Microbiology* **24**, 545–553 (1997).

110. Ramachandra, L., Noss, E., Boom, W. H. & Harding, C. V. Processing of Mycobacterium tuberculosis Antigen 85B Involves Intraphagosomal Formation of Peptide–Major Histocompatibility Complex II Complexes and Is Inhibited by Live Bacilli that Decrease Phagosome Maturation. *Journal of Experimental Medicine* **194**, 1421–1432 (2001).

111. Gatfield, J. & Pieters, J. Essential Role for Cholesterol in Entry of Mycobacteria into Macrophages. *Science* **288**, 1647–1651 (2000).

112. Tanigawa, K. *et al.* Tryptophan aspartate-containing coat protein (CORO1A) suppresses Toll-like receptor signalling in Mycobacterium leprae infection. *Clinical & Experimental Immunology* **156**, 495–501 (2009).

113. Schüller, S., Neefjes, J., Ottenhoff, T., Thole, J. & Young, D. Coronin is involved in uptake of Mycobacterium bovis BCG in human macrophages but not in phagosome maintenance. *Cellular Microbiology* **3**, 785–793 (2001).

114. Gogulamudi, V. R., Dubey, M. L., Kaul, D., Atluri, V. S. R. & Sehgal, R. Downregulation of host tryptophan–aspartate containing coat (TACO) gene restricts the entry and survival of Leishmania donovani in human macrophage model. *Front. Microbiol.* **6**, (2015).

115. Pethe, K. *et al.* Isolation of Mycobacterium tuberculosis mutants defective in the arrest of phagosome maturation. *PNAS* **101**, 13642–13647 (2004).

116. Stewart, G. R., Patel, J., Robertson, B. D., Rae, A. & Young, D. B. Mycobacterial Mutants with Defective Control of Phagosomal Acidification. *PLOS Pathogens* **1**, e33 (2005).

117. Nathan, C. & Shiloh, M. U. Reactive oxygen and nitrogen intermediates in the relationship between mammalian hosts and microbial pathogens. *PNAS* **97**, 8841–8848 (2000).

118. Spagnolo, L. *et al.* Unique Features of the sodC-encoded Superoxide Dismutase from Mycobacterium tuberculosis, a Fully Functional Copper-containing Enzyme Lacking Zinc in the Active Site*. *Journal of Biological Chemistry* **279**, 33447–33455 (2004).

119. Flynn, J. L. & Chan, J. Immune evasion by Mycobacterium tuberculosis: living with the enemy. *Current Opinion in Immunology* **15**, 450–455 (2003).

120. Chatterjee, D., Roberts, A. D., Lowell, K., Brennan, P. J. & Orme, I. M. Structural basis of capacity of lipoarabinomannan to induce secretion of tumor necrosis factor. *Infect Immun* **60**, 1249–1253 (1992).

121. Gold, B. *et al.* Identification of a copper-binding metallothionein in pathogenic mycobacteria. *Nat Chem Biol* **4**, 609–616 (2008).

122. Botella, H. *et al.* Mycobacterial P1-Type ATPases Mediate Resistance to Zinc Poisoning in Human Macrophages. *Cell Host & Microbe* **10**, 248–259 (2011).

123. Rowland, J. L. & Niederweis, M. Resistance mechanisms of Mycobacterium tuberculosis against phagosomal copper overload. *Tuberculosis (Edinb)* **92**, 202–210 (2012).

124. Dallenga, T. *et al.* M. tuberculosis-Induced Necrosis of Infected Neutrophils Promotes Bacterial Growth Following Phagocytosis by Macrophages. *Cell Host & Microbe* **22**, 519-530.e3 (2017).

125. Lerner, T. R. *et al*. Mycobacterium tuberculosis replicates within necrotic human macrophages. *The Journal of cell biology* **216**, 583–594 (2017).

126. Astarie-Dequeker, C. *et al*. Phthiocerol Dimycocerosates of M. tuberculosis Participate in Macrophage Invasion by Inducing Changes in the Organization of Plasma Membrane Lipids. *PLOS Pathogens* **5**, e1000289 (2009).

127. Noss, E. H. *et al*. Toll-Like Receptor 2-Dependent Inhibition of Macrophage Class II MHC Expression and Antigen Processing by 19-kDa Lipoprotein of Mycobacterium tuberculosis. *The Journal of Immunology* **167**, 910–918 (2001).

128. Mahamed, D. *et al*. Intracellular growth of Mycobacterium tuberculosis after macrophage cell death leads to serial killing of host cells. *eLife* **6**, e22028 (2017).

129. Andersson, A.-M., Larsson, M., Stendahl, O. & Blomgran, R. Efferocytosis of Apoptotic Neutrophils Enhances Control of Mycobacterium tuberculosis in HIV-Coinfected Macrophages in a Myeloperoxidase-Dependent Manner. *J Innate Immun* **12**, 235–247 (2020).

130. Lehar, S. M. *et al*. Novel antibody-antibiotic conjugate eliminates intracellular S. aureus. *Nature* **527**, 323–8 (2015).

131. Kaiser, P. *et al*. Cecum Lymph Node Dendritic Cells Harbor Slow-Growing Bacteria Phenotypically Tolerant to Antibiotic Treatment. *PLOS Biology* **12**, e1001793 (2014).

132. Adams, K. N. *et al*. Drug Tolerance in Replicating Mycobacteria Mediated by a Macrophage-Induced Efflux Mechanism. *Cell* **145**, 39–53 (2011).

133. Szumowski, J. D., Adams, K. N., Edelstein, P. H. & Ramakrishnan, L. Antimicrobial efflux pumps and Mycobacterium tuberculosis drug tolerance: Evolutionary Considerations. *Curr Top Microbiol Immunol* **374**, 10.1007/82_2012_300 (2013).

134. DesJardin, L. E. *et al*. Mycobacterium tuberculosis-infected human macrophages exhibit enhanced cellular adhesion with increased expression of LFA-1 and ICAM-1 and reduced expression and/or function of complement receptors, FcgammaRII and the mannose receptor. *Microbiology (Reading, England)* **148**, 3161–71 (2002).

135. Jacobs, A. J., Mongkolsapaya, J., Screaton, G. R., McShane, H. & Wilkinson, R. J. Antibodies and tuberculosis. *Tuberculosis (Edinburgh, Scotland)* **101**, 102–113 (2016).

136. Achkar, J. M. & Casadevall, A. B cells and antibodies in the defense against Mycobacterium tuberculosis infection. *Immunological Reviews* 167–181 (2015) doi:10.1111/imr.12276.

137. Joosten, S. A. *et al*. Patients with Tuberculosis Have a Dysfunctional Circulating B-Cell Compartment, Which Normalizes following Successful Treatment. *PLOS Pathogens* **12**, e1005687 (2016).

138. Ulrichs, T. *et al*. Human tuberculous granulomas induce peripheral lymphoid follicle-like structures to orchestrate local host defence in the lung. *The Journal of pathology* **204**, 217–28 (2004).

139. Marin, N. D., Dunlap, M. D., Kaushal, D. & Khader, S. A. Friend or Foe: The Protective and Pathological Roles of Inducible Bronchus-Associated Lymphoid Tissue in Pulmonary Diseases. *The Journal of Immunology* **202**, 2519–2526 (2019).

140. Dunlap, M. D. *et al*. Formation of Lung Inducible Bronchus Associated Lymphoid Tissue Is Regulated by Mycobacterium tuberculosis Expressed Determinants. *Frontiers in Immunology* **11**, 1325 (2020).

141. Lu, L. L. *et al*. IFN-γ-independent immune markers of Mycobacterium tuberculosis exposure. *Nature Medicine* (2019) doi:10.1038/s41591-019-0441-3.

142. Li, H. *et al*. Latently and uninfected healthcare workers exposed to TB make protective antibodies against Mycobacterium tuberculosis. *Proceedings of the National Academy of Sciences of the United States of America* **114**, 5023–5028 (2017).

143. Mahamed, D. *et al*. Intracellular growth of Mycobacterium tuberculosis after macrophage cell death leads to serial killing of host cells. *eLife* **6**, e22028 (2017).

144. Rodel, H. E. *et al*. Aggregated Mycobacterium tuberculosis Enhances the Inflammatory Response. *Frontiers in Microbiology* **12**, 3436 (2021).

145. Khan, I. H. *et al*. Plasma Antibody Profiles as Diagnostic Biomarkers for Tuberculosis. *Clinical and Vaccine Immunology* **18**, 2148–2153 (2011).

146. Shete, P. B. *et al*. Evaluation of antibody responses to panels of M. tuberculosis antigens as a screening tool for active tuberculosis in Uganda. *PLOS ONE* **12**, e0180122 (2017).

147. Kunnath-Velayudhan, S. *et al*. Dynamic antibody responses to the Mycobacterium tuberculosis proteome. *Proceedings of the National Academy of Sciences of the United States of America* **107**, 14703–8 (2010).

148. Kunnath-Velayudhan, S. *et al*. Proteome-scale antibody responses and outcome of Mycobacterium tuberculosis infection in nonhuman primates and in tuberculosis patients. *The Journal of infectious diseases* **206**, 697–705 (2012).

149. Zvi, A., Ariel, N., Fulkerson, J., Sadoff, J. C. & Shafferman, A. Whole genome identification of Mycobacterium tuberculosis vaccine candidates by comprehensive data mining and bioinformatic analyses. *BMC medical genomics* **1**, 18 (2008).

150. Steingart, K. R. *et al.* Performance of purified antigens for serodiagnosis of pulmonary tuberculosis: a meta-analysis. *Clinical and vaccine immunology : CVI* **16**, 260–76 (2009).

151. Kapopoulou, A., Lew, J. M. & Cole, S. T. The MycoBrowser portal: A comprehensive and manually annotated resource for mycobacterial genomes. *Tuberculosis* **91**, 8–13 (2011).

152. Ortalo-Magne, A. *et al.* Molecular composition of the outermost capsular material of the tubercle bacillus. *Microbiology* **141**, 1609–1620 (1995).

153. Hu, Y., Movahedzadeh, F., Stoker, N. G. & Coates, A. R. M. Deletion of the Mycobacterium tuberculosis alpha-crystallin-like hspX gene causes increased bacterial growth in vivo. *Infection and immunity* **74**, 861–8 (2006).

154. Yuan, Y., Crane, D. D. & Barry, C. E. Stationary phase-associated protein expression in Mycobacterium tuberculosis: function of the mycobacterial alpha-crystallin homolog. *J Bacteriol* **178**, 4484–4492 (1996).

155. Yuan, Y. *et al.* The 16-kDa α-crystallin (Acr) protein of Mycobacterium tuberculosis is required for growth in macrophages. *Proc Natl Acad Sci U S A* **95**, 9578–9583 (1998).

156. Williams, A. *et al.* Passive protection with immunoglobulin A antibodies against tuberculous early infection of the lungs. *Immunology* **111**, 328–333 (2004).

157. Balu, S. *et al.* A novel human IgA monoclonal antibody protects against tuberculosis. *Journal of immunology (Baltimore, Md. : 1950)* **186**, 3113–9 (2011).

158. Pelaez, E. C. *et al.* Detection and quantification of HspX antigen in sputum samples using plasmonic biosensing : toward a real Point-of-Care (POC) for tuberculosis diagnosis. (2020) doi:10.1021/acsinfecdis.9b00502.

159. Zhang, C. *et al.* Mycobacterium tuberculosis Secreted Proteins As Potential Biomarkers for the Diagnosis of Active Tuberculosis and Latent Tuberculosis Infection. *Journal of Clinical Laboratory Analysis* **29**, 375–382 (2015).

160. Castro-Garza, J. *et al.* Detection of anti-HspX antibodies and HspX protein in patient sera for the identification of recent latent infection by Mycobacterium tuberculosis. *PLOS ONE* **12**, e0181714 (2017).

161. Soong, J. X., Chan, S. K., Lim, T. S. & Choong, Y. S. Optimisation of human VH domain antibodies specific to Mycobacterium tuberculosis heat shock protein (HSP16.3). *Journal of Computer-Aided Molecular Design* **0**, 0 (2019).

162. Copin, R., Coscollá, M., Efstathiadis, E., Gagneux, S. & Ernst, J. D. Impact of in vitro evolution on antigenic diversity of Mycobacterium bovis bacillus Calmette-Guerin (BCG). *Vaccine* **32**, 5998–6004 (2014).

163. Wilkie, M. *et al.* A phase I trial evaluating the safety and immunogenicity of a candidate tuberculosis vaccination regimen, ChAdOx1 85A prime – MVA85A boost in healthy UK adults. *Vaccine* **38**, 779–789 (2020).

164. Sørensen, A. L., Nagai, S., Houen, G., Andersen, P. & Andersen, A. B. Purification and characterization of a low-molecular-mass T-cell antigen secreted by Mycobacterium tuberculosis. *Infect Immun* **63**, 1710–1717 (1995).

165. Mariotti, S. *et al.* Dormant Mycobacterium tuberculosis Fails To Block Phagosome Maturation and Shows Unexpected Capacity To Stimulate Specific Human T Lymphocytes. *The Journal of Immunology* **191**, 274–282 (2013).

166. Zimmermann, N. *et al.* Syndecans promote mycobacterial internalization by lung epithelial cells. *Cellular Microbiology* **18**, 1846–1856 (2016).

167. Menozzi, F. D. *et al.* Identification of a heparin-binding hemagglutinin present in mycobacteria. *The Journal of experimental medicine* **184**, 993–1001 (1996).

168. Raze, D. *et al.* Heparin-Binding Hemagglutinin Adhesin (HBHA) Is Involved in Intracytosolic Lipid Inclusions Formation in Mycobacteria. *Front. Microbiol.* **9**, (2018).

169. Hougardy, J.-M. *et al.* Heparin-Binding-Hemagglutinin-Induced IFN-γ Release as a Diagnostic Tool for Latent Tuberculosis. *PLOS ONE* **2**, e926 (2007).

170. Shin, A.-R. *et al.* Mycobacterium tuberculosis HBHA protein reacts strongly with the serum immunoglobulin M of tuberculosis patients. *Clinical and vaccine immunology : CVI* **13**, 869–75 (2006).

171. Pethe, K. *et al.* The heparin-binding haemagglutinin of M. tuberculosis is required for extrapulmonary dissemination. *Nature* **412**, 190–4 (2001).

172. Gonzalo-Asensio, J. *et al.* The Mycobacterium tuberculosis phoPR Operon Is Positively Autoregulated in the Virulent Strain H37Rv. *Journal of Bacteriology* **190**, 7068–7078 (2008).

173. Vidyarthi, A. *et al.* Antibody response against PhoP efficiently discriminates among healthy individuals, tuberculosis patients and their contacts. *PLOS ONE* **12**, e0173769 (2017).

174. Teitelbaum, R. *et al.* A mAb recognizing a surface antigen of Mycobacterium tuberculosis enhances host survival. *Proceedings of the National Academy of Sciences* **95**, 15688–15693 (1998).

175. Siev, M. *et al.* Correlation between serum and plasma antibody titers to mycobacterial antigens. *Clinical and vaccine immunology : CVI* **18**, 173–5 (2011).

176. Zimmermann, N. *et al.* Human isotype-dependent inhibitory antibody responses against Mycobacterium tuberculosis. *EMBO molecular medicine* **8**, 1325–1339 (2016).

177. Ginsberg, A. M. TB Vaccines: Pipeline Overview and Status of Late-stage Candidates. (2019).

178. McShane, H. Insights and challenges in tuberculosis vaccine development. *The Lancet Respiratory Medicine* **7**, 810–819 (2019).

179. Tatsis, N. *et al.* Chimpanzee-origin adenovirus vectors as vaccine carriers. *Gene Ther* **13**, 421–429 (2006).

180. Dicks, M. D. J. *et al.* A Novel Chimpanzee Adenovirus Vector with Low Human Seroprevalence: Improved Systems for Vector Derivation and Comparative Immunogenicity. *PLOS ONE* **7**, e40385 (2012).

181. Arnberg, N. Adenovirus receptors: implications for targeting of viral vectors. *Trends in Pharmacological Sciences* **33**, 442–448 (2012).

182. Stasiak, A. C. & Stehle, T. Human adenovirus binding to host cell receptors: a structural view. *Med Microbiol Immunol* **209**, 325–333 (2020).

183. Stylianou, E. *et al.* Improvement of BCG protective efficacy with a novel chimpanzee adenovirus and a modified vaccinia Ankara virus both expressing Ag85A. *Vaccine* **33**, (2015).

184. Zwerling, A. *et al.* The BCG World Atlas: A Database of Global BCG Vaccination Policies and Practices. *PLOS Medicine* **8**, e1001012 (2011).

185. Chee, C. B. E. & James, L. The Singapore Tuberculosis Elimination Programme: the first five years. *Bull World Health Organ* **81**, 217–221 (2003).

186. WHO statement on BCG revaccination for the prevention of tuberculosis. *Bulletin of the World Health Organization 1995 ; 73(6) : 805-806* (1995).

187. Glynn, J. R. *et al.* The effect of BCG revaccination on all-cause mortality beyond infancy: 30-year follow-up of a population-based, double-blind, randomised

placebo-controlled trial in Malawi. *Lancet Infect Dis* S1473-3099(20)30994–4 (2021) doi:10.1016/S1473-3099(20)30994-4.

188. Nemes, E. *et al.* Prevention of *M. tuberculosis* Infection with H4:IC31 Vaccine or BCG Revaccination. *New England Journal of Medicine* **379**, 138–149 (2018).
189. Marinova, D., Gonzalo-Asensio, J., Aguilo, N. & Martin, C. MTBVAC from discovery to clinical trials in tuberculosis-endemic countries. *Expert Review of Vaccines* **16**, 565–576 (2017).
190. Tameris, M. *et al.* Live-attenuated Mycobacterium tuberculosis vaccine MTBVAC versus BCG in adults and neonates: a randomised controlled, double-blind dose-escalation trial. *The Lancet Respiratory Medicine* **7**, 757–770 (2019).
191. Didierlaurent, A. M. *et al.* Adjuvant system AS01: helping to overcome the challenges of modern vaccines. *Expert Review of Vaccines* **16**, 55–63 (2017).
192. Tait, D. R. *et al.* Final Analysis of a Trial of M72/AS01 E Vaccine to Prevent Tuberculosis. *New England Journal of Medicine* 1–12 (2019) doi:10.1056/nejmoa1909953.
193. Nieuwenhuizen, N. E. *et al.* The Recombinant Bacille Calmette–Guérin Vaccine VPM1002: Ready for Clinical Efficacy Testing. *Frontiers in Immunology* **8**, 1147 (2017).
194. Fehr, A. R. & Perlman, S. Coronaviruses: An Overview of Their Replication and Pathogenesis. *Coronaviruses* **1282**, 1–23 (2015).
195. The woman who discovered the first coronavirus. *BBC News* (2020).
196. Almeida, J. June Almeida (née Hart). *BMJ* **336**, 1511.1-1511 (2008).
197. Almeida, J. D. & Tyrrell, D. A. The morphology of three previously uncharacterized human respiratory viruses that grow in organ culture. *The Journal of general virology* **1**, 175–178 (1967).

198. Kirchdoerfer, R. N. *et al.* Pre-fusion structure of a human coronavirus spike protein. *Nature* **531**, 118–121 (2016).

199. Nicol, M. P. *et al.* A Longitudinal Study of the Epidemiology of Seasonal Coronaviruses in an African Birth Cohort. *Journal of the Pediatric Infectious Diseases Society* **10**, 607–614 (2021).

200. Dube, F. S. *et al.* Respiratory microbes present in the nasopharynx of children hospitalised with suspected pulmonary tuberculosis in Cape Town, South Africa. *BMC Infectious Diseases* **16**, (2016).

201. Vlasova, A. N. *et al.* Novel Canine Coronavirus Isolated from a Hospitalized Pneumonia Patient, East Malaysia. *Clinical Infectious Diseases* (2021) doi:10.1093/cid/ciab456.

202. CHAN-YEUNG, M. & XU, R. SARS: epidemiology. *Respirology* **8**, S9–S14 (2003).

203. Eckstein, S. *et al.* Prevalence of Middle East Respiratory Syndrome Coronavirus in Dromedary Camels, Tunisia - Volume 27, Number 7—July 2021 - Emerging Infectious Diseases journal - CDC. doi:10.3201/eid2707.204873.

204. Ngere, I. *et al.* High MERS-CoV seropositivity associated with camel herd profile, husbandry practices and household socio-demographic characteristics in Northern Kenya. *Epidemiol Infect* **148**, e292 (2020).

205. Aljasim, T. A. *et al.* High Rate of Circulating MERS-CoV in Dromedary Camels at Slaughterhouses in Riyadh, 2019. *Viruses* **12**, E1215 (2020).

206. Lefkowitz, E. J. *et al.* Virus taxonomy: the database of the International Committee on Taxonomy of Viruses (ICTV). *Nucleic Acids Research* **46**, D708–D717 (2018).

207. Wu, F. *et al.* A new coronavirus associated with human respiratory disease in China. *Nature* **579**, 265–269 (2020).

208. Huo, X., Chen, J. & Ruan, S. Estimating asymptomatic, undetected and total cases for the COVID-19 outbreak in Wuhan: a mathematical modeling study. *BMC Infectious Diseases* **21**, 476 (2021).

209. Listings of WHO's response to COVID-19. https://www.who.int/news/item/29-06-2020-covidtimeline.

210. Naming the coronavirus disease (COVID-19) and the virus that causes it. https://www.who.int/emergencies/diseases/novel-coronavirus-2019/technical-guidance/naming-the-coronavirus-disease-(covid-2019)-and-the-virus-that-causes-it.

211. Zehender, G. *et al.* Genomic characterization and phylogenetic analysis of SARS-COV-2 in Italy. *Journal of Medical Virology* **92**, 1637–1640 (2020).

212. World Health Organization. WHO-convened global study of origins of SARS-CoV-2: China Part. https://www.who.int/publications-detail-redirect/who-convened-global-study-of-origins-of-sars-cov-2-china-part.

213. Apolone, G. *et al.* Unexpected detection of SARS-CoV-2 antibodies in the prepandemic period in Italy. *Tumori* 0300891620974755 (2020) doi:10.1177/0300891620974755.

214. Deslandes, A. *et al.* SARS-CoV-2 was already spreading in France in late December 2019. *International Journal of Antimicrobial Agents* **55**, 106006 (2020).

215. Dong, E., Du, H. & Gardner, L. An interactive web-based dashboard to track COVID-19 in real time. *The Lancet Infectious Diseases* **20**, 533–534 (2020).

216. Sanmarchi, F. *et al*. Exploring the Gap Between Excess Mortality and COVID-19 Deaths in 67 Countries. *JAMA Netw Open* **4**, e2117359 (2021).

217. Olsen, S. J. *et al*. Decreased Influenza Activity During the COVID-19 Pandemic - United States, Australia, Chile, and South Africa, 2020. *MMWR Morb Mortal Wkly Rep* **69**, 1305–1309 (2020).

218. CDC. Coronavirus Disease 2019 (COVID-19) – Symptoms. *Centers for Disease Control and Prevention* https://www.cdc.gov/coronavirus/2019-ncov/symptoms-testing/symptoms.html (2021).

219. Qin, J. *et al*. Estimation of incubation period distribution of COVID-19 using disease onset forward time: A novel cross-sectional and forward follow-up study. *Science Advances* **6**, eabc1202 (2020).

220. Ng, S. H.-X. *et al*. Estimating Transmission Parameters for COVID-19 Clusters by Using Symptom Onset Data, Singapore, January-April 2020. *Emerg Infect Dis* **27**, 582–585 (2021).

221. Du, Y. *et al*. Clinical Features of 85 Fatal Cases of COVID-19 from Wuhan. A Retrospective Observational Study. *Am J Respir Crit Care Med* **201**, 1372–1379 (2020).

222. Del Valle, D. M. *et al*. An inflammatory cytokine signature predicts COVID-19 severity and survival. *Nat Med* **26**, 1636–1643 (2020).

223. Dorward, D. A. *et al*. Tissue-Specific Immunopathology in Fatal COVID-19. *Am J Respir Crit Care Med* **203**, 192–201 (2021).

224. Huertas, A. *et al*. Endothelial cell dysfunction: a major player in SARS-CoV-2 infection (COVID-19)? *Eur Respir J* **56**, 2001634 (2020).

225. Herrmann, J., Mori, V., Bates, J. H. T. & Suki, B. Modeling lung perfusion abnormalities to explain early COVID-19 hypoxemia. *Nat Commun* **11**, 4883 (2020).

226. Gattinoni, L. *et al.* COVID-19 Does Not Lead to a "Typical" Acute Respiratory Distress Syndrome. *Am J Respir Crit Care Med* **201**, 1299–1300 (2020).

227. Group, R. C. *et al.* Casirivimab and imdevimab in patients admitted to hospital with COVID-19 (RECOVERY): a randomised, controlled, open-label, platform trial. *medRxiv* 2021.06.15.21258542 (2021) doi:10.1101/2021.06.15.21258542.

228. Dexamethasone in Hospitalized Patients with Covid-19. *New England Journal of Medicine* **384**, 693–704 (2021).

229. Abani, O. *et al.* Tocilizumab in patients admitted to hospital with COVID-19 (RECOVERY): a randomised, controlled, open-label, platform trial. *The Lancet* **397**, 1637–1645 (2021).

230. COVID-19 vaccine tracker and landscape. https://www.who.int/publications/m/item/draft-landscape-of-covid-19-candidate-vaccines.

231. Corbett, K. S. *et al.* SARS-CoV-2 mRNA vaccine design enabled by prototype pathogen preparedness. *Nature* **586**, 567–571 (2020).

232. Tracking SARS-CoV-2 variants. https://www.who.int/activities/tracking-SARS-CoV-2-variants.

233. Cele, S. *et al.* Escape of SARS-CoV-2 501Y.V2 from neutralization by convalescent plasma. *Nature* **593**, 1–9 (2021).

234. Madhi, S. A. *et al.* Efficacy of the ChAdOx1 nCoV-19 Covid-19 Vaccine against the B.1.351 Variant. *New England Journal of Medicine* **384**, 1885–1898 (2021).

235. NIH. Statement on Anti-SARS-CoV-2 Monoclonal Antibodies EUA. *COVID-19 Treatment Guidelines* https://www.covid19treatmentguidelines.nih.gov/therapies/statement-on-anti-sars-cov-2-monoclonal-antibodies-eua/ (2021).

236. Taylor, P. C. *et al*. Neutralizing monoclonal antibodies for treatment of COVID-19. *Nat Rev Immunol* 1–12 (2021) doi:10.1038/s41577-021-00542-x.

237. Mlcochova, P. *et al*. SARS-CoV-2 B.1.617.2 Delta variant emergence, replication and immune evasion. *bioRxiv* 2021.05.08.443253 (2021) doi:10.1101/2021.05.08.443253.

238. Li, B. & et al. Viral infection and transmission in a large well-traced outbreak caused by the Delta SARS-CoV-2 variant - SARS-CoV-2 coronavirus / nCoV-2019 Genomic Epidemiology. *Virological* (2021).

239. BBC News. Covid: Is China's vaccine success waning in Asia? - BBC News. https://www.bbc.com/news/world-asia-57845644 (2021).

240. Frampton, D. *et al*. Genomic characteristics and clinical effect of the emergent SARS-CoV-2 B.1.1.7 lineage in London, UK: a whole-genome sequencing and hospital-based cohort study. *The Lancet Infectious Diseases* **21**, 1246–1256 (2021).

241. Ong, S. W. X. *et al*. Clinical and virological features of SARS-CoV-2 variants of concern: a retrospective cohort study comparing B.1.1.7 (Alpha), B.1.315 (Beta), and B.1.617.2 (Delta). *Clinical Infectious Diseases* (2021) doi:10.1093/cid/ciab721.

242. Kemp, S. A. *et al*. SARS-CoV-2 evolution during treatment of chronic infection. *Nature* **592**, 277–282 (2021).

243. Purpura, L. J. *et al.* Prolonged severe acute respiratory syndrome coronavirus 2 persistence, attenuated immunologic response, and viral evolution in a solid organ transplant patient. *Am J Transplant* (2021) doi:10.1111/ajt.16837.

244. Truong, T. T. *et al.* Persistent SARS-CoV-2 infection and increasing viral variants in children and young adults with impaired humoral immunity. *medRxiv* 2021.02.27.21252099 (2021) doi:10.1101/2021.02.27.21252099.

245. Karim, F. *et al. Persistent SARS-CoV-2 infection and intra-host evolution in association with advanced HIV infection*. http://medrxiv.org/lookup/doi/10.1101/2021.06.03.21258228 (2021) doi:10.1101/2021.06.03.21258228.

246. Aylward, B. (WHO); L. Report of the WHO-China Joint Mission on Coronavirus Disease 2019 (COVID-19). **2019**, 16–24 (2020).

247. Xiao, X., Newman, C., Buesching, C. D., Macdonald, D. W. & Zhou, Z.-M. Animal sales from Wuhan wet markets immediately prior to the COVID-19 pandemic. *Sci Rep* **11**, 11898 (2021).

248. Lau, S. K. P. *et al.* Severe acute respiratory syndrome coronavirus-like virus in Chinese horseshoe bats. *Proc Natl Acad Sci U S A* **102**, 14040–14045 (2005).

249. Zhou, H. *et al.* A Novel Bat Coronavirus Closely Related to SARS-CoV-2 Contains Natural Insertions at the S1/S2 Cleavage Site of the Spike Protein. *Current Biology* **30**, 2196-2203.e3 (2020).

250. Lv, L., Li, G., Chen, J., Liang, X. & Li, Y. Comparative Genomic Analyses Reveal a Specific Mutation Pattern Between Human Coronavirus SARS-CoV-2 and Bat-CoV RaTG13. *Front. Microbiol.* **0**, (2020).

251. Wacharapluesadee, S. *et al.* Evidence for SARS-CoV-2 related coronaviruses circulating in bats and pangolins in Southeast Asia. *Nature Communications* **12**, 972 (2021).

252. Zhou, H. *et al.* Identification of novel bat coronaviruses sheds light on the evolutionary origins of SARS-CoV-2 and related viruses. *Cell* (2021) doi:10.1016/j.cell.2021.06.008.

253. Li, W. *et al.* Bats Are Natural Reservoirs of SARS-Like Coronaviruses. *Science* **310**, 676–679 (2005).

254. Rihtarič, D., Hostnik, P., Steyer, A., Grom, J. & Toplak, I. Identification of SARS-like coronaviruses in horseshoe bats (Rhinolophus hipposideros) in Slovenia. *Arch Virol* **155**, 507–514 (2010).

255. Menachery, V. D. *et al.* A SARS-like cluster of circulating bat coronaviruses shows potential for human emergence. *Nature Medicine* **21**, 1508–1513 (2015).

256. Wang, M. *et al.* SARS-CoV Infection in a Restaurant from Palm Civet. *Emerg Infect Dis* **11**, 1860–1865 (2005).

257. Enserink, M. Clues to the Animal Origins of SARS. *Science* **300**, 1351–1351 (2003).

258. Song, H.-D. *et al.* Cross-host evolution of severe acute respiratory syndrome coronavirus in palm civet and human. *Proc Natl Acad Sci U S A* **102**, 2430–2435 (2005).

259. Freuling, C. M. *et al.* Susceptibility of Raccoon Dogs for Experimental SARS-CoV-2 Infection. *Emerg Infect Dis* **26**, 2982–2985 (2020).

260. Lam, T. T.-Y. *et al.* Identifying SARS-CoV-2 related coronaviruses in Malayan pangolins. *Nature* 1–6 (2020) doi:10.1038/s41586-020-2169-0.

261. Xiao, K. *et al.* Isolation of SARS-CoV-2-related coronavirus from Malayan pangolins. *Nature* **583**, 286–289 (2020).

262. Peacock, T. P. *et al.* The furin cleavage site of SARS-CoV-2 spike protein is a key determinant for transmission due to enhanced replication in airway cells. 2020.09.30.318311 (2020).

263. Shi, J. *et al.* Susceptibility of ferrets, cats, dogs, and other domesticated animals to SARS–coronavirus 2. *Science* eabb7015 (2020) doi:10.1126/science.abb7015.

264. Barrs, V. R. *et al.* SARS-CoV-2 in Quarantined Domestic Cats from COVID-19 Households or Close Contacts, Hong Kong, China. *Emerging infectious diseases* **26**, (2020).

265. Colitti, B. *et al.* Cross-Sectional Serosurvey of Companion Animals Housed with SARS-CoV-2–Infected Owners, Italy - Volume 27, Number 7—July 2021 - Emerging Infectious Diseases journal - CDC. doi:10.3201/eid2707.203314.

266. McAloose, D. *et al.* From People to Panthera: Natural SARS-CoV-2 Infection in Tigers and Lions at the Bronx Zoo. *mBio* **11**, e02220-20.

267. Brielle, E. S., Schneidman-Duhovny, D. & Linial, M. The SARS-CoV-2 Exerts a Distinctive Strategy for Interacting with the ACE2 Human Receptor. *Viruses* **12**, 497 (2020).

268. Flint, J., Racaniello, V. R., Rall, G. F., Hatziioannou, T. & Skalka, A. M. *Principles of Virology, 5th Edition*. (2020).

269. Jackson, L. *et al.* SARS-CoV-2 cell-to-cell spread occurs rapidly and is insensitive to antibody neutralization. *bioRxiv* 2021.06.01.446516 (2021) doi:10.1101/2021.06.01.446516.

270. Buchrieser, J. *et al.* Syncytia formation by SARS-CoV-2-infected cells. *The EMBO Journal* **39**, e106267 (2020).

271. Hou, Y. J. *et al.* SARS-CoV-2 Reverse Genetics Reveals a Variable Infection Gradient in the Respiratory Tract. *Cell* **182**, 429-446.e14 (2020).

272. Rihn, S. J. *et al.* A plasmid DNA-launched SARS-CoV-2 reverse genetics system and coronavirus toolkit for COVID-19 research. *PLoS Biol* **19**, e3001091 (2021).

273. Bosch, B. J., van der Zee, R., de Haan, C. A. M. & Rottier, P. J. M. The coronavirus spike protein is a class I virus fusion protein: structural and functional characterization of the fusion core complex. *J Virol* **77**, 8801–8811 (2003).

274. Pallesen, J. *et al.* Immunogenicity and structures of a rationally designed prefusion MERS-CoV spike antigen. *PNAS* **114**, E7348–E7357 (2017).

275. Qiu, Z. *et al.* Endosomal Proteolysis by Cathepsins Is Necessary for Murine Coronavirus Mouse Hepatitis Virus Type 2 Spike-Mediated Entry. *Journal of Virology* **80**, 5768–5776 (2006).

276. Wu, Y. & Zhao, S. Furin cleavage sites naturally occur in coronaviruses. *Stem Cell Research* **50**, 102115 (2021).

277. Winstone, H. *et al.* The Polybasic Cleavage Site in SARS-CoV-2 Spike Modulates Viral Sensitivity to Type I Interferon and IFITM2. *Journal of Virology* **95**, (2021).

278. Hoffmann, M., Kleine-Weber, H. & Pöhlmann, S. A Multibasic Cleavage Site in the Spike Protein of SARS-CoV-2 Is Essential for Infection of Human Lung Cells. *Molecular Cell* **78**, 779-784.e5 (2020).

279. Mosca, J. D. & Pitha, P. M. Transcriptional and posttranscriptional regulation of exogenous human beta interferon gene in simian cells defective in interferon synthesis. *Mol Cell Biol* **6**, 2279–2283 (1986).

280. Hale, B. G. Avoiding culture shock with the SARS-CoV-2 spike protein. *eLife* **10**, e69496 (2021).

281. Ogando, N. S. *et al.* SARS-coronavirus-2 replication in Vero E6 cells: Replication kinetics, rapid adaptation and cytopathology. *Journal of General Virology* **101**, 925–940 (2020).

282. Lau, S.-Y. *et al.* Attenuated SARS-CoV-2 variants with deletions at the S1/S2 junction. *Emerging Microbes & Infections* **9**, 837–842 (2020).

283. Ou, T. *et al.* Hydroxychloroquine-mediated inhibition of SARS-CoV-2 entry is attenuated by TMPRSS2. *PLOS Pathogens* **17**, e1009212 (2021).

284. Sasaki Id, M. *et al.* SARS-CoV-2 variants with mutations at the S1/ S2 cleavage site are generated in vitro during propagation in TMPRSS2-deficient cells. (2021) doi:10.1371/journal.ppat.1009233.

285. Johnson, Bryan A. *et al.* Loss of furin cleavage site attenuates SARS-CoV-2 pathogenesis. *Nature* **591**, 293–299 (2021).

286. Dulbecco, R. & Vogt, M. Some Problems of Animal Virology as Studied by the Plaque Technique. *Cold Spring Harb Symp Quant Biol* **18**, 273–279 (1953).

287. Schmidt, F. *et al.* Measuring SARS-CoV-2 neutralizing antibody activity using pseudotyped and chimeric viruses. *Journal of Experimental Medicine* **217**, (2020).

288. Crawford, K. H. D. *et al.* Protocol and reagents for pseudotyping lentiviral particles with SARS-CoV-2 spike protein for neutralization assays. *Viruses* **12**, (2020).

289. Nie, J. *et al.* Establishment and validation of a pseudovirus neutralization assay for SARS-CoV-2. *Emerging Microbes and Infections* **9**, 680–686 (2020).

290. Tan, C. W. *et al.* A SARS-CoV-2 surrogate virus neutralization test based on antibody-mediated blockage of ACE2–spike protein–protein interaction. *Nat Biotechnol* **38**, 1073–1078 (2020).

291. Tan, C.-W. *et al.* Pan-Sarbecovirus Neutralizing Antibodies in BNT162b2-Immunized SARS-CoV-1 Survivors. *New England Journal of Medicine* **385**, 1401–1406 (2021).

292. Spinelli, M. A. *et al.* SARS-CoV-2 seroprevalence, and IgG concentration and pseudovirus neutralising antibody titres after infection, compared by HIV status: a matched case-control observational study. *The Lancet HIV* **8**, e334–e341 (2021).

293. Ortega, N. *et al.* Seven-month kinetics of SARS-CoV-2 antibodies and role of pre-existing antibodies to human coronaviruses. *Nat Commun* **12**, 4740 (2021).

294. Abani, O. *et al.* Convalescent plasma in patients admitted to hospital with COVID-19 (RECOVERY): a randomised controlled, open-label, platform trial. *The Lancet* **397**, 2049–2059 (2021).

295. Harvey, W. T. *et al.* SARS-CoV-2 variants, spike mutations and immune escape. *Nature Reviews Microbiology* 1–16 (2021) doi:10.1038/s41579-021-00573-0.

296. Pinto, D. *et al.* Broad betacoronavirus neutralization by a stem helix–specific human antibody. *Science* (2021) doi:10.1126/science.abj3321.

297. Cho, H. *et al.* Ultrapotent bispecific antibodies neutralize emerging SARS-CoV-2 variants. *bioRxiv* 2021.04.01.437942 (2021) doi:10.1101/2021.04.01.437942.

298. Tehrani, Z. R. *et al.* Performance of nucleocapsid and spike-based SARS-CoV-2 serologic assays. *PLOS ONE* **15**, e0237828 (2020).

299. Burbelo, P. D. *et al.* Sensitivity in Detection of Antibodies to Nucleocapsid and Spike Proteins of Severe Acute Respiratory Syndrome Coronavirus 2 in Patients With Coronavirus Disease 2019. *J Infect Dis* **222**, 206–213 (2020).

300. Allen, N. *et al.* Serological markers of SARS-CoV-2 infection; anti-nucleocapsid antibody positivity may not be the ideal marker of natural infection in vaccinated individuals. *Journal of Infection* (2021) doi:10.1016/j.jinf.2021.08.012.

301. Dan, J. M. *et al.* Immunological memory to SARS-CoV-2 assessed for up to 8 months after infection. *Science* eabf4063 (2021) doi:10.1126/science.abf4063.

302. Moriyama, S. *et al.* Temporal maturation of neutralizing antibodies in COVID-19 convalescent individuals improves potency and breadth to circulating SARS-CoV-2 variants. *Immunity* S1074761321002594 (2021) doi:10.1016/j.immuni.2021.06.015.

303. Gaebler, C. *et al.* Evolution of antibody immunity to SARS-CoV-2. *Nature* 1–10 (2021) doi:10.1038/s41586-021-03207-w.

304. Xiao, F. *et al.* Evidence for Gastrointestinal Infection of SARS-CoV-2. *Gastroenterology* **158**, 1831-1833.e3 (2020).

305. Hsieh, C.-L. *et al.* Structure-based design of prefusion-stabilized SARS-CoV-2 spikes. *Science* **369**, 1501–1505 (2020).

306. Edwards, R. J. *et al.* Cold sensitivity of the SARS-CoV-2 spike ectodomain. *bioRxiv* 2020.07.12.199588 (2020) doi:10.1101/2020.07.12.199588.

307. Khoury, D. S. *et al.* Neutralizing antibody levels are highly predictive of immune protection from symptomatic SARS-CoV-2 infection. *Nature Medicine* 1–7 (2021) doi:doi:10.1038/s41591-021-01377-8.

308. Gao, Q. *et al.* Development of an inactivated vaccine candidate for SARS-CoV-2. *Science* **369**, 77–81 (2020).

309. Tanriover, M. D. *et al.* Efficacy and safety of an inactivated whole-virion SARS-CoV-2 vaccine (CoronaVac): interim results of a double-blind, randomised, placebo-controlled, phase 3 trial in Turkey. *The Lancet* **398**, 213–222 (2021).

310. Thiagarajan, K. What do we know about India's Covaxin vaccine? *BMJ* **373**, n997 (2021).

311. Tatsis, N. & Ertl, H. C. J. Adenoviruses as vaccine vectors. *Molecular Therapy* **10**, 616–629 (2004).

312. Rosen, L., Baron, S. & Bell, J. A. Four Newly Recognized Adenoviruses. *Proceedings of the Society for Experimental Biology and Medicine* **107**, 434–437 (1961).

313. Logunov, D. Y. *et al.* Safety and immunogenicity of an rAd26 and rAd5 vector-based heterologous prime-boost COVID-19 vaccine in two formulations: two open, non-randomised phase 1/2 studies from Russia. *The Lancet* **396**, 887–897 (2020).

314. Bos, R. *et al.* Ad26 vector-based COVID-19 vaccine encoding a prefusion-stabilized SARS-CoV-2 Spike immunogen induces potent humoral and cellular immune responses. *npj Vaccines* **5**, 1–11 (2020).

315. Sadoff, J. *et al.* Safety and Efficacy of Single-Dose Ad26.COV2.S Vaccine against Covid-19. *N Engl J Med* **384**, 2187–2201 (2021).

316. Folegatti, P. M. *et al.* Safety and immunogenicity of the ChAdOx1 nCoV-19 vaccine against SARS-CoV-2: a preliminary report of a phase 1/2, single-blind, randomised controlled trial. *The Lancet* **396**, 467–478 (2020).

317. Zhu, F.-C. *et al.* Immunogenicity and safety of a recombinant adenovirus type-5-vectored COVID-19 vaccine in healthy adults aged 18 years or older: a randomised, double-blind, placebo-controlled, phase 2 trial. *The Lancet* **396**, 479–488 (2020).

318. CanSinoBIO's COVID-19 vaccine 65.7% effective in global trials, Pakistan official says. *Reuters* (2021).

319. Bangaru, S. *et al*. Structural analysis of full-length SARS-CoV-2 spike protein from an advanced vaccine candidate. *Science* **370**, 1089–1094 (2020).

320. Heath, P. T. *et al*. Safety and Efficacy of NVX-CoV2373 Covid-19 Vaccine. *New England Journal of Medicine* **0**, null (2021).

321. Shinde, V. *et al*. Efficacy of NVX-CoV2373 Covid-19 Vaccine against the B.1.351 Variant. *New England Journal of Medicine* **384**, 1899–1909 (2021).

322. Karikó, K. *et al*. Incorporation of Pseudouridine Into mRNA Yields Superior Nonimmunogenic Vector With Increased Translational Capacity and Biological Stability. *Molecular Therapy* **16**, 1833–1840 (2008).

323. Hassett, K. J. *et al*. Optimization of Lipid Nanoparticles for Intramuscular Administration of mRNA Vaccines. *Molecular Therapy - Nucleic Acids* **15**, 1–11 (2019).

324. Baden, L. R. *et al*. Efficacy and Safety of the mRNA-1273 SARS-CoV-2 Vaccine. *New England Journal of Medicine* **384**, 403–416 (2021).

325. Polack, F. P. *et al*. Safety and Efficacy of the BNT162b2 mRNA Covid-19 Vaccine. *New England Journal of Medicine* **383**, 2603–2615 (2020).

326. Hoffmann, D. *et al*. CVnCoV and CV2CoV protect human ACE2 transgenic mice from ancestral B BavPat1 and emerging B.1.351 SARS-CoV-2. *Nat Commun* **12**, 4048 (2021).

327. Lowe, D. CureVac Comes Up Short | In the Pipeline. //blogs.sciencemag.org/pipeline/archives/2021/06/17/curevac-comes-up-short (2021).

328. CureVac Provides Update on Phase 2b/3 Trial of First-Generation COVID-19 Vaccine Candidate, CVnCoV. *CureVac*

https://www.curevac.com/en/2021/06/16/curevac-provides-update-on-phase-2b-3-trial-of-first-generation-covid-19-vaccine-candidate-cvncov/ (2021).

329. Jewell, B. L. *et al.* Potential effects of disruption to HIV programmes in sub-Saharan Africa caused by COVID-19: results from multiple mathematical models. *The Lancet HIV* **7**, e629–e640 (2020).

330. Wong, E. B. *et al.* Convergence of infectious and non-communicable disease epidemics in rural South Africa: a cross-sectional, population-based multimorbidity study. **9**, 10 (2021).

331. Parker, A. *et al.* High HIV prevalence in an early cohort of hospital admissions with COVID-19 in Cape Town, South Africa. *South African Medical Journal* **110**, 982–987 (2020).

332. Inciarte, A. *et al.* Clinical characteristics, risk factors, and incidence of symptomatic coronavirus disease 2019 in a large cohort of adults living with HIV: a single-center, prospective observational study. *AIDS* **34**, 1775–1780 (2020).

333. Gervasoni, C. *et al.* Clinical Features and Outcomes of Patients With Human Immunodeficiency Virus With COVID-19. *Clinical Infectious Diseases* **71**, 2276–2278 (2020).

334. Sigel, K. *et al.* Coronavirus 2019 and People Living With Human Immunodeficiency Virus: Outcomes for Hospitalized Patients in New York City. *Clinical Infectious Diseases* **71**, 2933–2938 (2020).

335. Etienne, N. *et al.* HIV infection and COVID-19: risk factors for severe disease. *AIDS* **34**, 1771–1774 (2020).

336. Western Cape Department of Health in collaboration with the National Institute for Communicable Diseases, S. A. Risk Factors for Coronavirus Disease 2019 (COVID-19) Death in a Population Cohort Study from the Western Cape

Province, South Africa. *Clinical Infectious Diseases* (2020) doi:10.1093/cid/ciaa1198.

337. Bhaskaran, K. *et al.* HIV infection and COVID-19 death: a population-based cohort analysis of UK primary care data and linked national death registrations within the OpenSAFELY platform. *The Lancet HIV* **8**, e24–e32 (2021).
338. Chanda, D. COVID-19 Severity and COVID-19–Associated Deaths Among Hospitalized Patients with HIV Infection — Zambia, March–December 2020. *MMWR Morb Mortal Wkly Rep* **70**, (2021).
339. Hariyanto, T. I., Rosalind, J., Christian, K. & Kurniawan, A. Human immunodeficiency virus and mortality from coronavirus disease 2019: A systematic review and meta-analysis. *South Afr J HIV Med* **22**, 1220 (2021).
340. Weifenbach, N., Jung, A. & Lötters, S. COVID-19 infection in CVID patients: What we know so far. *Immunity, Inflammation and Disease* **n/a**,.
341. Dorward, J. *et al.* The impact of the COVID-19 lockdown on HIV care in 65 South African primary care clinics: an interrupted time series analysis. *The Lancet HIV* **8**, e158–e165 (2021).
342. Faust, L. & Raithby, L. The 100th Anniversary Of A Vaccine Against A Deadly Disease: Not A Cause For Celebration | Health Affairs Blog. https://www.healthaffairs.org/do/10.1377/hblog20210503.703348/full/.
343. Madhi, S. Safety and efficacy of the ChAdOx1 nCoV-19 (AZD1222) Covid-19 vaccine against the B.1.351 variant in South Africa. **19**, 1–26 (2021).
344. Sadoff, J. *et al.* Safety and Efficacy of Single-Dose Ad26.COV2.S Vaccine against Covid-19. *N Engl J Med* (2021) doi:10.1056/NEJMoa2101544.

345. Touizer, E. *et al.* Failure to seroconvert after two doses of BNT162b2 SARS-CoV-2 vaccine in a patient with uncontrolled HIV. *The Lancet HIV* **8**, e317–e318 (2021).

346. Sharing COVID-19 vaccines can help save lives. https://www.gatesfoundation.org/ideas/articles/covid19-vaccine-doses-covax.

347. Sigal, A. *et al.* Generation of a fluorescently labeled endogenous protein library in living human cells. *Nature protocols* **2**, 1515–27 (2007).

348. Huang, J. *et al.* Isolation of human monoclonal antibodies from peripheral blood B cells. *Nature protocols* **8**, 1907–15 (2013).

349. Morgenstern, J. P. & Land, H. Advanced mammalian gene transfer: high titre retroviral vectors with multiple drug selection markers and a complementary helper-free packaging cell line. *Nucleic acids research* **18**, 3587–96 (1990).

350. Carbonate-bicarbonate buffer stock (pH 9.2). *Cold Spring Harbor Protocols* **2011**, pdb.rec12398-pdb.rec12398 (2011).

351. Georgiev, I. S. *et al.* Delineating antibody recognition in polyclonal sera from patterns of HIV-1 isolate neutralization. *Science (New York, N.Y.)* **340**, 751–6 (2013).

352. Tiller, T. *et al.* Efficient generation of monoclonal antibodies from single human B cells by single cell RT-PCR and expression vector cloning. *Journal of Immunological Methods* **329**, 112–124 (2008).

353. Benckert, J. *et al.* The majority of intestinal IgA+ and IgG+ plasmablasts in the human gut are antigen-specific. *The Journal of clinical investigation* **121**, 1946–55 (2011).

354. Camus, J.-C., Pryor, M. J., Medigue, C. & Cole, S. T. Re-annotation of the genome sequence of Mycobacterium tuberculosis H37Rv | Microbiology Society.

https://www.microbiologyresearch.org/content/journal/micro/10.1099/00221287-148-10-2967#tab2.

355. Nimmo, C. *et al*. Population-level emergence of bedaquiline and clofazimine resistance-associated variants among patients with drug-resistant tuberculosis in southern Africa: a phenotypic and phylogenetic analysis. *Lancet Microbe* **1**, e165–e174 (2020).

356. Trombetta, J. J. *et al*. Preparation of single-cell RNA-Seq libraries for next generation sequencing. *Current Protocols in Molecular Biology* **2014**, 4.22.1-4.22.17 (2014).

357. Case, J. B., Bailey, A. L., Kim, A. S., Chen, R. E. & Diamond, M. S. Growth, detection, quantification, and inactivation of SARS-CoV-2. *Virology* **548**, 39–48 (2020).

358. Mendoza, E. J., Manguiat, K., Wood, H. & Drebot, M. Two Detailed Plaque Assay Protocols for the Quantification of Infectious SARS-CoV-2. *Current Protocols in Microbiology* **57**, (2020).

359. Balu, S. *et al*. A novel human IgA monoclonal antibody protects against tuberculosis. *Journal of immunology (Baltimore, Md. : 1950)* **186**, 3113–9 (2011).

360. Zimmermann, N. *et al*. Human isotype-dependent inhibitory antibody responses against Mycobacterium tuberculosis. *EMBO molecular medicine* **8**, 1325–1339 (2016).

361. Pinna, D., Corti, D., Jarrossay, D., Sallusto, F. & Lanzavecchia, A. Clonal dissection of the human memory B-cell repertoire following infection and vaccination. *European Journal of Immunology* **39**, 1260–1270 (2009).

362. Guinn, K. M. *et al.* Individual RD1-region genes are required for export of ESAT-6/CFP-10 and for virulence of Mycobacterium tuberculosis. *Mol Microbiol* **51**, 359–370 (2004).

363. Hsu, T. *et al.* The primary mechanism of attenuation of bacillus Calmette–Guérin is a loss of secreted lytic function required for invasion of lung interstitial tissue. *Proc Natl Acad Sci U S A* **100**, 12420–12425 (2003).

364. Yu, X. *et al.* Multiplexed Nucleic Acid Programmable Protein Arrays. *Theranostics* **7**, 4057–4070 (2017).

365. Lu, L. L. *et al.* A Functional Role for Antibodies in Tuberculosis. *Cell* **167**, 433-443.e14 (2016).

366. Ackerman, M. E. *et al.* A robust, high-throughput assay to determine the phagocytic activity of clinical antibody samples. *Journal of immunological methods* **366**, 8–19 (2012).

367. Gunn, B. M. & Alter, G. Modulating Antibody Functionality in Infectious Disease and Vaccination. *Trends in Molecular Medicine* **22**, 969–982 (2016).

368. Reljic, R. *et al.* Intranasal IFNγ extends passive IgA antibody protection of mice against Mycobacterium tuberculosis lung infection. *Clinical and Experimental Immunology* **143**, 467–473 (2006).

369. Rengarajan, J., Bloom, B. R. & Rubin, E. J. Genome-wide requirements for Mycobacterium tuberculosis adaptation and survival in macrophages. *PNAS* **102**, 8327–8332 (2005).

370. Chen, T. *et al.* Association of Human Antibodies to Arabinomannan With Enhanced Mycobacterial Opsonophagocytosis and Intracellular Growth Reduction. *Journal of Infectious Diseases* **214**, 300–310 (2016).

371. Huang, L. *et al.* The Deconstructed Granuloma: A Complex High-Throughput Drug Screening Platform for the Discovery of Host-Directed Therapeutics Against Tuberculosis. *Frontiers in cellular and infection microbiology* **8**, 275 (2018).

372. Yabaji, S. M., Dhamija, E., Mishra, A. K. & Srivastava, K. K. ESAT-6 regulates autophagous response through SOD-2 and as a result induces intracellular survival of Mycobacterium bovis BCG. *Biochimica et Biophysica Acta (BBA) - Proteins and Proteomics* **1868**, 140470 (2020).

373. Luukinen, H. *et al.* Priming of innate antimycobacterial immunity by heat-killed Listeria monocytogenes induces sterilizing response in the adult zebrafish tuberculosis model. *Dis Model Mech* **11**, dmm031658 (2018).

374. Vijayan, V., Wagener, F. A. D. T. G. & Immenschuh, S. The macrophage heme-heme oxygenase-1 system and its role in inflammation. *Biochemical Pharmacology* **153**, 159–167 (2018).

375. Kelley, V. A. & Schorey, J. S. Mycobacterium's Arrest of Phagosome Maturation in Macrophages Requires Rab5 Activity and Accessibility to Iron. *MBoC* **14**, 3366–3377 (2003).

376. Abdalla, M. Y., Ahmad, I. M., Switzer, B. & Britigan, B. E. Induction of heme oxygenase-1 contributes to survival of Mycobacterium abscessus in human macrophages-like THP-1 cells. *Redox Biology* **4**, 328–339 (2015).

377. Scharn, C. R. *et al.* Heme Oxygenase-1 Regulates Inflammation and Mycobacterial Survival in Human Macrophages during Mycobacterium tuberculosis Infection. *The Journal of Immunology* **196**, 4641–4649 (2016).

378. Banerjee, A. *et al.* Isolation, Sequence, Infectivity, and Replication Kinetics of Severe Acute Respiratory Syndrome Coronavirus 2. *Emerging infectious diseases* **26**, 4–7 (2020).

379. Alrubayyi, A. *et al.* Characterization of humoral and SARS-CoV-2 specific T cell responses in people living with HIV. *Nat Commun* **12**, 5839 (2021).

380. Sanders, K., Suleman, F., Yadav, P., Bradford Vosburg, K. & Sabot, O. Monoclonal Antibodies For COVID-19 In Africa: A Complex Web Of Opportunities And Challenges | Health Affairs Blog. https://www.healthaffairs.org/do/10.1377/hblog20210224.158341/full/.

381. ter Meulen, J. *et al.* Human Monoclonal Antibody Combination against SARS Coronavirus: Synergy and Coverage of Escape Mutants. *PLoS Medicine* **3**, e237 (2006).

382. Snyman, J. *et al.* Similar antibody responses against SARS-CoV-2 in HIV uninfected and infected individuals on antiretroviral therapy during the first South African infection wave. *Clinical Infectious Diseases* (2021) doi:10.1093/cid/ciab758.

383. Karim, F. *et al.* HIV status alters disease severity and immune cell responses in beta variant SARS-CoV-2 infection wave. *eLife* **10**, e67397 (2021).

384. Sziemel, A. M. *et al.* Development of highly potent neutralising nanobodies against multiple SARS-CoV-2 variants including the variant of concern B.1.351. *bioRxiv* 2021.04.11.439360 (2021) doi:10.1101/2021.04.11.439360.

385. Guruprasad, L. Human SARS CoV-2 spike protein mutations. *Proteins: Structure, Function, and Bioinformatics* **89**, 569–576 (2021).

386. Calu-3 | ATCC. https://www.atcc.org/products/htb-55.

387. Hu, W. T. *et al.* Antibody Profiles According to Mild or Severe SARS-CoV-2 Infection, Atlanta, Georgia, USA, 2020. *Emerg Infect Dis* **26**, 2974–2978 (2020).

388. Meyer, B. *et al.* Validation and clinical evaluation of a SARS-CoV-2 surrogate virus neutralisation test (sVNT). *Emerging Microbes & Infections* **9**, 2394–2403 (2020).

389. Robbiani, D. F. *et al.* Convergent antibody responses to SARS-CoV-2 in convalescent individuals. *Nature* (2020) doi:10.1038/s41586-020-2456-9.

390. Moyo-Gwete, T. *et al.* Cross-Reactive Neutralizing Antibody Responses Elicited by SARS-CoV-2 501Y.V2 (B.1.351). *New England Journal of Medicine* **384**, 2161–2163 (2021).

391. Sykes, W. *et al.* Prevalence of anti-SARS-CoV-2 antibodies among blood donors in Northern Cape, KwaZulu-Natal, Eastern Cape, and Free State provinces of South Africa in January 2021. *Res Sq* (2021) doi:10.21203/rs.3.rs-233375/v1.

392. Ng, K. W. *et al.* Preexisting and de novo humoral immunity to SARS-CoV-2 in humans. *Science* **370**, 1339–1343 (2020).

393. Kaplonek, P. *et al.* Early cross-coronavirus reactive signatures of humoral immunity against COVID-19. *Science Immunology* **0**, eabj2901.

394. Buchrieser, J., James, W. & Moore, M. D. Human Induced Pluripotent Stem Cell-Derived Macrophages Share Ontogeny with MYB-Independent Tissue-Resident Macrophages. *Stem Cell Reports* **8**, 334–345 (2017).

395. Karim, F. *et al.* HIV infection alters SARS-CoV-2 responsive immune parameters but not clinical outcomes in COVID-19 disease. *medRxiv* (2020) doi:10.1101/2020.11.23.20236828.

396. UNAIDS. Country factsheets: South Africa 2020. https://www.unaids.org/en/regionscountries/countries/southafrica.

397. Mukumbang, F. C., Kriel, E., Wyk, B. van & Kruger, J. A. Desperate times call for desperate measures: Adapting antiretroviral service delivery in the context of the COVID-19 pandemi. *South African Medical Journal* **110**, 711–712 (2020).

398. Mendelsohn, A. S. & Ritchwood, T. COVID-19 and Antiretroviral Therapies: South Africa's Charge Towards 90–90–90 in the Midst of a Second Pandemic. *AIDS Behav* **24**, 2754–2756 (2020).

Appendix A: Sequences of monoclonal antibody variable regions

Donor ID (last 4 digits)	**Well ID**	**Heavy chain (gamma) variable region**	**Light chain variable region**
6037	P1 F06	gaggtgcagctggtggagtctgggggaggcctggtcaagcctgggggtccctgagactctcctgtgcagcctctggattcaccttcagtagctatagcataaactgggtccgccaggctccagggaaggggctggagtgggtctcatccattagtagtagtagtaactacatttactacgcagactcagtgaagggccgattcaccatctccagagacaacgccaagaactcactgtatctgcaaatgaacagcctgagagccgaggacacggctgtgtattattgtgcgagaggacgaggatattgtactaatggtgtatgttataccgttgactactggggccagggaaccctggtcaccgtctcctcag	(Kappa light chain) gacatccagatgacccagtctccatcctccctgtctgcatctgtaggagacagagtcaccatcacttgccgggcaagtcagagcattagcagctatttaaattggtatcagcagaaaccagggaaagcccctaagctcctgatctatgctgcatccagtttgcaaagtggggtcccatcaaggttcagtggcagtggatctgggacagatttcactctcaccatcagcagtctgcaacctgaagattttgcaacttactactgtcaacagagttacagtacccctcgcacttttcggcggagggaccaaggtggagatcaaac

Donor ID (last 4 digits)	Well ID	Heavy chain (gamma) variable region	Light chain variable region
6037	P2 C02	gaagtgcaggtggtggagtctgggggaggcttagtacatccagggcggtccctgagactctcctgtacaacttctggattcacctttggtgattatcctatgagctgggtccgccgggctccagggaaggggctggagtgggtaggttttattagaggcaaagctgatggaggggcaacagagtacgccgcgtctgtgaaaggcaggttcaccatctccagagatgattccaaaagcgtcgcctttctgcatctgaacaatctgaaatccgaggacacagccgtatattttgtgctagagaagggggggactggttatcagacccatactactattccggcatggacctctggggccaagggaccacggtcaccgtctcctca	(Lambda light chain) cagtctgccctgactcagtccccctcagcgtctgggacccccgggcagaggtcaccatctcttgttctggaagcacctccaacatcgggactaactatgtgttctggtaccagcaacttcctggaacggcccccaaactcctcatctataaaaatagacagcggccttcaggggtccctgaccgcttctctggctccaagtctggcacctcagcctccctggccatcagtgggctccggtccgaggatgaggctgattatttctgtgcatcatgggatgacaagctgagtggttgggtgttcggcggagggaccaaactgaccgtccta
6037	P2 E04	gaagtgcagctggtggagtctggaggaggcttggcccagcctgggggtccctgagactctcctgtgcagcctctgggctcaccgtcagtagcaactacatgaactgggtccgccaggctccagggaaggggctggagtgggtctcagttatttttagcggtggtttcacatactatgccgactccgtgaaggccgattcaccatctccagacacaattcccagaacacggtctatcttcaaatgaacagcctgagacctgaagacacggccgtctattactgtgcgagagtccggagaagtggttaccgccaacccctaggtctggacgtctgggggccaagggaccacggtcaccgtcctcca	(Lambda light chain) cagtctgccctgactcagccgccctcagtgtctggggccccagggcagaggtcaccatctcctgcactgggagcagctccaacatcggggcaggttatgatgtacactggtaccagcagcttccaggaacagcccccaaactcctcatctatggtaacagcaatcggccctcagggtccctgaccgattctctggctccaagtctggcacctcagcctccctggccatcactgggctccaggctgaggatgaggctgattattactgccagtcctatgacagcagcctgagtggtgctgtggtattcggcggagggaccaagctgaccgtcctag

Donor ID (last 4 digits)	Well ID	Heavy chain (gamma) variable region	Light chain variable region
6037	P2 F10	caggttcagctggtgcagtctgga gctgaggtgaagaagcctggggcc tcagtgaaggtctcctgcaaggct tctggttacacctttaccagctac ggtatcagctgggtgcgacaggcc cctggacaagggcttgagtggatg ggatggatcagcgcttacaatggt aacacaaactatgcacagaagctc cagggcagagtcaccatgaccaca gacacatccacgagcacagcctac atggagctgaggagcctgagatct gacgacacggccgtgtattactgt gcgatcacccggtacgatttttgg agtggttattatgaagactcgata gactggggccagggaaccctggtc accgtctcctcag	(Lambda light chain) cagcttgtgctgactcaatcgccct ctgcctctgcctccctgggagcctc ggtcaagctcacctgcactctgagc agtgggcacagcagctacgccatcg catggcatcagcagcagccagagaa gggccctcggtacttgatgaagctt aacagtgatggcagccacagcaagg gggacgggatccctgatcgcttctc aggctccagctctggggctgagcgc tacctcaccatctccagcctccagt ctgaggatgaggctgactattactg tcagacctggggcactggctccctg gtgttcggcggagggaccaagctga ccgtcctag
6037	P2 G10	caggtgcagctgcaggagtcgggc ccaggactggtgaagccttcacag accctgtccctcacctgcactgtc tctggtggctccatcagcagtggt ggttactactggagctggatccgc cagcacccagggaagggcctggag tggattgggtacatctattacagt gggagcacctactacaacccgtcc ctcaagagtctagttaccatatca gtagacacgtctaagaaccagttc tccctgaagctgagctctgtgact gccgcggacacggccgtgtattac tgtgcgagaggggtattactatgg ttcgggggggccgaacaaactgg ttcgacccctggggccagggaacc ctggtcaccgtctcctcag	(Kappa light chain) gacatcgtgatgacccagtctccag actccctggctgtgtctctgggcga gagggccaccatcaactgcaagtcc agccagagtgttttatacagctcca gcaataagaactacttagcttggta ccagcagaaaccaggacagcctcct aagctgctcatttactgggcatcta cccgggaatccggggtccctgaccg attcagtggcagcgggtctgggaca gatttcactctcaccatcagcagcc tgcaggctgaagatgtggcagttta ttactgtcagcaatattatagtact cccttgacgttcggccaagggacca aggtggaaatcaaac

Donor ID (last 4 digits)	Well ID	Heavy chain (gamma) variable region	Light chain variable region
0219 (lymph node)	D02	(alpha heavy chain) caggtgcagctgcaggagtcgggc ccaggactggtgaagccttcggag accctgtccctcacctgcactgtc tctggtggctccatcagcagtagt agttactactggggctggatccgc cagcccccagggaaggggctggag tggattgggagtatctattatagt gggagcacctactacaacccgtcc ctcaagagtcgagtcaccatatcc gtagacacgtccaagaaccagttc tccctgaagctgagctctgtgacc gccgcagacacggctgtgtattac tgtgcgagactcgcggtctccaca tatagcagcagctggtacgtaacc tactactactactactacatggac gtctggggcaaagggaccacggtc accgtctcctcagca	(kappa) gacatccagatgacccagtctccak ycaccctgtctgcatctgtaggaga cagagtcaccatcacttgccgggcc agtcagagtattgataactggttgg cctggtatcagcagagaccagggag agcccctaacctcctgatctataag gcatctactttagagagtggggtcc catctaggttcagcggcagtggatc tgggacagaattcactctcaccatc agcagcctgcagcctgatgattttg caacttactactgccaacaatatag aacttattccaattttggccagggg accaagctggagatcaaacgaact
0219 (lymph node)	C03	(gamma heavy chain) cagctgcaactgcaggagtcgggc ccaggactggtgaagccttcggag accctgtccctcacctgcactgtc tctggtggctccatcagcactatt agttactactgggcctggatccgc cagcccccagggaagggactggag tggattgggagtatgtattatagt gggaacacctacttcaacccgtcc ctcaagagtcgggtcaccatatcc gtagacacgtccaagaaccaggtc tccctgaagctgaactctgtgacc gccgcagacacggctgtgtattac tgtgcgagacatgggggtatagca gtgcaaaacggtgacaactggttc gacccctggggccagggtaccctg gtcaccgtctcctcagcc	(lambda) cagtctgtgctgactcagccaccct cagcgtctgggacccccgggcagac ggtcaccatctcttgttctggaagc agctccaacatcggaaggaattatg tatactggtaccagcacctcccagg aacggcccccaaactcctcatctat aggaatgatcagcggccctcagggg tccctgaccgattctctggctccaa gtctggcacctcagcctccctggcc atcactgggctccggtccgaggatg aggctgattattcctgtacaacatg ggatgacagcctgagtggtcagata ttcggcggagggaccaagctgaccg tccta